DOTTORATO DI RICERCA IN
SCIENZE DELLA TERRA

CICLO XXXIII

COORDINATORE Prof. Lorella Francalanci

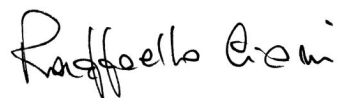# The genesis, transport and deposition of volcanic ash in the context of Vulcanian activity

Dottorando

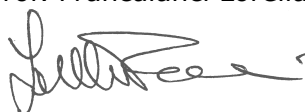Dott. Gabellini Pietro

Tutore

Prof. *Cioni Raffaello*

Co-Tutore

Dr. *Mattia de'Michieli Vitturi*

Coordinatore
Prof. Francalanci Lorella

Anni 2017/2020

Table of Contents

3. Eruptive dynamics and fragmentation mechanisms during cyclic Vulcanian activity at Sakurajima volcano (Japan)

4. Shear-induced, non-explosive magma fragmentation in Vulcanian activity: evidences from the 1888-90 eruption at La Fossa di Vulcano (Aeolian Islands)

5. Mechanisms of ash production and recycling during low-energy, mid-intensity eruptions: the March 2016 low-intensity activity of Copahue volcano (Argentina)

6. External features and internal structures of ash aggregates from Sakurajima volcano

7. Physical and aerodynamical parametrization of particle clusters at Sakurajima volcano

8. Conclusive remarks

9. References

Abstract

Key processes and parameters controlling the unsteady dynamics of low-to-mid intensity, high-frequency and cyclic 'Vulcanian' eruptions are to date only partially understood. Vulcanian eruptions are classically decribed as low-to-mid intensity and transitory phenomena involving only moderate amounts of tephra materials and resulting from the sudden pressure releases of an over-pressurized magma conduit. This classical definition, still widely used in the literature for the description of these eruptions, does not efficiently represent and entirely capture the natural complexity associated to these cyclic and transitory phenomena, which actually represents the typical and more frequent eruptive style of many active volcanoes around the world. The presented work aims to characterize and better constrain different aspects that are involved in the natural life-cycle of volcanic ash in the context of the mid-intensity, unsteady and cyclic Vulcanian activity.

In the recent years, volcanic ash has progressively claimed an increasing attention by the volcanological community, due to its high informative potential upon the dynamics of explosive eruptions. The study of tephra fallout products (i.e. ash, lapilli and ballistics projectiles) under a depositional and morpho-textural perspective has traditionally represented a valid approach in order to study the physical processes controlling explosive volcanism, and still now it is widely employed to intepret the erupive dynamics of ongoing explosive eruptions. The morphological and textural characterization of volcanic ash and ballistic products represents the basic data to intepret the compositional variability often encountered in the analysis of tephra products. The morpho-textural approach to the study of fallout products represent also a valuable analytical instrument for the understanding of the complex interplay between the different processes involving magma prior, during and after its fragmentation in the conduit, also in the case of the ash-dominated, Vulcanian-like eruptions. . In fact, the mutual interaction of these processes is interpreted as the main factor which actively controls the dynamics of cyclic and unsteady eruptions. For example, inside the conduit, different mechanisms of primary magma fragmentation and pre-fragmented material transport (e.g. fine ash elutriation) can superimpose, and the morpho-textural characterizatics of volcanic ash can provide important insights for discriminating the role of all these processes in affecting the style and the intensity of an eruption. On the other hand, the dispersal of high quantities of volcanic ash resulting from this high-frequency eruptive activity can represent a significant factor of risk for human activities (e.g. air transport) and infrastructures localized in the close proximity of active volcanoes (e.g. Casadeval 1994). Ash aggregation has proved to represent a key process able to largely control the atmospheric dispersal of volcanic ash and modify its ground deposition both in proximal and in distal areas. However, still now, the important effects of the aggregation process appear as not properly considered inside the numerical models aimed at forecasting the atmospheric dispersal of volcanic plumes. In fact, even the most recent numerical schemeslacks of an acceptable parametrization of the ash aggregation process and suffer of an inappropriate calibration of the forecasting results through affordable field data.

As a matter of facts, being the volcanic ash a common subject of all these lines of interest, this project is intended to investigate some of the main factors controlling the different stages of the ash life-cycle, from its genesis, to transport (within the conduit, inside the vent area and during plume dispersal), and finally to ground deposition. During this thesis, a large dataset of fallout tephra products was acquired and involved from ash, to ash aggregates and ballistic prjectiles, derived from a broad range of Vulcanian-like activity contexts (i.e. recent activity of Sakurajima volcano, Japan; 1888-1890 activity of Vulcano, Italy; March 2016 activity of Copahue, Argentina). The main morphological and textural features (i.e. GSD, Shape, internal texture) of the samples were accurately described, also in the light of the ongoing dynamic of the eruption (where possible), and quantitatively characterized. The obtained results allowed us to present innovative insights upon the complex dynamics that actively control the transitory and unsteady evolution of small-to-moderate scale, ash-dominated Vulcanian eruptions. In particular, we pointed out the main parameters controlling the shallow conduit dynamics of the recent Vulcanian activity of Sakurajima, the importance of alternative process of ash production in the context of the 1888-90 Vulcanian activity at La Fossa cone of Vulcano, and the importance of the ash recycling processes at Copahue volcano. Furthermore, the cyclic and high-frequency ash-dominated Vulcanian activity also represents a great opportunity to observe and characterize fallout tephra. In fact, field experiments aimed at a realistic description and quantitative characterization of natural volcanic ash aggregates were designed. The results contributed to singinfanctly extend the knowledge upon the systematics of aggregates populating vulcanian plumes, and to provide large database of filed measures which are of primary interest for the validation of numerical schemes aimed at a correct parametrization of the process of ash dispersal.

Table of Contents

3. Eruptive dynamics and fragmentation mechanisms during cyclic Vulcanian activity at Sakurajima volcano (Japan)

4. Shear-induced, non-explosive magma fragmentation in Vulcanian activity: evidences from the 1888-90 eruption at La Fossa di Vulcano (Aeolian Islands)

5. Mechanisms of ash production and recycling during low-energy, mid-intensity eruptions: the March 2016 low-intensity activity of Copahue volcano (Argentina)

6. External features and internal structures of ash aggregates from Sakurajima volcano

7. Physical and aerodynamical parametrization of particle clusters at Sakurajima volcano

8. Conclusive remarks

9. References

Chapter 1

Introduction

Overview

In this chapter a brief introduction is provided for all the principal topics of interest that will be addressed in this thesis. They concern various aspects of the life-cycle of volcanic ash produced during high-frequency, mid-intensity Vulcanian activity. A large dataset of samples was acquired from several ongoing eruptions and significant stratigraphic sequences, in order to capture as many aspects as possible of the variability of eruptive phenomena involved in the Vulcanian activity. Therefore, at the end of each introductive sections a brief presentation of the acquired datasets and samples is reported, together with the main aspects that characterized the investigated activity.

1.1 The unsteady, ash-dominated Vulcanian activity

Eruptive style is a function of magma composition, magma volatile content and crystallinity, exsolution and degassing processes, magma feeding and discharge rates, conduit geometry, magma reservoir pressure and can be modulated by the access of external water. Originally, in volcanology, explosive eruptions were classified according to qualitative observation on eruptive processes like ash plumes or the presence and type of pyroclastic density currents. Then, scientific studies evidenced numerous and straightforward links existing between the features of the erupted pyroclasts and specific mechanisms associated to the different eruptive styles (e.g. Heiken and Wholetz, 1985). This is valid for several eruption styles such as Plinian or Strombolian eruptions and Hawaiian fountaining. However, the classification and the objective description of vulcanian eruptions still represents a complex topic for modern volcanology, since Vulcanian eruptions encompass a wide spectrum of plume heights or magma compositions, being also occasionally associated to the emplacement and the repetitive destabilization of viscous lava domes (Clarke et al., 2015).

Vulcanian eruptions inherited their name from the accurate description of the AD1888-1890 eruption of La Fossa crater in the island of Vulcano (Aeolian Islands, Italy), provided by Mercalli and Silvestri (1891) (Fig. 1.1).

Fig. 1.1 A collection of images of the historical AD1888-1890 eruption of La Fossa di Vulcano cone (Vulcano), that gave the name to the class of 'Vulcanian eruptions'. Images display different moments of the eruption that account for important fluctuations observed in the plume eight and in the intensity of the explosions. Images taken by A. Silvestri in 'Le cronache di Mercalli'.

This term typically identifyies an impulsive and dynamically unsteady phenomenon, consisting in a series of discrete explosions, or, at least, a sequence of few blasts that result from the sudden decompression of an over-pressured, nearly static magma conduit (Hoblitt, 1986; Belousov et al., 2002; Driutt et al., 2002; Taddeucci et al., 2004; Diller et al., 2006; Clarke et al., 2013; Miwa et al., 2013b). The name 'Vulcanian eruption' is commonly used in the scientific literature to identify a wider spectrum of eruptive activities, involving low-to-mid intensity explosions, associated with the cyclic emission of variable amounts of volcanic ash and characterized by an unsteady eruptive dynamics, dominated by strong-transients in the intensity and style of the eruptions (Fig. 1.2) (e.g. Self et al., 1978; Ishihara 1985; Cas and Wright, 2012; Turcotte et al., 1990; Woods and Bower, 1995; Morrissey & Mastin, 2000; Clarke et al., 2002b; Clarke et al., 2013; Yokoo et al., 2013). A common feature of Vulcanian eruptions is their strict association with high viscosity magmas (Clarke et al., 2013).

Estimated plume height

| 100 - 500 m | up to 4500 m | 400 - 600 m |

Time duration of the eruptive phases

| 0 | 72 hours | 5-10 minutes | 30-60 minutes |
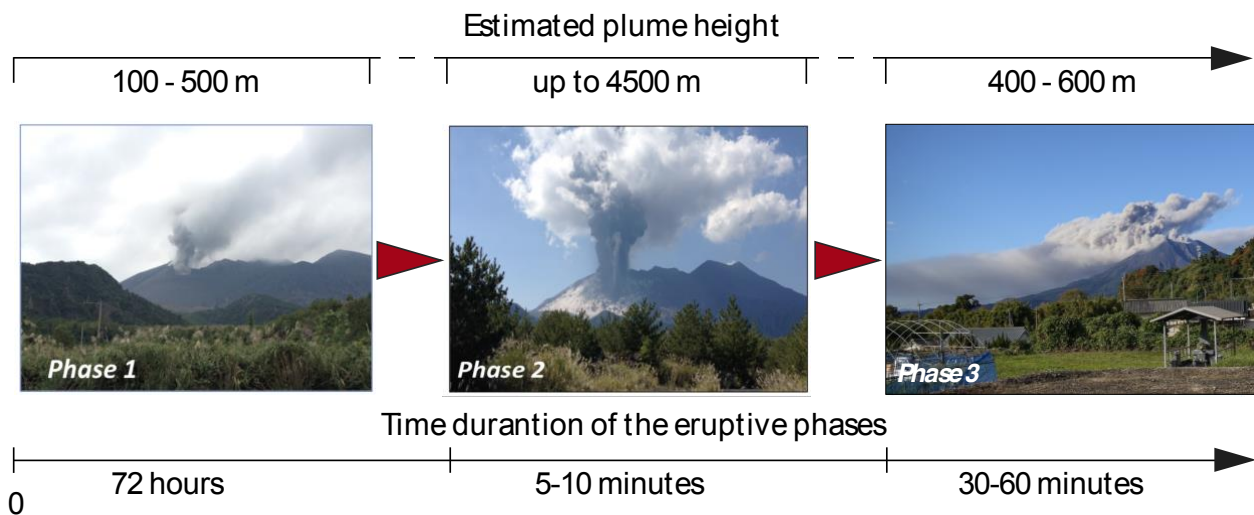
Fig. 1.2 Transitory phases during cyclic Vulcanian activity. This image footage represents the typical cyclic vulcanian activity at Sakurajima volcano (Kyushu, Japan), and display important variations both in intensity and in the style of the eruptions. In this case, the high unsteadiness of the eruptive dynamic is evidenced by sudden variations revealed for the estimated plume heights (above the crater terrace), which corresponds to very short-time intervals (the total duration of the event barely exceeds 3 days). Importantly, despite the scale of this eruption was moderate, important amounts of ash were dispersed in the atmosphere and in the vicinity of the volcano.

This low-to-mid scale, high-frequency explosive activity represents the typical behavior of many volcanoes worldwide, and important amounts of volcanic ash are emitted every year associated with this type of activity. However, the conduit dynamics and the conduit mechanisms controlling the high variability in the style and intensity of these eruptions appear to date still poorly understood, and often not fully investigated. In fact, the classical definition provided for Vulcanian eruptions only partially represents the natural complexity affecting the eruptive dynamics of this activity. Generally, Vulcanian eruptions are described as sudden pressure releases of an over-pressurized magma column resulting in a transitory event lasting from seconds to few minutes, and involving moderate amount of material (Clarke et al., 2013; Hall et al., 2015; Gaunt et al., 2020).

Several studies point out the presence of a viscous plug or dome at the top of the conduit that seals a progressively less viscous and gas-richer magma column; this configuration would represent the main factor responsible for the pressure charging of the system. It is almost clear that Vulcanian eruptions start as the internal pressure overcomes the cumulative contributes of both the gravity load and the tensile strength limit of the viscous plug or domes, formed at the top of the volcanic conduit by magma degassing and outgassing (loss of gas phases from the system). The plug disruption typically occurs in consequence of a progressive pressure increase localized in the underlying magma conduit, as a consequence of continuously uprising of the magma column (Hoblitt, 1986; Tait and Jaupart, 1989; Stix et al., 1997). Also, the ingression of phreatic water inside the system can induce an impulsive uprise of pressure into the conduit, due to sudden water vaporization, representing thus the trigger of explosions characterized by transient dynamics (Self et al., 1978; Zimanowski et al., 2015) (Fig. 1.3); these events have been described as Vulcanian eruptions, however it is important to distinguish them as phreatomagmatic eruptions.
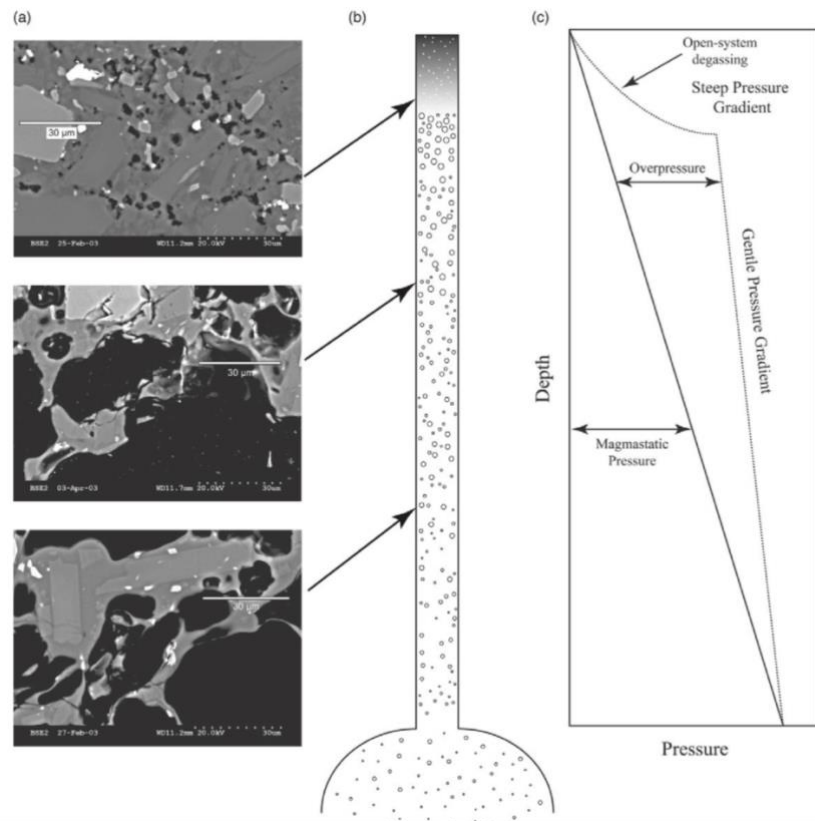
Fig. 1.3 Schematic representation of a magma conduit during a Vulcanian eruption (from Clarke et al., 2013). (a) The vertical layering of the magma conduit is clearly evidenced by the variation in the internal texture (i.e. vesicularity and crystal contents) with depth. (b) The layering of conduit due to outgassing promotes the formation of a degassed and highly crystallized magma plug (upward darker shaded area), in which bubble collapse progressively reduces permeability and gradually results in the sealing of the upper conduit, preventing further gas escape. (c) Magma pressure profiles corresponding with magma-static and over-pressurized state conditions can alternatively characterize the magma column, depending on the system degassing conditions. The ingression and vaporization of external water in the system can contribute to establish the overpressure.

Pre-explosion pressure can usually range from <1MPa up to 10MPa, in reason of both the tensile strength of the plug and the amount of volatile exsolution from magma. When plug dislodging occurs and the eruption starts, two simultaneous pressure waves are generated by the sudden decompression of the conduit. A decompression-induced wave closely followed by a fragmentation wave travel down into the magma column, while a shock wave propagates from the vent up to the atmosphere at the local speed of sound (or even higher). A mixture of gas and pyroclasts is thus ejected from the vent by the existing pressure differential, with a speed usually in the order of 400 ms^{-1}. The plume is typically not-sustained and typical durations of Vulcanian-triggered explosions span from minutes to hours. The vertically ascending plume generally result either in a buoyant (thermal force dominated) either in a momentum (inertial force dominated) plume, or in a combination of them (forced-thermal) (Clarke et al., 2013). Generally, plumes produced by Vulcanian eruptions do not rise up above 10 km in the atmosphere. Nevertheless, there are some extreme cases during which column heights above 10 km a.s.l. have been measured (Rose et al., 1978; Glaze et al., 1989; Stix et al., 1997; Druitt et al., 2002; Wright et al., 2007). Depending on the physical characteristics of the pyroclastic mixture (initial momentum) escaping from the vent, and on the atmospheric entrainment, pyroclastic density currents are likely to be associated with this volcanic activity (Hoblitt, 1986; Druitt et al., 2002; Clarke et al., 2002a).

As reported by Clarke et al. (2013), Vulcanian fall deposits are characterized by a wide range of dispersal areas and fragmentation degrees. They are typically thin and products range from meter-sized fragments to fine ash. The height of the plume is commonly not sufficient to induce a stratospheric injection even of the finest ash. Ballistic bombs of half meter in size can reach considerable distances (3-6 km) from the vent, thus imposing also a high risk to people living nearby (Waitt et al., 1995; de'Michieli Vitturi et al., 2010; Biass et al., 2016).

The total energy released during a single explosion is considerably lower with respect to Plinian and Sub-Plinian eruptions. The total amount of erupted magma rarely exceeds 0.1 km^3 DRE (Dense Rock Equivalent) and a mass in the order of $10^9 \sim 10^{11}$ kg (Morrissey & Mastin, 2000). This is partially explained by their highly unsteady vent conditions coupled with a not-sustained eruptive dynamics, which contributes to make them distinct from sustained and quasi-steady eruptions. This discrepancy takes rise from differences existing in the fragmentation dynamics (Turcotte et al., 1990; Woods and Bower, 1995), that in turn depend on several mutually connected factors like as the magma rheology, the overall eruptible magma volume and the discharge rate. However, it is important to note that the high-frequency and cyclic patterns of the activity often characterizing Vulcanian eruptions, make them able to eject large amounts of tephra in relatively short time lapses (from months to years). For example, according to data provided by Kagoshima Prefectural Government and Japan Meteorological Agency (JMA), Sakurajima volcano (Japan), in the period of a single year, dispersed in the atmosphere an estimated mass of ash-fall ranging between 32×10^8 kg (in 2009) and 66×10^5 t (in 2012) (excluding the mass of ballistics).

Because of the complex competing processes, the expected eruptive dynamics of a Vulcanian eruption sequence is difficult to predict. Vulcanian explosions could last up to few minutes, even if the typical duration of such events is generally limited to a single explosion of several seconds. However, in many instances, the explosion may be not discrete in time. It is frequent to observe the occurrence of an explosion sequence in a relative restricted time lapse (hours to days) with respect to the normal activity rate of the volcano (Clarke et al., 2013). This eruptive trend is very diffuse in the eruptive behavior of several volcanoes around the world. Furthermore, Vulcanian eruptions have been frequently observed as representing a transitional eruptive style which drives the process toward a low intensity effusive activity (Hoblitt, 1986; Melnik and Sparks, 2002, 2005), or toward a more energetic and sustained activity. As an example, Plinian activity in Mt. Pinatubo (1991), in Philippines, was introduced by a Vulcanian activity sequence (Clarke et al., 2013). The unsteadiness that often characterizes Vulcanian activity involves fluctuations of either the intensity and style of the eruption, and affects the eruptive pattern on a wide range of scales and times (seconds to hours or days). However, this latter topic appears as poorly defined and constrained in terms of how these fluctuations are related to the wide spectrum of processes occurring during transport of magma along the conduit, how these eruptive instabilities interact with processes of secondary fragmentation occurring within the vent area, or how they affect ash transport and dispersal in the plume.

Large parts of this thesis are devoted to give an objective description and quantitative characterization of the transients recorded in the style and intensity of Vulcanian eruptions. Chapter 3 is dedicated to

the interpretation of the key processes which control the eruptive dynamics of a typical cyclic, mid-intensity ash-dominated Vulcanian activity of Sakurajima volcano (Japan), in order to give insight on the causes of unsteadiness.

An large dataset of tephra fallout samples representative of the recent Vulcanian activity of Sakurajima volcano were collected during an eruptive sequence observed in October 2014. The common activity of Sakurajima consists of high-frequency, cyclic and transitory Vulcanian eruptions displaying important short-time variations both in the style and in the intensity of the explosions. Activity is lasting here from 1955 to present days, and therefore this constantly active volcano maybe represents one of the best case-study worldwide to directly investigate the Vulcanian activity.

Strong transients were observed in the studied cycle of Vulcanian activity at Sakurajima. Eruptive activity, in terms of the magma supply rates and conduit processes controlling the production of ash, was investigated monitoring the variations of in composition, in morphology and internal texture of the volcanic ash and lapilli samples, which were collected during distinct and representative phases of the ongoing activity. This allowed me to make inferences about the dominating effect of degassing and crystallization processes respect to magma supply rates in the control of eruptive style and intensity at Sakurajima. Results also provided important insights into the role of the different mechanisms of magma fragmentation and ash production occurring during complex-dynamic, cyclic Vulcanian eruptions.

1.2 Morphological and textural characterization of volcanic ash: an instrument to investigate dynamics of ash-dominated eruptions

A fundamental goal of modern volcanology is to relate conditions of magma ascent to the resulting eruptive style using information preserved in volcanic deposits. In the case of Vulcanian eruptions, this task has always suffered for several difficulties like the large variability of morphological, chemical, and physical characteristics of the products, for the logistic difficulties related with the direct sampling of ash-dominated eruptions (Heiken & Wohletz, 1985), and for the intrinsic difficulty to work on the past, generally thin deposits of these eruptions, easily erodible and badly preserved.

Before the occurrence of a vulcanian explosion, magma piles up in the conduit and generally experiences a prolonged storage during which differential crystallization and volatile exsolution (due to pressure and temperature variations) are likely to produce well defined textural and compositional gradients into the magma. All of those petrological processes are in general well resolvable in terms of textural and morphological variability of the erupted ash and ballistic ejecta.

Beside qualitative descriptions of the external ash features based on observations with scanning electron microscope (SEM) (Heiken & Wohletz, 1985), several approaches have been employed to quantitatively characterize volcanic ash shape, and a variety of shape descriptors have been introduced over the last few decades. Shape descriptors are mathematical functions that require previous determination of

dimensional variables, such as values of length, diameter, perimeter, area or volume. A well-known class of shape descriptors are the 1D form factors (e.g. flatness and elongation), that are defined based on the particle lengths measured in three dimensions. These parameters are useful to calculate the 2D shape descriptors, which are determined through image analysis of particle shape projected in two-dimensional space (also called shadowgraphs or silhouettes) (Dellino and Liotino, 2002; Riley et al., 2003; Lin and Miller, 2005; Ersoy et al., 2010; Mills and Rose, 2010; Asahina and Taylor, 2011; Garboczi et al., 2012; Ersoy et al, 2010; Alfano et al., 2011). Quantitative textural characterization of the erupted products involves an exhaustive description of the physical characteristics for both vesicle and crystals, together with a quantification of their volumetric abundancy (Crystallinity, Vesicularity) and distribution (Vesicle number density, VND; Microlite number density, MND; Crystal size distribution, CSD) (Sparks and Brazier 1982; Houghton and Wilson 1989; Marsh 1988, 1998; Toramaru 1989, 1990; Cashman et al., 1992; Cashman and Blundy 2000; Higgins 2000; 2006; Burgisser and Gardner, 2004; Giachetti et al., 2010; shea et al., 2010; 2017). Information about the textural features of volcanic ash has been largely used by volcanologists to investigate a variety of processes controlling the dynamics and the style of explosive eruptions (e.g. Cashman and Marsh 1988; Hammer et al., 1999; Cashman & Hoblitt, 2004; Shea et al. 2010; Rust and Cashman 2011; Cioni et al., 2014; Cashman, 2020). For example, data on MND were used to infer the degassing and decompression rates of magma during ascent (e.g. Hammer et al., 1999; Noguchi et al., 2006, 2008; Toramaru et al., 2008; Befus et al., 2015), and CSD was used to estimate modalities of magma emplacement and crystallization kinetics (e.g. Marsh, 1988; Mangan, 1990; Higgins et al., 1996). Together, ash componentry, shape, crystallinity, vesicularity, density and H_2O contents in residual glass represent precious information which are very useful for the understanding of the complex processes that actively controls the dynamics of high-unsteady Vulcanian eruptions (Taddeucci et al., 2004; Yamanoi et al., 2008; Miyagi et al., 2010; Cas and Wright, 2012; Miwa et al., 2013b).

In the first, pioneering work of Heiken & Wohletz, (1985), information about morphology of volcanic ash particles was correlated to different eruptive styles and dominant conditions of magma fragmentation. The work evidenced the importance of the study of volcanic ash from a morpho-textural perspective, and declared it as a fundamental instrument for the investigation of the complex interplay between conduit processes that actively controls the eruptive dynamics of the low-to-mid intensity activity. After this seminal work, several theoretical and experimental studies (e.g. Rust and Cashman 2011; Gonnermann and Houghton 2012; Degruyter et al. 2012; Nguyen et al. 2013; Schmith et al., 2017) proved that magma viscosity, ascent rate, vesiculation processes, fragmentation style and explosion dynamics all efficiently imprint characteristic and measurable properties on the groundmass textures and morphology of volcanic ash particles. In fact, volcanic ash was also used to investigate and interpret the evolutive dynamics of explosive eruptions, showing high-transients in the style of activity (e.g. Miwa et al., 2009; Miwa et al., 2013b; Cioni et al., 2014). For example, the morpho-textural approach was employed for past eruptions to discriminate between the occurrence of purely magmatic and/or magma–water interactions processes (e.g. Dellino and La Volpe, 1996a; Büttner et al., 1999; Ersoy et al., 2007; Cioni et al., 2008) or it was commonly used to infer the magma discharge rates

and eruptions dynamics (Taddeucci et al., 2002; Andronico et al., 2009; Miwa et al., 2009; Wright et al., 2012; Eychenne et al., 2015; Cioni et al., 2014). This information is crucial to understand the dynamics of open-vent volcanic systems, where short-lived paroxysms may occur, in both basaltic, such as Etna, Stromboli and Kilauea, (Taddeucci et al., 2002; Andronico et al., 2009; Schiavi et al., 2010; Eychenne et al., 2015) and more evolute andesitic-dacitic contexts dominated by cyclic Vulcanian activity, like Colima, Merapi, Sakurajima and Tungurahua (Savov et al., 2008; Yamanoi et al., 2008; Wright et al., 2012; Eychenne et al., 2013 and references therein). Routine monitoring of volcanic ash characteristics was also used in the follow up of ongoing eruptions, where the occurrence of juvenile ash grains in the fallout deposits of phreatic outbursts has been interpreted as precursory signals of incoming magmatic eruptions (e.g. Watanabe et al., 1999; Cashman & Hoblitt, 2004; Suzuki et al., 2013). In particular, morphological, textural and granulometric studies of volcanic ash produced during explosive activity represent one of the few existing analytical techniques which provide detailed insights into the mechanisms of fragmentation, and help to shed light on the interactions between the different processes implicated in the magma ascent along the conduit (Heiken and Wohletz, 1985; Sheridan and Marshall, 1987; Palladino and Taddeucci, 1998).

Information on the shape of ash grains has been also used to examine transport-related processes in the context of volcanic plumes dispersal (Riley et al., 2003; Mele et al., 2011). Distinctive features of Vulcanian activity are the coarse ballistic ejecta, which represent fragments of the dislodged viscous plug as well as of deeper portions of the magma column (Wright et al., 2007; Gaunt et al., 2020) that are involved in the fragmentation during higher intensity explosions. Together with the analysis of ash fragments, the study of petrographic and textural features of these ballistic blocks, including also componentry analysis and information about their distribution all around the crater area, can give important hints about the vertical and/or lateral layering of the conduit in terms of textural characteristics of the piled magma (e.g. Wright et al., 2007). Textural analysis of both ash and ballistics products, along with information about trends recorded in the eruptive activity, are crucial to obtain an accurate and realistic interpretation of the volcanic conduit architecture (Wright et al., 2003; Wright et al., 2007). The sizes, trajectories, ranges and the internal textures of blocks are also very useful to derive pre-explosion and vent conditions, and to make inferences on possible fluctuations in the intensity of the eruptions during a prolonged eruptive sequence (Benage et al., 2014).

Furthermore, size and shape of the ash particles play an important role in various processes, with large implications for the assessment of hazards connected to dispersion and sedimentation of volcanic particles (Wilson and Huang, 1979; Bonadonna et al., 1998; Dellino et al., 2005; Scollo, 2005; Coltelli et al., 2008; Alfano et al., 2011), and to aviation and public health (Horwell et al., 2003; Horwell and Baxter, 2006; Rose and Durant, 2009; Durant et al., 2009; Alfano et al., 2011).

As a matter of facts, quantitative characterization of both morphological and textural features of volcanic ash particles represent together a powerful instrument to investigate the eruptive dynamics and further connected aspects with the ash transport along the conduit and into the plume. Morpho-textural analysis of the ash has been extensively used in this study to extract information about selected ash deposits, in order to make inferences and provide insights into the processes responsible for the magma

transport inside the conduit, fragmentation and ash dispersal. In particular, in Chapter 3 these data are used to discuss eruption dynamics of an entire cycle of explosion at Sakurajima volcano (Japan).

A set of samples collected at Copahue volcano (Chile, Argentina) was used, in conjunction with the results of a coupled geophysical monitoring, to draw information about fragmentation processes and low-intensity ash dispersal. Results of this study are presented and discussed in Chapter 5. Several tephra fallout samples were collected from the low-intensity, continuous ash-dominated eruption of Copahue volcano during five-day sampling in February-March, 2016. Activity of Copahue in that period consisted in a low-level emission of ash, without major explosions. Information derived from the infrasound monitoring of the activity was combined with evidences extracted from the compositional and morpho-textural analysis of the collected ash in order to infer the dynamics of magma fragmentation in the context of low-energy driven activity. Textural features revealed for the analyzed ash also allowed us to make inferences on the importance of ash recycling processes operating during low-intensity, ash-dominated eruptions.

1.3   The genesis of volcanic ash: explosive vs. non-explosive, shear-induced magma fragmentation processes

Several studies have evidenced that the grain size distribution and the morphological features of ash fragments are basically related to the combination of local magma properties (e.g. porosity, viscosity, permeability) and the specific mechanism/s operating during the fragmentation of magma (Cashman & Scheu, 2015). At fragmentation, a continuous liquid phase with dispersed gas bubbles is transformed into a gas phase with dispersed magma fragments (pyroclasts). The formation of volcanic ash from highly viscous melts (typical of Vulcanian eruptions) can be typically reconducted to three mechanisms of magma fragmentation. Frequently, all these fragmentation mechanisms can coexist in the same eruptive event (e.g Heiken and Wohletz, 1985; Clarke et al., 2013; Liu et al., 2017), leaving a complex imprint on ash morphology and texture. The first, highly efficient mechanism of magma fragmentation is driven by the exsolution of volatiles from the magma in the conduit, as a consequence of the decompression experienced by magma during ascent toward the surface. This is the most frequent process driving explosive eruptions and it is generally interpreted as a rigid response of the melt to a rapid expansion of bubble due to decompression. A second fragmentation mechanisms involves the interaction between magma and phreatic or 'free surface' water, which can be present in the surroundings of the volcanic conduit. The direct interaction between magma and liquid water can result in the explosive fragmentation of magma, usually producing very large amounts of fine fragments (e.g. Sheridan and Wohletz, 1983; Wohletz, 1986). The last fragmentation mechanism is driven by the sudden release of a pressurized mixture of gas or vapor phase accumulating in a portion of a nearly static magma column with strong internal permeability gradients. This involves the break-up and comminution of the overlying magma and vent walls by the outward directed blast, as well as the downward

propagation of a decompression wave able to fragment part of the lower portions of the magma column. In some cases, this process results in the production of coarse material without directly involving the still active portions of magma (Alidibirov and Dingwell, 2000).

Beside these classical fragmentation mechanisms, in which ash is produced as a consequence of some kinds of explosive process, other non-explosive mechanisms have been postulated for the fragmentation of magma and for the corresponding genesis of ash.

Cashman et al., (2008) showed the efficiency of non-explosive ash production mechanisms inside fault-gauges as a consequence of the shear-induced comminution of viscous magma along the walls of a slow extruding lava dome. The shear-induced mechanisms of rock failure and comminution is a well-known mechanism in structural geology as related to faults dynamics, and it was recently shown as related to vent and conduit dynamics dominated by slow ascent of an extensively degassed magma, like those typical of the Vulcanian activity (Tuffen & Dingwell, 2005; Tuffen et al., 2008; Castro & Dingwell, 2009; Gaunt et al., 2016). This non-explosive mechanism of magma fragmentation could be responsible for the production of important quantities of comminuted materials, particularly in those systems characterized by high-silica magma (dacite-rhyolite) and slow ascent rates of the magma column, which are typically dominated by the presence at the top of the conduit of a viscous magma plug or of an extruding lava dome (Cashman, 2008). This is particularly evident in case of explosion pulses occurring at a very high frequency and low energy (as an example, during the 1888-90 eruptions of Vulcano Islands, Mercalli described low energy phases of activity characterized by dozens of explosions for day), for which it is difficult to hypothesize a classical process of magma fragmentation largely disrupting the upper portions of the magma column during each pulse. Therefore, this non-explosive process of ash production clearly represents one of aspects of Vulcanian activity which should deserve great attention by the scientific community, since it represents to date a not well accounted and studied topic. Evidences directly observable on coarse fragmented material also suggest that this process can produce significant quantities of pre-fragmentated and comminuted material, which can be made available during the sudden release of a gas overpressure related to each Vulcanian pulse.

Ash dispersed during Vulcanian events can so derive both from the active, explosive fragmentation of magma, or from the involvement of previously fragmented portions of the magma plug. In addition, the pulsating character of Vulcanian activity generally results in the accumulation of considerable amounts of fragmented material in the crater area (Cashman et al., 1992). This material clearly follows a complex thermal history, with the iteration of cooling-quenching cycles, when involved in the eruptive plume, and periods of re-heating in the hot ambient of the crater. The role of this material in eruptive dynamics should be carefully evaluated, and the implications in plume dynamics during atmospheric dispersal are all topics currently poorly (or not at all) considered by the state-of-the-art models describing Vulcanian activity. In fact, the presence of important quantities of hot, vent hosted materials may deeply influence the thermodynamic stability of the plume during both the thermal convective and the wind advective phases, thus influencing the mid-to-long range tephra dispersal (D'Oriano et al., 2014).

Investigation on the long-lasting storage of pre-fragmentated materials is also important in order to assess the role of the ash recycling processes in modifying the general energy balance of ash production.

Experiments of ash particle reheating (D'Oriano et al., 2013, 2014; Deardorff and Cashman, 2017) show that the textural and morphological features of volcanic ash can be used to identify and track the occurrence of intra-crateric recycling processes. The impact of these processes could be particularly important in moderate scale, low-energy, ash-dominated eruptions.

A detailed description of the ash characteristics is useful to resolve the competing imprints of all the different fragmentation processes and to define the role of different mechanisms of ash formation, in the way of defining a general balance for the ash production in Vulcanian activity contexts (e.g. Taddeucci et al., 2002; Yamanoi et Al., 2008; Miwa et al., 2009; Miyagi et al., 2010; D'Oriano et al., 2011; Wright et al., 2012; Miwa et al., 2013a; Cioni et al., 2014).

All the samples datasets that were previously presented were used to make inferences on the modalities of magma fragmentation and aspects connected with the transport of produced ash along the conduit.

In particular, ash samples from Copahue volcano (Chapter 5) were used to highlight the importance of the processes of ash recycling in the interpretation of eruptive dynamics, and for the ash plume dispersal. Conversely, samples collected at Sakurajima (Chapter 3) were used also to investigate alternative mechanisms of magma fragmentation, both in the low and in the high-intensity phases. Finally, in Chapter 4, a set of samples was collected from the historical activity of Vulcano (AD 1888-1890) and mostly used to explore the alternative processes of ash production by mechanical, non-explosive fragmentation of magma. Ash samples were used to characterize the eruptive dynamics of the 'original' activity giving the name to the Vulcanian eruptions style. Two stratigraphic sequences of ash fallouts, resulting from the first ash-dominated phase of the activity, were accurately described and the ash nature and morphometry characterized in order to monitor eventual transients in the activity and interpret them in the light of variations revealed in the characteristic of produced ash. At the same time, coarse ballistic ejecta were described in the field and classified according to their external and internal textrual features. Comminuted, partially welded and veins-hosted ash fragments (from coarse to fine ash) were revealed to extensively characterize the brecciated regions of numerous dense blocks. Morpho-textural features of comminuted materials were characterized and used to investigate the role of both the non-explosive, shear-induced magma fragmentation process, and of pre-fragmented ash elutriation process in the context of the general balance of ash production during Vulcanian activity.

1.4   Processes of ash transport and atmospheric dispersal: the importance of ash aggregation

Hazards related to Vulcanian activity generally concern a restricted area around the volcanic edifice and they are almost never related to a global effect, such as it may occurs in case of Plinian or even Sub-Plinian events. Nevertheless, Vulcanian explosions cannot be underestimated since they may have significant effects on local populations, and they can represent an effective risk for aviation (e.g. Clarke et al., 2013; Durant, 2015) because of the large amount of fine ash ejected in the first 10 km of the

atmosphere. At a global scale, large amounts of volcanic ash are continuously dispersed into the atmosphere by several volcanoes characterized by cyclic, ash-dominated Vulcanian activity. Atmospheric dispersal of volcanic ash represents a serious risk for a variety of human activities located not only in the close proximity of active volcanoes. In fact, it is recent in the memory the heavy impact that the ash-dominated and prolonged 2010 eruption of Eyjafjallajökull volcano (Iceland) had on the European economy. Dispersal and deposition of ash during explosive eruptions strongly affect the surrounding environment and distal atmosphere, with important hazards posed to agriculture and public health, and disruptive consequences on local communities and both land and aviation transport (Blong, 1984; Guffanti et al., 2010). Air-borne formation of ash aggregates is well known to affect sedimentation of eruptive plumes, and particularly of finer ash fractions (< 64 µm). Formation of particle clusters considerably modifies the residence time of ash into the atmosphere (e.g. Lane et al., 1993; Brown et al., 2012; Durant, 2015). The fate of a single particle, and its residence time before settling, are mostly controlled by size, density and by the air drag (which depends on the shape) of the particle. Consequently, the type/s of formed aggregates (and hence the associated physical parameters) is of primary importance (Rose & Durant, 2011). Based on the combined effects of these variables, the fate of an ash aggregate could result in a variation of the residence time into the atmosphere respect to what predicted based on gravitational settling of single ash grains (Durant, 2015). Therefore, consideration of the contribution of particle aggregation to ash settling dynamics is fundamental for the implementation and adoption of numerical models for volcanic ash transport and ash dispersal forecasting. Otherwise, dispersal models can fail to accurately describe both particle deposition in proximal areas and atmospheric ash concentration in the far field, with important implications for both hazard assessment and real-time ash forecasting (e.g. Brown et al., 2012; Folch et al., 2010).

The importance of aggregation on ash dispersal is widely recognized by the scientific community; following the pioneering work of Moore and Peck (1962), and starting from the first experimental works of Gilbert and Lane (1994) and Schumacher and Schmincke (1995), several studies reported accurate descriptions of ash aggregates observed during fallout or in pyroclastic deposits of past eruptions, (Brown et al., 2012 and references therein). As a result, many efforts have been made to improve the description of aggregates and our understanding of aggregation processes (e.g., James et al., 2002, 2003; Bonadonna et al., 2002a, 2011; Taddeucci et al., 2011; Brown et al., 2012; Bagheri et al., 2016a, Burns et al., 2017; Vogel et al., 2019; Van Eaton et al., 2012, 2013), as well as to provide increasingly accurate numerical descriptions for more effective hazard assessments (Cornell et al., 1983; Veitch and Woods 2001; Bonadonna et al., 2002b; Textor et al., 2006; Costa et al., 2010). Despite the importance of aggregation, due to the low preservation potential of particle clusters in tephra-fallout deposits, only a few examples exist documenting the fundamental physical and aerodynamic parameters of ash aggregates, such as their bulk density, terminal velocity and size distribution of the constitutive particles (Bonadonna et al., 2002a, 2011; Taddeucci et al., 2011; Van Eaton et al., 2012; Bagheri et al., 2016a; Burns et al., 2017; Miwa et al., 2020). The lack of detailed and ground-based data for ash aggregates importantly affects the reliability of numerical model results (Brown et al., 2012). Recently, the direct filming of falling aggregates during eruptions has emphasized the importance of a field-based approach

to study particle clusters ('*PC*', according to the nomenclature introduced by Brown et al., 2012). In fact, such a strategy allows for the direct measurement or derivation of physical and aerodynamical parameters of particle clusters, before they disrupt at the moment of impact on the ground (Taddeucci et al., 2011; Bagheri et al., 2016a; Miwa et al., 2020). Quantifying the aerodynamics and the internal structure of different types of aggregates represents an important topic to be addressed by the scientific community. Particularly, particle clusters deserve high attention since they are rarely preserved in the deposits, despite their occurrence is very common also in plumes dominated by dry conditions. The production of a comprehensive database that accurately describes the physical and aerodynamical characteristics of volcanic ash aggregates is of primary importance for the validation and calibration of numerical schemes that describe particle aggregation.

Importantly, ash aggregation processes are interesting to be studied as associated with the considered mid-intensity, ash-dominated eruptions, as the unsteadiness in the eruptive parameters can deeply influence and thus illuminate the mechanisms and modalities controlling the airborne formation of aggregates.

Chapter 7 of this work is aimed at providing better constraints to the different processes of ash aggregation, especially for what concerns the textural and physical parameters typical of the different types of ash aggregates. To do this, a large dataset of natural volcanic ash aggregates and tephra samples was directly collected at Sakurajima volcano during an ongoing, intermittent sequence of activity (July-August, 2013). In Chapter 8, aggregates were used to provide a first comprehensive dataset of the internal structure (morphometry of the core and thickness of the aggregating shell), aerodynamical properties (e.g., size, density, terminal velocity) and grain size of constituting particles of a variety of aggregate types. Properties were derived based on the combination of High-Resolution-High-Speed videos, Scanning Electron Microscope analysis of aggregates collected on adhesive paper and analysis of bulk tephra samples. Information on the grain size of tephra samples was used to infer a correlation with the grain size of shells and with the internal cores of aggregates, confirming thus the key role played by aggregation processes in fine ash deposition at Sakurajima.

Chapter 2

Sampling and Analytical Methods

Overview

This thesis deals with different aspects connected with the genesis and transport of both volcanic ash and ballistic blocks. Therefore, a large variety of methodologies and technical instrumentations was employed during sample collection and data processing. The samples collection was performed in association with different research groups from different universities (University of Florence (LGS lab), University of Geneva, and University of Pisa) depending on the specific case-study; further details will be provided inside the dedicated chapters.

In this chapter are presented the main methods and procedures adopted for the collection of volcanic ash samples from ongoing activities (e.g. Sakurajima and Copahue samples, in Chapters 3 and 5), for their post-processing and for the evaluation of the uncertainties related with the measured quantities. The different techniques and instrumentations used for volcanic ash analysis will be accurately described, in order to make the obtained results the more reproducible as possible. However, specific information concerning the analyzed ash samples (e.g. number of samples, or sites of data collection) will be provided directly in the dedicated chapters. This is valid also for very specific and dedicated experiments employed in the investigation of ballistic blocks dispersion (Chapter 4) and natural aggregates collection (Chapter 6-7), and also for the estimation of the relative uncertainties.

2.1 Sampling of volcanic ash samples and grain size distributions of total deposits

In the case of direct ash collection from an ongoing activity samples of total tephra fallout were collected placing plastic trays of variable size and for a variable time in the field, possibly in the close proximity of the eruptive plume. According to the dominant wind velocity that affected plume dispersal, ash samples were often collected at different sites. The trays are generally placed in appropriate places to avoid from possible contamination due to ash resuspension, and stored in sealed plastic bags to be carried in the labs. A standard laboratory procedure was then adopted in order to process and analyze the collected ash samples.

Ash samples were initially dried in oven (80 degree for 24 hours), in order to avoid from possible aggregation of particles due to inherited humidity, and then weighted. The grain size distribution (GSD) of deposits was measured by splitting the sample into a coarser fraction (size-classes coarser than 250 µm), which was processed using mechanical sieving, and a finer fraction (size-classes below 250 µm), which was instead analyzed using an automatic particle analyzer (Morphologi G3SE[TM] by Malvern Panalytical Instruments[TM]) at the Earth Science Dept., University of Florence. Resulting GSDs respectively of the coarser and the finer deposit fraction, were then merged to provide the total GSD curve, assuming equivalence between volume-based and weight-based percentages for the <250 µm fraction of deposits. The size-dependent heterogeneities in vesicularity and composition is generally moderate in the analyzed samples, therefore, the variability in the density of the different constituents populating this finer grained fraction is very low (see for example Bagheri et al., 2016 for what concerns typical density values of Sakurajima ash particles).

The Morphologi G3se from Malvern (Fig. 2.1) is an innovative automated optical particle analyzer useful for the statistic characterization of the particle size and morphometrics (Leibrandt et al., 2015).

Fig. 2.1 Morphologi G3se, from Malvern
Panalytical[TM].

The instrument is normally used in the medical industry for the quality control of granular materials since it allows the rapid investigation of large numbers of grains (e.g. 10^6 particles analyzed in about 1 hour). Differently from the dynamic particle-size analyzer, based on the laser-diffraction method (Storti and Balsamo, 2010), it operates in a static condition. It yields a set of geometrical measurements and indexed bitmap images of the single particles, that turns into a robust statistic morphometrical and morphological features of the apparent projected external particles outline (APASH: Leibrandt et al., 2015). The optical module, is provided with five different magnifications (2.5x, 5x, 10x, 20x, 50x) and it is coupled with a 5 MPixel CCD camera, that ensures a high-sensitivity, high-resolution analysis for particles comprised in a range from several millimeters down to sub-microns in size. The software unit, dedicated to the analysis of images, extracts a set of primary and derived parameters that fully describe the morphometrics of particles projected on the two-dimensional (2D) plane. In fact, image analysis

captures a 2D image from a 3D particle, and calculates various size and shape parameters from this 2D image. Therefore, in the process of the GSD calculation, the size of volcanic ash particles is estimated as the circular equivalent diameter (D_{eq}), defined as the diameter of the circle with the same area as the 2D image of the particle (Fig. 2.2).
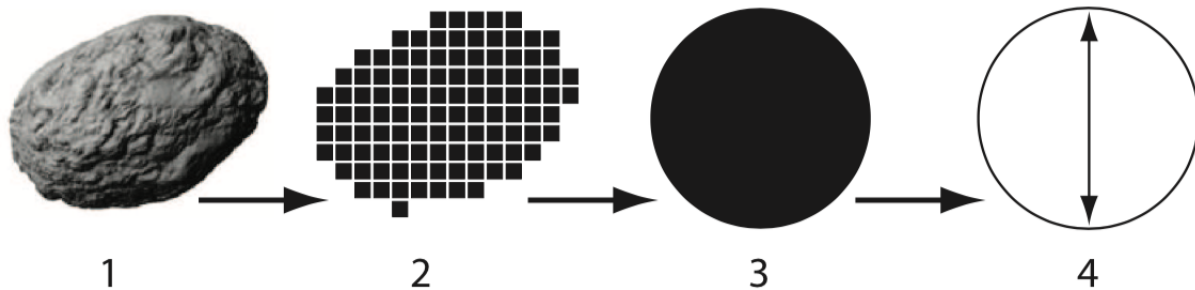
Fig. 2.2 Visual steps summarizing the process of particle size determination via image analysis. The real three-dimensional shape of the particle (step 1), is transformed through a quantization process by the CCD camera sensor into a raster two-dimensional image (step 2). The black circle (step 3) has an area corresponding to the number of pixels of the raster image, and its diameter (D_{eq}) is used to estimate the size of the natural volcanic particle.

The D_{eq} was used to estimate the size of the particles and to convert the areal information obtained from 2D images into volumetric information, by assuming a spherical shape for the particles. The volume of the equivalent sphere was thus calculated for the particles to produce the GSD curve of the finer fraction of deposits. This GSD was then connected with the GSD derived from mechanical sieving. A constant density for the full range of ash particles was assumed, thus implicitly translating the Vol% values in the wt% values.

2.2   Ash componentry and SEM imaging

The modal class of the grain size (variable according to the sample) was generally selected to provide analyses of ash componentry. Where possible, the ash componentry was determined also for the coarser grain sizes in order to test the reliability of the recognized ash classes and to account for possible variations of componentry with the grain size of deposit. Ash componentry of each sample was evaluated through visual inspection using a stereo microscope on a subset of 300-350 randomly picked ash particles to ensure a valuable statistic, representative of the bulk ash deposits. The ash category distinctions are based on the characteristic textural features of the particle external surfaces. This allowed to provide a first textural description of the grain surfaces in terms of morphology, surface roughness, color and apparent vesicularity. A subset of around 30-50 grains was manually selected to represent each of the ash categories identified to populate the deposits. These particles were mounted

alternatively on carbon coated supports (Figs. 2.3a and b, respectively) in order to be analyzed with a Zeiss Evo MA15 Scanning Electron Microscope at the MEMA (Microscopia Elettronica e Microanalisi) Laboratories of the University of Florence.
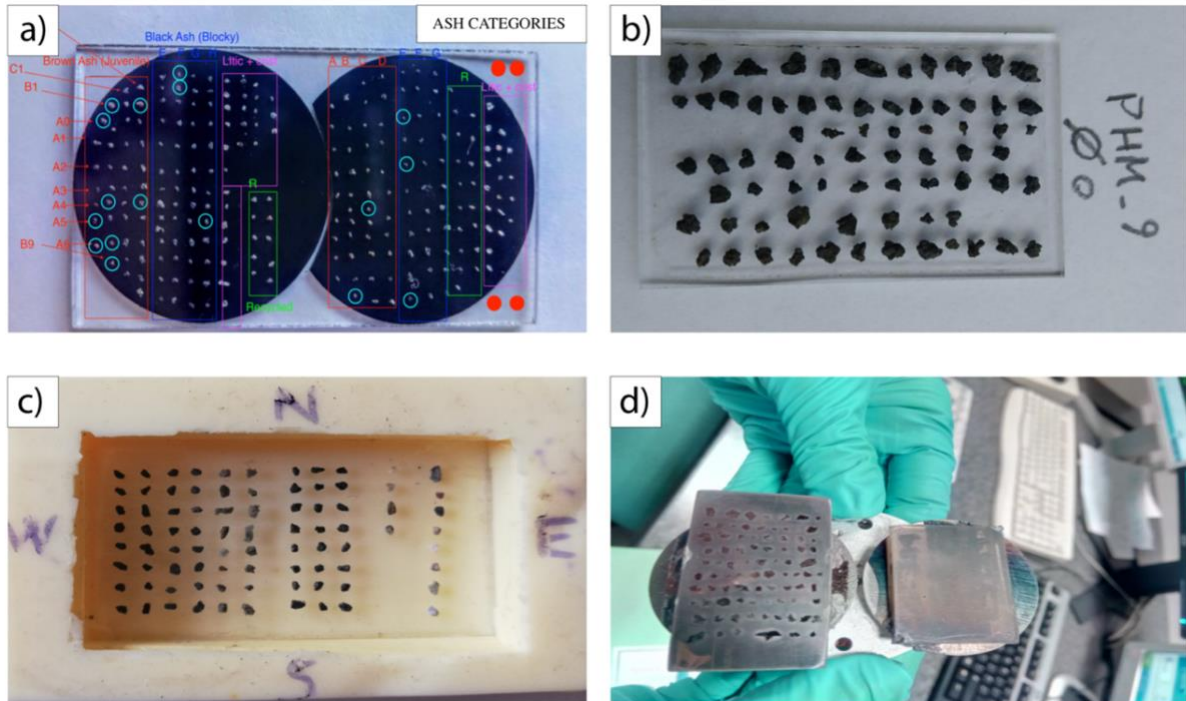
Fig. 2.3 Example of volcanic ash samples prepared for analysis with SEM. (a,b) Selected particles representing the different categories identified in the ash deposits, mounted on carbon coated and thin glass supports; c) Particles embedded in epoxy resin and polish-sectioned along the major cross-sectional axis of particles; d) Conductive samples mounted on a specific stub ready to be analyzed with the SEM microscope.

Secondary electron images (SE-SEM images) of the selected particles were collected to investigate with high-detail their external features (Fig. 2.4 a,c) and characterize the shape of the recognized ash components. Accelerating voltages of 20 kV and a working distance of 9.5 mm were employed during the acquisition of images.
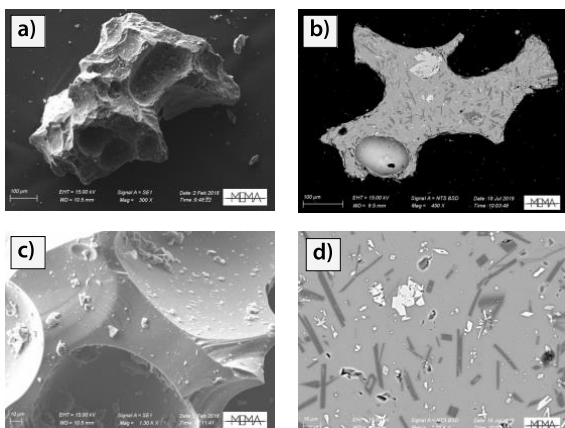
Fig. 2.4 Textural and morphological description of volcanic ash particles. External and internal features of a volcanic ash particle imaged with SEM used both in secondary electrons mode (a), and in back scattered electrons mode (b). Details of the fine ash particles coating the external surface (c), and the internal structures of microlites growth (d).

-

The particles were then embedded in resin, sectioned, polished and carbon coated in order to be reanalyzed with SEM using the back-scattered electrons mode (BSE-SEM) to obtain images representative of the internal characteristics of the same set of ash grains. BSE-SEM images were then used to extract quantitative information on the internal groundmass textures and correlate them with the external features (Fig. 2.4 a,b). This second image acquisition was carried out using an accelerating voltage of 15kV. Where needed, EDS microanalysis was used to detect qualitative chemical composition of the surface glass or secondary minerals (like salt precipitates or evidence of secondary crystal growth) (Fig. 2.4). This technique has been very useful to be sure about the distinction between volcanic glass and crystal structures.

2.3 Morphological and textural analysis of selected volcanic ash fragments

Each collected image, was used to extract dimensional and morphometrical information on particles, microlites and vesicles. SE-SEM images of selected particles representing the different ash components were processed to describe external features of volcanic ash particles and to quantitatively characterize the apparent projected shape of ash grains (APASH) (Leibrandt et. al., 2015). Image analysis was done using *Fiji,* a dedicated software (Schindelin et al., 2012) that allows the extraction of fundamental geometrical parameters from the grey-scale images of the volcanic particles (Tab. 2.1).

Symbol	*Parameter*	*Definition*
$D_{eq}D$	Circle Equivalent Diameter	Diameter of the circle having equivalent area (A)
A	Area of the particle	Surface extent of the particle outline (μm^2)
A_{CH}	Area of the Convex Hull	Surface internal to the convex envelope of the particle outline
P	Perimeter of the particle	Length of the particle outline
P_{CH}	Perimeter of the Convex Hull	Length of the convex envelope of the particle outline
P_{CE}	Perimeter of the D_{eq}	Perimeter of the circular equivalent diameter
L	Particle Length	Maximum distance between pixels along the Major axis of the particle
w	Particle Width	Maximum distance between pixels along the Minor axis of the particle
Feret	Maximum Feret diameter	Maximum caliper distance along the perimeter
MinFeret	Minimum Feret diameter	Minimum caliper distance along the perimeter
b	Baricenter	Center of mass of the particle

Tab. 2.1 List of fundamental parameters measured during image analysis.

Quantities reported in Table 2.1 were used to calculate a set of descriptive adimensional shape parameters (Fig. 2.5). An automated procedure designed to be compatible with *Fiji* was used to measure the fundamental parameters and to calculate those derived. According to Liu et al. (2015), four parameters were considered to account for the main morphological variability of volcanic particles: Axial Ratio (AR), Solidity (SLD), Convexity (CVX), and Circularity (Circ). As suggested by visual sketch reported in Figure (2.5), different shape parameters accounts for different aspects of particle morphology.
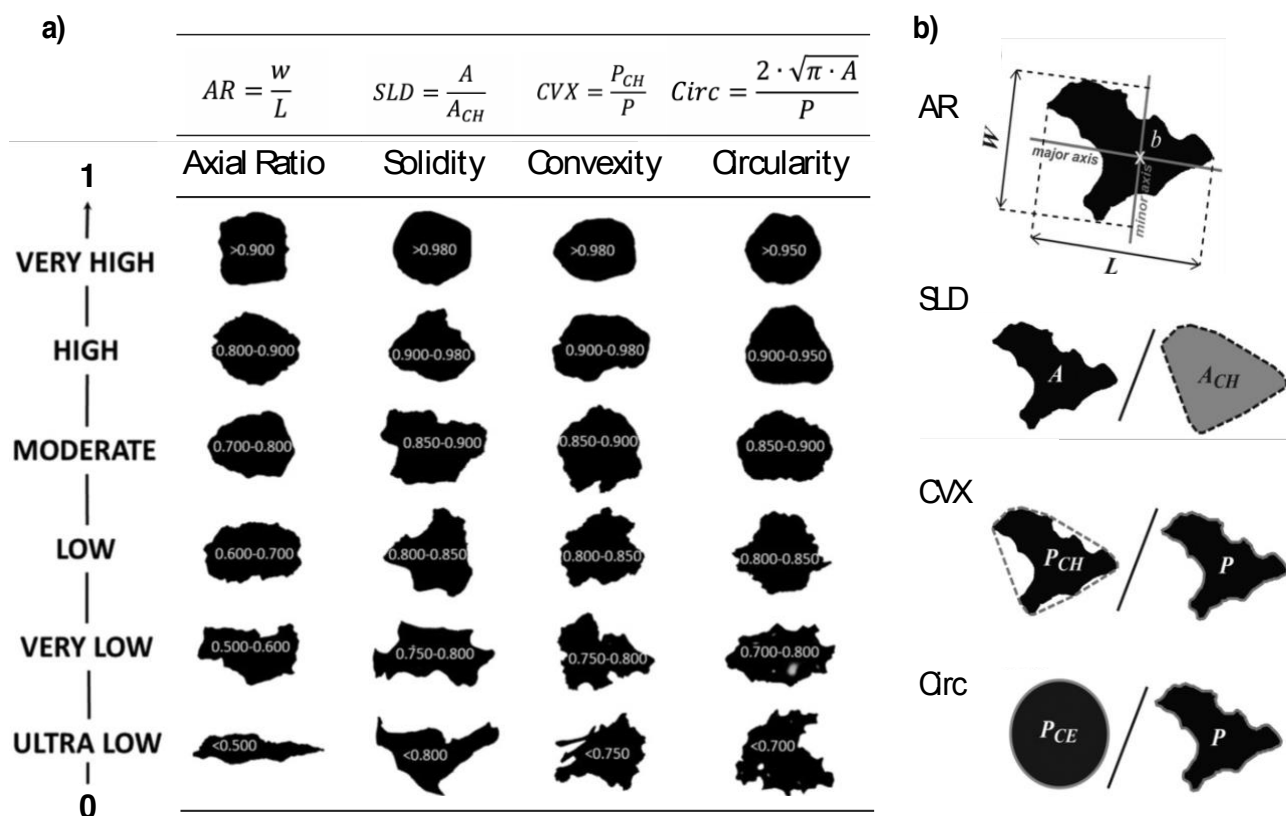
Fig. 2.5 Geometrical shape factors used to characterize the morphology of volcanic ash particles. a) Mathematical definition of the shape factors together with variability of 2D outlines of volcanic particles sorted based on their systematic variations in terms of the selected shape parameters (comprised in the range 0-1); the value of the corresponding parameters is also reported above the particle outline. From left to right in the columns: Axial-ratio, Solidity, Convexity and Circularity. b) Graphical definition of the shape factors. Image modified from Leibrandt et al., (2015).

The variability range of the considered shape parameters is comprised between 0 and 1 (Fig. 2.6). AR is the ratio of width (w) over length (L) of the particle. AR describes the degree of elongation of an object; therefore, it is often rearranged in a different form and defined Elongation (El=1-AR). Solidity corresponds to the ratio of the particle area (A) to the area of the convex hull (A_{CH}), which represent the convex envelop of the particle outline. SLD accounts for the total surface of 'bends' or 'lobes' present along the particle outline. CVX correspond to the ratio of the perimeter of the convex hull (P_{CH}) to the perimeter of the particle P, and accounts for finer asperities affecting the particle outline. Importantly, while the Solidity accounts for the larger scale asperities affecting the overall shape of the particle outline, Convexity represents an estimate of its fine roughness. Finally, Circularity quantifies how close the shape is to a perfect circle, and it is defined as the ratio of the circumference of a circle

equal to the particle's projected area to the perimeter of the particle. Uncertainty associated to the estimation of these parameters from raster images is discussed below in Section 2.5.2.

Using a similar approach, also BS-SEM images were processed with *Fiji* to extract dimension and spatial abundancy of vesicles and microlites. Vesicularity and crystal abundance were calculated respectively as the ratio of the total vesicle surface and the total crystal surface to the analyzed cross-sectional area. The shape of the vesicles was measured directly from the images, and their size was estimated as the diameter of the equivalent circle (D_{eq}). The 2D maximum and minimum lengths of plagioclase microlites were used to derive the Crystal Size Distribution (CSD) (Fig. 2.6) for the different ash grains by means of the software *CSDcorrections* (Higgins, 2000).
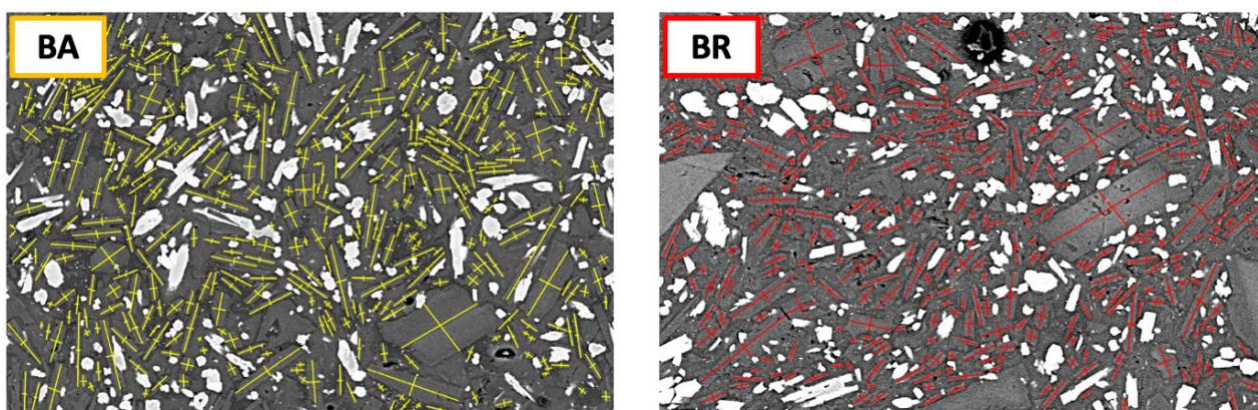
Fig. 2.6 Textural analysis of Feldspar in different ash components. The maximum and minimum axis of Feldspars were manually tracked with *Fiji*.

The *CSDslice* database (Morgan & Jerram 2006) was also used to extract data upon the distribution of microlite axial ratio and to compare our data with existing data in literature. Finally, information about mineral abundance and the shape of microlites was acquired for the other phases composing the mineral assemblage of ash grains.

2.4   APASH analysis of ash fragments using a Static Particle Analyzer

Finally, the automated particle analyzer was used to provide a statistically robust analysis of the ash shape.

Randomly selected aliquots (around 13 mm^3) in the deposit fraction with Deq<250 μm were picked from the samples, and the APASH was calculated for a large number of particles ($10^5 < \# < 10^6$) belonging to the most representative dimensional classes of the deposits. The morphometry of the ash grains was quantified considering the same set of shape parameters previously defined (i.e. Elongation, Solidity, Convexity and Circularity). Analyses were carried out using dedicated Standard Operative Procedures (SOP) according to the specific characteristics of the ash sample. Samples were analyzed

using an appropriate set of optical magnifications (5x; 10x; 20x) in order to maintain the Image Resolution (IR; i.e. number of pixels entering within the 2D particle projection) as constant as possible for particles having very different size, and avoid thus scaling effects due to 'pixellation' of the outlines of the finer particles. At the same time, the use of the SOPs allowed us to provide comparable analyses upon different samples, since an invariant optical setting was used to process all of them. This helped also to avoid bias in the measured parameters introduced by the changing resolution of objects having the same size.

2.5 Treatment of the uncertainties associated to the estimated quantities

Quantities extracted from the processing of images are likely to be affected by uncertainties. Hereafter, we examine and discuss the different sources of uncertainty connected with the different steps of data processing.

2.5.1 Uncertainty on the calculation of GSDs via image analysis

The GSD of the finer fraction of fallout deposits was calculated converting the dimensional information obtained from 2D images for irregular volcanic particle into 3D volume of their equivalent spheres. In the latter process we assume that the shape of particles is spherical. In fact, the real shape of particles (i.e. the shape in three-dimensional space), can effectively influence the D_{eq}, particularly in the case of highly irregular objects (e.g. elongated or flat particles). The higher the irregularity of the object (intended as the distance from a perfect spherical shape), the higher the error associated to the estimates of circular equivalent diameter. However, the D_{eq} represents an objective and repeatable way of measuring particle size, representing also one of the few techniques available for the dimensional characterization of finer deposit fractions (below 64 µm), that present difficulties to be treated with classical techniques (i.e. mechanical sieving). On the other hand, assumption of a spherical shape is also common in other different grain size methods (e.g. laser diffraction, sedimentation).

Furthermore, a second assumption is involved in the process of the GSD calculation: a constant density for the full range of ash particles was also assumed, thus implicitly translating the Vol% values in the wt% values. This assumption has been evaluated as reasonable by the fact that all the collected samples did not show any important difference neither in the magma composition, nor in the vesicularity of the observed ash particles.

2.5.2 Uncertainty on parameters extracted from image analysis

In using the geometrical shape parameters with raster images, it is of fundamental importance the adopted image resolution (IR) with respect to the scaled size of the object. Using constant optical setting and magnification, the smaller is the size of the object with respect to the resolution of the image, the

lower will be the number of pixels (n) covering the entire shape. As a consequence, the error in defining the shape of the particles is directly related to the specific ratio between pixel and linear units (μm). The higher this ratio and the number of pixels covering the particles area, the lower the error introduced in the measure. To avoid bias errors introduced by scaling effects due to a change in the resolution of the particles in different images, the image acquisition was performed using an invariant optical setting (5x-10x zooming and 5 MPixels sensor) that allowed to keep as higher as possible the resolution for the observed particles. The IR depending on the chosen optical setting was constant at 1.76 pixel/μm (for particles down to 6.5μm) and at 3.77 pixel/μm (for particles below 6.5 μm). This resulted in a number of around 11800 pixels defining a particle with Deq ~ 64 μm. This pixel value is orders of magnitude higher than the confident limit suggested by Leibrandt et al., (2015) (i.e. around 630 pixels defining the smallest particle). Considering either that the number of pixels defining the area of a particle increases with n^2 with respect to the particle diameter, we are comfortable in considering that the resolution of the larger particles images has a negligible influence in modifying the overall shape.

2.5.3 The statistical reproducibility and robustness of the optical particle analyzer output data

The SOP procedures used for the analysis of the GSDs with the particle analyzer involve several steps comprehensive of operator-dependent procedures that could result in a lack of reproducibility. The statistical validity of the obtained results (i.e. their reproducibility) along with the influence of the operator-dependent procedures involved in the sample preparation and dispersion, were tested with a series of repeated analysis.

Before starting with analysis, the autocalibration function of the instrument was set on to correct from possible instrumental bias errors. Then, a set of routine analyses, useful to test several aspects involved in the data processing, were accomplished on a selected set of granular samples. Finally, the reproducibility of data was evaluated comparing obtained results.

i. The reproducibility of *the process of sample mixing and pouring* from bags was tested selecting a natural volcanic fallout tephra and following a standardized procedure to homogenize it (e.g. a number/time of bag tourn over), and repeating the analysis for a different aliquot of the same sample. A certain volume (around 13mm³) of sample was poured from the sample bag and measured using a calibrated SOP. After cleaning the instrument another aliquot (same volume) of sample was measured using the same SOP. Results were compared in terms of the total number of analyzed particles in the deposit, the number frequency distribution of D_{eq} (NFD), and the GSD.

ii. The efficiency and reproducibility of the particle dispersion operated by the system dispersion unit (SDU) to separate and resolve the different particles before the image analysis was tested measuring the properties of a same sample over different local area-selections. The sample was dispersed using specifically designed SOPs, and distinct regions of the sample dispersion were analyzed, and results compared. Results were compared in terms of: Total number of analyzed particles in the deposit, number frequency distribution of D_{eq} (NFD), and GSD.

iii. The efficiency of available optical configurations were tested repeating the measurement of the same sample employing different SOPs designed to acquired data using different optical settings. This approach allowed us to estimate the sensitivity of the different optical settings to the grain size distribution of the deposits, depending on their optical resolution limits. Results were compared in terms of GSDs.

iv. Evaluating the minimum eligible volume of a sample to produce statistically representative analyses of the whole sample population. In order to evaluate the statistical representativity of these small volumes of analyzed sample we measured increasing volumes of the same sample, using an invariant analytical configuration, and we compared obtained results in terms of GSDs.

2.6   Three-dimensional description of unbroken ash aggregates

During this thesis a large dataset of preserved ash aggregates produced during different phases of Vulcanian activity were collected. A representative selection of them were analyzed using a micro computed tomography (micro-CT) in order to produce realistic 3D models of the different aggregates types useful to provide a detailed description of their internal features.

2. 6. 1 Sample preparation and processing

During May 2018 and November 2019, a large set of natural ash aggregates was collected at Sakurajima volcano (Japan). Aggregates were collected using thin sections covered by organic starch in order to preserve as well as possible their airborne structures. This approach allowed us to collect several particle clusters that entirely preserved their original structures, since the layer of organic starch used for the collection proved to be very efficient in preventing disaggregation of the particle clusters at the moment of their impact (i.e. sedimentation) with the dedicated support.

Using a stereo-microscope, unbroken aggregates of different types were described and selected based on their external features. A total of 16 aggregates were embedded in epoxy resin and mounted into specific 6mm wide plastic and brass tubes (Fig. 2.7) in order to be analyzed with a Bruker SkyScan 1173 X-Ray micro-CT at Earth Science Department (ISTE), University of Lausanne (Switzerland).

Fig. 2.7 Conductive brass tubes used for the micro-CT analysis of aggregates.

2. 6. 2 The micro-CT analysis

Micro-CT is a non-destructive 3D imaging technique that employs X-rays to provide a composite 2D scanning of the object, slice by slice (Fig. 2.8). Micro-CT scanners capture a series of 2D cross-sectional images from different point of view and reconstruct the data to provide a 3D model of the object, also providing volumetric information about the microstructures.
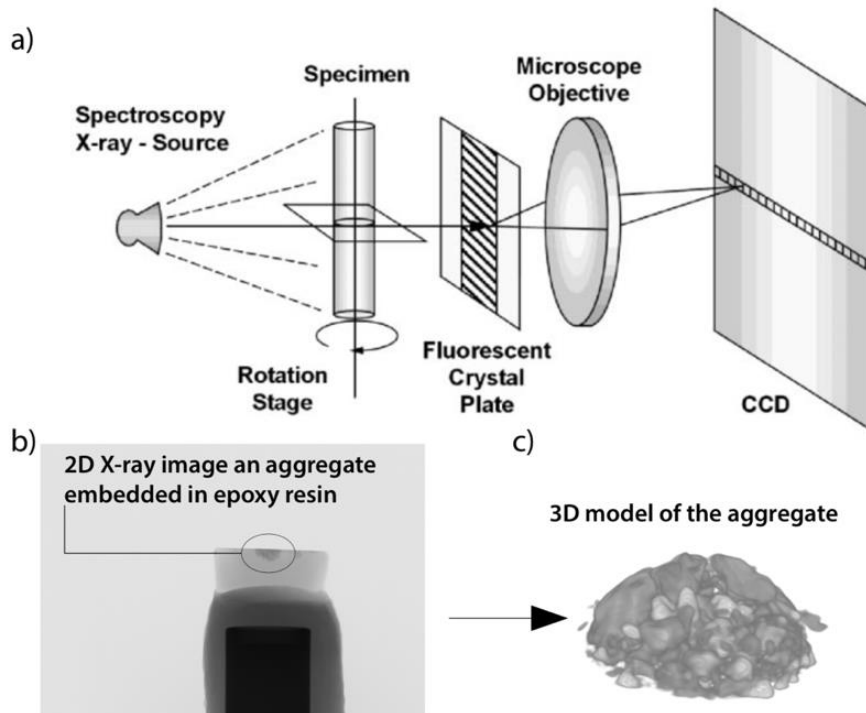
Fig. 2.8 Schematic representation of the working principle of a micro-computed x-ray. (a) X-rays are generated in an X-ray source, transmitted through the sample, and collimated by a specific lens (Fluorescent crystal plate, and Microscope

Objective) to the CCD detector as a 2D projection image. The sample is free to rotate on the rotational stage, where several X-ray projection images are taken depending on the angular resolution required (down to fraction of degree). The series of X-ray projection images (b) is then computed into cross-sectional images through the computational process called "reconstruction". (c) These slices can be analyzed and processed to produce 3D models of the aggregates.

A non-destructive, high-resolution (IR ~ 4µm/pixel) 3D rendering model of the internal structures of unbroken particle clusters was thus obtained and used to provide a more direct and broad description of the internal structures (i.e. spatial arrangement of coarser grains and modalities of grains interlocking), that characterize the different types of aggregates.

The median cross-sectional plane of each aggregate was finally exposed from the UV resin by polishing. The polished sections were then carbon coated in order to be analyzed with SEM microscope. Grain size distribution and textural features of a representative set of aggregates was thus investigated using the SEM either in Back Scattered and Secondary mode, to acquire a high-resolution footage of the aggregates internal structure, and to compare them with results from the 3D imaging. Images allowed us to provide information on the distribution of ash fragments composing the aggregates for even the finer class-sizes (below the resolution limits of micro-CT analysis), and to investigate their mineral assemblage and textural features.

Chapter 3

Eruptive dynamics and fragmentation mechanisms during cyclic Vulcanian activity at Sakurajima volcano (Japan)

Overview

Since many years the attention in studying products associated to ash-dominated eruptions has continuously grown principally due to the numerous hazards associated with the dispersion of ash into the atmosphere and in highly anthropized areas. The quantitative analysis of morphological and textural features of volcanic ash is now considered one of the most effective tools to characterize the style of ash-dominated volcanic activity and to investigate the complex interplay between conduit processes and the associated eruptive dynamics. However, many questions remain still unanswered about the role of fragmentation processes in controlling the eruptive dynamics of high-transients, unsteady Vulcanian activity. For this reason, ash deposits produced during a complete eruptive sequence encompassing all the styles of activity typical of Sakurajima volcano (Japan) during the recent period, were collected and investigated in terms of the external morphometry and internal textures. Three main intra-eruptive phases were recognized based on visual observations and morphometrical information for thousands of particles associated with the recognized phases derived. On the other hand, the crystallinity of ash grains, together with the crystal size distribution of microlites in the groundmass were quantified for a representative set of ash particles. Links existing between the intra-eruptive dynamics and the dominant processes of magma fragmentation are here discussed, monitoring the variation of the morpho-textural features of ash throughout the whole eruptive sequence. The resulting information on the eruptive dynamics of Sakurajima is of primary importance for a wider comprehension of the low-to-mid intensity, ash-dominated explosive activities.

3.1 Introduction

A large amount of volcanic ash is frequently produced during low- to mid-intensity explosive eruptions at many active volcanoes around the world (e.g. Heiken and Wohletz, 1985; Sparks et al., 1997; Dingwell et al., 2012; Makie et al., 2016; Bernad et al., 2016; Oishi et al., 2018; Battaglia et al., 2019). The sudden ash discharge related with explosive eruptions often represents a critical source of hazard for population living near active volcanoes, as well as, in a wider perspective, for the civil aviation (Casadevall and Krohn, 1995; Sparks et al., 1997; Guffanti et al., 2010). Despite the high frequency of the ash dominated activity and its relevant societal impact, the mechanisms responsible for the ash generation and dispersal during these eruptions are still not fully understood. On the other hand, volcanic ash has shown to represent a powerful tool for the investigation of the eruptive dynamics and all the processes affecting magma during its upward migration in the conduit. Consequently, many efforts have been made by the scientific community to improve the knowledge about physical processes responsible for the ash production, transport and dispersal (e.g. Dellino & La Volpe, 1996; Cioni et al., 2008; Miwa & Geshi 2012; Cioni et al., 2014; Bonadonna et al., 2015; Cashman & Scheu, 2015; Liu et al., 2015; Liu et al., 2017; Durant, 2015). Since the pioneering work of Heiken and Wholetz (1985), who first did a comparative study of the ash textural and morphological features over various types of eruptive styles, several studies have been focused on volcanic ash to investigate in detail both conduit and eruptive processes, and to make inferences on the nature of magma fragmentation mechanisms (Papale, 1999; Buttner et al., 1999; Cashman et al., 2008; Miwa et al. 2013b; Cioni et al., 2014; Jordan et al., 2014; Leibrandt et al., 2015; Battaglia et al., 2019). The quantification of physical features of volcanic ash, like vesicularity, crystallinity, external and surface morphology, helped to better define different mechanisms of magma fragmentation, and to shed light on their role respect to the eruptive dynamics (Cashman & March, 1988; Cashman et al. 1992; Cashman & Hoblitt, 2004; Aldibirov & Dingwell, 2000; Miwa et al. 2013a,b; Cioni et al., 2014; Cashman & Scheu, 2015; Gaunt et al., 2016; Liu et al., 2017). On the other hand, textural analysis has been widely used to interpret the processes occurring to magma during its ascent in conduit prior to reach the fragmentation threshold (D'Oriano et al., 2011; Cioni et al., 2008; Dellino et al., 2012). Importantly, analyses on the internal texture of ash were also used to better understand and interpret the transient behavior often observed in the dynamics of mid-intensity and high-frequency explosive eruptions (Miwa et al., 2009; Cashman et al., 2008; Miwa et al., 2013a-b; Cioni et al., 2014). As a matter of facts, while a lot of work has been done in the comprehension of large sustained volcanic activity (e.g. Plinian eruptions), several unanswered questions still remain open about the effective mechanisms of magma fragmentation in controlling the eruptive dynamics in the context of low- to mid-intensity, ash-dominated activities showing a large intra-eruptive variability in the intensity and style of eruption.

The results of an extended study of the ash products related to recent, high-transient, and unsteady activity at Sakurajima volcano (Japan) is presented in this chapter, aimed at their quantitative morphological and textural characterization. Ash was directly collected during an entire five-days long eruptive sequence (22-25 October 2014) characterized by rapid (from seconds to hours) transitions in intensity and style of the activity. This aspect makes the samples as extremely valuable for the

investigation of the mechanisms that are responsible for the important variations observed in the eruptive dynamics. At least three different phases of activity were identified encompassing a large spectrum of intensity of the eruptions. We applied several state-of-the-art methodologies for the quantitative description of the most important characteristics of ash products (grain size, morphology, crystallinity and texture) related to the different eruptive stages, making inferences on conduit dynamics and changing eruptive styles, and discussing them in the light of the underlying magma fragmentation processes.

All the evidences presented in this chapter suggest the presence at Sakurajima of a highly stratified and degassed magma conduit, suggesting an interpretation of the transient dynamics of these eruptions in terms of a variable process of magma fragmentation which drives and strongly control the vulcanian eruption during its different stages. As a whole, the detailed analysis of the ash features (e.g. crystallinity, vesicularity and grain size distribution of microlits) also provides important insights on the variable origin of the classified ash fragments and thus, on the different regions of the magma conduit involved in the production of ash during the phases of activity composing the eruptive cycle.

3.1.1 The recent Vulcanian activity at Sakurajima Volcano

Sakurajima is an andesitic stratovolcano located in the Kagoshima prefecture (southern Kyushu, Japan; Fig. 3.1a) well known for the high-frequency Vulcanian activity nearly continuous since 1955 (Miwa et al., 2013b; Iguchi et al., 2008).
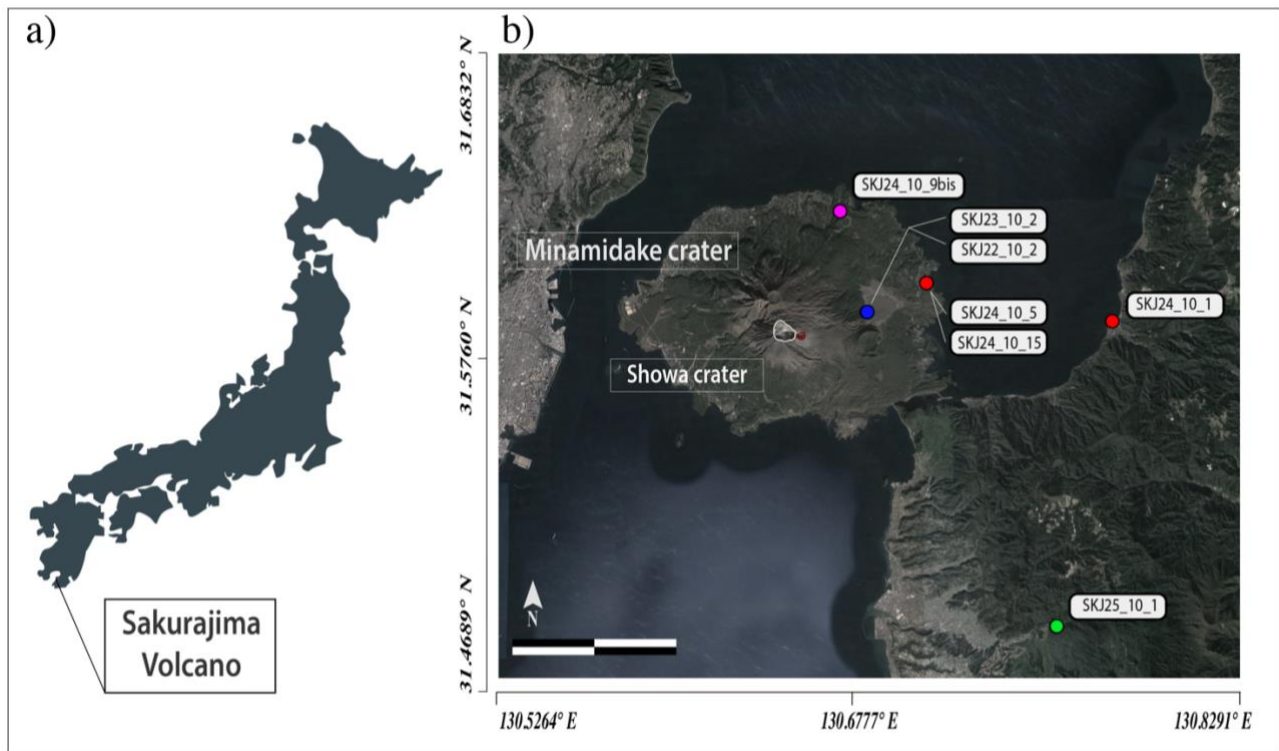
Fig. 3.1 (a) Location of Sakurajima volcano indicated within a sketch map of the Japan archipelago; (b) locations of the ash samples (indicated with circles) are reported in the map with variable colors according with the different stages of eruptive activity: Weak Ash Emission (blue circle), Vulcanian Explosion (red circles), Continuous ash venting (violet circle), and activity renewal (green circle).

This complex stratovolcano is formed by two overlapping cones, Kitadake, which ended its activity at 4850 ka, and Minamidake, presently active (*https://volcano.si.edu/volcano.cfm?vn=282080*). Since 1955 the activity occurred mainly at Minamidake summit crater, with no significant change in the chemical composition of the erupted products. However, during June 2006, a drastic change of the activity occurred, with a shift to the parasitic Showa crater and the corresponding deactivation of Minamidake crater (Iguchi, 2013b). In August 2015 activity has interrupted for several months until February 2016, when it restarted first from Showa crater, with small explosive events, and then (March 2016) also from Minamidake crater, with high intensity explosions (*on-line resources from Japan Meteorological Agency, JMA; http://www.jma.go.jp/jma/indexe.html*). Since 2016, activity alternated between the two vents, with variable energy, intensity and frequency. As reported by the JMA, Vulcanian activity of Sakurajima is still ongoing and it consists of an almost continuous succession of small tephra emissions culminating in strong vulcanian explosions, eventually separated by a short period during which no ash emission is observed (Oba et al., 1980; Ishihara, 2000; Yamanoi et al., 2008; Iguchi et al., 2008; Iguchi, 2013b; Miwa et al., 2013a). A recurrent eruptive pattern comprising different eruptive styles and intensity was identified to constantly characterize the activity of this recent period (e.g. Kamo, 1978; Fukuyama, 1981; Ishihara, 1990; Yamanoi et al., 2008; Iguchi et al., 2008; Iguchi et al., 2013a; Miwa et al., 2013b). Monitored variations in the dynamics of the volcanic activity, together with recorded ground deformations and geophysical signals, allowed to quantitatively characterize the typical eruptive pattern at Sakurajima as a sequence of specific events (Iguchi et al., 2008; Iguchi, 2013b; Yokoo et al., 2013). Normally, an eruptive cycle starts with the migration of andesitic magma that accumulates in a shallow reservoir, as testified by the distribution of volcano-tectonic hypocenters and by the volcanic edifice inflation preceding, from hours to several days, the onset of an eruption (Ishihara, 1990; Iguchi et al., 2008; Iguchi et al., 2013a, Yokoo et al., 2013). Yokoo et al. (2013) identified, for the eruptions occurring at Showa crater a depth for the magma accumulation comprised between 0 and 2 km beneath the crater, which resulted considerably shallower respect to the magma reservoir previously identified by Ishihara (1990) for the eruptions occurring at the Minamidake summit crater, located between 2 and 6 km below the vent. During this stage the eruptive activity is typically marked by the onset of a low-intensity, intermittent activity characterized by the alternation of phases of no or weak ash or gas emission punctuated by small explosions associated with the ejection of ballistic bombs and lapilli at short distances (e.g. Miwa et al., 2013a); this activity pattern can last from hours to days. An increasing trend of upward tilting is associated with major explosions; an extensional strain ranging between 0.01 to 0.2 ~rad (volcano inflation) starts from minutes to several hours (~20 h) before the onset of the explosion, turning to a downward and contractive signal immediately before and after the eruption occurs (Iguchi et al., 2013a; Iguchi, 2013b, Yokoo et al., 2013). At the same time, a decrease in the SO_2 discharge rate is recorded together with the progressive weakening of the nighttime glowing (Yokoo et al., 2013). These evidences were interpreted by Ishihara (1985) and Yokoo et al. (2013) as due to the progressive formation of a degassed and viscous magma plug sealing the upper part of the Sakurajima volcanic conduit prior to the occurrence of a vulcanian explosion. Aerial photos and

textural evidences on ash reported by Miwa et al., (2013b) all suggest the presence of a viscous and outgassed plug in the upper conduit of Sakurajima. Typically, a Vulcanian explosion occurs after a variable period of quiescence or very weak intermittent activity, as the magma column attains sufficient pressure to overcome the lithostatic pressure of the plug and its strength (Tameguri et al., 2002). Prominent Vulcanian eruptions are typically associated to the production of variably ash-laden plumes that can reach heights of some kilometers in the atmosphere (up to 5-6 km during stronger events: e.g. eruption of October 7, 2000). Large ballistic fragments are often ejected up to a few km far from the vent during larger explosions (Iguchi et al., 2008). Larger events are also accompanied by violent air-shocks (exceeding 500 Pa at 2.7 km from the vent) that commonly precede the formation of the ash-rich plumes. Miwa et al. (2013a), interpreted the intensity of the produced air shocks as related to the amount of gas accumulated in the magma conduit before eruptions. Immediately after the strong Vulcanian eruptions, it is frequent to observe a phase of continuous ash venting, accompanied by a persistent tremor without any visible associated explosion. This activity typically lasts from minutes to hours and it is characterized by the quasi-sustained emission of gas and tephra to form a weak, dense, low-level ash plume rising up from the vent (Kamo and Ishihara, 1989; Nogami et al., 2006; Yamanoi et al., 2008; Iguchi et al., 2008; Iguchi et al., 2013a; Miwa et al., 2013b). Typically, the ash emission ceases together with a gradual decrease in frequency and intensity of the seismic signals (Iguchi et al., 2008). After each vulcanian explosion, a variable period lasting from hours to days of no apparent activity commonly precedes the start of a new cycle. While the sequence of activity of the different vulcanian outbursts is clear and well described by geophysics, the mechanisms of magma fragmentation related to the different phases of activity are not fully clear and unequivocally explained (Yokoo et al., 2013).

3.1.2 Previous studies on volcanic ash from Sakurajima activity

Analyses of ash texture and morphology has been used since long times to discuss the dynamics of Sakurajima activity. The first quantitative studies and descriptions of Sakurajima ash were made by Oba et al. (1980), who distinguished ash components based on the color differences observed for the fragments. They basically identified two types of fragments: 'red ash', interpreted as a mixture of hydrothermally altered and juvenile ash particles, and 'black ash', representing ash produced by the disruption of the plug hosted in the vent. Then, Miyagi et al. (2010) described Sakurajima ash deposits as formed by juvenile dense-glassy and angular blocky fragments, together with minor pumiceous and fluidal particles. Finally, in their very detailed works, Miwa et al. (2013a,b) distinguished juvenile components from lithics based on external features like smooth (or glossy) surfaces, typical of juvenile components, and non-smooth surfaces, interpreted as indicative of non-juvenile material. Miwa et al. (2013b) also showed that pumice-like and fluidal fragments are poorly present at Sakurajima, except for those periods in which the intensity of major explosions is particularly high (Oishi et al., 2018). The pumice fragments described by Miwa et al. (2013) show a complex external outline related to the presence of abundant, spherical vesicles (on average 40% in volume), while blocky, dense fragments are defined by angular outlines surrounded by planar surfaces with few large and irregular vesicles.

They also recognized the presence of fluidal particles, characterized by glassy, smooth external surfaces reflecting the molten state of magma at the time of fragmentation. Basing on the study of ash features, many authors tried to interpret the dynamics of the activity in terms of the processes affecting magma during the ascent in the conduit. A variation in vesicularity coupled with a variation in Cl and F contents of the groundmass glass of the ash from different stages of activity, led Nogami et al. (2006) to suggest the occurrence of two distinct magma components with different volatile contents, as a possible explanation of the large variability observed in the eruptive patterns. In particular, fragmentation of a more volatile-rich magma was related with an ash emission activity described as 'Strombolian-like emission' by Nogami et al. (2006), while a more degassed magma was related to activity like vulcanian eruptions and continuous ash venting. Alternatively, Yamanoi et al. (2008) discussed the difference in the characteristics of ash particles from strombolian-type, vulcanian-type and continuous ash emission activity concluding that eruptive dynamics is controlled by the migration of vesicles in the shallower part of the magma column prior to vulcanian explosions, resulting in a vertical internal layering of magma. Finally, Miwa et al. (2013b) and Iguchi et al., (2013b), based on ash textures and seismic signals, identified in the gradual formation of a sealing plug at the top of the system and in the repeated upward migration of magma from the shallow reservoir, two important processes controlling both the intensity and the dynamics of vulcanian explosion at Sakurajima.

3.2 The 22-25 October 2014 eruptive sequence

As discussed above, activity at Sakurajima largely varies in frequency and intensity over time. It generally alternates from variably intense degassing and low-level ash emission lasting from hours to several days, to variably powerful and sudden vulcanian explosions, to short periods (from minutes to hours) of intense ash emission immediately following these explosions. A complete sequence of activity encompassing all these different eruptive styles was observed in the period from 22 to 25 October 2014, and the ash produced by the different activity stages was collected (Fig. 3.2).

Based on Oishi et al. (2018) and JMA reports (Japan Meteorological Agency; http://www.jma.go.jp/jma/indexe.html) , the activity rate of Sakurajima during the whole month of October 2014 was classified as "moderate" in terms of frequency of the explosions, with a total of 19 major vulcanian explosions recorded, associated to ash plumes up to height of 2.5-3.5 km a.s.l. During the whole month, the alert level of the volcano was set to 3 in a scale of 5. Sample collection started on 22 October during a continuous, low-intensity weak ash emission. Before that date, three major explosions occurred on 14-17 of October, then the activity consisted of intermittent, weak ash emissions. After two days of weak emissions (22-23 October) (Fig. 3.2a), a strong vulcanian explosion from Showa crater was recorded on 24 October at 12:05 Japanese Standard Time (JST) (Fig. 3.2b), forming an ash plume that reached a height of 4.6 km a.s.l. and drifted E (http://www.jma.go.jp/jma/indexe.html).

Estimated Plume Height

| 100 - 500 m | up to 4500 m | 400 - 600 m |

a) Phase 1
b) Phase 2
c) Phase 3

Time Duration of the Eruptive Phases

| 0 | 72 hours | 5-10 minutes | 30-60 minutes |

| 1.91 E-06 kg/m²/s | 2.38 E-05 kg/m²/s | 2.54 E-04 kg/m²/s |

Tephra Sedimentation Rate
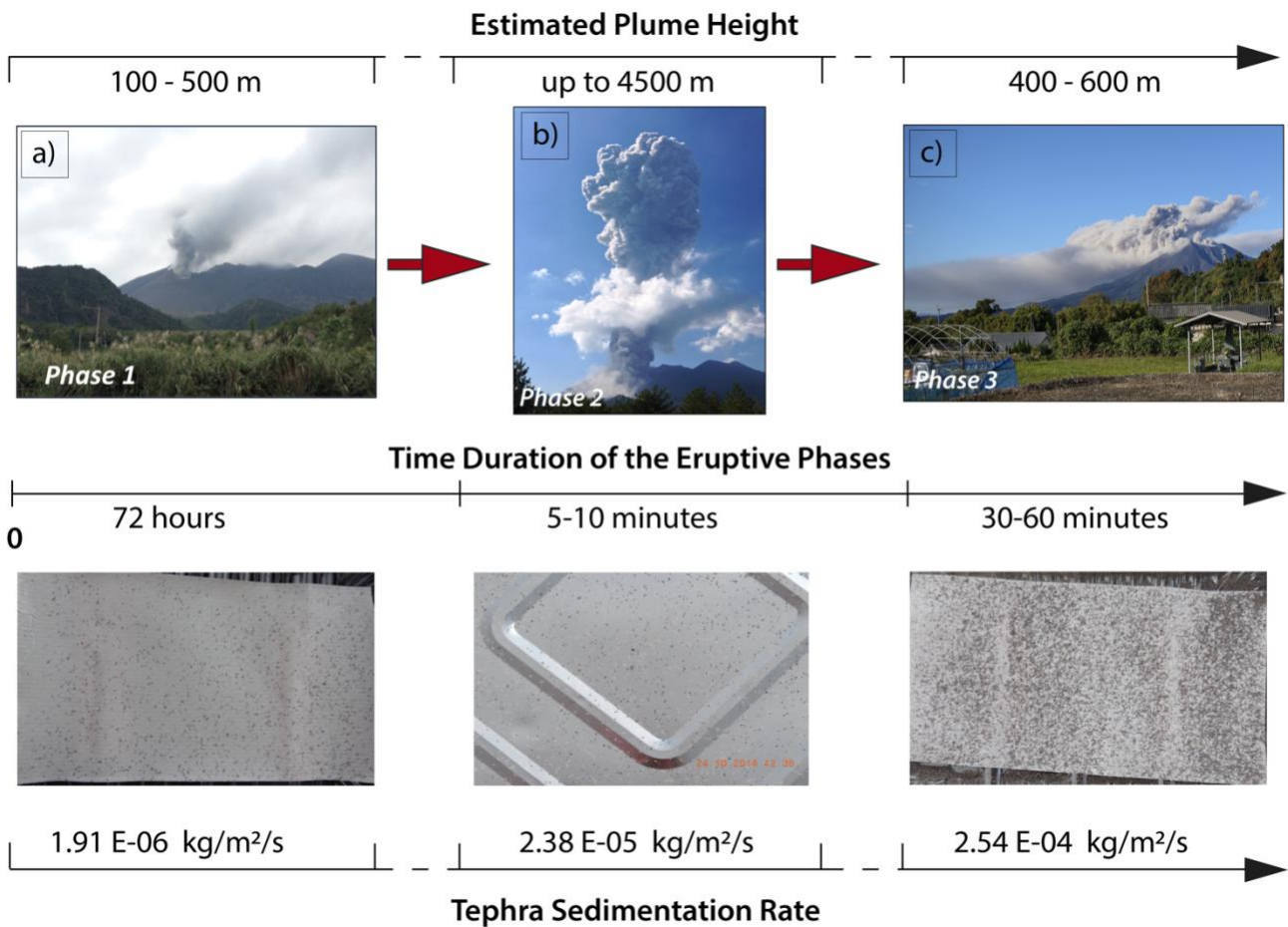
Fig. 3.2 Phases of the Vulcanian eruption considered in this study. Important transients clearly characterize either the style and the intensity of the captured eruptive phases (a,b,c). Eruptive parameters (Temporal duration and estimated plume height) and information about tephra sedimentation (tephra sedimentation rates and images of the impact tracks left by the settling particles during fallout) associated to the different phases are also reported.

The thermal imagery of the first 60 s following the onset of the eruption (Fig. 3.3) indicates an apparent maximum temperature reached by the ejected mixture of around 140°C.

Thermal Imaging of the Vulcanian Explosion

eruption onset   5 s   15 s   60 s
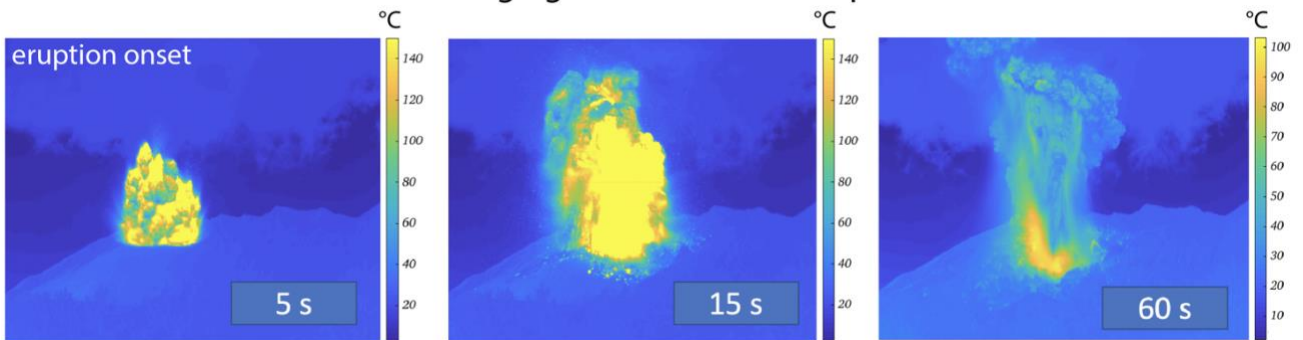
Fig. 3.3 Thermal imagery of the first 60 s after the onset of the prominent Vulcanian explosion. Courtesy image of M.Ripepe from the LGS (Univ. of Florence).

The intensity of this explosion is similar to the typical intensities recorded for major events at Showa crater (http://www.jma.go.jp/jma/indexe.html).

After few minutes (2-5) from the onset of the explosion, a prolonged phase (20-30 minutes) of continuous ash-venting started, producing a dense and low-level, ash-rich plume which spread out to northeast from the crater, ejecting important quantities of fine ash (Fig. 3.2c). This activity progressively decreased and the ash emission ceased completely after about one hour. Activity resumed around 3 hours later as a weak ash emission similar to that preceding the explosion.

Ash fallout samples representative of the different phases of the complete eruptive cycle were collected and analyzed. Ash samples were collected using plastic trays (area of ash collection: 33 x 39 cm) located just under the dispersal axis of the plume at a distance from the vent of about 2 to 5 km (Fig. 3.1b). Two deposits representative of the Vulcanian event were collected at two different locations during the ash fallout: the first sample (SKJ24-10-5) was collected around 5 km distance from the active vent few minutes after the onset of explosion, while the second sample (SKJ24-10-14bis) was collected a couple of hours after the explosion, approximately at 11 km of distance from the vent (Fig. 3.1b).

Ash from the different activities were thus classified as follows and associated to a specific style of eruption:

i) Weak Ash Emission (Fig. 3.2a): characterized by no evident explosive activity, a low intensity ash emission and with a low sedimentation rate (1.91E-06 $kg/m^2/s$).

ii) Vulcanian Explosion (Fig. 3.2b): strong and impulsive explosion associated with the production of an ash-rich plume reaching about 3 km in height, with a settling rate of 2.38 E-05 $kg/m^2/s$ at a distance of about 6 km.

iii) Continuous Ash Venting (Fig. 3.2c): weak, highly-concentrated ash plume emitted continuously from the vent few minutes after the onset of the *Vulcanian explosion*, resulting in a high sedimentation rate (2.54 E-04 $kg/m^2/s$)

iv) Post-event Weak Ash Emission: observed to occur several hours later as a weak ash emission with no visible explosions. This activity could be considered prodromal to another *Vulcanian explosion*.

The analyzed samples are representative of a four-days sequence of Vulcanian activity during which strong transients either in the intensity and in style of the eruptive activity were recorded.

3.3 Analytical Methods

A total of 8 fallout tephra samples were collected during deposition from the ash plume just under the dispersal axis at different locations in the field using plastic trays (Fig. 3.1). Additionally, the sample relative to the onset of the *Vulcanian explosion* (SKJ 24-10-15), of selected lapilli was collected over the leaves approximatively at the same place as SKJ 24-10-5 after the paroxysmal explosion. The latter sample was excluded from the analysis of Grain Size Distribution (GSD).

Samples were processed following analytical procedures that are described in Chapter 2 (Methods) of this thesis.

The GSD of ash samples was calculated through a combined approach of mechanical sieving and optical analysis of the ash fragments. Resulting GSDs were fitted and described using deconvolution into one or two gaussian subpopulations (SP1 and SP2) with acceptable residuals (R^2 higher than 0.96). The ratio

between the deposit fractions (in % respect to the total weight) represented by the finer (SP2) and coarser (SP1) subpopulation (*SP-ratio*) was then used to characterize each distribution together with the main statistical parameters of each subpopulation (Tab. 3.1).

Ash componentry of each deposit was evaluated investigating the modal class of the grain size (250-500 µm) through visual inspection and textural description of the grain surfaces (morphology, surface roughness, color and apparent vesicularity). Where possible, a coarser grain size (500-707 µm) was also considered. Analysis of external surfaces and internal groundmass textures was carried out for the selected ash particles, using SEM. The shape of a subset of 20-30 selected grains was quantitatively determined calculating a set of four shape parameters on the 2D projected outlines of the particles. Therefore, the characteristic 2D shape of the identified ash components was fully described. BS-SEM images on polished sections of the same grains were analyzed to extract information on the size and content of bubbles and microlites. Vesicularity was measured using a wide-angle image of the particles, while information on microlites were extracted using high-magnification images, in order to ensure a good representativity also for the smallest classes of microlites. Moreover, images allowed us to derive the Crystal Size Distributions (CSD) of plagioclase microlites in ash grains of different type. The data extracted about plagioclase size distribution and morphometry (Axial Ratio) were also compared with existing data from the literature. Finally, the Malvern Morphology 3GS automatic static particle analyzer was employed to provide a statistical analysis of the APASH of the ash grains, representative of each collected ash deposit. During analysis, the shape of large sets of ash grains (2000 - 3000) from each size class (half-Phi) in the range 2 - 4 Phi (64~350 µm) was calculated using selected shape parameters defined according to Liu et al., (2015) and Leibrandt et al., (2015) (Solidity, Convexity, Elongation and Circularity).

Eruptive phase	Sample ID	Sampling location	Collection timing	Median	Mode	Sorting	Skewness	Kurtosis	Fraction SP1	MdPhi SP1	σ SP1	VolFraction SP2	MdPhi SP2	σ SP2	SP-ratio
			(JST)	(Phi)	(Phi)	-	-		(%)	(Phi)		(%)	(Phi)		-
Weak Ash Emiss.	SK22_10_2	31.586536° 130.688517°	15:30-17:30	2.4	2.5	0.82	0.12	1.0772	86	2.5	0.68	14	3.6	0.87	0.16
Weak Ash Emiss.	SK23_10_2	Ibid.	11:30-12:35	2.4	2.5	0.77	0.15	1.206	94	2.5	0.61	6	4.3	0.43	0.06
Vulcanian Explos.	SK24_10 5	31.5835878° 130.7001617°	12:25-12:35	1.0	1.0	0.44	0.06	1.0384	98	1.2	0.38	2	4	0.50	0.02
Vulcanian Explos. (distal sample)	SK24_10_14bis	31.574815° 130.778268°	nd	2.8	3.0	0.55	0.07	1.0757	98	3.0	0.48	2	5.2	0.23	0.02
Continuous Ash Venting	SK24_10_9bis	31.61984° 130.6780°	12:50-13.00	2.8	3.0	1.56	0.58	1.6235	71	2.8	0.50	29	5.1	1.78	0.42
Continuous Ash Venting	SK24_10_10	Ibid.	12:50-13:25	2.9	3.0	1.70	0.59	1.3305	65	2.9	0.51	35	5.2	1.87	0.53
Continuous Ash Venting	SK24_10_11	Ibid.	13:25-13:35	3.7	3.5	1.23	0.41	1.405	65	3.6	0.56	35	4.9	1.14	0.54
Activity Renewal	SK25_10_1	31.4826667° 130.762016°	during the night of 25th	4.1	4.5	0.51	-0.02	1.0211	100	4.3	0.48	-	-	-	-

Tab. 3.1 Information relative to bulk ash deposits. Sampling location of collected bulk ash samples are reported together with a set of statistical descriptors (defined according to Folk, 1968) characterizing the GSDs of tephra-fallouts deposits and information upon deconvoluted subpopulations internal to the total deposits. In particular, the '*VolFraction*' columns report also the deposit fraction (*Volume %*) corresponding to the coarser and, where present, the finer subpopulations (SP1 and SP2, respectively); the relative importance of these subpopulations is pointed out by the values of *SP-ratio* (*Vol.*(%) *SP2* / *Vol.*(%) *SP1*).

3.4 Results

3.4.1 Grain size distributions

The GSDs of 8 ash samples, representative of the different eruptive styles observed throughout the activity, show significant differences both in terms of shape (i.e. unimodal or bimodal) (Fig. 3.4) and in the corresponding parameters of skewness and sorting (Tab. 3.1).

On the other hand, deposits resulting from a same phase of activity, collected at different times (e.g., deposits from the *Continuous Ash Venting*) or places (e.g. *Vulcanian explosion*), display very similar and consistent GSDs (Fig. 3.4).
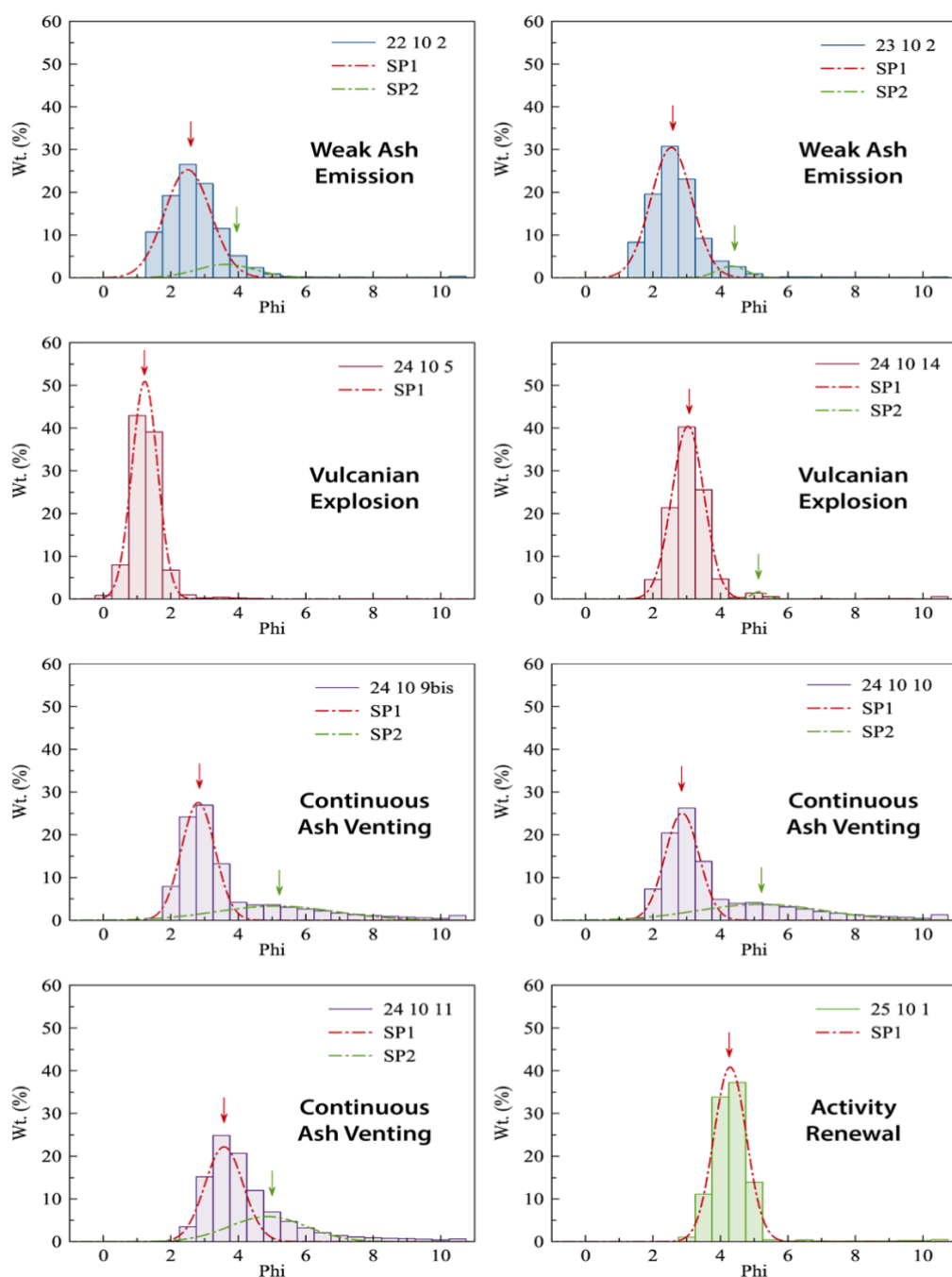
Fig. 3.4 Grain size distributions (GSDs) of tephra fallout samples collected during different stages of eruptive activity (colors). The internal subpopulation of the total deposits are displayed with dotted lines (SP1=red and SP2=green).

In general, either the mode and the relative volume fraction of subpopulations (SP1 and, where present SP2) forming the bulk deposits, display significant variations according to the stages of activity (Tab. 3.1). Ash from the *Vulcanian Explosion* clearly differentiates from the other phases due to its nearly symmetric (Skewness = 0.05), leptokurtic (Kurtosis = 1.04) GSDs (Fig.3.4, Tab. 3.1).

The GSD of the sample SKJ24-10-5 (proximal deposit; 5 km from the vent, Figure (3.3), shows a major subpopulation (SP1) well constrained between 0.5 and 2 Phi, with an Md(Φ) of 1.2 Phi (Tab. 3.1) which accounts for the 98 wt. % of the deposit. The secondary subpopulation (SP2) shows an Md(Φ) of around 4 Phi and represents the residual fraction of the deposit (around 2 wt. %). The distal deposit related to the *Vulcanian Explosion* (11 km from the vent, still along the dispersal axis) still shows a prominent coarser subpopulation (SP1, with Md(Φ) = 3; Tab. 1) still with an only minor contribution of a second, finer-grained subpopulation (SP2, with Md(Φ) = 5.2 Phi; Tab. 1) accounting again for the 2 vol.% of the bulk GSD. The samples from the *Continuous Ash Venting* phase, collected with a different timing during this phase (Tab. 3.1), are characterized by positively skewed distributions (Skewness from 0.41 to 0.59; Tab. 3.1) and a main mode set between 3-3.5 Phi. In particular, samples from the *Continuous Ash Venting* show a very pronounced fine-grained tail, with a secondary mode at 5 Phi (in two out of three samples; Fig. 3.4). Again, the bulk GSD can be deconvoluted (with residuals higher than 0.96) as the sum of two sub-populations; about 30-35 wt. % of the deposit is represented by the finer sub-population (SP2), with an Md(Φ) set at around 5 Phi, while SP1 has an Md(Φ) between 2.8-3.6 Phi (Fig. 3.4 and Tab. 3.1). Interestingly, the Md(Φ) value of SP1 of the samples from the *Continuous Ash Venting* phase registers a continuous increment towards higher values with the time of collection (from sample 24-10-9bis to sample 24-10-11; Tab. 3.1) together with an increment of the relative weight (from 29 to 35%) and no visible change in the Md(Φ) value of SP2.

The two phases of *Weak Ash Emission,* preceding and following the main explosion, were sampled at different distances (4 km for the pre-explosion phase, and 14 for the post-explosion phase). The GSD of the proximal sample can be well related to the contribution of the two SPs: the most abundant (SP1), is peaked at 2.5 Phi and accounts for about 90% of the total sample, and the secondary (SP2) peaked at 3.6-4.3 Phi (Tab. 3.1). On the other hand, the sample related to the reappraisal of the activity, collected at a larger distance than the other, is characterized by a unimodal distribution and a single population with descriptive parameters (Md(Φ) = 4.3; $\sigma(\Phi)$= 0.48) very close to the SP2 of the other samples of *Weak Ash Emission*. The latter aspect, suggests a good similarity between these two phases of eruption not only for the eruptive pattern but also for the associated products.

3.4.2 Characterization of the ash components

Several authors provided analyses of ash componentry on tephra products erupted during different phases of activity at Sakurajima (Oba et al., 1980; Miwa et al., 2009; Miwa et al., 2013a; Miwa et al., 2013b, Kurniawan et al., 2016). Regardless of the nomenclature assigned to the different ash components, we found a substantial agreement in the identification of the main ash types. Generally, ash deposits from the different phases of activity are dominated by glassy, dense and blocky particles showing variably glossy external surfaces with conchoidal fractures and sharp edges, and with variable

roundness. The different fragments are characterized by colors ranging from intense and shiny dark to a translucent grey; in many cases opaque grey colored particles were also recognized, characterized by pitted and non-glossy external surfaces. Vesicular particles, translucent, brownish to dark in color, are also primary in the componentry of the deposits of the high intensity *Vulcanian Explosion*. Loose broken crystals (i.e. plagioclase, clinopyroxene, orthopyroxene, Fe-Ti Oxides and rare olivine), together with sparse lithics, variably colored from white to yellow and brownish-red, are also present as a very minor component. For this reason, these will not be further considered in the analysis.

Based on these general observations, three classes of ash fragments were based on the external morphology and internal textures (Fig. 3.5).
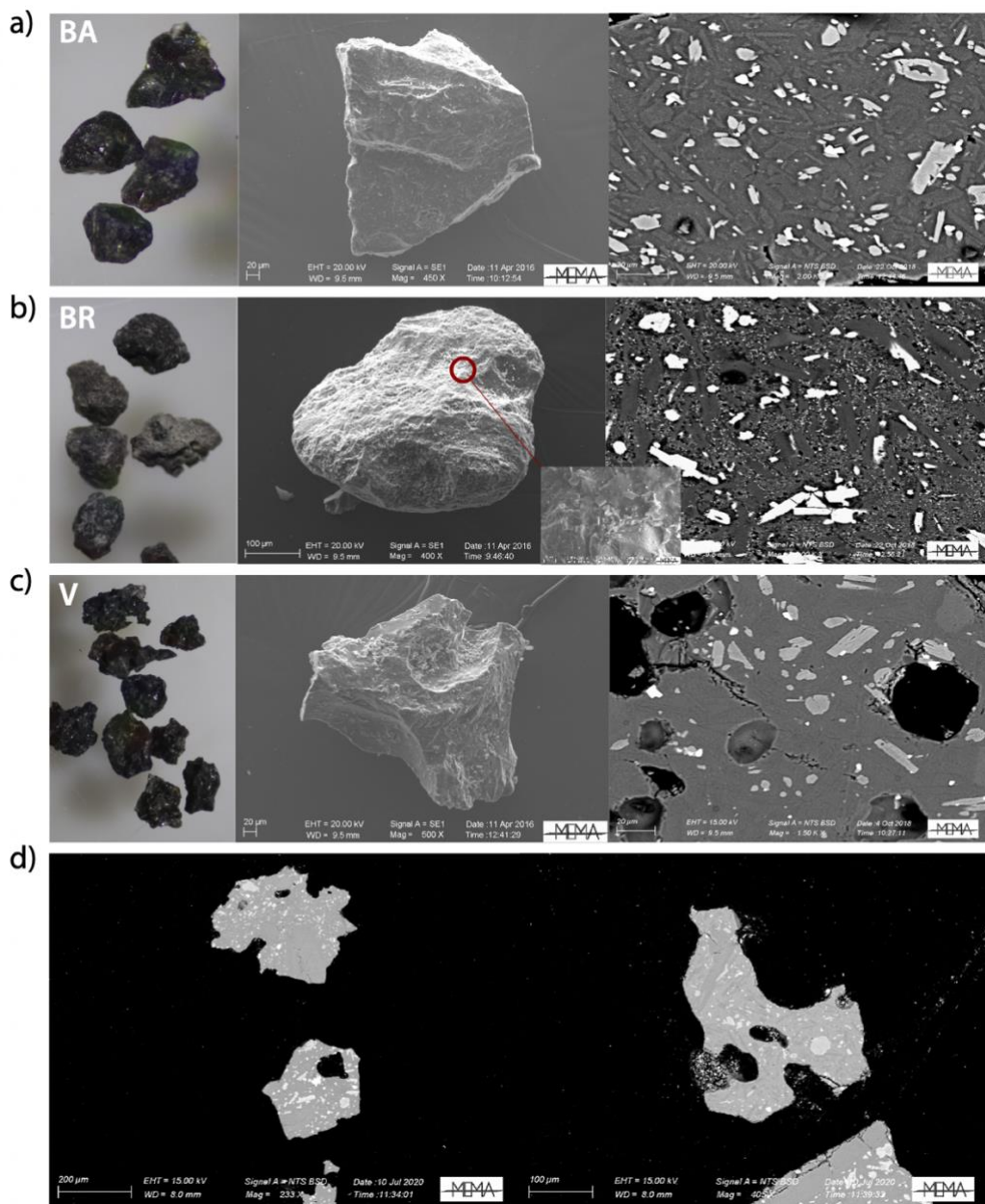
Fig. 3.5 Images of the identified ash components: (a) Blocky Angular (BA), (b) Blocky Rounded (BR) and (c-d) Vesicular (V). Characteristic features of external surfaces are displayed in stereo-binocular and SE-SEM images (used in secondary electron mode), while images of the internal textures are shown in BS-SEM images (used in back scattered mode). The characteristic low vesicularity shown by the V type particles is also clearly shown in (d).

i. ***Blocky Angular** (*BA) (Fig. 3.5a) – BA component is formed by very poorly vesicular to dense, blocky particles with sharp edges and regular outlines, characterized by variably glossy and shining surfaces, sometimes intercepting sparse, large and isolated vesicles, 100-200 µm in diameter. These clasts commonly show planar surfaces with typical indentation patterns, possibly resulting from brittle fracturing. The external surfaces are typically characterized by a sparse, small-scale roughness, where asperities (generally in the order of few micrometers) are mainly related to crystallization of microlites from the groundmass glass. The average values of Solidity and Convexity (for details see Appendices, section 3.7) determined for selected BA particles are 0.930 ± 0.025 and 0.876 ± 0.022, indicating significantly convex external outlines (Tab. 3.2). The average value of Circularity is 0.794 ± 0.040, indicating fairly circular outlines (Tab. 3.2). However, fragments with smoother external surfaces are also present. The most abundant groundmass microlites are represented by euhedral and elongated (20-60 µm), sometimes acicular microlites of plagioclase, followed by pyroxene and sparse oxide crystals. A secondary population, only occasionally present within the BA clasts, is represented by sparse clusters, irregularly arranged in space, of Fe-Ti oxides crystals typically smaller than 5 µm in size. Up to 60 vol.% of the groundmass is represented by residual glass. BA particles possibly correspond to the *'High-Crystallinity-Particles (HCP)'* showing "*glossy surfaces*" reported by Miwa et al. (2013b, and previous works) and with the *"Black Volcanic Rocks" (BVR)* described in the study of Kurniawan et al. (2016).

ii. ***Blocky Rounded** (*BR) (Fig. 3.5b) – BR clasts are blocky, massive, poorly vesicular to dense particles, with average values for Solidity and Convexity of 0.954 ± 0.015 and 0.889 ± 0.019, respectively (Tab. 3.2). The average Circularity of 0.830 ± 0.029 accounts for the sub-rounded to rounded outlines, and along with the pitted and frosted aspect of the external surfaces (Fig. 3.5b), generally associated to opaque from dark to grey colors, make the BR particles very distinct from the BA particles. The groundmass glass is clearly characterized by the presence of two populations of microlites associated with lower amounts of interstitial glass (45 vol.%). The coarser-grained population (in the range of 15-30 µm) is made up of plagioclase, mafic minerals (cpx, opx, and rare olivine) and Fe-Ti oxide crystals, while the finer-grained population is represented by abundant, very small (< 5 µm) clusters of Fe-Ti Oxides crystals. Respect to BA particles, a more diffuse fine-grained roughness affects external surfaces, corresponding to a slightly higher crystallization of the groundmass glass. Differently from BA, the groundmass texture shows a diffuse glass recrystallization particularly by small Fe-Ti oxides (Fig. 3.5b). Occasionally, small acicular salt crystals are found above the external surfaces. BR clasts are very similar in the external aspect to those briefly described by Miwa et al. (2013b) as non-juvenile particle showing *'non-glossy'* surfaces (corresponding to the NS-Type of Miwa et al. 2009). On the other hand, the diffuse recrystallization of the groundmass glass is strongly suggestive of recycling of previously ejected juvenile material under high-T conditions (D'Oriano et al., 2011, 2014). Further comparative textural analyses of BR and BA fragments allowed us to discuss in more detail the significance and possible genesis of BR material.

iii. ***Vesicular*** (V) (Fig. 3.5c) – V clasts are vesicular particles with external surfaces intercepting sparse vesicles from 30 to 60 μm in size. Both Solidity and Convexity show average values that are significantly lower (0.915 ± 0.036 and 0.838 ± 0.038, respectively; Table 3.2) respect to the other categories, testifying for more irregular and convoluted external outlines (Fig. 3.5c). Also, the Circularity of particles is significantly lower respect to other categories, with an average value of 0.756 ± 0.059. Vesicles never form interconnected channels and their abundance is largely variable, from few percent up to 30 vol. % Very high values of vesicularity, typical of pumice-like material, have been never observed in the analyzed material, although they have been described in other eruptions (Miwa et al., 2009). V clasts always present a fresh aspect of the glass and glossy external surfaces, translucent-brown to dark in color. Groundmass texture is microlite-poor (crystal content around 30 vol. %) when compared with the other two categories. Microlites are dominated by a single population, with an average size of 10-20 μm consisting of euhedral plagioclase, mafic minerals and oxides. Importantly, the population of small Fe-Ti oxide clusters is totally absent in these clasts. V clast can be easily associated with the *'vesicular'* and *'Low-Crystallinity-Particles (LCP)'* presented by Miwa et al. (2013b), and with the "Black Vesicular Volcanic Rocks" (BVVR) of Kurniawan et al. (2016). On the other hand, they result significantly different from the *pumiceous particles* identified by Miwa et al., (2009) due to their lower and isolated vesicularity (rarely exceeding 30%). *Lithic* fragments are always very rare, in agreement with the low energy of the observed activity. They are generally recognized for the incipient to pervasive alteration of the fragment, and mainly correspond to fragments of preexisting lava flows.

Particle Type	Shape of the Identified ash components			
	Solidity	Convexity	Elongation	Circularity
BA in Phase 1	0.911 ± 0.039	0.855 ± 0.033	0.217 ± 0.099	0.771 ± 0.050
BA in Phase 2	0.941 ± 0.017	0.888 ± 0.017	0.277 ± 0.160	0.801 ± 0.037
BA in Phase 3	0.937 ± 0.020	0.886 ± 0.016	0.276 ± 0.101	0.810 ± 0.032
Average	*0.930 ± 0.025*	*0.876 ± 0.022*	*0.257 ± 0.120*	*0.794 ± 0.040*
BR in Phase 1	0.940 ± 0.019	0.870 ± 0.031	0.264 ± 0.128	0.799 ± 0.040
BR in Phase 2	0.960 ± 0.014	0.898 ± 0.016	0.210 ± 0.094	0.845 ± 0.025
BR in Phase 3	0.962 ± 0.011	0.898 ± 0.010	0.224 ± 0.079	0.845 ± 0.022
Average	*0.954 ± 0.015*	*0.889 ± 0.019*	*0.233 ± 0.100*	*0.830 ± 0.029*
V in Phase 1	0.889 ± 0.071	0.831 ± 0.045	0.336 ± 0.186	0.736 ± 0.089
V in Phase 2	0.930 ± 0.010	0.823 ± 0.037	0.221 ± 0.026	0.757 ± 0.036
V in Phase 3	0.925 ± 0.026	0.861 ± 0.033	0.316 ± 0.137	0.774 ± 0.053
Average	*0.915 ± 0.036*	*0.838 ± 0.038*	*0.291 ± 0.116*	*0.756 ± 0.059*

Tab. 3.2 The ash morphometry is quantified through four a-dimensional shape parameters, according to Liu et al. (2015): Solidity, Convexity, Elongation, Circularity; see Appendices, section 3.7 for the definition of

the shape parameters. Values of apparent 2D projected ash shape of the identified ash component is provided together with its standard deviation, for particles collected during the three eruptive phases: Phase 1,2 and 3 corresponds respectively to the *Weak Ash Emission, Vulcanian Explosion,* and the *Continuous Ash Venting.*

The relative proportions of the different components change with the stages of eruptive activity (Tab. 3.3). The ash componentry is largely dominated by BA and BR clasts. Although V clasts represents only a minor fraction in the *Weak Ash Emission* deposit (less than 10%), they tend to significantly increase in the relative abundance respect to BA as the eruptive sequence progresses (the V/(BA+V) ratio increases from 0.17 to 0.52; Tab. 3.3).

Relative abundance ratios	Weak Ash Emission	Vulcanian Explosion	Continuous Ash Venting
BR/(BA+V)	0.53	0.39	0.24
BA/(BR+V)	1.19	1.07	0.64
BR/BA	0.64	0.54	0.50
V/BA	0.20	0.39	1.07
Lithics/total	0.04	0.03	0.05
Cryst./total	0.04	0.09	0.22

Tab. 3.3 Relative abundance of the different ash components in the analyzed deposits throughout the three activity stages. Ash componentry is determined over a set of 300 randomly picked particles from to the modal class of the GSDs (250-500 µm).

An opposite trend is shown either by the BA and the BR clasts, whose relative abundances progressively decrease respect to V clasts throughout the sequence, with a minimum registered in the phase of *Continuous Ash Venting* (ratios BR/(BA+V) and BA/(BR+V) in Tab. 3.3*)*. As a matter of facts, the dense fraction (BA and BR) is shown to be by far dominant respect to the vesicular fraction during all the stages of the eruptive sequence. Conversely, the relative proportions of BA vs. BR remain nearly constant throughout the entire sequence (Tab. 3.3).

Finally, while the abundance of the Lithic component is always very low and nearly constant, loose crystals progressively increase (from 4 to 18%) along the sequence (Tab. 3.3). Unfortunately, the very fine grain size of the *Post-event Weak Ash Emission* has not allowed us to estimate the ash componentry for this stage of activity.

3.4.3 Quantitative characterization of ash groundmass textures

Analysis of groundmass textures allowed us to exhaustively characterize the different mineral phases identified during the image analysis with the following information:
i) Relative abundance of vesicles and crystals, and MND of different ash components (Tab. 3.4) ii) Morphometry of Plagioclase microlites (Tab. 3.5). Moreover, crystal size distributions (CSDs) were also derived for Plagioclase microlites since they proved to effectively control the total crystal abundance of the analyzed ash fragments (Figs. 3.6 a, b).
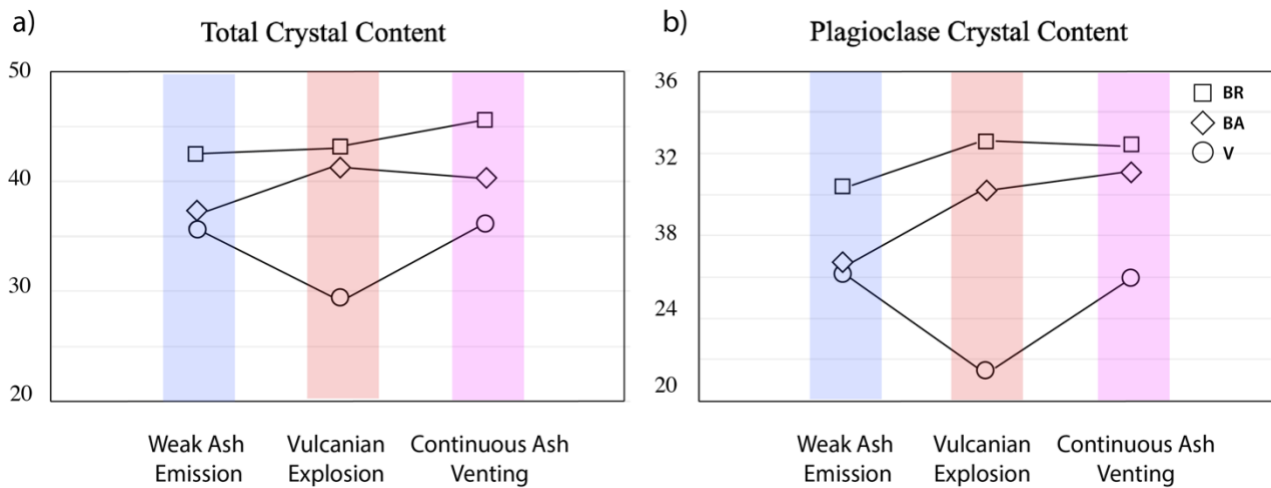
Fig. 3.6 Average microlites contents measured for the three ash components collected during different stages of activity. Variations of the total crystal contents (a) are compared with plagioclase contents (b). Squares (BR), diamonds (BA) and circles (V). Values are all corrected for the contents of vesicles.

The averaged values calculated for the microlite contents (Tab. 3.4) of BA and BR clasts are similar and quite constant at around 40-45% throughout all the eruptive sequence, with BR clasts displaying the highest value (45.6%) in the *Continuous Ash Venting* stage (Fig. 3.6).

Phase of Activity	Particle type	Tot. crystal abund.	Vesicle abund.	Oxides abund.	Femics abund.	Plagioclase abund.	Residual glass	Areal MND [#NumCryst/Area]
		(%)	(%)	(%)	(%)	(%)	(%)	(mm^{-2})
Weak Ash Emission	BA	37.1	0.6	1.2	9.5	26.4	62.4	44616
	BR	42.5	1.1	1.5	10.5	30.4	56.9	51078
	V	35.7	21.6	1.0	8.3	26.3	58.9	20144
Vulcanian Eruption	BA	41.3	1.8	1.3	9.7	30.3	57.8	22077
	BR	43.1	0.4	1.3	9.3	32.6	56.7	38693
	V	29.4	17.9	1.0	6.9	21.5	50.5	18797
Continuous Ash Venting	BA	40.3	0.8	0.8	8.4	31.1	59.3	33829
	BR	45.6	0.1	1.7	11.4	32.4	54.4	29354
	V	36.1	11.6	1.4	8.7	26.0	63.9	32446

Tab. 3.4 Relative crystal abundance and areal MND of the ash grains in the different stages of activity. Average relative abundance of the different crystal phases and vesicles are reported together with the MND calculated for the three classes of components considering the whole mineral assemblage. Relative abundance and MND calculated for single particles are reported in Tab. A2 and Tab. A3 at the end of this Chapter, in the Sections of Appendices. Note that vesicularity is measured using a wider-angle magnification respect to microlites in order to ensure a good compromise between resolution and representativity.

V clasts show instead a larger variability of crystal content, and an overall different trend of variation respect to BA and BR along the analyzed sequence (Fig. 3.6a). Crystal content of V clasts is comprised between a minimum value of around 29 vol.% during the *Vulcanian Explosion,* up to a maximum value of around 36 vol.% during both the other phases. All these values are strongly in accord with the crystal content reported by Miwa et al. (2013b) for HCP and LCPs ash fragments, and by Smith et al. (2018).

The areal microlite number density (MND) was calculated for several fragments considering all the mineral phases identified during the image analysis of BS-SEM images. MND displays a variation which is mostly comprised between $1.88*10^4$ and $5.1*10^4$ mm^{-2} (Tab. 3.4) (respectively corresponding to minimum and maximum values of 7561 and 83634 for each single particle: Tab. A3), in good agreement with data reported by Kurniawan et al. (2016).

Results of the size distribution analysis of plagioclase microlites are reported in Figure (3.7).

The CSDs calculated for plagioclase microlites in the investigated deposits show similar linear trends (Fig. 3.7a) for all the different types of clasts, and for the different phases of the eruption. A single BR sample, from the *Continuous Ash Venting* phase (red squares in Fig. 3.7a) exhibit a more pronounced tail in the coarser size regions (more than 100 μm; Fig. 3.7a).
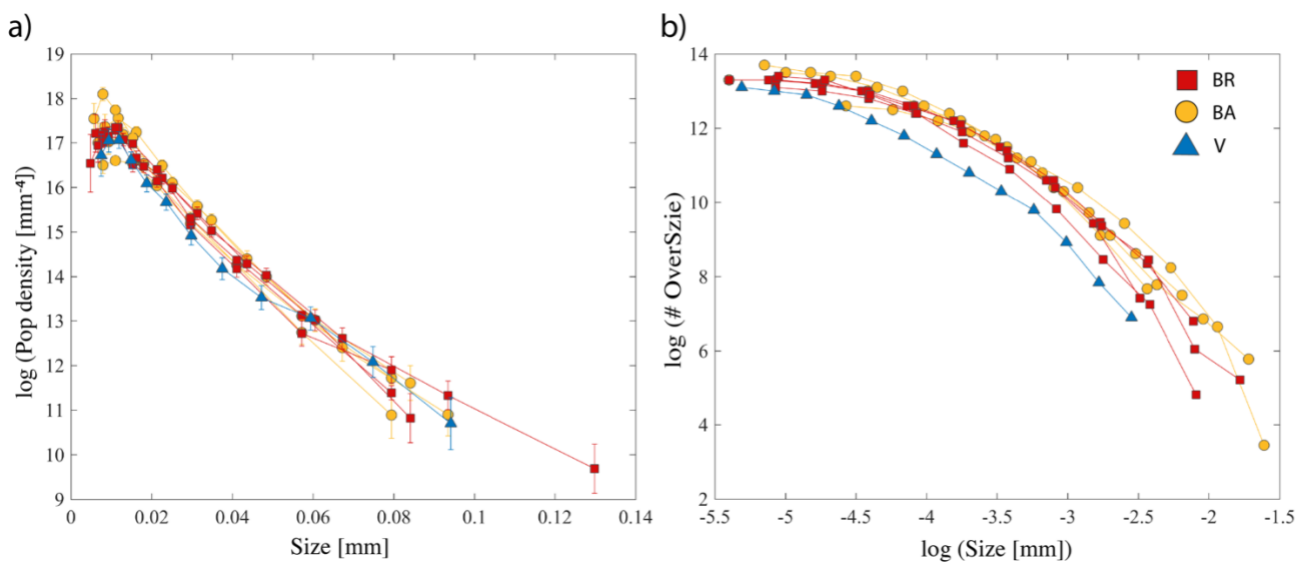
Fig. 3.7 a) 3D crystal size distributions (CSDs) of plagioclase microlites for the different ash components (different colors, as specified in the legend) selected from the three phases of activity: the size is compared to the logarithm of the population density of plagioclase crystals. b) Frequency distribution of the plagioclase size '*log(Size)*' against the number of particles coarser than the size '*log(#OverSize)*'.

CSDs display a regression slope (-1/G*t) variable between -77 and -109, resulting in a dominant size of microlites (3*Gt) on average around 30-40 μm (Tab. 3.6); nuclei number density (corresponding to the regression intercept of the CSD, n_0) is generally invariant among all the analyzed samples.

All the trends clearly display an overturn of the population density for the size classes smaller than 10 μm, also present in CSD data by Miwa et al. (2013b). Typical axial ratios (short; intermediate; long) of plagioclase in the different phases are nearly constant (1 : 3.4 : 9, 1 : 4 : 10 and 1 : 3.4 : 10, for *Weak Ash Emission*, *Vulcanian Explosion*, and *Continuous Ash Venting*, respectively) (Tab. 3.5). Again, these values are very close to those reported by Miwa et al. (2013b) for plagioclase microlites in both LCPs and HCP fragments (1: 2.3 : 9 and 1 : 3.2 : 10, respectively).

In addition, the distributions frequency of the plagioclase size in the bi-logarithmic space (Fig. 3.7b), display curvilinear, and therefore not self-similar distribution trends. The narrow distribution of data in this plot further confirms the substantial invariancy of the ash features with the eruptive phase.

	Shortest axis	Intermediate axis	Longest axis	R^2
Weak Ash Emission	1	3.4	9	0.75
Vulcanian explosion	1	4	10	0.67
Continuous Ash Venting	1	3.4	10	0.75

Tab. 3.5 Ratios of the shortest, Intermediate and Longest axis of Feldspar crystals for the three main phases of activity. The determination coefficient (R^2) refers to the goodness of fit from the software 'CSD slice' (Morgan and Jerram, 2006).

Particle ID	Particle Type	Regr. Slope ($-1/G*t$)	Dominant crystal size ($3*Gt$)	Regression Intercept (n_0)	Areal MND	Volumetric MND (N_v)	Time-scale for the plug formation	
		(mm)			(mm^{-2})	(mm^{-3})	Min. (days)	Max. (days)
23 10 1	BA	-90 ± 3.7	0.033	18.53 ± 0.11	9584	626000	14	26
23 10 1	BR	-87 ± 4.0	0.035	18.14 ± 0.12	7202	533000	15	27
23 10 1	V	-81 ± 3.7	0.037	17.66 ± 0.12	5045	341000	16	29
24 10 15	BA	-77 ± 1.8	0.039	17.56 ± 0.06	5093	311000	17	30
24 10 15	BR	-91 ± 1.6	0.033	18.26 ± 0.05	6849	478000	14	25
24 10 14bis	BA	-109 ± 4.0	0.028	18.75 ± 0.10	8118	729000	12	21
24 10 14bis	BR	-84 ± 3.8	0.036	17.88 ± 0.12	5958	405000	15	27
24 10 9bis	BA	-81 ± 3.8	0.037	18.06 ± 0.12	7336	498000	16	29
24 10 9bis	BR	-77 ± 3.0	0.039	17.87 ± 0.10	6955	420000	17	30

Tab. 3.6 Information on the crystal size distribution (CSD) extracted for a set of ash fragments representing different phase of activity, using the software *CSDcorrections*. The microlite number density (MND) is calculated as the ratio between the number of plagioclase crystals to the analyzed area. The last two columns report the minimum and maximum times estimated for plug formation calculated using respectively the averaged values of Plagioclase growth rates in the 1980-1986 dacitic magmas from Mt. S. Helens (2.7*10E-8; Cashman, 1992) and the 1992 mafic andesites from Mt. Spurr (1.5*10E-8; Cashman & Blundy, 2000).

3.4.4 Quantitative investigation of the ash shape

The variability of ash morphology along the sequence is well described by some selected shape parameters (Cioni et al., 2014; Liu et al., 2015; Leibrandt et al., 2015), and by their variations with ash size. Following the suggestion of Liu et al. (2015), the selected shape parameters are representative of clast form (Circularity, Elongation), and textural (Convexity) and morphological roughness (Solidity). Ash from *Weak Ash Emission* and *Continuous Ash Venting* phases shows very similar trends of variation with size and, more importantly, very similar values of all the different shape parameters analyzed (Fig. 3.8). Conversely, ash from the *Vulcanian Explosion* is generally different from that of the other phases, also presenting a marked variability with particle size (Fig. 3.8). In general, ash from all the samples is characterized by a quite regular outline, with high Solidity and Convexity values (higher than 0.94 and 0.96, respectively), and by a quite elongated shape (Circularity < 0.91, Elongation between 0.25 – 0.30).
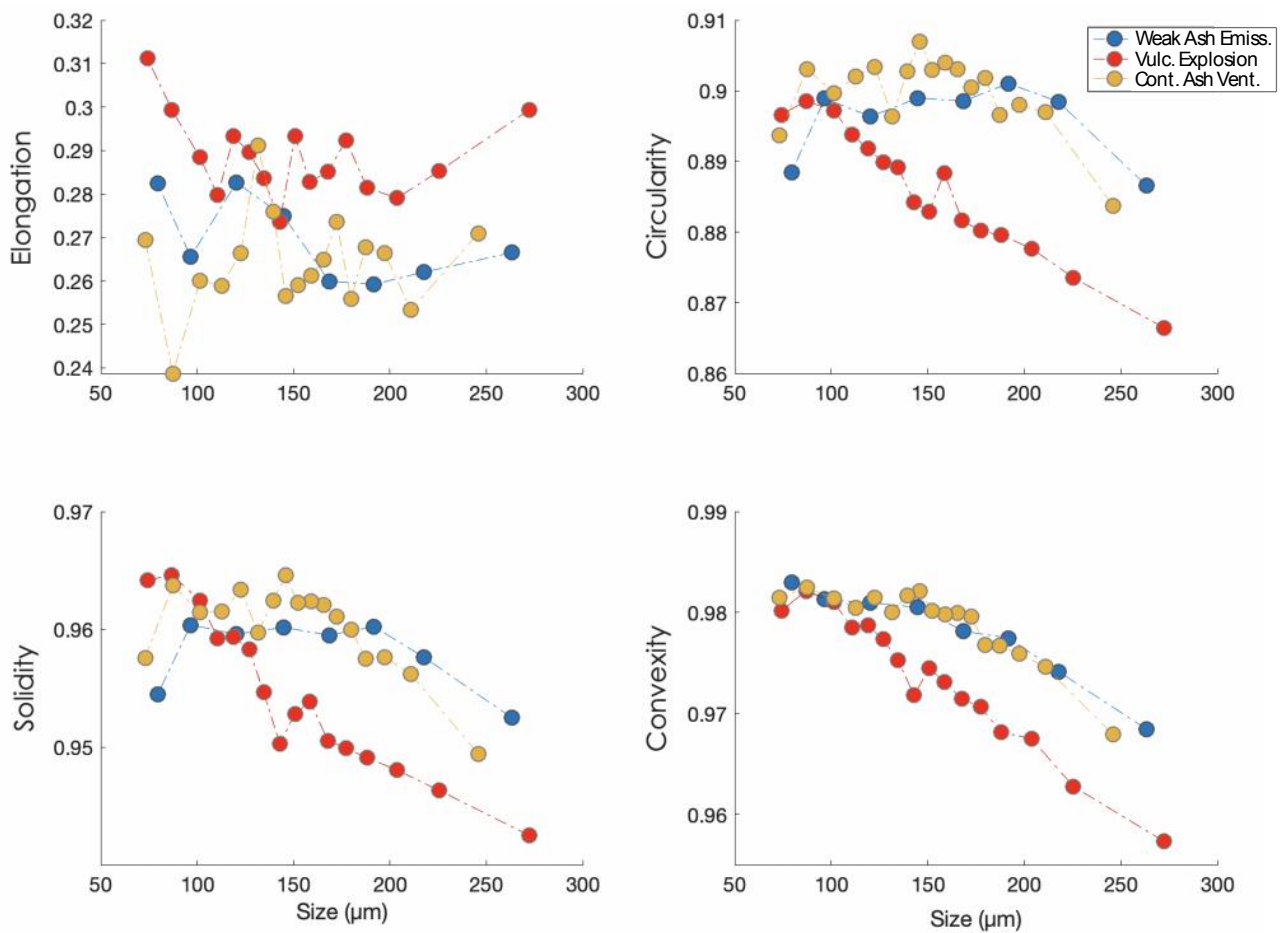
Fig. 3.8 The shape-versus-size trends of ash resulting from different activity styles was quantified based on four representative shape parameters (Elongation, Circularity, Solidity and Convexity). Different colors of dots in the plots refer to the identified styles of activity.

As suggested by Elongation and Circularity values (Fig. 3.8a, b) particle shape is nearly invariant respect to ash size for samples from the *Weak Ash Emission* and *Continuous Ash Venting* phases, while Circularity shows a marked, progressive increase with decreasing size for the sample from the *Vulcanian Explosion* (Fig. 3.8b). On the other hand, a consistent variation of the particle shape with size is evident for Solidity and Convexity (Fig. 3.8c, d), suggesting the prevalence of a coarse roughness (lower values of the two parameters) on the particle outline. Again, this trend is more marked for the ash from the *Vulcanian Explosion*, while the values of the different parameters for the ash from the other two phases are always very similar (Fig. 3.8). Importantly, the trends of Circularity, Solidity and Convexity for the ash of the *Vulcanian Explosion* clearly diverge from the trends of the ash from the other phases starting from particles greater than 100 and 150 μm in diameter (Fig. 3.8). This suggests a constant size for the outline roughness, possibly coarser than about 100 μm. We interpret these differences as related to larger amounts of vesicular particles (generally having a more irregular contour) ejected during the *Vulcanian Explosion* and to the presence of a vesicle population with a size possibly between 50-100 μm, which mainly affects and modifies the external shape of the coarser particles.

3.5 Discussion

High-frequency, ash-dominated cyclic explosive activity represents the typical behavior of many volcanoes worldwide which are mainly characterized by the eruption of mildly-evolved magmas. Sakurajima can be considered a typical representative of these volcanoes, characterized by cyclic activity represented by stages of weak and nearly continuous low-level gas and ash emission interrupted by the periodic occurrence of large Vulcanian explosions and immediately followed by a short phase of intense ash venting. Differently from most of the previous works on Sakurajima, which were mainly focused on the investigation of the larger, prominent vulcanian explosions, the dataset presented in this study allowed an exhaustive description of the ash products ejected during the different phases of a complete cycle defining a vulcanian eruption, thus characterized by significant variations in the style and intensity of the activity. Data allow us to critically discuss the main conduit and fragmentation processes involved in such cycles, and how they can be reconciled with the general knowledge about the mechanisms driving classical Vulcanian activity, not only at Sakurajima. In fact, several questions are currently pending about the conduit processes that effectively control the occurrence of high-frequency Vulcanian explosions:

- What are the internal gradients (i.e., vesicularity, crystal contents, permeability, viscosity) of the magma plug and which portions of the magma conduit are involved in the process of ash production during the different phases of the eruptive sequence?
- What drives the sudden transition that is often observed between passive ash emission and vulcanian explosions?
- Is fresh, volatile-rich magma coming from the deep always a portion which is directly involved into the activity?
- Which is the approximate volume of the magma conduit involved in each phase, also in the light of the characteristic time of plug re-generation and recharge?
- Which is the variability with time of explosive processes (and of the plug features) over periods much longer than a cycle?

All these questions will be addressed in the following sections, discussing our results and comparing them with the numerous data existing in the literature on Sakurajima activity.

3.5.1 Insights into the structure of the volcanic conduit from the morpho-textural features of ash components

Generally, vulcanian activity is described as the result of the fragmentation of a rigid to visco-plastic, variably crystallized and variably degassed magma plug or lava dome sealing the top of a volcanic conduit (Clarke et al., 2002b; Clarke et al., 2013; Gaunt et al., 2020). Formation of summit lava domes at Sakurajima has been observed to occur very sporadically. Conversely, a variably degassed, vertically stratified magma plug is considered to be commonly present, sealing the upper portions of the conduit and generally modulating the dynamics of gas escape (Ishihara 1990; Miwa et al., 2013b; Iguchi et al., 2013a, 2013b; Yokoo et al., 2013; Oláh et al., 2019). Morpho-textural analysis of ash fragments

efficiently informs about the variability of the internal structure of the fragmented portions of magma. Accordingly, the relative proportions of ash components can help to define the internal gradients of the magma conduit and to identify those processes which are responsible for the magma fragmentation (e.g. Cioni et al., 2014).

The detailed analysis of the different components forming the deposits of the different phases of a vulcanian cycle at Sakurajima reveal some important characteristics of the internal structure of the upper portion of the magma column and of its short-time evolution. The general invariancy with eruption progress recorded in the characteristics of the different ash components (constant type of components involved (Fig. 3.5), invariancy in the CSD of plagioclase microlites (Fig. 3.7a-b)) suggests a common pre-eruptive evolution for the different parcels of magma from which these components derive. Conversely, features like the (limited) variability in the total crystal content indicate a progressive, although generally slight, change of the erupted material along the cycle (Fig. 3.6).

All the samples of the studied sequence are characterized by the common presence of three types of ash fragments (Fig. 3.5) which have been here characterized based on the external shape and internal texture. Their textural features can be easily correlated with those of the ash components described by several authors studying previous stages of activity at Sakurajima (Oba et al., 1980; Miwa et al., 2009; Miwa et al., 2013b; Kurniawan et al., 2016). Differently from what observed by Miwa et al. (2013b) for the 2010 activity, no particles with 'fluidal' external morphology as well as no pumice-like particles (Miwa et al., 2013a; Kurniawan et al., 2016) characterized by very high vesicularity were recognized in the products, despite the styles of the observed activity and the intensity of the prominent event were entirely comparable with the typical intensity and activity patterns of Sakurajima (JMA on-line reports). A possible explanation for the generally low abundance of highly-vesicular material in the studied 2014 deposits can be found in the lower rates of the volcano activity respect to other periods investigated by other authors, as indicated by data reported in Oishi et al. (2018) (Tab. A1, section of Appendices). In fact, V clasts always represent in all the analyzed deposits a minor volume fraction, furthermore displaying a low average vesicularity which rarely exceeds 20 vol%, considerably lower respect to values of up to 60 vol% reported for the pumiceous fragments by Miwa and Toramaru (2013) (Fig. 3.5c, d).

As a matter of facts, several considerations on the features of the main clasts present in the deposits are strongly suggestive that these clasts can be related to the rigid fragmentation of a highly degassed, highly crystallized region of the magma column, developed in the topmost portion of the magma plug. All the analyzed deposits were shown to be largely dominated by particles represented particularly by BA clasts, characterized by high microlite contents (mostly comprised between 35 and 40 vol. %) very low vesicularity (around 1 vol.%), and sharp external outlines with planar, shiny and glossy external surfaces (Fig. 3.5a; Tab. 3.4). All these features are typical of fragments derived from the disruption of a high viscosity (although still molten) magma portion, in agreement also with the rhyolitic composition of the residual melt determined for similar fragments by Kurniawan et al. (2016) (SiO_2 = 74.2 ± 1.7 wt. %; BVR fragments). This hypothesis is also supported by the relatively low thermal anomaly measured for the prominent Vulcanian Explosion (reaching up to maximum 140 °C) suggesting a scarce participation of hot and fresh magma from the deeper reservoir (Fig. 3.3). Further elements supporting

this interpretation come from the textural analysis of the ash fragments. In particular, the observed turn-down of the linear trends of CSD for crystals smaller than 10 μm (Fig. 3.7a), possibly indicates the occurrence of a coarsening process typical of highly crystallized melts (Higgins, 2006). Furthermore, the non-fractal distribution trends of plagioclase microliths (Fig. 3.7b) and their acicular morphologies (Tab. 3.5), likely indicates the occurrence of continuous crystallization stages under significant undercooling (Morgan and Jerram, 2006; Brugger and Hammer, 2010b) or important stages of decompression-induced crystallization (Cassidy et al., 2015). Both these possibilities would suggest stalling, or very slow ascent, of the magma responsible for the origin of these ash fragments at low-pressure, thus confirming the interpretation that BA clasts derive from a highly viscous, nearly rigid magma-plug.

BR clasts share several morphological and textural features with BA clasts, although differing from them mainly for the lower angularity of the external outlines (Circularity: 0.830 ± 0.029; Tab. 3.2), the diffuse, low-scale surface roughness and the dull color of the external surfaces (Fig. 3.5b). The μm-sized population of Fe-Ti oxides overprinted on sub-euhedral microlites (Fig. 3.5b) is very similar to that produced during experimental re-heating of glass-bearing fragments that are interpreted as thermally-indiced glass recrystallization during recycling in the vent area (D'Oriano et al., 2011, 2014; Deardorff and Cashman, 2017). These features, together with the general similarity with BA clasts, suggest that BR clasts invariably derive from the intra-crateric recycling of mostly BA-type particles fragmented and ejected during preceding cycles of activity. This is also indirectly confirmed by the invariant groundmass textures of this type of fragments among all the different phases of activity, as testified for example by their constant microlite abundance and invariant CSD features (Figs. 3.6 and 3.7). The gradual decrease in the relative abundance of these clasts from the initial phase of *Weak Ash Emission* to the final *Continuous Ash Venting* phase (Tab. 3.3) possibly reflects the progressive clearing of the vent area due to the increase in the intensity of the activity, and consequently the increasing importance of the involvement of newly fragmented ash in the progressing eruptive cycle.

It is important to note that BR clast type has never been accurately described in previous studies, as they were possibly classified alternatively as not-vesicular, not-smooth, glassy juvenile material (Miwa et al., 2009), as lithic clasts (Kurniawan et al., 2016), or even included in the altered material (Miwa et al., 2013b, 2015). This possibly explains also our generally lower estimates of Lithic fragments respect to what reported from other authors (Kurniawan et al., 2016). In fact, Lithic clasts display very low relative abundances (less than few vol%) in all the analyzed deposits, in agreement with the low to moderate energy of the observed activity. This aspect should not be regarded as a minor difference. If our interpretation of BR ash as recycled, thermally-altered, hot vent-hosted material is correct, this important portion (in terms of mass) of the ash, although not directly involved in the process of primary magma fragmentation, could still have a first order role in driving the convective ascent of the plume, thanks to its high temperature and abundance. The not involvement of BR clasts in active fragmentation is also in agreement with the high abundance of these type of clasts during periods of quasi-constant emission of ash characterized by a very low energy of the activity (Iguchi et al., 2008), like during the phase of *Weak Ash Emission* (BR/(BA+V) = 0.53, thus considerably higher than other phases; Tab. 3.3). For all these reasons, we suggest that the presence of significant quantities of high-temperature, pre-

fragmented and remobilized material occupying the crater area during low energy activity represents an aspect of primary importance for the definition of a general energy balance for ash production and emission, not only at Sakurajima volcano. In fact, also in the 2009-2010 activity of Tungurahua volcano "Vitreous oxidized" ash particles, representing up to 15% of the emitted fallout deposit, were interpreted as vent-hosted and recycled materials, and their abundancy patterns throughout the eruptive sequence are similar to that observed at Sakurajima with lowering through to more energetic and vulcanian stages of the activity (Battaglia et al., 2019).

Finally, V particles are always less abundant than the other types, as indicated by the ash componentry (Tab. 3.3) and confirmed by the analysis of the ash shape parameters (Fig. 3.8). They mainly differ from BA and BR fragments for the higher vesicularity, although on average lower than 20 vol%. This vesicularity value, the generally rounded shape and the isolated nature of the vesicles (Fig. 3.5c, d) concur in indicating a low permeability for the originating magma portion. The planar external surfaces, with no signs of fluidal deformation, and the microlite-rich groundmass (29.4-36.1 vol%), although with a slightly lower MND values (18797-32446 mm^{-2}, Tab. 3.5) than the other components, still testify to a rigid behavior at fragmentation for these clast, possibly related with the rhyolitic composition of the residual melt also of this magma portion (average SiO_2 =70.7 ± 1.5 wt. %; BVVR fragments, Kurniawan et al., 2016). Therefore, also for V fragments we suggest a derivation from a still rigid portion of the plug, although slightly volatile-richer and microlite-poorer respect to that originating the BA fragments. We suggest that the portion of magma originating V type clasts was possibly deeper respect to that forming BA particles. This part of the magma plug could correspond to the region where several authors (Ishihara, 1990; Yokoo et al., 2013) identified the presence of a gas pocket interpreted to be responsible for the violent pressure shock waves released at the onset of the Vulcanian explosions. The absolutely invariant CSDs (Fig. 3.7) recorded in all the different types of ash fragments can be used to try to constrain the timing of plug reformation. Using a possible range of growth rates data for plagioclase crystals in magmas of comparable composition (2-7*E-08 [Cashman, 1992] - 1.5*E-08 [Cashman and Blundy 2000]; Tab. 3.6), the time scale for plug formation is in the order of around 1 month, thus confirming the fact that newly arrived magma is not involved in the eruption.

3.5.2 Insights into the dynamics of the recent Vulcanian activity at Sakurajima

The systematic variation revealed in the GSDs of the ash deposits, along with the sudden shifts observed in the style of the activity (Fig. 3.2, Tab. 3.1), seem to suggest that eruptive conditions, and thus possibly fragmentation mechanisms, consistently varied during the observed sequence of activity at Sakurajima. A critical review about the dynamics of variation of the conduit processes operating during the different stages of Vulcanian activity at Sakurajima is now possible thanks to the evidences obtained from data collected on tephra GSD, and to the conduit stratification discussed above based on ash componentry and morpho-textural features of the clasts.

The phase of *Weak Ash Emission* preceding the *Vulcanian Explosion* is mainly characterized by a puffing-style, low-energy degassing, dispersing very low amounts of fine ash at short distances, with very low sedimentation rates (1.91E-06 kg/m^2/s; Figs. 3.1, 3.3). The absence of clear signs of explosive

activity during this phase suggests that magma fragmentation was not driven by a large pressure accumulation within the magma plug, but it was possibly driven by nearly continuous low-pressure gas release from the open fracture network of the upper portion of the plug. Under these conditions, ash conveyed in the plume was possibly derived from the fragmented material present in the crater infilling and produced during previous explosions, or taken from the numerous fractures of the plug itself and produced through not-explosive, brittle fragmentation mechanisms like friction/shear (similar to fault gouges fragmentation observed in several plugs/domes elsewhere; e.g. Cashman et al., 2008 or chapter 4 of this thesis). Elutriation from an ash-filled crater or from ash-filled fractures in the plug could be a feasible mechanism for justifying the high abundance of BR type clasts in the plume (Tab. 3.3). Given the average size of the fragments (Md(Φ) = 180μm), gas ascent velocities of the order of few ms^{-1} could be enough for the fluidization of these beds and elutriation of the sampled material (Tasirin & Geldart, 1999). Low ascent velocities of the gas-ash plume are also testified by the observed rapid, low-level drifting of the plume under low wind velocity.

Conversely, the *Vulcanian Explosion* phase represents a powerful event able to eject both large ballistic blocks along the slopes of the volcano and to form a convective plume rapidly ascending up to 3-4 km height, before being drifted away by the wind. Despite the high energy of this activity, related ash deposits are still largely populated by dense to poorly vesicular, microlite-rich particles, indicating also for this stage of activity the prevalence of a brittle magma fragmentation mechanism. On the other hand, the lack of the fluidal or pumice-like material often observed during other periods of Sakurajima activity, and the substantial invariancy revealed in the CSDs of plagioclase microlites and in the ash componentry, all suggest that activity was possibly fueled by the progressive magma degassing and by gas accumulation into the upper portion of the conduit, rather than an increased pressure directly related to advection of new, volatile-richer magma into the volcanic plumbing system. Magma migration is possibly due to the gradual development of high permeability regions in correspondence of the upper viscous portion of the conduit, due to the increased internal shear of the ascending and degassing viscous magma column. This hypothesis accords very well also with the significantly lower rate of explosive activity that characterized Sakurajima in October 2014 (Oishi et al., 2018). This is also confirmed from what reported by Yokoo et al. (2013) who, interpreting geophysical signals, recognized the unlikelihood for the injection of new magma from the deeper magma reservoir to actively participate and trigger the onset of the eruption itself, as instead suggested by several other authors (Iguchi et al., 2008; Miwa et al., 2009; Miwa and Toramaru 2013). Moreover, a significant temporal stagnation in terms of both activity and seismic signals is often observed to characterize the time-lapse between the input of new fresh magma and the consequent Vulcanian activity (Yokoo et al., 2013). All these data, suggest that the mechanisms responsible for triggering at least part of the vulcanian explosions at Sakurajima are mostly related to the gradual over-pressurization of the upper portions of a rigid plug by progressive volatile exsolution without important outgassing in the plug itself. Conversely, mechanisms of pressure increase like the progressive loading by a slowly-ascending viscous magma from beneath, or the arrival of a new volatile-rich magma batch, are so possibly interpreted to the trigger major explosions during the high-rate activity periods (high frequency of explosions).

Importantly, as already discussed for the phase of *Weak Ash Emission*, the large presence of recycled clasts with clear thermally-induced glass recrystallization (BR clasts) also during the Vulcanian phase can be of primary importance in determining the convective power of the resulting plume. In fact, albeit these clasts can be generally classified as lithic material since they were already fragmented at the moment of being engulfed in the plume, they can still represent an important heat source for the plume development, due to their hot state and their abundance in the ejected material (up to around 50 vol%). BR clasts so assume a primary role in the total heat budget driving the plume ascent and ash dispersal at Sakurajima. The convective power of the plume related to the Vulcanian phase of activity is mainly testified by the thermal imaging (Fig. 3.3). Also, the coarser average grain size of the transported material (around 500 μm), considerably larger than that of the previous phase, and the higher sedimentation rate (2.38 E-05 kg/m^2/s) are, in part, evidence of the forced thermal nature of the plume. The comparison of proximal with distal deposits of this phase (Fig. 3.4, Tab. 3.1) evidences the practical absence of a fine-grained subpopulation (SP2). This can be related to two concurrent processes: the inefficiency of ash aggregation and the absence of an actively fragmentating region of high vesicularity magma. In fact, in the absence of processes like magma-water interaction, very fine ash is often produced by the disintegration of the thin septa between the vesicles of a highly vesicular foam, not present in this phase (Dufek et al., 2012). Although clearly inferred from visual observations of the ash deposits (Fig. 3.2), ash aggregation had in fact only a minor impact in terms of mass of fine material involved in early sedimentation, possibly for the general absence of a very fine-grained subpopulation (SP2). The high-energy, explosive fragmentation of the plug during the *Vulcanian Explosion* is however clearly evidenced by the concurrent abundance of both BA and V fragments (Tab. 3.3), suggestive of the involvement in the explosion of a large part of the upper portion of the plug. The generally increased contribution of vesicular material (V clasts) in the *Vulcanian Explosion*, well indicated by the solidity and convexity values of ash fragments in the range 50-300μm (Fig. 3.8), further confirms a more intense and deeper fragmentation of the plug during this phase. In this respect, it is interesting to note that the very low, around 0.2 wt.%, water content measured by Miwa et al. (2013a) in the glass of BA-type ash with MND similar to that measured here in the October 2014 fragments, converts into a saturation pressure of only few bars (Newman and Lowenstern, 2002) and to a maximum depth of around 40-50 m. Consequently, we suggest that only the very upper portion of the plug was destroyed by the explosion, also according to the average mass emitted during similar explosions (Oishi et al., 2018) and to the observed upper diameter of the plug (10-20 m; Iguchi et al., 2010).

Very fine ash is instead mostly erupted during the *Continuous Ash Emission* phase which immediately follows the prominent explosion. This activity can be interpreted as a continued degassing phase following the partial unloading of the plug and the depressurization determined by the removal of its upper part during the Vulcanian Explosion. In these terms, the large amount of fine ash subpopulation (around 5 φ) could be the result of the sudden foaming and partial fragmentation of a slightly deeper, volatile-richer portion of the plug. The general highly crystallized groundmass texture, and especially the important increase of the free crystals recorded during the *Continuous Ash Venting* phase (Tab. 3.3), clearly denote that fragmentation always occurred over a largely crystallized magma.

All the above considerations can be used to discuss and integrate the model proposed on the basis of geophysical observations by Yokoo et al. (2013) about the Vulcanian activity at Showa crater. Several lines of evidence revealed by geophysics well agree in fact with the characteristics of the observed products. First of all, pattern of deformation preceding and accompanying vulcanian activity from the Showa crater reveals a quite shallow source (few hundred of meters), interpreted by Yokoo et al. (2013) through the possible build-up and following explosive disruption of a gas pocket. In this view, the fragmentation of this viscous, degassed portion of the conduit triggered a decompression wave travelling throughout the most rigid part of the plug. This well agrees with our observation of a very shallow derivation of the erupted material, and with the generally small volume ejected during each explosion (Oishi et al., 2018). Similarly, evolution of deformation preceding each large eruption shows a long-term (up to several hours) inflation of the upper part of the volcano, during which the gas pocket is formed and some gas can be leaked from the upper part of the plug, possibly carrying and elutriating ash particles already present in the fracture network or in the crater area. The final continuous contraction of the system, following the Vulcanian Explosion, is characterized by the rapid degassing of the unloaded, gas-richer portion of the magma below the removed part of the plug, occurring under unconfined conditions. Conversely, no evidence derives from our data supporting the alternative hypothesis of Yokoo et al. (2013) about the origin of gas accumulation as possibly related to the occurrence of repeated events of magma migration at a depth between 0-2 km. This aspect can be reconciled considering the low activity rates of Sakurajima during the investigated period. This could also explain the generally lower energy associated with explosions from Showa crater respect to those occurring from Minamidake crater (Iguchi et al., 2010), that often show the presence of highly vesicular, poorly crystallized, pumice-like material or of fluidal, vesicular material that we never observed in the studied sequence.

3.6. Conclusion

The studied eruptive sequence encompassed the whole spectrum of eruptive activities that are typically associated to Vulcanian eruptions at Sakurajima, being characterized by episodes of highly energetic explosions interspersed within prolonged periods of variably intense, not-explosive ash and gas emission. Differently from previous works on Sakurajima ash, mainly focused on the products of single prominent eruptions, we investigated here the cyclic styles of activity procuring and following a prominent Vulcanian eruption, identifying three different phases that were all analyzed in detail; a low-energy, preparatory activity of *Weak Ash Emission,* preceding a main *Vulcanian Explosion*, then followed by a typical activity of *Continuous Ash Venting.* This approach allowed us to clarify the critical role of conduit processes in controlling the mechanisms of ash formation have and the eruptive dynamics in a typical Vulcanian activity, and to critically discuss pre-existing models concerning the dynamics of Sakurajima activity.

Analyzed deposits from the different phases of activity revealed to be largely dominated by degassed and largely crystallized particles, despite significant variability observed both in the intensity and in the eruptive style of the activity. The morpho-textural variability of the analyzed ash samples suggests that a significant layering and differentiation in terms of physical properties (i.e. vesicularity and crystallinity), and hence magma rheology, must have characterized the volcanic conduit of Sakurajima prior and/or during the observed activity. The specific characteristics of the different ash components also suggest that a variable mechanism of magma fragmentation operated during the eruptive sequence. Consequently, we register a large variability of conduit processes participating to the dynamics of the eruptive sequence at Sakurajima.

Based on the comparison with data reported from previous studies on Sakurajima ash, a general large-scale temporal invariancy of the textural features is revealed to characterize the products of typical Vulcanian activity. This aspect, together with reported evidences on ash texture concurs to indicate the dominancy at Sakurajima of a cyclic, degassing-driven eruptive dynamics, which is mostly controlled by a quasi-static column of vertically stratified, poorly permeable, high-crystallinity (40%) magma conduit. We estimated a characteristic time-scale for the plug renewal to be around 30 days. Our data also confirm what yet suggested by Yokoo et al. (2013) about the possibility that gas accumulation in the plug, and not the arrival of a new, volatile-richer magma batch as suggested by other authors (Iguchi et al., 2013b; Miwa et al., 2013b), can be the most probable trigger for Vulcanian explosions at Sakurajima during periods of "ordinary" activity. Based on these evidences we interpret the dynamics of Vulcanian eruptions at Sakurajima as controlled by the progressive pressurization of a degassed upper portion of the conduit, comprised in a range of depth between 10 and 50 m, that undergoes brittle fragmentation as the tensile strength of the viscous magma cap is reached. Finally, based on the general high-frequency occurrence of Vulcanian explosion at Sakurajima (typically from 20 up to 400 eruption per month), and according with the long time-scale estimates provided for the plug regeneration, we suggest that the magma cap is only partially removed during the Vulcanian events.

3.7   Appendices

A 3.7.1 Comparison with other study in terms of the Sakurajima activity rate

The monthly number of explosions represents a valuable estimate of the activity rate at Sakurajima, as reported by Oishi et al. (2018). During the recent period of vulcanian activity, Sakurajima showed important variations in the rate of the activity from both the recently active craters, alternating periods of high frequency activity punctuated by more than 400 eruptions per month to periods characterized by a very low number of explosions per month, down to 10. Data in Tab. A1 summarize the Sakurajima activity rate at the moment of sample collection for the present study and for similar data presented by other authors making a comparison in terms of the volcano activity rate with the samples analyzed in this study, and also evidencing significant difference in the monthly rate of eruptions.

Reference	Period of samples collection	Active crater	Activity rate
Miwa et al. 2009	17 vulcanian eruptions from 1974 to 1987	Minamidake	between 100 and 500
Miwa&Toramaru 2013a	18 vulcanian eruptions from 1974 to 1987	Minamidake	between 100 and 500
Miwa et al. 2013b	14-17 January 2010	Showa	150
Kurniawan et al. 2016	January 2011 - November 2012	Showa	between 50 and 200
Smith et al. 2018	29 May – 5 June 2015	Showa	between 100 and 250
Present study	*22-25 October 2014*	*Showa*	*19*

Tab. A1 Comparison in terms of Sakurajima rate of activity between the samples collected in the present study and those analyzed by other authors from the literature. The activity rate (as the number of explosions registered in the corresponding month) at the moment of sample collection, together with indication of the active crater helps to depict the state of Sakurajima activity and to discuss our results in light of those reported by other authors.

A 3.7.2 Textural data on ash grains

Particle ID	Particle type	Tot. crystal abund.	Vesicle abund.	Oxydes abund.	Femics abund.	Plagioclase abund.	Residual glass
		(%)	(%)	(%)	(%)	(%)	(%)
23 10 1 A1	BA	41.5	0.0	1.4	10.3	29.8	58.5
24 10 1 A3	BA	40.6	0.9	1.7	11.7	27.1	58.9
23 10 1 F9	BA	27.3	1.6	1.1	6.0	20.2	71.6
23 10 1 C5	BA	39.3	0.0	0.7	9.9	28.6	60.7
23 10 1 C2	BR	37.8	0.4	1.7	8.5	27.5	61.9
23 10 1 C4	BR	43.0	1.7	0.5	13.5	28.9	56.1
23 10 1 F6	BR	46.6	1.2	2.2	9.6	34.8	52.8
23 10 1 C9	V	45.9	19.2	1.1	7.4	37.4	54.1
23 10 1 C8	V	30.1	35.0	1.3	9.3	19.5	69.9
23 10 1 F4	V	31.4	17.1	0.9	9.0	21.5	56.9
23 10 1 F7	V	35.3	15.3	1.0	7.7	26.6	54.8
24 10 14bis B2	BA	33.8	0.2	1.3	9.3	23.2	66.1
24 10 14bis E4	BA	34.9	1.9	1.3	13.2	20.4	63.9
24 10 14bis C1	BA	36.6	0.0	0.8	7.3	28.5	63.4
24 10 14bis A3	BR	49.5	1.8	1.3	7.8	40.4	49.6
24 10 14bis B7	BR	33.2	0.4	0.5	8.2	24.4	66.6
24 10 14bis B8	BR	38.5	0.0	1.5	10.6	26.3	61.5
25 10 14bis I4	V	34.1	8.3	1.8	7.3	25.0	25.8
24 10 15 A1	BA	40.3	0.0	1.8	9.0	29.6	59.7
24 10 15 A3	BA	40.3	0.2	1.1	9.1	30.1	59.6
24 10 15 A6	BA	44.6	0.0	1.9	9.2	33.5	55.4
24 10 15 B9	BA	58.3	0.0	1.1	10.1	47.0	41.7
24 10 15 C2	BA	45.2	0.0	2.1	9.9	33.2	54.8
24 10 15 E5	BA	43.4	0.0	1.6	6.2	35.6	56.6
24 10 15 G1	BA	48.9	0.0	1.8	10.4	36.7	51.1
24 10 15 G4	BA	52.8	0.0	1.4	11.8	39.5	47.2
24 10 15 H7	BA	54.2	26.5	1.4	9.5	43.3	33.5
24 10 15 G6	BR	50.6	0.0	1.7	8.1	40.8	49.4
24 10 15 C1	BR	41.9	0.0	1.2	10.4	30.3	58.1
24 10 15 F1	BR	51.4	0.0	1.2	8.9	41.2	48.6
24 10 15 F5	BR	41.4	0.0	1.0	12.4	28.0	58.6
24 10 15 F6	BR	42.9	0.0	2.1	7.6	33.2	57.1
24 10 15 H3b	BR	47.2	0.0	1.9	10.3	35.0	52.8
24 10 15 B4	BR	46.0	0.0	1.3	9.7	35.0	54.0
24 10 15 I1	V	35.0	9.2	1.1	8.0	25.9	65.0
24 10 15 I3	V	35.1	10.2	0.2	8.1	26.8	64.9
24 10 15 I7	V	45.0	22.1	1.2	10.0	33.9	55.0
24 10 15 I8	V	48.7	9.9	0.9	10.7	37.1	51.3
24 10 15 I9	V	35.4	6.5	0.9	6.0	28.5	60.3

Particle ID	Clast type						
24 10 9bis A6	BA	37.2	0.1	1.1	10.4	25.7	62.8
24 10 9bis C2	BA	45.0	2.9	1.1	9.0	34.9	53.4
24 10 9bis B3	BA	39.2	0.0	0.6	6.2	32.5	60.8
24 10 9bis B4	BA	39.9	0.0	0.6	7.9	31.4	60.1
24 10 9bis B1	BR	38.1	0.0	0.8	11.5	25.8	61.9
24 10 9bis A5	BR	46.4	0.1	2.0	13.4	31.0	53.5
24 10 9bis B6	BR	51.0	0.0	1.8	9.5	39.8	49.0
24 10 9bis C4	BR	54.5	0.0	1.8	12.1	40.6	45.5
24 10 9 bis B5	BR	40.3	0.0	1.1	9.7	29.4	59.7
24 10 9bis A1	BR	43.0	0.4	2.6	12.4	28.0	56.7
24 10 9bis A4	V	35.6	16.5	0.5	9.3	25.7	64.4
24 10 9bis A3	V	33.0	5.1	2.1	6.1	24.8	67.0
24 10 9bis A7	V	39.9	13.2	1.7	10.8	27.4	60.1

Tab. A2 Relative abundancy of the different crystal phases and vesicles for each analyzed ash fragment (Particle ID). Ash fragments are grouped in three panels by clast type.

A 3.7.3 Microlite Number Density:

Particle ID	Particle type	Tot. crystal count	Tot. analyzed area	Areal MND [#NumCryst/Area]
		(-)	(μm^2)	(mm^-2)
23_10_1_A1	BA	677	15388	43995
23_10_1_A3	BA	604	15177	39797
23_10_1_C5	BA	768	15343	50055
23_10_1_C2	BR	813	15511	52414
23_10_1_C4	BR	778	15316	50797
23_10_1_F6	BR	768	15343	50023
23_10_1_C9	V	348	11340	30689
23_10_1_F4	V	323	22205	14546
23_10_1_F7	V	267	17571	15196
24_10_14bis B2	BA	572	15204	37621
24_10_14bis C1	BA	431	15351	28077
24_10_14bis E4	BA	287	14353	19996
24_10_14bis B7	BR	724	15600	46411
24_10_14bis A3	BR	369	15081	24468
24_10_14bis B8	BR	1219	14575	83634
24_10_14bis I4	V	158	5331	29638
24_10_15 A1	BA	1291	121811	10598
24_10_15 A2	BA	982	58241	16861
24_10_15 A6	BA	1165	60342	19307
24_10_15 B4	BR	825	59696	13820
24_10_15 C1	BR	984	60830	16176
24_10_15 F5	BR	5790	121511	47650
24_10_15 I1	V	921	121809	7561
24_10_15 I3	V	2746	121509	22599
24_10_15 I9	V	2495	162115	15390
24_10_9bis A3	BA	242	14572	16607
24_10_9bis A6	BA	555	11558	48017
24_10_9bis B1	BA	743	15540	47813
24_10_9bis B3	BA	229	10009	22879
24_10_9bis A5	BR	436	15340	28422
24_10_9bis A1	BR	588	15522	37882
24_10_9bis B5	BR	333	15304	21759
24_10_9bis A7	V	295	8757	33689
24_10_9bis A4	V	406	13012	31202

Tab. A3 The areal microlite number density (MND) is calculated for the different ash components considering all the mineral phases (Plagioclase, Femic minerals, Fe-Ti Oxydes) that were identified during the image analysis.

Chapter 4

Shear-induced, non-explosive magma fragmentation in Vulcanian activity: evidences from the 1888-90 eruption at La Fossa di Vulcano (Aeolian Islands)

4.1 Introduction

Vulcanian activity inherited the name from the description of the AD1888-1890 eruptive sequence at La Fossa cone (Vulcano, Aeolian Arcipelago, Southern Italy), provided by Mercalli and Silvestri in 1891. In this Chapter we will focus on the study of the products associated with this prototypal eruption, in order to investigate the mechanisms of ash formation and better characterize the dynamics of 'Vulcanian' eruption.

Important and very accurate information about the Vulcanian activity sequence occurred in the AD1888-90 derives from the visual description of the eruption provided in the form of daily *chronicles* by Mercalli and Silvestri in 1891 ("*Le eruzioni dell'isola di Vulcano incominciate il 3 Agosto 1888 e terminate il 22 Marzo 1890*"). According to these authors, the entire eruptive sequence was characterized by two distinct periods of activity separated by a pause of around 13 days. The first period lasted about 3 days (3-5 August 1888), and was characterized by violent explosions which were associated to the important production of ash, representing thus a paroxysmal phase of the eruption. Conversely, the second eruptive phase (18 August 1888 - 22 March 1890) was very prolonged in time and consisted in the occurrence of a variety of eruptive phenomena, from high-frequency explosions of low-to-moderate scale, associated to the sudden release of important amounts of ash and ballistics blocks of variable nature and size ('Vulcanian bombs') and accompanied by a loud noise, to periods with low level, sporadic explosions. A brief excerpt from the *chronicles* in which Mercalli describes this second eruptive period and introduces the classification of the observed explosions: "*The second phase, very prolonged both for the frequency and for the largely variable strength of the explosions….[] In addition, (these) have been classified on the base of their intensity as absolutely strong, very strong, strong, quite strong, intermediate, weak and very weak.*" {"*La seconda fase, prolungatissima, sia per*

la frequenza che per la forza molto variabili delle esplosioni, che per la natura dei materiali eruttati…[].Sono state classificate, inoltre, in base all'intensità in fortissime, molto forti, forti, abbastanza forti, mediocri, deboli e debolissime."}.

The important fluctuations in the intensity of the explosions described by Mercalli and Silvestri (1891), associated to the high variability in the nature and modalities of tephra emission, possibly reflect the alternation of different processes of magma fragmentation throughout the eruptive sequence, which operated as the main controlling factors of the highly unsteady eruptive dynamics.

Several studies have been focused in the recent years on the characterization of the shallow magmatic system controlling the past and the most recent activity of Vulcano (De Astis & La Volpe, 1997; Clochiatti et al., 1994; Gioncada et al., 2003; Vetere et al., 2015). However, not much has been done in detail to interpret the accurate reports of the eruption provided by Mercalli & Silvestri (1891) in the light of the newly acquired insights on the mechanisms controlling the dynamics of vulcanian eruptions. The term *'Vulcanian eruption'* can have a double and somewhat misleading meaning in the scientific literature. Formally, Vulcanian eruptions are defined as discrete and short-lived (from seconds to a few minutes) explosions in which a mixture of gas and fragmented pyroclasts is ejected from the vent due to the sudden decompression of a pressurized volcanic systems (e.g. Self et al., 1978; Diller et al., 2006; Morrissey and Mastin, 2000; Clarke et al., 2013). On the other hand, in some scientific texts (e.g. Schmincke, 2012) an interpretation of Vulcanian activity as strictly related to magma-water interaction processes still persists, mainly deriving from the interpretation of the characteristics of the typical associated deposits. The recent eruptive activity of many volcanoes worldwide, often characterized by the formation and following disruption of lava domes or plugs (Sparks, 2003), present modalities of the eruptive phenomena that are commonly associated to Vulcanian activity (e.g. 1995-1999 activity of Soufriére Hills, Montserrat [Druitt et al., 2002]; 2013-2014 activity of Tungurahua [Hall et al., 2015; Gaunt et al., 2020]). On a wider perspective those activities, characterized by repeated cycles of low-to-mid scale eruptions often associated to unsteady eruptive dynamics, are also interpreted as Vulcanian eruptions (e.g. Kienle et al., 1979; Clarke et al., 2002; Wright et al., 2007; Yamamoto et al., 2008; Iguchi et al., 2010; Battaglia et al., 2020; Miwa et al., 2013b; Cioni et al., 2014; Clarke et al., 2015). Vulcanian explosions are often associated to a variety of explosive phenomena and activities which are actually characterized by very different style and intensity of the eruptions, and by various modalities of ash production (e.g. Miwa et al., 2013b). These eruptions, characterized by sudden transients in the intensity of the explosions and in the modality of ash emission, represent the cyclic eruptive pattern of several ongoing or recent activities worldwide (e.g. Sakurajima in the Southern Japan; Tungurahua in Ecuador; Fuego in Guatemala). The hazards associated to this kind of activity involve different eruptive phenomena, from the impact of ballistic projectiles with the built environments (e.g. Biass et al., 2016), to risks related to the invasion of inhabited regions of small scale pyroclastic density currents (Jenkins et al., 2013), to human health-related risks due the constant release of important amounts of fine ash and acidic volcanic gases (Horwell & Baxter, 2006; Baxter & Horwell, 2015). Despite the importance of these eruptive phenomena, to date several aspects of the complex eruptive dynamics of these

eruptions are still debated, and direct data on the related products can continue to give important, further insights into these phenomena.

The quantitative investigation of the morpho-textural characteristics of the ash products represents a valid instrument in order to interpret the physical processes controlling the explosive volcanism, and it was geneally used to study the eruptive dynamics of several explosive events (e.g. Heiken & Wholtez, 1985). In particular, information on the internal textures of ash was largely used to shed light over the interplay of processes affecting magma during its ascent into the conduit which is responsible for the unsteady dynamics that often characterize the explosive eruptions (Cashman and Marsh 1988; Hammer et al., 1999; Cashman & Hoblitt, 2004; Cioni et al., 2008; Miwa et al., 2009; Wright et al., 2012; Miwa et al., 2013a; Cioni et al., 2014). On the other hand, size distribution and morphological analysis on ash fragments can efficiently inform about the physical properties of magma at the fragmentation threshold, thus representing a powerful instrument to characterize the mechanisms of ash production occurring during ash-dominated eruptions (Scasso & Carey, 2005; Buttner et al., 1999; Taddeucci et al., 2002; Liu et al., 2015; Liu et al., 2017).

This study is aimed to address the topic of the variable processes of magma fragmentation during Vulcanian activity, by providing an exhaustive morphometrical and textural description of both ash and ballistic products associated with the historical sequence of the 1888-90 Vulcanian eruptions of La Fossa cone (Vulcano Island). Both external and internal features of the recognized vulcanian bombs were accurately described through an extensive field survey, and the morpho-textural characteristics of volcanic ash discussed in the light of the major processes controlling eruptive dynamics. Morphological and textural features revealed for the ash fallout deposits were compared with those derived for poorly compacted and clastic fragments collected inside the breccia-bearing portions of several bombs, in order to investigate efficiency and influence of possible alternative processes of ash production in the context of the Vulcanian activity.

4.2   Fieldwork and samples collection

During May 2018, a systematic and comprehensive field survey was carried out at Vulcano Island. The field work was aimed at providing a quantitative description of the ash fallout deposits of the AD 1888-90 eruption of the La Fossa cone, and to characterize the nature and the spatial distribution of the ballistic projectiles deposited on the crater terrace during the different pulses of the eruption. Dedicated strategies were adopted during the field operations in order to count, manually measure and describe the bombs. These strategies ensured the investigation of representative areas during the survey and allowed to identify different types of bombs. In particular, the field survey revealed the significative presence of a specific type of dense blocks characterized by extensive portions of finely comminuted materials in the form of breccia-filled veins or fractures. The bedding structure, the granulometry, the clast distribution of these breccia samples were accurately described during the field survey, and several samples of breccia were collected in order to provide analyses on either the internal structures of the

veins, and on the morphometry of the comminuted pyroclasts. At the same time, two stratigraphic sequences of the tephra fallout deposits associated to the whole eruptive activity were investigated and described, and ash samples representative of the main eruptive phases collected.

4.2.1 Collection and analysis of volcanic ash samples

Two stratigraphic sequences of pyroclastic deposits located at a different distance from the present crater (Fig. 4.1) were described in detail (Fig. 4.2), and a total of 19 ash samples (Fig. 4.3) were collected.
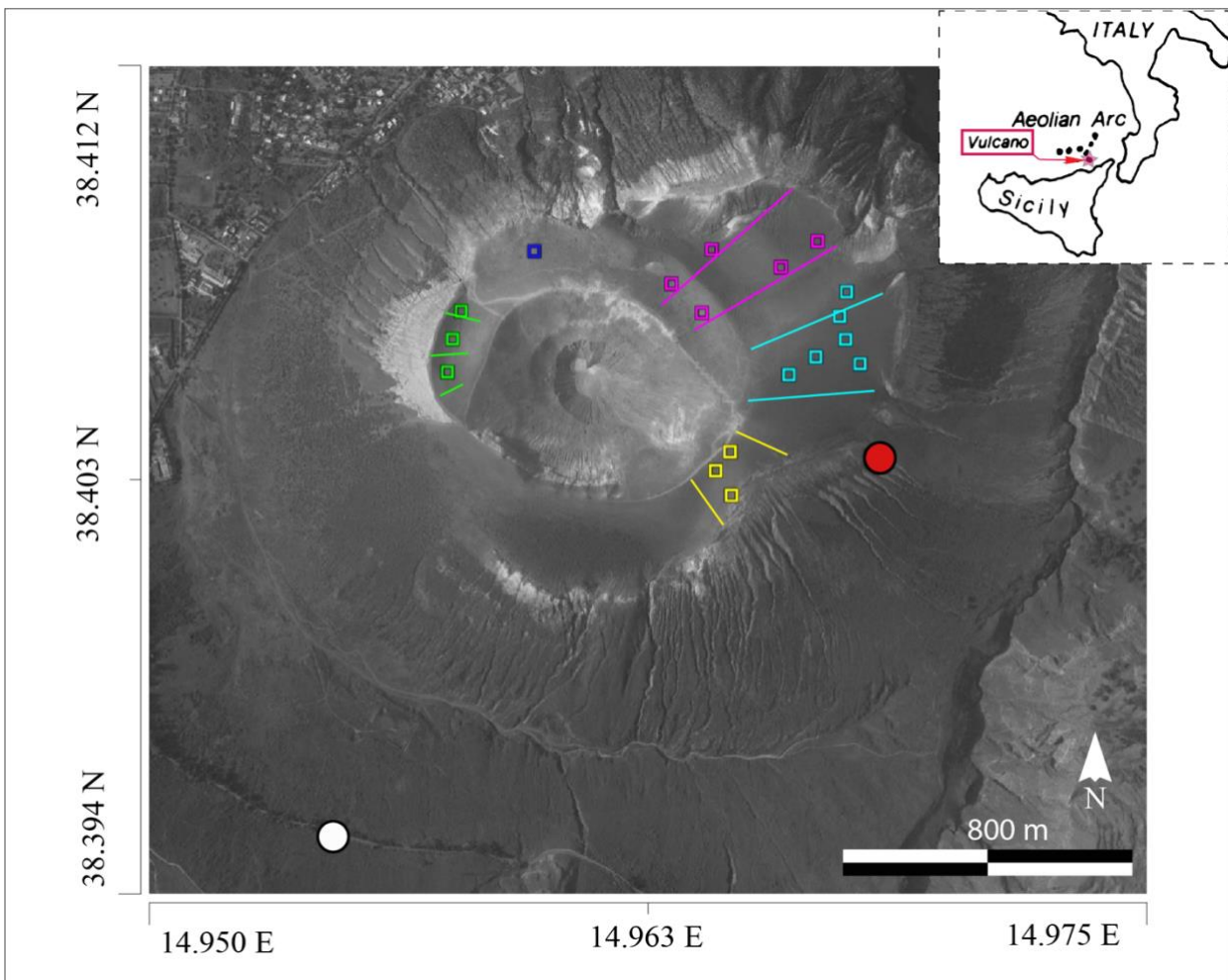
Fig. 4.1 Location of the Vulcano Island (top right) and satellite image of the La Fossa di Vulcano cone, with GPS locations considered for the ash sampling (circles) and for the bombs survey and collection (squares and lines). Red and white circles correspond respectively to the location of the proximal and medio-proximal site described for ash samples collection. Colored squares indicate the sites considered during the investigation of bombs in different sectors of the crater terrace, and lines indicate the limits of the sectors, namely North (blue), North East (violet), East (cyan), South-East (yellow) and West sector (green). Coordinates in UTM reference system.

The first section is located along the southern slopes of the volcanic edifice (red dot in Fig. 4.1) and represents a proximal fallout sequence (0.6 km from the vent) from which a total of 11 ash samples

were collected (Fig. 4.3). Additionally, 8 ash samples were collected from a medio-proximal section (Fig. 4.3), located from a cliff within the Palizzi valley, at the foot of the La Fossa cone, around 1.2 km far from to the crater (white dot in Figure 4.1).

A schematic representation of the two stratigraphic sequences is reported in Figure (4.3). The proximal and the medio-proximal successions presents a total thickness of 71.5 cm, and of 22.6 cm, respectively. The upper portion of the two sequences consists in the repeated alternation of light-colored, moderately fine to coarse ash layers, with interbedded darker-colored, coarser ash and lapilli fragments, which are mostly located at the top the sequences. The thickness of the beds generally thin upward from the base to the top in both the successions. The medio-proximal sequence is characterized by an erosional contact at the top (dotted line, Fig. 4.2), however some correlations between the two deposits successions were traced based on visually recognized "guide layers" sharing stratigraphical similarities (colored lines in Fig. 4.2, also reported in Fig. 4.3 as correlation lines). Both pyroclastic sequences share a common basal breccia layer, formed by altered ash and lapilli fragments displaying colors ranging from yellow to red (red layer in Fig. 4.2), and two fine ash layers located in the lower and in the upper portion of the successions (yellow and green layers). Very distinctive is the coarse ash layer located at the top of the sequences (cyan layer) and characterized by both vesicular and dense clasts. Importantly, all the ballistic were found at the top of the proximal succession, and no one was found during the excavation of the outcrops.
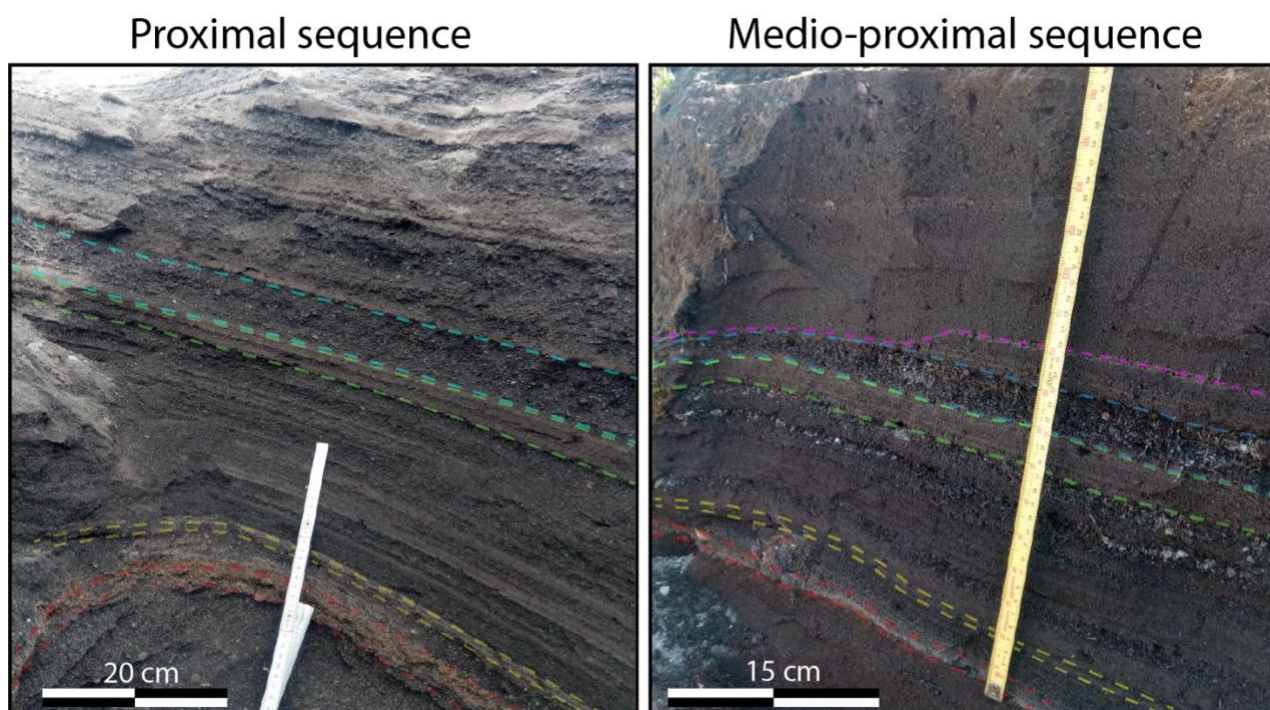
Fig. 4.2 Stratigraphic section associated to the AD 1888-90 activity of Vulcano. Proximal (image on the left) and medio-proximal (image on the right) stratigraphic sections investigated for the collection of ash. Colored lines indicate the lateral correlations inferred between beds from the two successions.

Ash samples have been collected in appropriate plastic bags and analyzed in the laboratory following the analytical procedures reported in the Chapter 2 of this thesis, in order to derive the grain size

distribution of the ash deposits and quantitative information about the nature and componentry of ash grains. A selected subset of particles was also investigated with the SEM in order to characterize both the morphological and the textural features of the different ash components. A large number of grains was also dispersed over thin glass and embedded in epoxy resin. Embedded grains were then sectioned and imaged with the static particle analyzer (Morphologi G3s) in order to quantify the 2D morphology of the sectioned outlines. The particle analyzer was finally used, together with the mechanical sieving, to quantify the GSDs of the different fallout deposits. Obtained GSD curves were thus characterized based on a set of statistical descriptors (Median '$Md(\phi)$', Standard deviation '$\sigma(\phi)$', Mode, graphical Mean of the grain size 'MeanGS', Sorting and Skewness). The GSDs of samples from the proximal section were fitted by two gaussian subpopulations with acceptable residuals ($R^2 > 0.88$) using MagicPlot software (https://www.magicplot.com). A coarser subpopulation (SP1) and a finer subpopulation (SP2) were thus identified to characterize each deposit and the volume fraction of the SPs was characterized together with their modal position '$Md(\phi)$' and Standard deviation '$\sigma(\phi)$'.
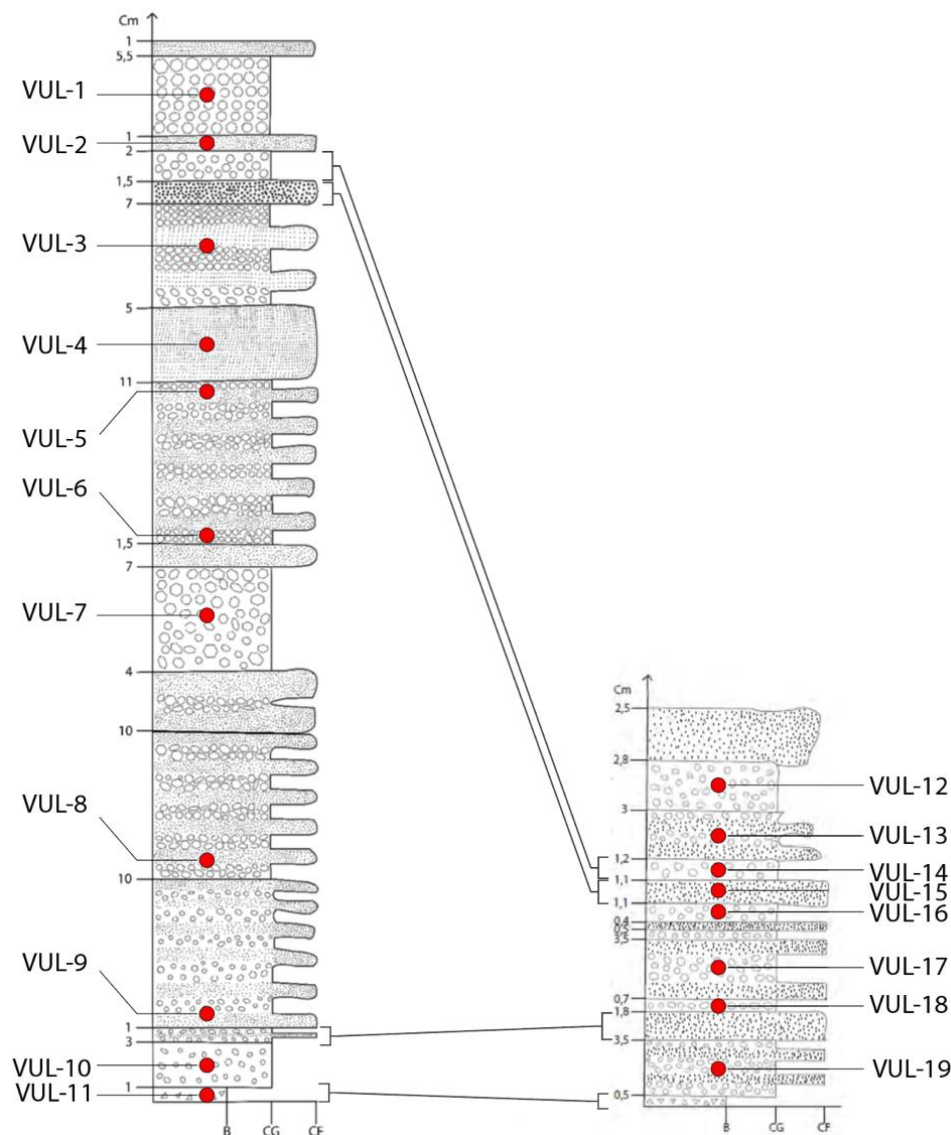
Fig. 4.3 Stratigraphic scheme of the pyroclastic sequences. Red circles indicate the layers selected for ash collection. A temptative cross-correlation of layers between the stratigraphic sections is represented by lines connecting the two columns. Numbers reported on the left of the columns indicate the thickness in cm of the layers, while letters reported at the bottom distinguish between breccia deposit (B), coarse ash (CG) and fine ash layers (CF).

4.2.2 Field survey of ballistic bombs

In order to characterize the nature and provide the spatial abundance of the different vulcanian bombs, the whole crater terrace of Vulcano was investigated and subdivided into five main sectors: West; South-East; East; North-East; North (Fig. 4.1). Within each sector, ballistic bombs of different types were described and measured in order to quantify the relative abundance of the different types in the different sectors; an example of data table results obtained during the survey is reported in Appendix (Tab. A2). The different bombs were classified directly in the field based on several features of their external and internal aspect, including: orientation and landing structures; external morphology; presence and thickness of an outer glassy rim (crust); abundance and characteristics of cracks and vesicles in the crust; characteristics of the internal texture like abundance and distribution of vesicles, crystals and xenoliths; presence of clastic portions stacked above the external surface or filling internal fractures.

A multi-scale approach was chosen during the fieldwork in order to achieve a good representativity of the large spatial and compositional variability shown by the bombs in the crater terrace. Initially, a large squared area of 100 m^2 was determined, in which all the bombs larger than 1 m were measured. The diameter of the bombs was determined by measuring and directly recording in the field the maximum, intermediate and minimum calipers. Then, a smaller area of 25 m^2 was defined, and all the bombs comprised between 1 m and 20 cm measured. Finally, an area of 1 m^2 located within the 25 m^2 area was considered to investigate bombs below 20 cm in size. Results deriving from the different areas were then weighted with respect to their relative surface ratio and integrated over the area. This approach allowed us to distinguish different types of ballistic bombs associated to the 1888-90 activity and to obtain information on their size distributions and on the relative abundance of bomb types within each of the five investigated sectors.

4.2.3 Analytical processing of breccia-bearing dense blocks

The field survey of the crater bomb field allowed the identification of several dense blocks displaying important amounts of clastic material, in the form of veins or fractures filled with a breccia, often included or partially covering external portions of the dense blocks. A total of 12 samples of breccia-bearing bombs were collected and their internal structures investigated at the Earth Science Department of the University of Florence.

Before sectioning, poorly compacted samples of the breccia-bearing blocks were consolidated using epoxy resin in order to ensure preservation of the internal structures and the original bedding of the veins. Samples were cut and polished, then embedded and polished for a second time using colored epoxy resin in order to highlight the porosity network internal to the breccia. High-resolution (HR; 4800

dpi) images of the polished sections were acquired using an Epson Perfection 4990 Photo scanner (Fig. 4.4a). Images were used to describe the macro structures and the bedding of the breccia portions. The morphometry of the clasts in the 2D sections were measured through image analysis using Adobe Photoshop and Fiji softwares, manually contouring the single grains (Fig. 4.4b) and quantifying the segmented images (Fig. 4.4c).
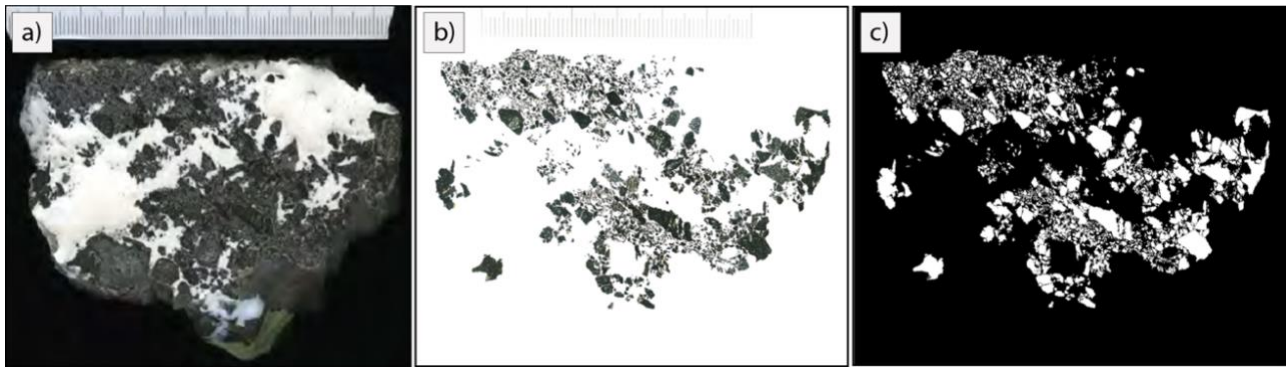
Fig. 4.4 HR image of a sectioned and resin embedded breccia sample. High-resolution scanning of the breccia portion of the block (a) with contoured images of fragments (b) and binarized image used for calculating particle size distribution (c).

The HR of images allowed to discriminate and analyze clasts down to a size of around 50-100 μm. The size of the clasts (S) was estimated in terms of circular equivalent diameter (see Chapter 2 for details) and cumulative clast distribution frequencies were derived for the different breccia samples. Then, the logarithm of S was plotted against the logarithm of the cumulative number of clasts having diameter higher than the considered size (#UnderSize), and log-log diagrams were constructed to derive the fractal dimension D of the distribution. D was conveniently defined as the negative slope of the least-squares interpolation of data distributions in the log-log space (e.g. Turcotte, 1992). This was useful to quantitatively characterize the grade of milling and transport suffered by the clasts contained in the breccia, and to discuss their process of formation (Wohletz et al., 1989; Heilbronner & Keulen, 2006). Additionally, thin sections of the breccia-bearing blocks were analyzed using an SEM microscope at MEMA laboratory (Univ. of Florence), and the images used to calculate the fractal dimension D of the fine-grained matrix (i.e. below the resolution limit of scanner images: 50-100 μm; Fig. 4.5). Thin sections were useful also to better characterize the micro-structures and the internal texture of the different clasts through the analysis with transmitted light microscope.
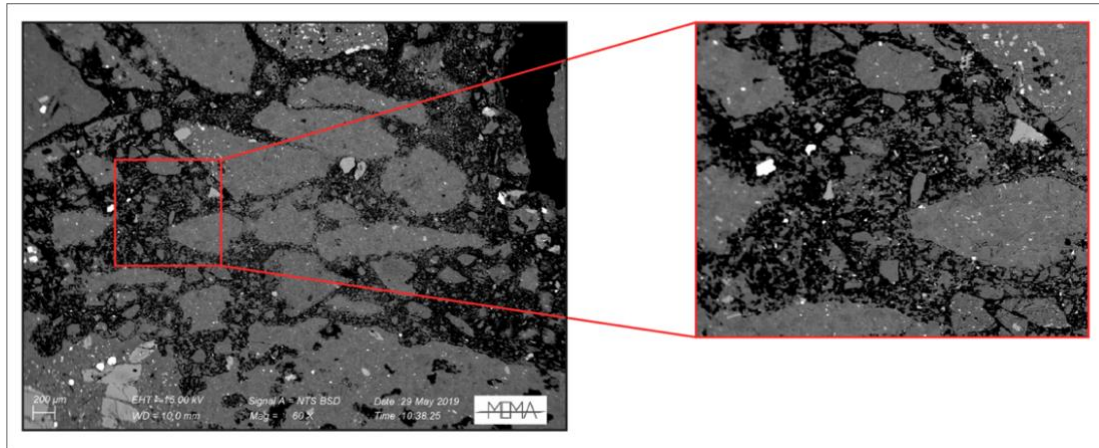
Fig. 4.5 SEM image of the fine matrix contained in the breccia samples.

A preserved sample of a breccia portion, clearly framed within two nearly planar surfaces, was selected for the analysis and a number of contiguous secondary electron images were collected to cover an entire transversal transect of the breccia. Images were then used to reconstruct two oriented photomosaic transects across the breccia portions (Fig. 4.6), from the visible contact with the host rock (baseline of transects in Figure 4.6b), down to the opposite embedding surface of the breccia (top of transects in Figure 4.6b). The two transects were investigated using the Fiji software to provide information on sedimentary micro-structures, and to characterize the variability in the shape and in the spatial distribution of forming clasts across the transects. The fractal dimension (D) of the clasts present in the transects was also calculated and discussed.

Furthermore, three poorly compacted breccia samples (VPC2, VPC4, VPC6; previously excluded from embedding operations) were selected to be analyzed with the static particle analyzer (Morphologi G3s, Malvern Panalytical) in order to characterize the granulometry of the clastic fragments included in the breccia-bearing blocks and to provide shape analysis for a large number of clasts. These were gently disaggregated and processed following the analytical procedures reported in Chapter 2, to provide GSDs and componentry analyses of the deposits. The main statistical descriptors (Mode, $Md(\phi)$, $\sigma(\phi)$, MeanGS, Sorting, Skewness) were then calculated in order to describe the GSD curves.

Finally, a representative aliquot of deposit from VPC2 breccia sample was embedded in epoxy resin and the polished section was then re-analyzed with the particle analyzer to extract information about the morphometry of a large number of clasts.
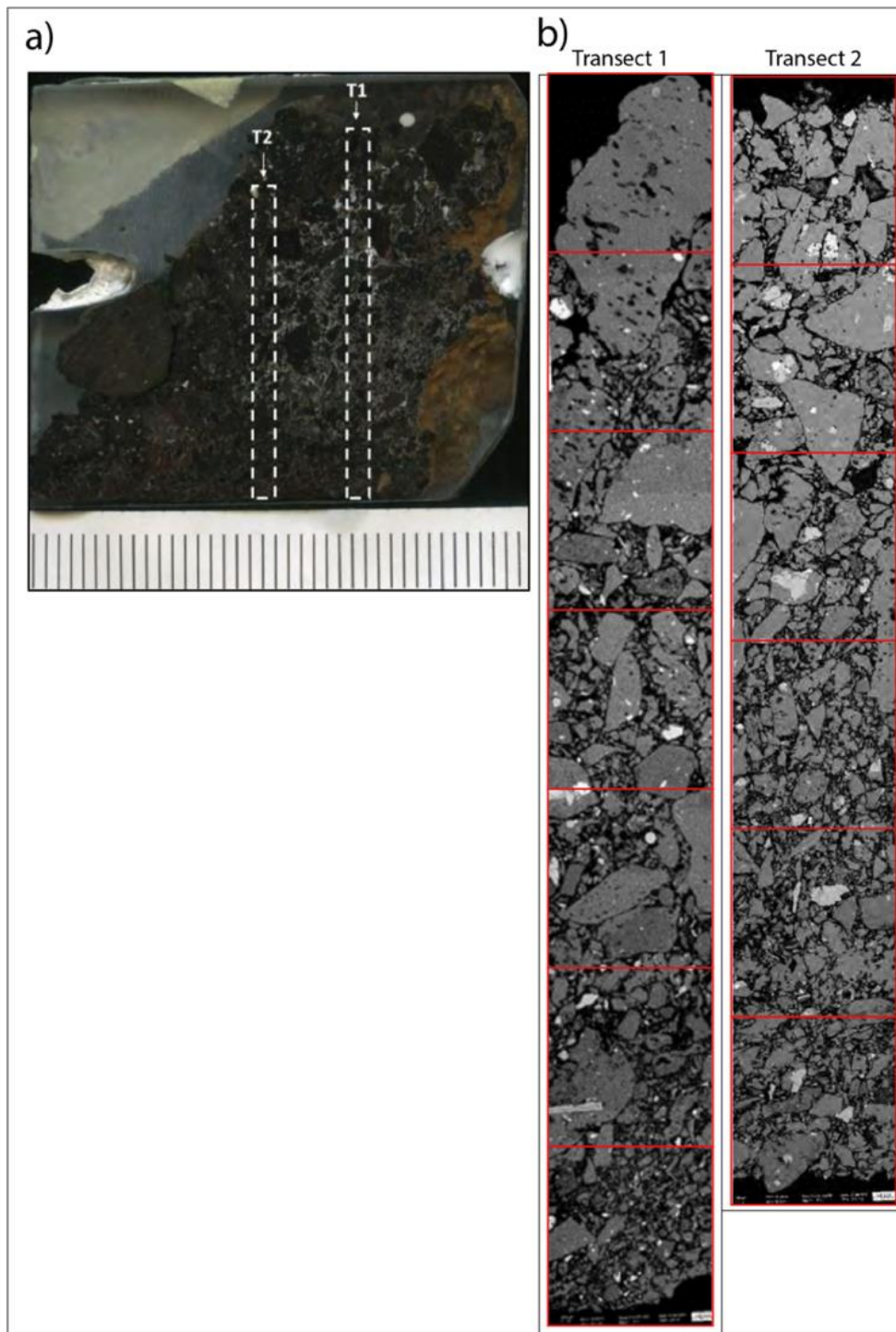
Fig. 4.6 Cross-sectional transects of the internal portions of a D-Br bomb. Two North-South oriented transects of the comminuted breccia were mounted from a contiguous footage of SEM images.

4.3 Field evidences

4.3.1 Description of Vulcanian bombs

Fieldwork performed at Vulcano revealed a very high variability of the bombs associated to the 1888-90 activity, both in terms of external morphology and internal texture.

A total of 4 main categories of bombs were recognized:

- o **BcB**: Bread-Crust Bombs → further divided in 3 sub-classes
- o **S**: Scoria Bombs
- o **D**: Dense blocks
- o **D-Br**: Breccia-Bearing Dense blocks

The categories are presented below together with images of representative end-members:

Bread-crust Bombs (BcB)

Bread-crust Bombs (Fig. 4.7) are characterized by the typical contrast between a quenched glassy layer forming a dark-coloured, high-density, variably thick and cracked external rind, and a high-vesicularity, low-density internal core generally showing a clear vesicularity gradient. The shape of BcB varies on average from spherical or sub-spherical (Fig. 4.7 a,c), but more prismatic shapes are also observed (Fig. 4.7e). Generally, the internal portions of the bombs show lighter colors respect to the external glass, ranging from grey to brownish yellow (Fig. 4.7 b). The total vesicularity, the distribution of size and the orientation of the vesicles are also largely variable within the single BcB. In particular, the total vesicularity is higher in the inner portions of the bombs, and progressively decreases as approaching the contact with the external crust (Fig. 4.7 d). Few sparse crystals and dark magmatic enclaves were found to characterize these internal portions of the BcB. On the other hand, the quenched rind shows variable thickness, from 2-4 millimeters up to 7-10 centimeters, and typically shows the presence of few and very small vesicles, associated to a low abundance of crystals. Three subcathegories can be macroscopically distinguished within BcB:

i) **Thin crusted BcB** (**BCB-Tn;** Fig. 4.7b): This class includes all the BcB showing low vesicular rind with thickness below 3 cm. Depending on the vesicularity of the internal portions, thin crusted bombs were further subdivided into high vesicularity (BCB-Tn-Hv; Fig. 4.7 d) and low vesicularity (BCB-Tn-Lv; Fig. 4.7b) bombs.

ii) **Thick crusted BcB** (**BCB-Tk**; Fig. 4.7 f): This class includes all the BcB showing low vesicular rind with thickness above 3 cm. Depending on the vesicularity of the internal portions, thick crusted bombs were further divided in high vesicularity (BCB-Tk-Hv) and low vesicularity (BCB-Tk-Lv; Fig. 4.7f) bombs.

iii) **Vesicular Rind BcB (BcB-Vr**; Fig. 4.7 g,h**)**: This class includes rare Bread Crust Bombs showing a highly vesicular rind.
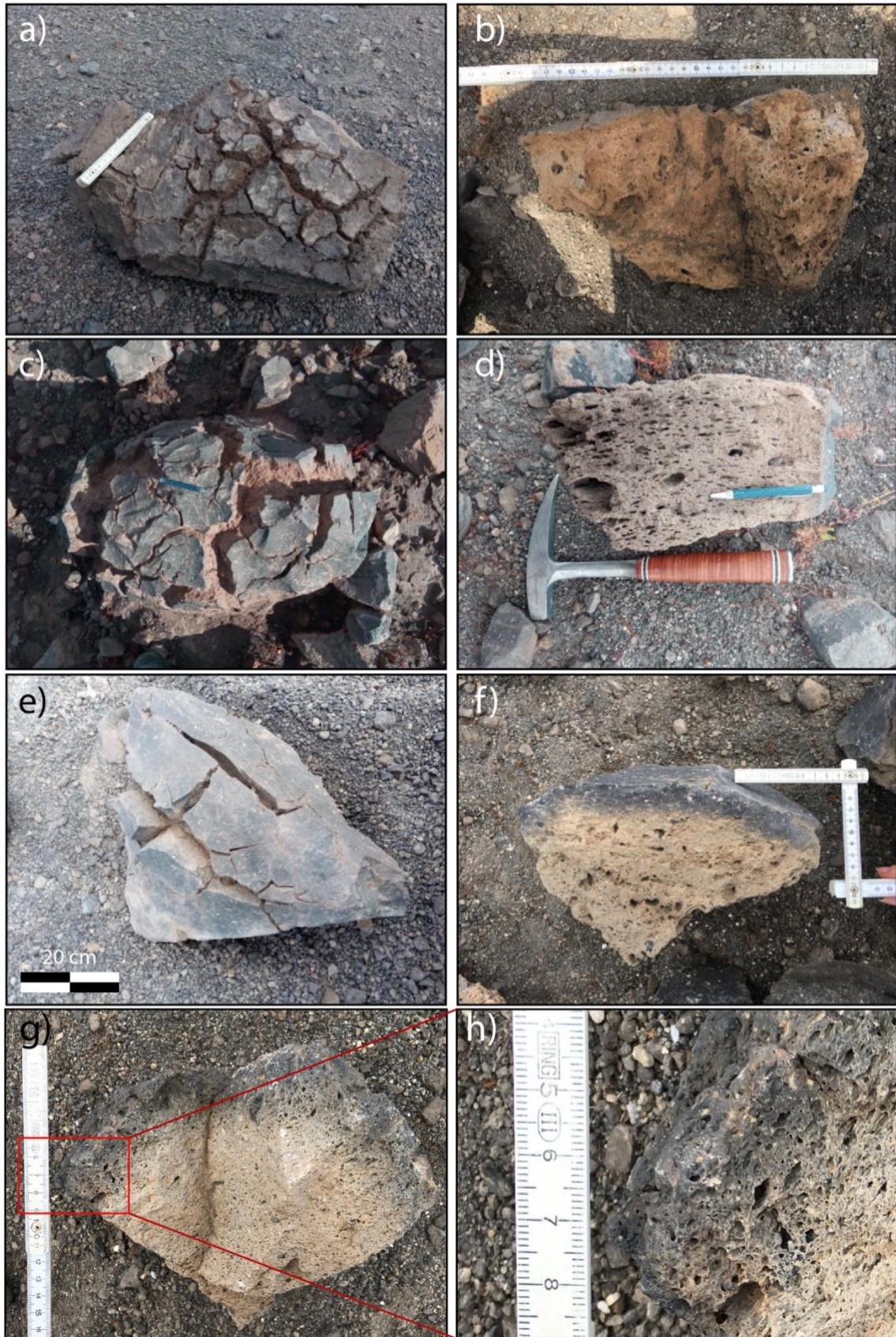
Fig. 4.7 Types of Bread crust Bombs observed in the field. The different external aspect of BcBs (a,c,e,g) is compared with their corresponding internal features (b,d,f,h).

Black Scoria Bombs (S):

Highly scoriaceous black bombs (Fig. 4.8) show equant and diffuse vesicularity, with diffuse whitish enclaves (possibly hydrothermally altered fragments) embedded in the black glass. S often present a thin (mm-sized) quenched crust evidenced by a weak gradient in vesicularity, which sometimes is very hard to distinguish. S are found to be only a minority percent among all the other bombs analyzed.

Fig. 4.8 Image of a Black scoria bomb (S).

Dense blocks (D):

D blocks are high-density, massive blocks showing barely shiny black to opaque dark grey colors and smooth glassy external surfaces (Fig. 4.9 a, b). They frequently show regular prismatic shapes with an external morphology defined by angular perimeters (Fig. 4.9b). They are characterized by the total absence of vesicles (only rare veins of aligned small vesicles were occasionally found) and by an overall textural homogeneity with high crystal contents and abundant presence of magmatic enclaves of variable shapes (from rounded to highly elongated). No gradient in the distribution of crystals and no evidence of surface quenching of the glass is generally visible. Occasionally, dense massive blocks showed important glass devitrification (Fig. 4.9c). These blocks generally present lighter colors of the external and internal portions. However, they preserve the same structure of the normal dense fragments with no crust observable and low vesicularity.

A clear pattern of cooling induced fractures, evidenced by a regular polygonal jointing (fractures at angles of 120°), often characterizes the surface of D blocks (Fig. 4.9 b,c). Many of them seem to preserve their original shape and appear fractured along thermal fracturing on place (Fig. 4.9 a). On the other hand, D blocks are often present as small blocks derived from the disaggregation, along the more penetrative cooling joints, of larger blocks at impact with the ground. The absence of fluidal or drop-like morphologies, together with the common polyhedral, prismatic shape and the common rupturing at impact all suggest a rigid behavior of magma forming D blocks.
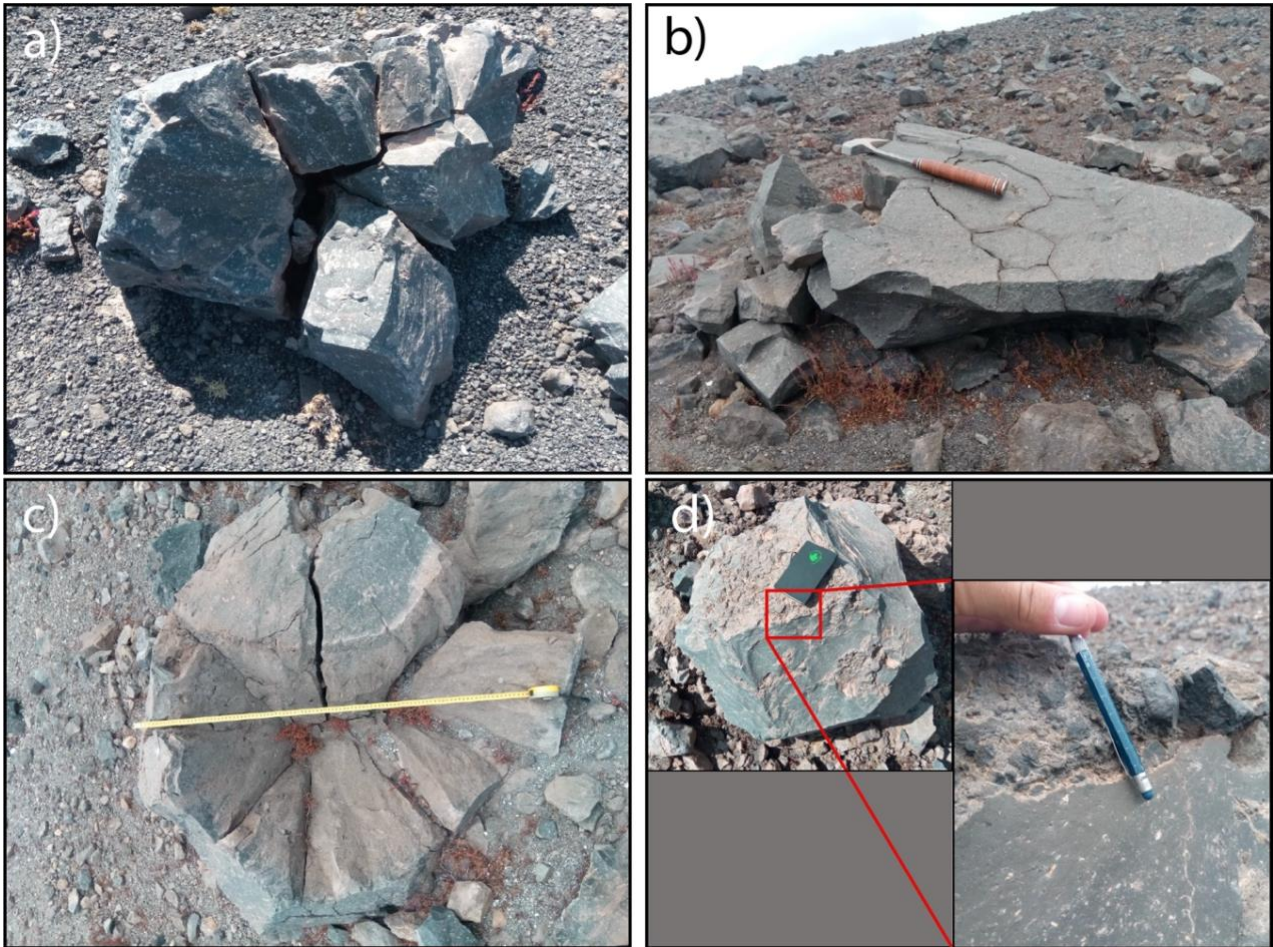
Fig. 4.9 Different types of Dense blocks. Dense blocks with thermal fracturing (a,b). The mutual influence of both thermal and collisional cracking (b) is clear: the thermal contraction due to rapid cooling induced the 120° oriented pre-jointing in the bombs, and the impact of the bomb with the ground resulted in the propagation and of this pre-existing network of fractures. Dense devitrified block (c), and typical portions of breccia-bearing materials associated to the dense blocks (d).

Importantly, D blocks were often found to be characterized by the presence of extensive breccia portions in the form of veins holding variably fine clastic material (Fig. 4.9d). Therefore, a special attention has been deserved to these breccia-bearing bombs.

Breccia-bearing Dense blocks (D-Br):

D-Br (Fig. 4.10) are similar to the D blocks since they share with them most of the morphological and textural features, however they often show larger size with respect to D blocks. D-Br are characterized by the presence of significative amounts of internally structured clastic aggregates which are typically distributed along large portions of the external surface of the blocks (Fig. 4.10a) or inside internal veins (Fig. 4.10e) to form a complex three-dimensional network of fractures. The pervasiveness of filled fractures is variable among the different blocks and unequally oriented, however in many cases the filled veins appear to be mutually interconnected.
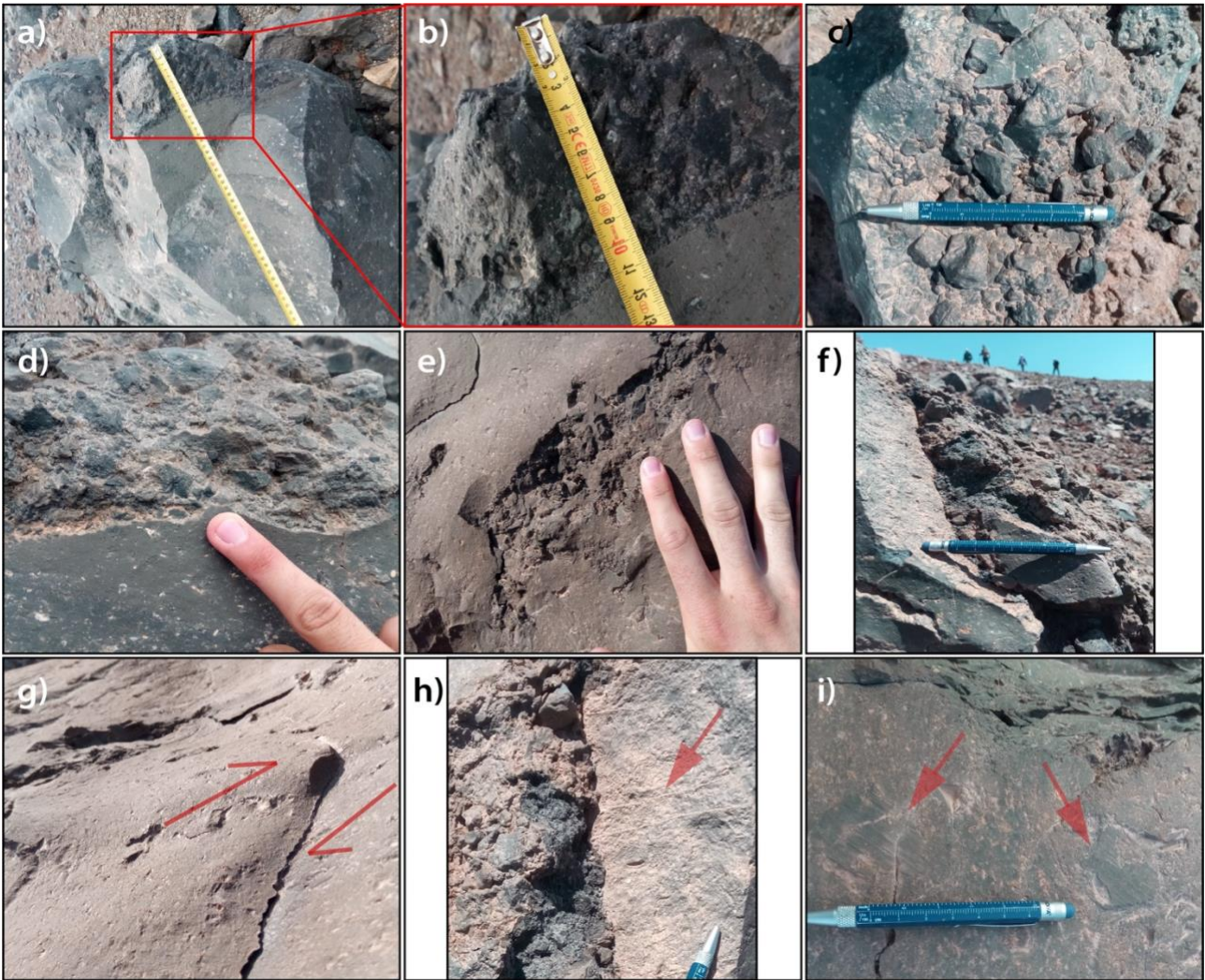
Fig. 4.10 Images of Breccia-bearing dense blocks with evident portions of comminuted material: The sharpness of the contact with the wall rock (a,b,d); Cross sectional view of a vein filled by clastic materials (e); Flat surface at the contact between large hosting dense blocks and poorly compacted breccia clasts (c,f); slickenside structures revealed on brecciated surfaces of the blocks with direction of relative motion indicated by red arrows (g,h); cinematic indicators of shearing motion (i) above the contact surface with the hosting blocks.

A sharp and planar surface (Fig. 4.10 b,d,f; Fig. 4.11) was observed to characterize the contact between the dense walls of the hosting blocks and the clastic material. This surface is also frequently characterized by the presence of slickenside structures and cinematic indicators suggesting a relative motion between the two side of the fracture (Fig. 4.10 g,h,i). A clear grain size gradation of the fragments across the vein (fracture) is evident in many samples, often showing a progressive decrease of particle size approaching one of the walls of the veins (Fig. 4.11 a,c). Close to the contact with one side of the hosting dense rock, the grade of clast comminution appears to be often higher respect to the internal portions of the veins or to the opposite surface (Fig. 4.11a). Conversely, an open-framework structure, dominated by numerous voids and accompanied by the diffuse presence of large angular clasts often characterizes the internal portions of the veins (Fig. 4.11).

The external morphology of the clasts filling the vein is also largely variable, with coarser particles generally showing the higher irregularity in external perimeters and angular outlines. The grade of

compaction ranges from low-to-moderate in many of the observed breccia, and structural voids are also present (white parts in Fig. 4.11a,b,c). Evidence of welding between fragments is generally lacking.
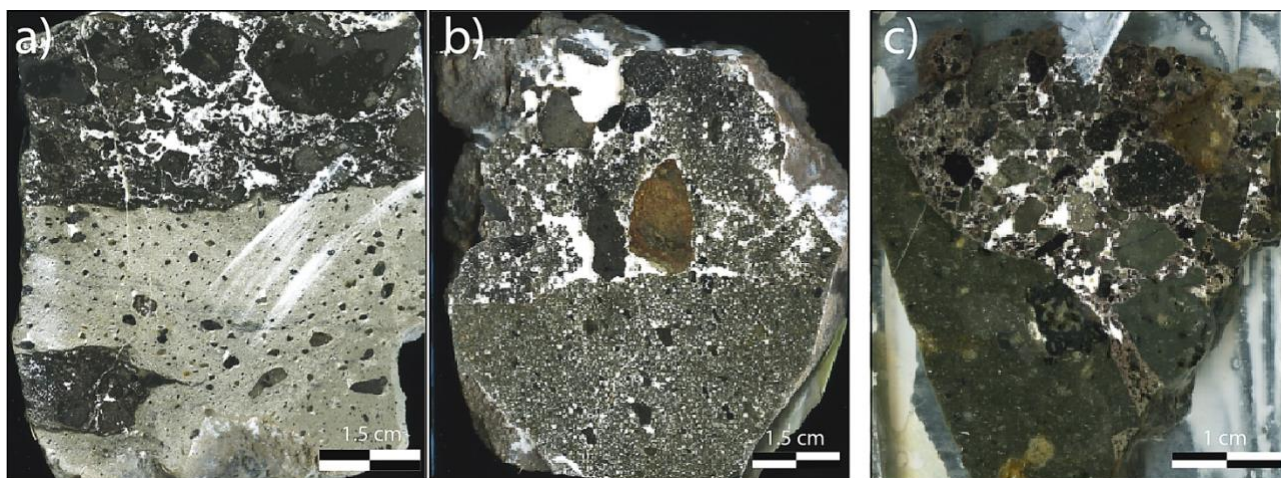
Fig. 4.11 HR-images of orthogonal breccia cross-sections. The white regions in the images corresponds to the diffuse breccia voids permeated by the colored resin.

From the analysis of polished and thin sections, the clastic materials of breccia samples appear to be characterized by significative textural heterogeneities (Fig. 11b; Fig. 4.12). Generally, the clastic material associated to the D-Br samples was characterized by massive, highly crystallized angular fragments with different cloros and texture (Fig. 4.12b). The vesicularity of the larger fragments is typically very low, and rarely exceeds 20%. The size of the grains is variable between few centimeters to sub-millimetric, however the presence of important amounts of very fine matrix (up to particles of few microns) discontinuously characterizes the interstices separating the coarser fragments. Clast componentry (Figs. 4.10 - 4.11 - 4.12) is dominated by blocky and poorly vesicular particles with a similar lithology to the hosting D blocks (light particle in the bottom-left corner of Fig. 4.12c).

In thin sections (Fig. 4.12), the fragments of the clastic portions display phaneritic textures characterized by the presence of sub-euhedral pheno and micro phenocrysts of plagioclase, sanidine and pyroxene embedded in a light brown aphyric groundmass. Sparse glomeroporphyritic, fine-grained aggregates are also present. Several types of glassy particles are present, ranging from brownish dark to light-grey and with clasts. The vesicularity of glassy clasts rarely exceeds 20%, and their morphology is generally angular although in many cases the external particle outlines appear poorly defined.
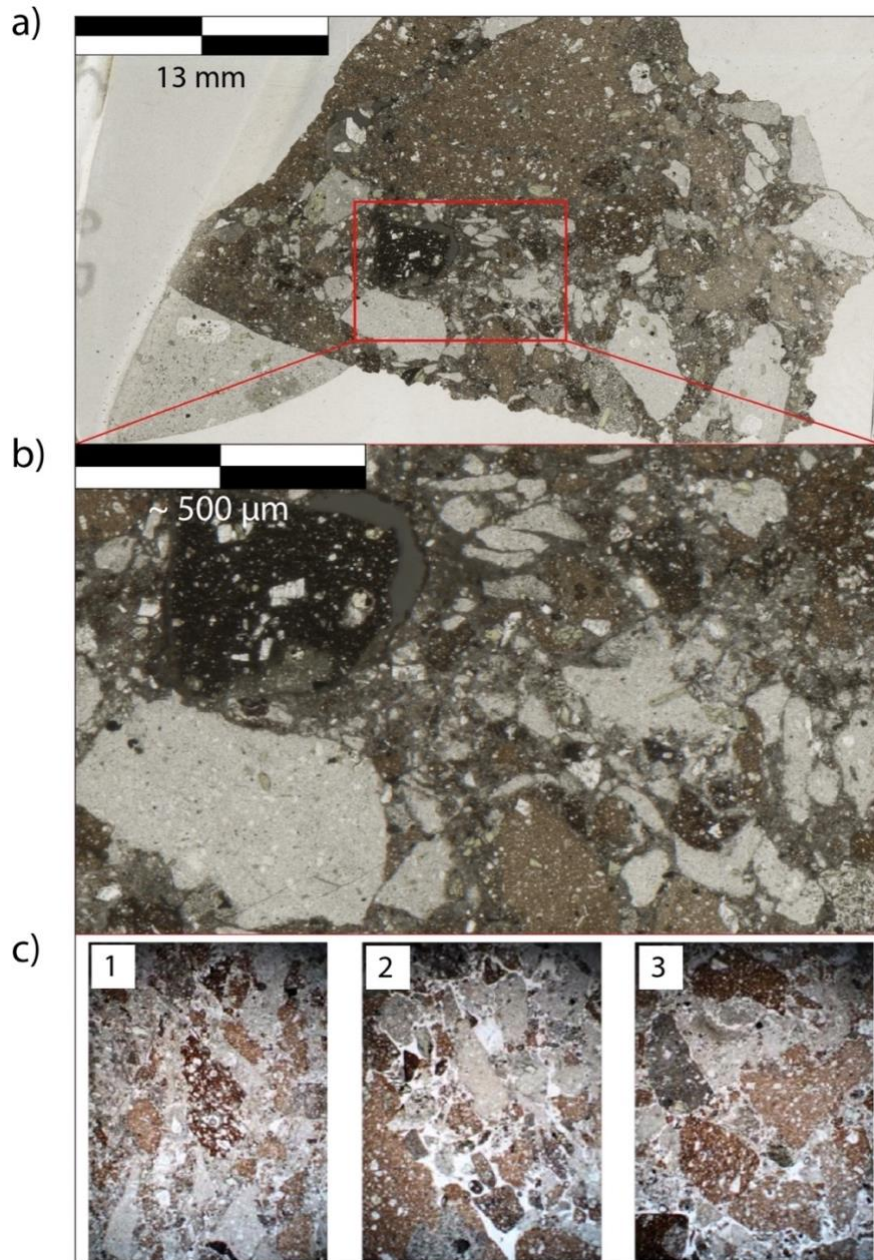
Fig. 4.12 Sections of Breccia samples in thin section.

4.3.2 Spatial distribution of the bombs across the crater terrace

Histograms of size distribution of bombs in the different sectors of the crateric rim are shown in Fig. (4.13). The bomb size distributions display important variations between the different sectors. These are characterized by a marked and diffuse polymodality. Generally, a prominent mode around -6 and -6.5 Phi (6.4-9.1 cm) characterizes the distributions of the North East, East and South sectors, and corresponds with the volumetrically most abundant bomb class-size in the field of Vulcano. On the other hand, both the distribution of the North and the West sectors display prominent modes set between -9.5 and -10 Phi (72.5-102.4 cm), indicating that the largest bombs were preferentially ejected toward these two sectors.
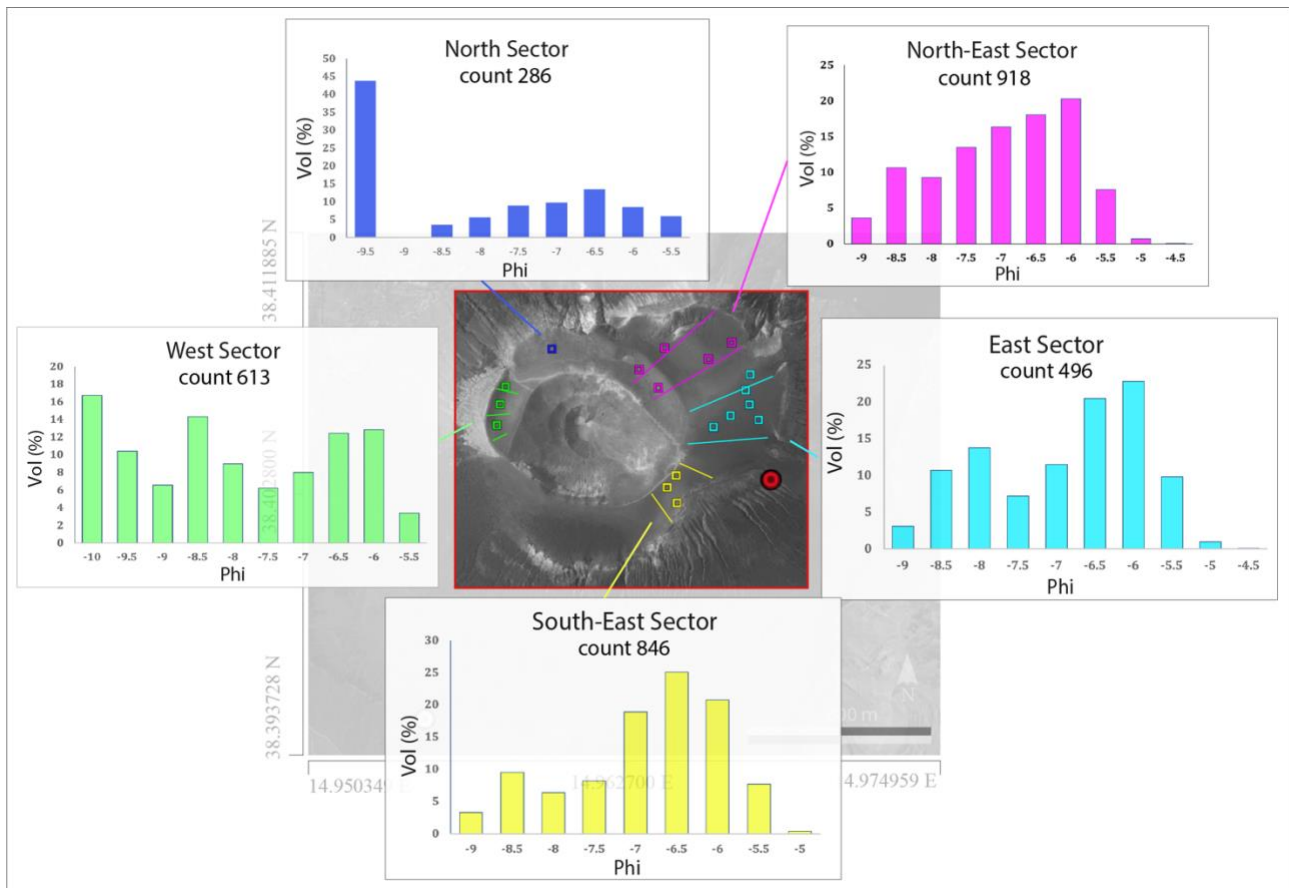
Fig. 4.13 Size distribution of bombs measured for different sectors of the crater area of Vulcano.

Pie diagrams showing the frequency distribution of the relative abundance of the different types of bombs were derived for the five sectors and reported in Fig. 4.14. D blocks largely dominate all the sectors confirming as the most abundant type of ejecta produced from the eruption. Importantly, D-Br are present in all the sectors, with not-negligible abundance comprised between 5 and 18%. On the other hand, the macro category of BcB appears, in general, poorly represented, despite Vulcano is largely known as a classical site for this type of bombs. Only very localized abundances, in the order of 20%, of BcB-Tk characterize the West and the South-East sectors. On the other hand, BcB-Tn seem to concentrate only in the North sector, where they reach abundances of around 20%. The vastity of the investigated area, and the large number of classified bombs testify for the statistical representativity of these data and confirm the significative presence of the D-Br blocks among the products of the 1888-90 eruption. Importantly, all these evidences resulting from the field description of D-Br indicated the presence in the pre or syn-eruptive magma conduit of Vulcano, of a three-dimensional structured internal network of fractures characterized by a significant infilling of fine materials. The ash present on these infillings can have variable origin, and it should be taken into account when discussing the provenance and mechanism of fragmentation of the important amount of ash released during Vulcanian activity. For this reason, an in-depth study of the breccia material can disclose important clues on the role of alternative mechanisms of ash production within the dense magma plug topping conduits during vulcanian activity. Therefore, we focused on the direct comparison between the main morphological

and textural features of volcanic ash present on the fallout deposits and the characteristics of the material contained inside the breccia-bearing dense blocks.
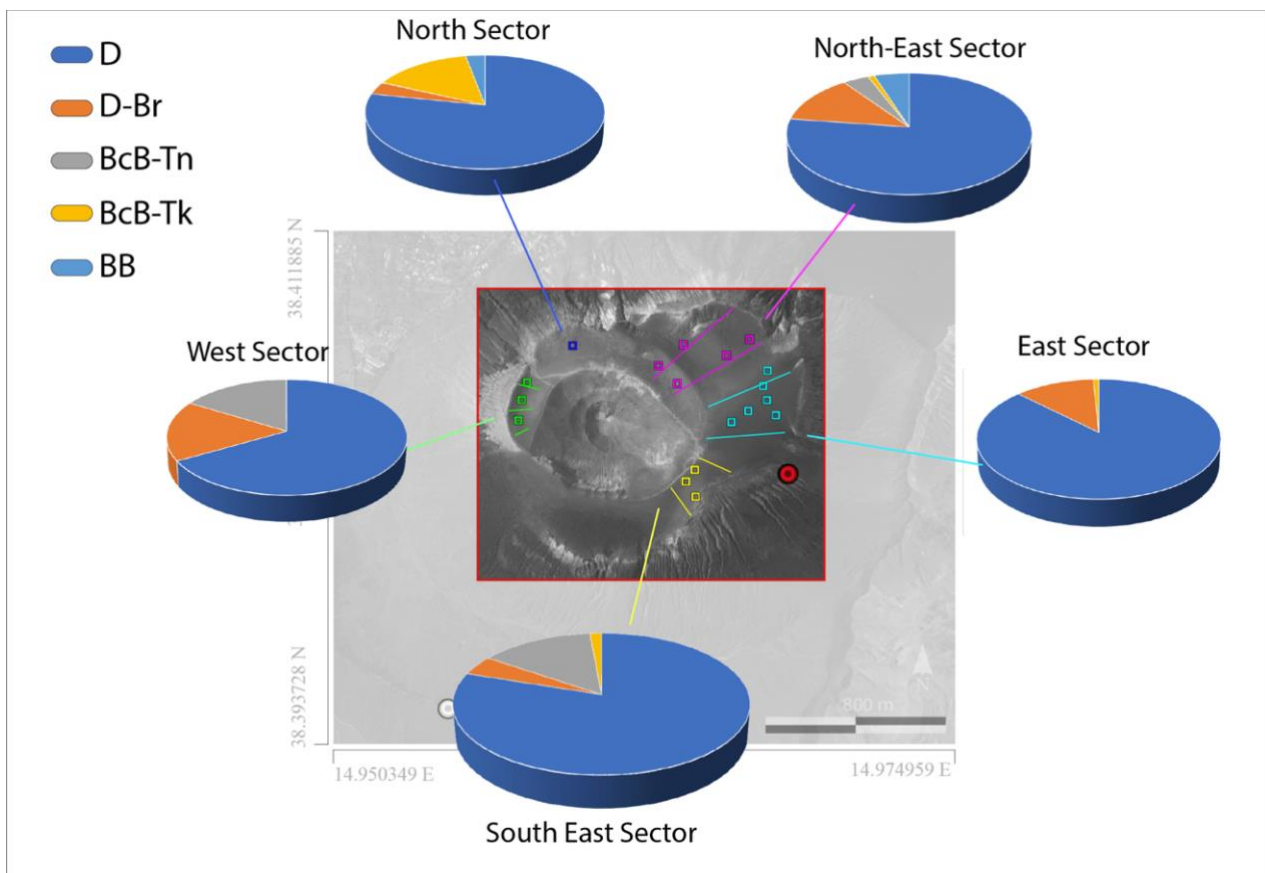
Fig. 4.14 Spatial frequency distribution of the different bomb types among the sectors considered during the fieldwork.

4.4 Analytical Results

4.4.1 Internal features of breccia samples

4.4.1.1 GSD and componentry of breccia deposits:

Three poorly compacted breccia samples were processed in order to quantify the grain size distributions (GSD) of the loose clastic material and characterize the relative componentry of the individual constituents (Fig. 4.15).

Both the total and the partial GSDs of the deposits are reported in the figure. Total GSDs are dominated by the presence of few coarse clasts in the size range comprised between -3.5 and -4.5 Phi. In order to resolve the granulometry of the finer populations and to better compare these results with those provided for the ash deposits we will consider the truncated GSDs (Fig. 4.15b) which include clasts with size below -1 Phi.

In this range of size, breccia samples display heavy tailed distributions characterized by high $\sigma(\phi)$ values, comprised between 1.05 and 2.13, and by a positive skewness (always higher than 0.4; Tab. 1).
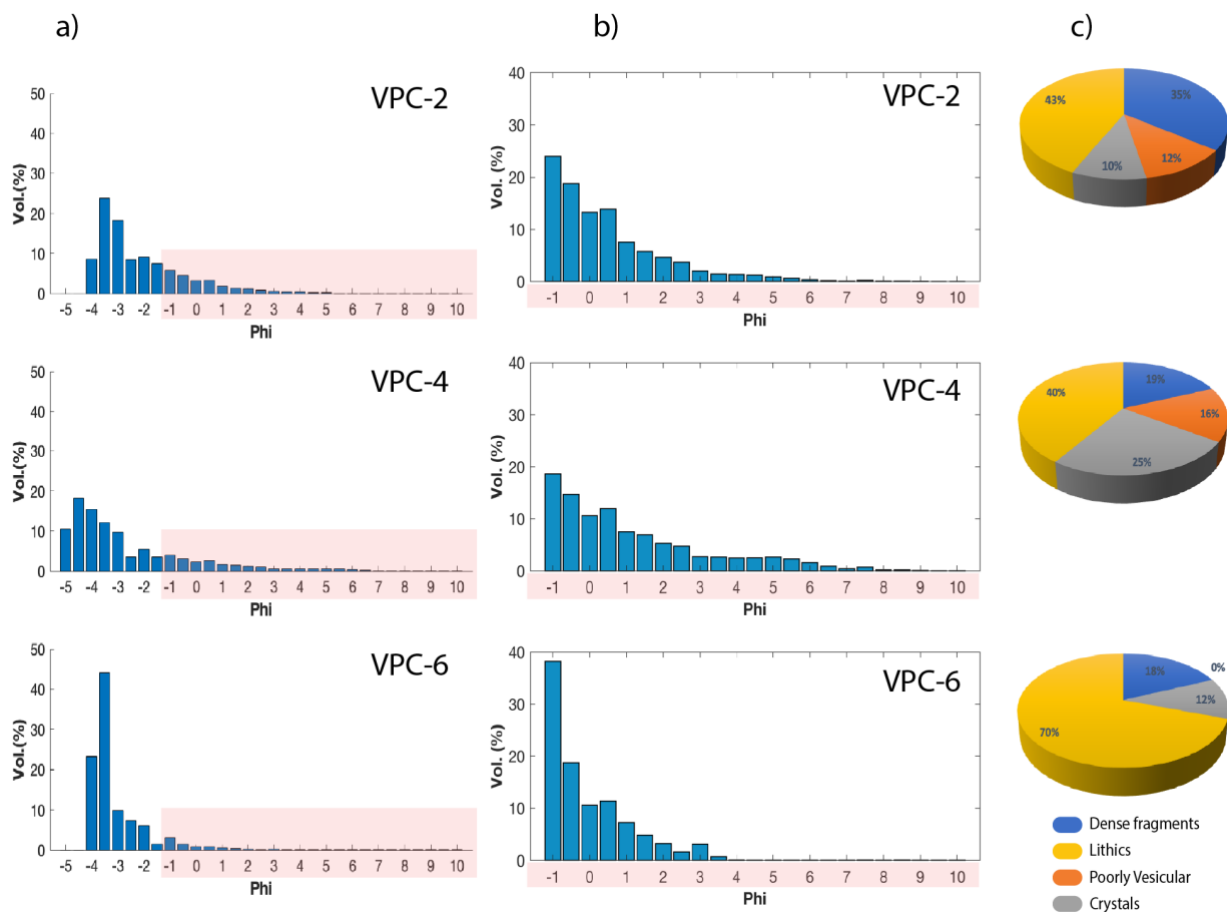
Fig. 4.15 Total grain size distribution of individual clasts forming the breccia samples (a); Grain size of the < -1Phi fraction where the finer modes of the deposits are better resolved (b); relative componentry displayed as pie charts (c), with the relative legend at the top-right corner in which the categories of fragments that form the breccia deposits are specified.

The distributions are all polymodal, with the main mode set at -3.5 - -4.5 Phi (2 mm) (Tab. 4.1), and two secondary modes placed respectively at 0.5 Phi and within the class-size interval comprised between 3 and 5 Phi. Two out of three of the analyzed samples present significative amounts of fine material distributed across the size classes as small as 6-7 Phi (7-10 µm). In particular VPC-4 displays a dispersed GSD characterized by higher sorting and standard deviation ($\sigma(\phi)$), and by finer Mean grain size (MeanGS) (Tab. 4.1).

Sample ID	First Mode	Second Mode	Third Mode	Fourth Mode	$Md(\phi)$	$\sigma(\phi)$	MeanGS	Sorting	Skewness
	Phi	*Phi*	*Phi*	*Phi*	*Phi*	*Phi*	*Phi*	*Phi*	*Phi*
VPC-2	-3.5	-2	0.5	-	-0.30	1.38	0.0698	1.384	0.4251
VPC-4	-4.5	-2	0.5	5	0.20	2.13	0.7822	2.116	0.444
VPC-6	-3.5	-1	0.5	3	-0.80	1.05	-0.3749	1.0707	0.5115

Tab. 4.1 Statistic descriptors calculated for the total breccia GSDs (Fig. 4.15a). '*Md(\phi)*' *and* '*σ(\phi)*' represent the median and the standard deviation of the distributions, respectively. '*MeanGS*' refers to the mean grain size of the deposit. All the parameters were calculated according to Inman, (1952).

Using the stereo microscope and considering the size interval of 0.5 Phi, four main types of clasts were visually identified, thus confirming a marked textural heterogeneity for the breccia clasts as already observed from visual observations of HR-images and thin sections. The relative abundance of the different clast categories is reported for each of the investigated deposits in the pie charts of Figure (4.15). *Dense Fragments* showing variable textures and hydrothermally altered *Lithic* clasts dominate the componentry of breccia samples, and always represent more than 60 % of the total deposit. The dense fragments show angular outlines and crystal-rich textures which are similar to the highly crystallized glass of the hosting blocks. On the other hand, lithics clasts are represented by lava fragments, and appear to be highly variable in terms of color and textures. Poorly vesicular particles (vesicularity < 10 %) and loose crystals of feldspar and pyroxene are also present in moderate amounts within the loose breccia deposits.

4.4.1.2 Spatial distribution, orientation and shape analysis of breccia fragments:

The cross-sectional transects T1 and T2 of SEM images were used to investigate the spatial distribution (Fig. 4.16a, Fig. 4.17a), the iso-orientation (Fig. 4.16b), the porosity (Fig. 4.17b) and the shape (Figs. 4.17c - 4.18) of the clastic material forming the breccia.

Two oriented transects are reported in Figure (4.16 a,b) with both the sides (topmost and bottom of the transects) corresponding to the contact with the dense hosting block.

The binarized image of transect 1 (Fig. 4.16a) show that internal constituents clasts are often not completely in contact with each other and have no evidence of plastic behavior along the external faces or edges, so indicating suggesting a very low degree of compaction and that the clastic material is not welded. The two the transects in Figure 4.16 (a,b), and the GSD analysis of crops provided for transect 1 (Fig. 16a), evidence a clearly organized spatial distribution of the clasts across the breccia. In particular, the grain size of the clastic material displays a progressive increase across the breccia from one contact surface to the opposite, with the $Md(\phi)$ values ranging from 1.5 Phi to -2.1 Phi, respectively. In addition, the analysis of clasts orientation (calculated as the angle of the Feret diameter (FA) with the horizontal plane of the transect), provided for transect 2 (Fig. 4.16 b), clearly shows a distinct iso-orientation of the largest and the smallest clasts, which were respectively aligned along two preferential directions of around 20-40° and 150-160° (note the light-blue and red particles distributed across the transect); values of the preferential clast orientations are reported in Table (4.2).
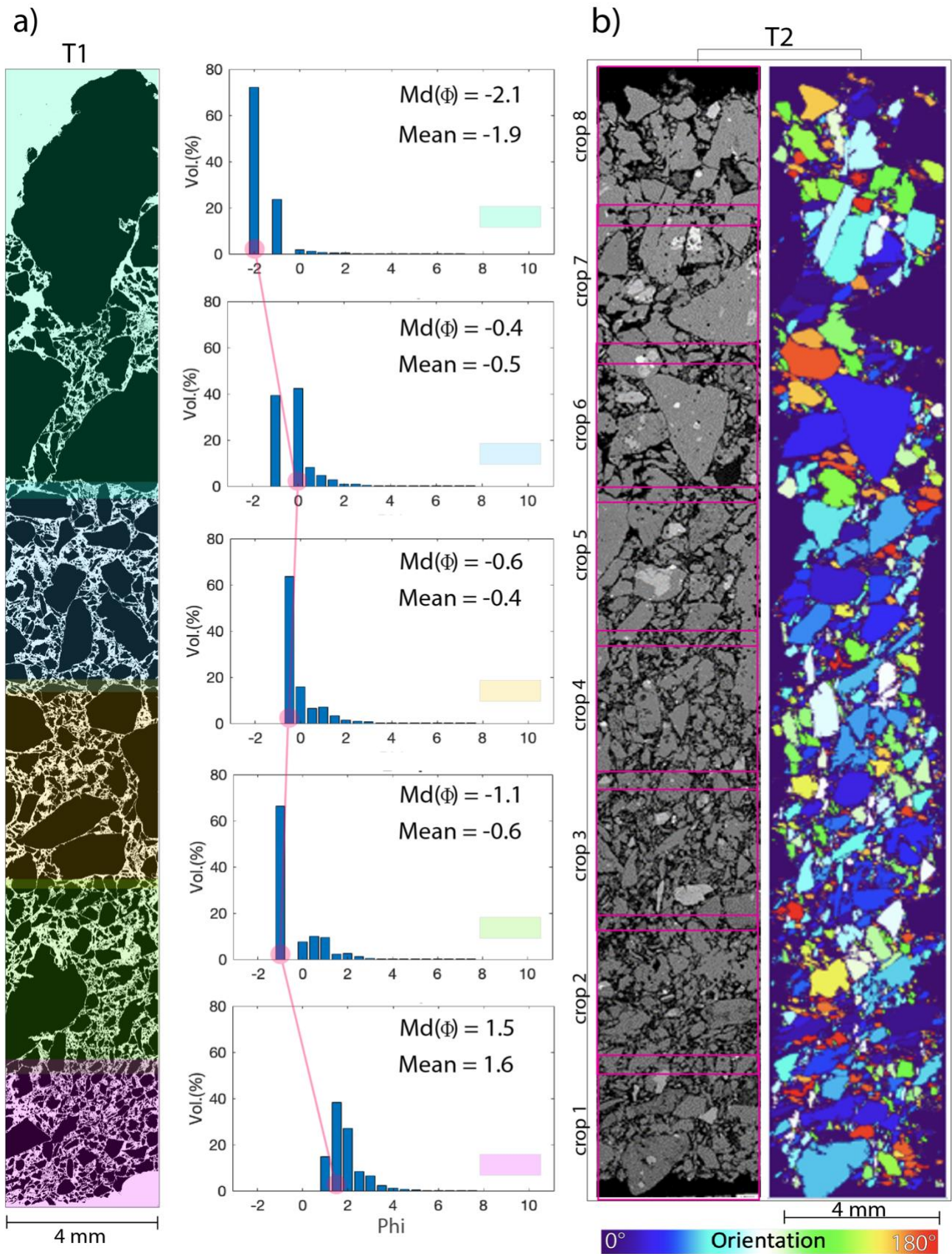
Fig. 4.16 Grain size distribution (a) of clasts in sequential crops of the T1 breccia transect, and iso-orientation (b) of the fragments in the T2 breccia transect. Colors reported in (a) refers to the different crops of the transect that were analyzed to derived the GSD plots. Colors in (b) refers to the orientation of the clast, which is calculated based on the angle of the Feret diameter (FA) with the horizontal plane of the transect (vertical plane of the image).

Crops of T2	Feret Angle (FA)
Crop 1	30° - 50° /160°
Crop 2	40° / 160°
Crop 3	30° - 40° / 160°
Crop 4	30°-40° / 160°
Crop 5	30° / 160°
Crop 6	30° / 170°
Crop 7	20° - 30° / 150° - 160°
Crop 8	20° / 160°

Tab. 4.2 Modal values in the distributions of clasts orientation (quantified through the angle of the maximum caliper distance of the particle outline ('FA')) reported for the different '*crops*' (magenta rectangles) relative to the analyzed T2 transect.

Detailed analysis provided on the spatial arrangement of clasts across the same transect also indicates a strong asymmetry in the distribution of the finer particles (Fig. 4.17a). In particular, a sharp increase in the areal density of particles (i.e. number of particles per area unit) is recorded across the transect moving from the upper crops (areal density of around 30 mm^{-2},) toward the bottom of the transect, where the maximum value (250 mm^{-2}) of particle number density was measured (Fig. 4.17a). These data are well in accord with those concerning the GSDs (Fig. 4.16a), and indicates that higher amounts of fine matrix and small fragments characterize the basal portion of the transect respect to the topmost portions, which is instead preferentially populated by the largest clasts. The basal portions of the T1 transect are also characterized by a higher porosity of the clastic materials (up to maximum 50%; Fig. 4.17b), also confirming the general low compaction and (possibly) high permeability of the breccia. The porosity progressively decreases as we move up to the transect toward the topmost portions, where values in the order of around 20% are measured (Fig. 4.17b). On the other hand, the binarized image of the transect (Fig. 4.17a) also shows that the porosity associated to these breccia portions is typically localized along the interstices between the larger fragments (Fig. 4.17b), forming channels characterized by an open-framework texture, with only few amounts of fine materials included, and possibly with a relatively high internal permeability.

The shape of the 2D sectioned outline of the clasts included in the T1 transect was also investigated in detail in order to monitor possible systematic variations in the morphology of clastic materials across the transect (Figs. 4.17b - 4.18).
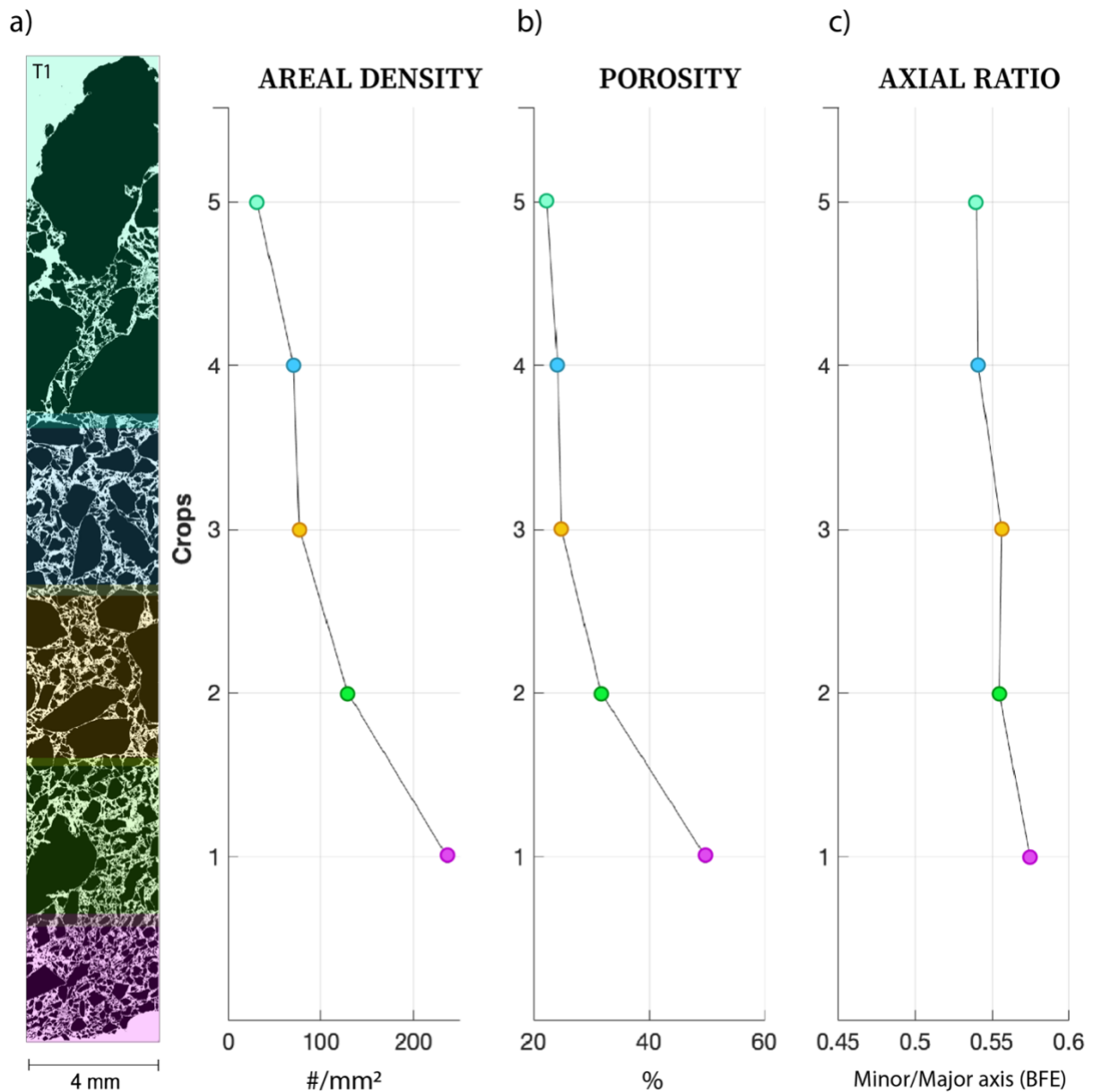
Fig. 4.17 Systematic variation of physical parameters extracted from the analysis of 5 different 'crops' in T1 transect (colored areas in the left image). From (a) to (c) is reported the variation of the areal density of particles (#/mm²), the average porosity of the clastic material (%) and the averaged Axial Ratio (minor/major axis of the BFE) of the clasts. The color of the marker points in the plots corresponds to the color of regions in the binarized photomosaic of the transect.

The average aspect ratio of the clasts included in the transect is poorly variable, being the average Axial Ratio (AR; minimum/maximum axis of the Best Fit Ellipse) mostly comprised between 0.53 and 0.57 among the different crops. A slight and progressive increase of AR is however observed from the top to the bottom of the transect, (Fig. 4.17c) thus suggesting a weak increase in the regularity of the clast shape possibly related to their size. The shape of the clasts outline is further investigated in Figure 4.18, and quantified in terms of Roundness, Convexity and Solidity values, that were calculated for clasts included the different crops.
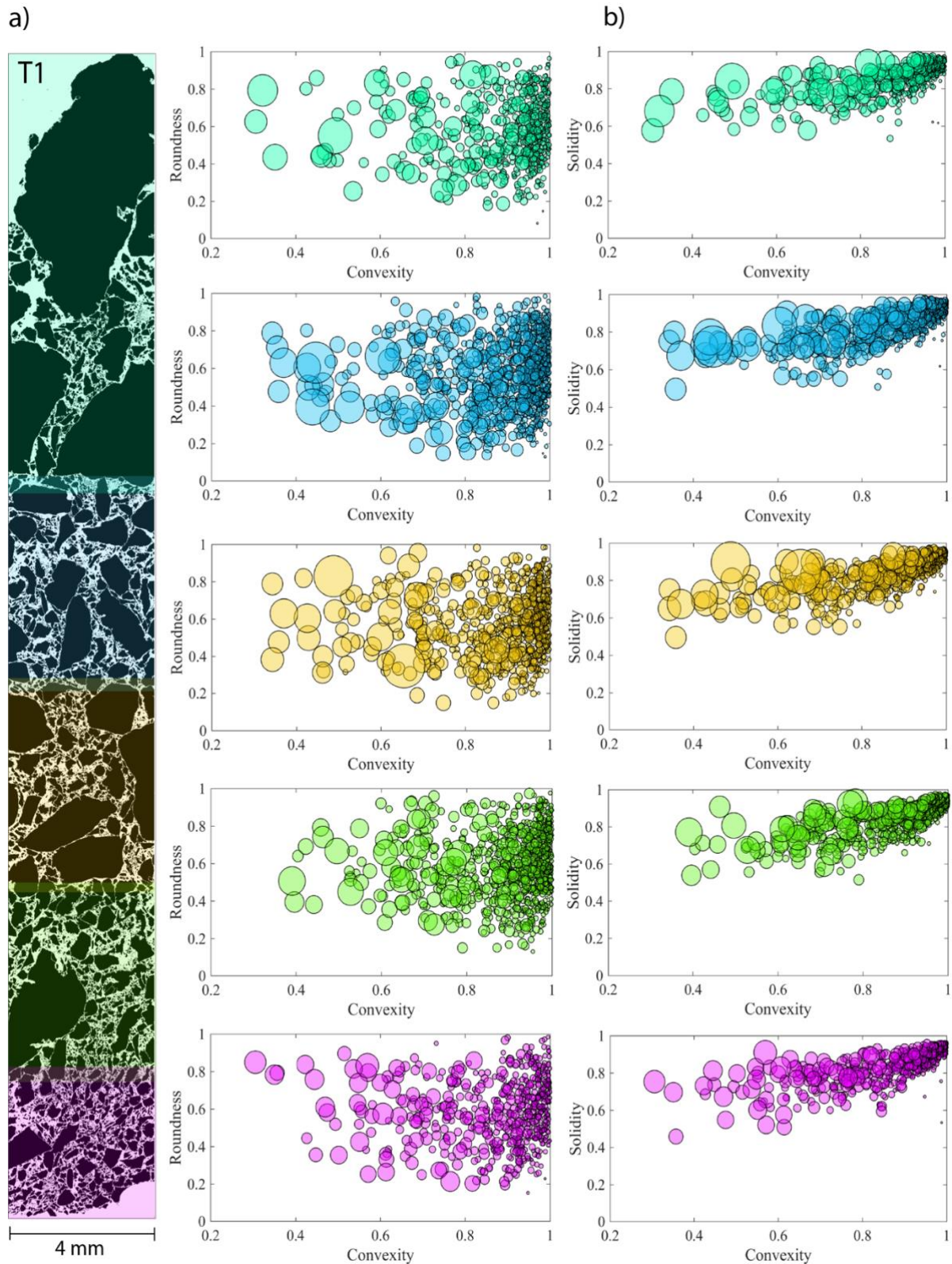
Fig. 4.18 Bubble plots of shape descriptors for different crops of T1 transect. In (a) Convexity of clasts is compared with the clast Roundness here defined as $4 \cdot \frac{Area}{\pi} \cdot MajorBFEaxis^2$; while in (b) Convexity is plotted against Solidity. The dimension of markers is representative of the size of the different clasts, while the colors are associated with the various analyzed crops in the transect. The clasts toughing the edges of the crops were excluded from this analysis.

The Roundness of clasts is widely dispersed in a constant range of values comprised from around 0.2 to 1 (Fig. 4.18a), indicating a high variability of the overall shape of the investigated clasts. Convexity

values (Fig. 4.18) are dispersed in a similar range of values (0.2-1) importantly indicating the presence of a variably fine roughness affecting the external clast outlines. Conversely, the variability of Solidity is constrained into a narrower range of values comprised between 0.5 and 1 (Fig. 4.18b), which testify for the substantial absence of large, concave asperities on the external perimeter of the clasts and thus for their blocky aspect. Finally, bubble plots in Figure 4.18 also inform about a clear variability in the morphology of the clast perimeters according to the clast size (i.e. represented by the dimension of bubble markers). In fact, while the larger clasts are preferentially characterized by low values of Convexity, mostly dispersed in the range of 0.2 – 0.6, the smaller ones are instead characterized by highly regular outlines, with Convexity values close to 1. This indicates that a fine perimetral roughness selectively affects the external outlines of only the larger clasts.

4.4.1.3 Fractal dimension of the breccia clasts

The analysis of the HR-images of the breccia cross-sections allowed us to investigate the grade of fragmentation of the internal constituent clasts by calculating the slope (D) of the linear fitting interpolating the clasts size distributions in a log-log space. The fractal nature of the size distribution of breccia-forming clasts was thus tested and results relative to the analyses of two samples are reported in Figure (4.19).
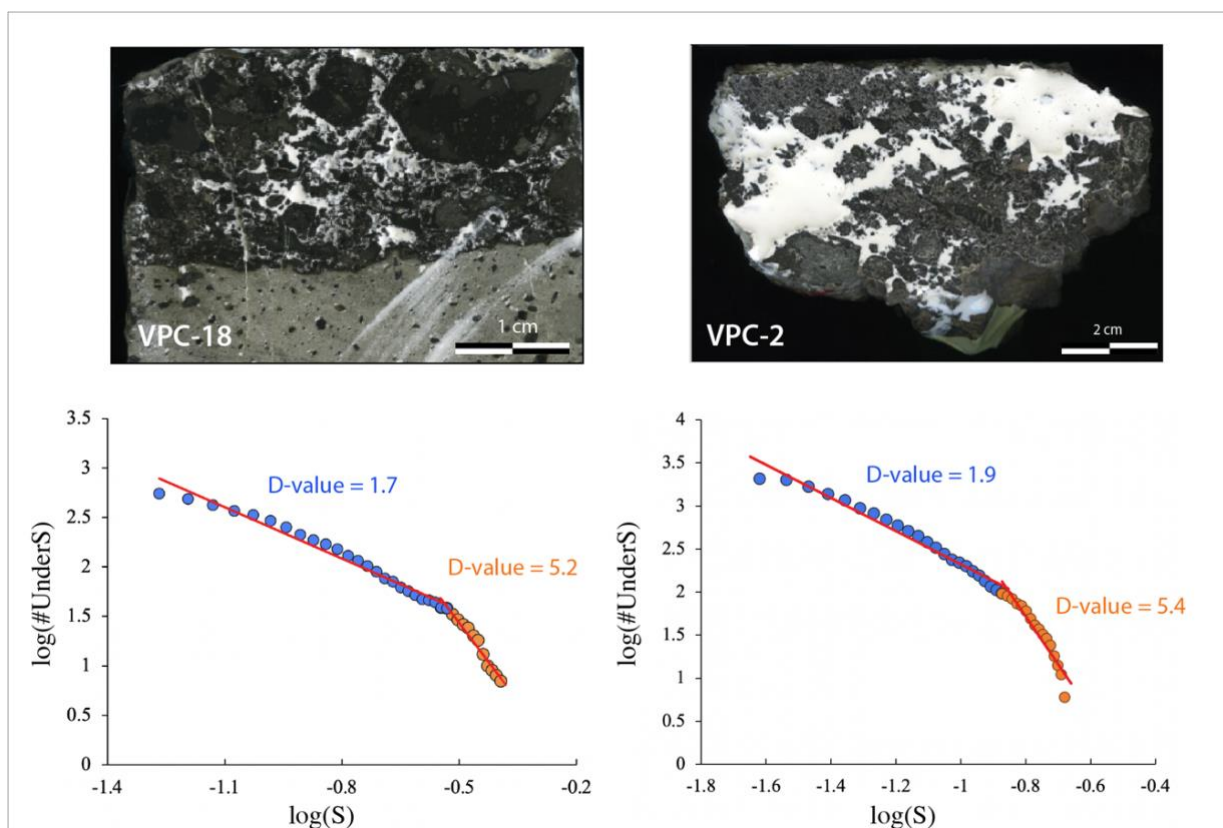
Fig. 4.19 Results of the fractal analysis provided on the individual constituent fragments of two breccia samples. D-values indicating the negative slope of the least-square fitting of the data-series (red straight lines) are reported with an appropriate color based on the fitted data trend. The logarithm of the particle diameter in cm (*log(S)*) is plotted against the logarithm of the number of particles having a dimeter higher than S (*Log(#UnderS)*).

In the bi-logarithmic space, size distributions are characterized by a fairly good linear trend, thus indicating a power-low distribution of the clast sizes for the considered breccia samples. In particular, variations are revealed in the slope of the data trends according to the considered ranges of particle-size (Fig. 4.19). Data trends were therefore interpolated by two linear fittings and a double D-value was determined for the coarser (log(S)>125~300μm) and the finer (log(S)<125~300μm) fractions of the breccia sample. The D-values inferred for the fine material (blue dots in the plots) of samples VPC-18 and VPC-2 are 1.7 and 1.9, respectively, while considerably higher D-values (i.e. D = 5.2 and 5.4) were measured for the coarser fraction of deposit, reflecting the control exerted on this portion of the size distribution by the occurrence of a very low number of coarse fragments.

The fractal dimension was also calculated for the size distributions of clasts obtained from the image analysis of the two analyzed breccia transects. The different images forming the transects were segmented and the fractal dimension of the clasts calculated. Results of the analysis are reported in Figure (4.20).
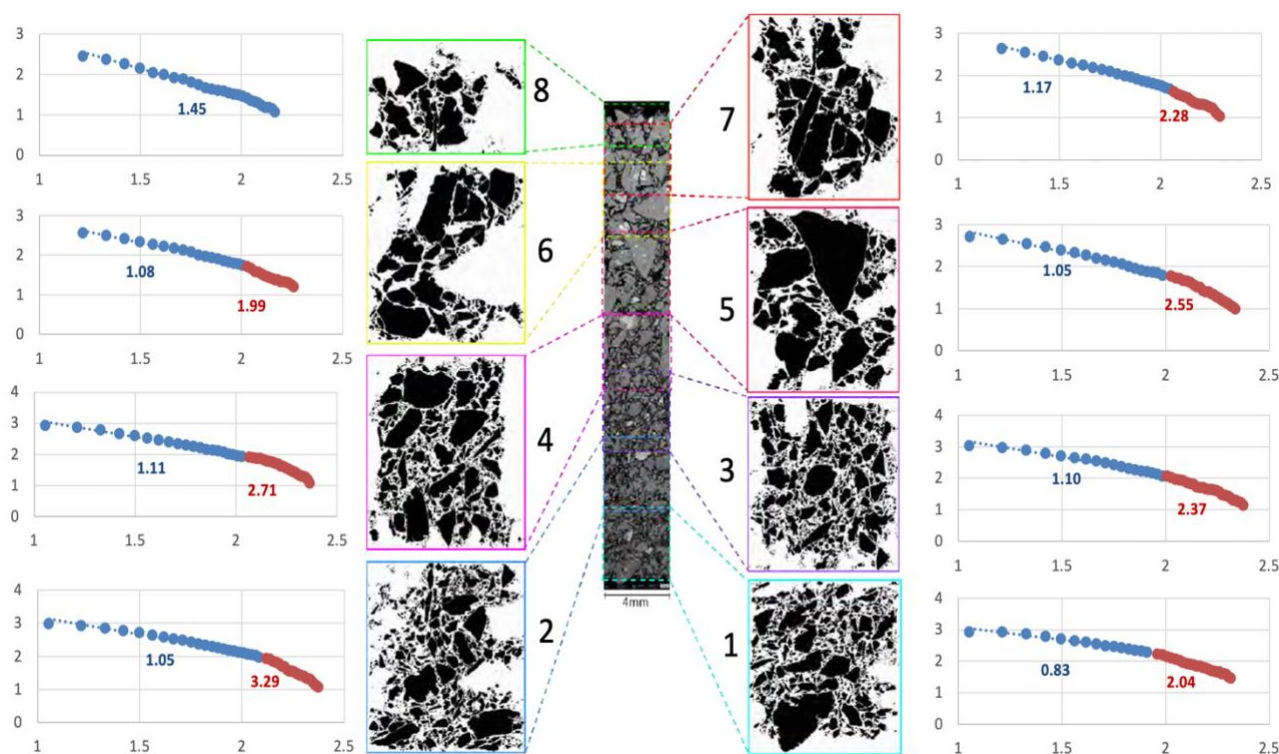
Fig. 4.20 Fractal dimension calculated for the size distribution of breccia fragments at different heights across the oriented breccia transect (colored rectangles). The baseline of the transect corresponds to the contact with the hosting block. Log-log plots of the clasts size frequency expressed in μm, are reported with the associated analyzed bitmaps, and progressive numbering that indicates the corresponding height in the transect (where 1 corresponds to base and 8 to the topmost region).

As previously discussed for two other breccia samples (Fig. 4.19), the size distribution of the clasts forming the breccia transects (Fig. 4.20) is, in most of the regions of the transect, again characterized by a double linear slope in the log-log space. In particular, a generally lower D-value, ranging from 0.83 up to 1.45, is associated to the fine particles, while the coarser particles have a D-value comprised between 1.99-3.29. The size thresholds that distinguish the two power-low distributions of data (red

and blue dots in Fig. 4.20) are set based on the quality of the linear fitting. Importantly, this threshold is substantially invariant between the different regions that were analyzed, and mostly set at around 100-125 µm (log 2 - log 2.1). Finally, results of the sequential analysis of the transect also show a progressive increase of the D-values relative to both the finer and the coarser fraction from one side of the breccia (top of the transect, Fig. 4.20), up to the still visible contact with the hosting block (baseline of the transect, Fig. 4.20).

4.4.1.4 Shape analysis of the clasts in the loose portions of the breccia

The external 2D outlines of a large number of clasts forming the VPC 2 breccia sample were characterized through the automatic particle analyzer. In accord with analyses provided for clasts included in the breccia transect, clast morphology was quantified calculating two shape parameters, i.e. solidity and convexity, which are indicative for the presence of either a structural and a finer textural roughness affecting the external particles perimeters. Analytical results for one of the two analyzed transects are reported in Figure (4.21).

Solidity values of the breccia clasts appear to be substantially unrelated with the clast size, since both the finer and coarser particles are characterized by high values of Solidity, mostly comprised between 0.75 and 0.95. On the other hand, the distribution of the Convexity values (Fig. 4.21b) displayed significant variations with the particle size. In fact, clasts representing the coarser fractions of the breccia (violet, green and red curves in Figure 4.21b) are characterized by very dispersed distributions and by very low mean values of convexity, in the range of 0.6-0.8. Conversely, strongly peaked distributions characterize the Convexity of the smaller particles, with very high comprised into a narrow range between 0.9 and 1.
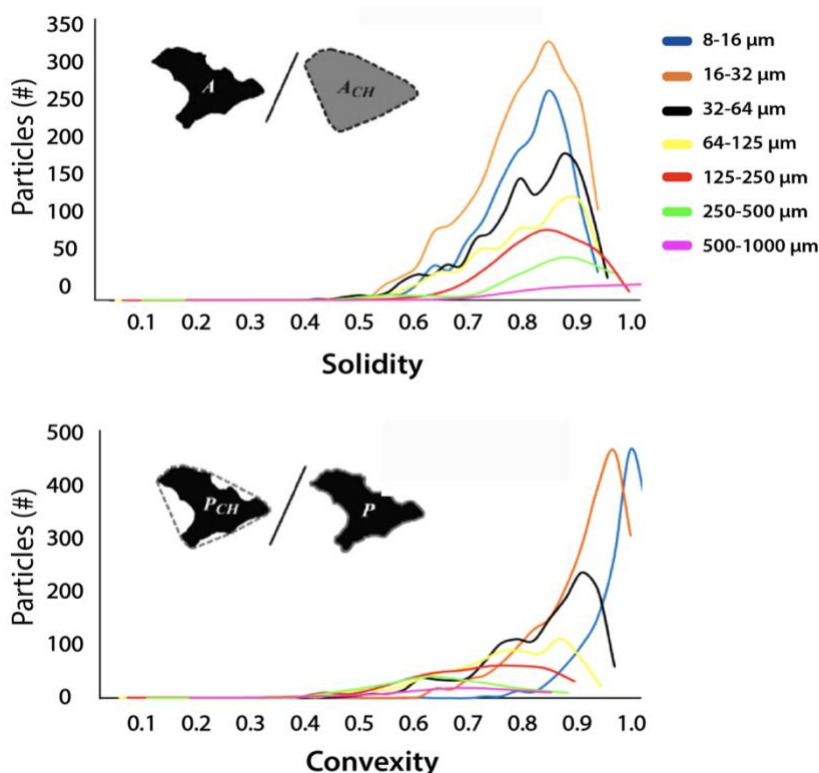
Fig. 4.21 Shape analysis of the 2D outlines of the breccia-forming clasts measured in the breccia transect. Frequency distribution of Solidity (a) and Convexity (b) values are reported for different interval of size of the clast (in the legend is specified the correspondence between colored curve and the relative class-size).

As a matter of facts, the variability of the clast shape as a function of the clast size is also confirmed from visual observation carried out during the SEM imaging. The largest clasts often display a cracked aspect associated to strongly irregular and complex perimeters. Conversely, the finer particles that form the most comminuted fraction of the breccia matrix, often show more regular outlines and lower complexity of the external perimeters. Thus, a clear difference in terms of perimetral complexity and roughness distinguish the large particles from the finely comminuted ash matrix involved in the breccia samples (Fig. 4.22).
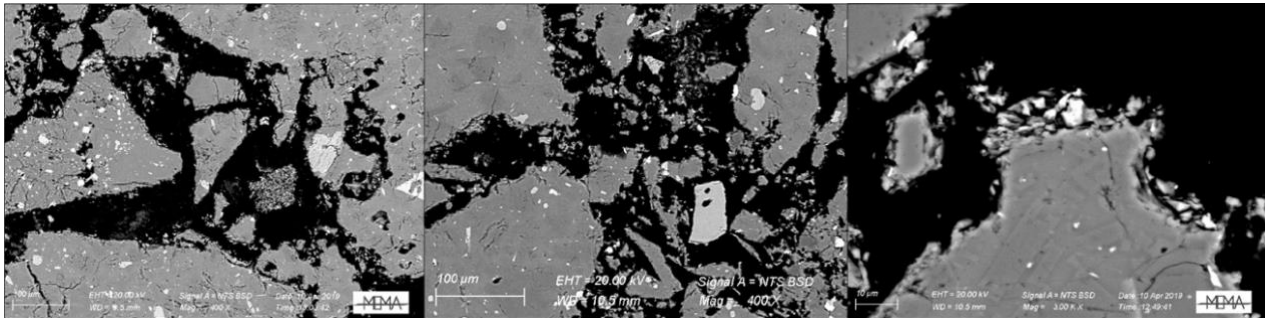
Fig. 4.22 Details of the external perimeters of the larger clasts included in the breccia transects. A progressive zooming on the high complexity outlines of the larger clast is provided with SEM from left to right. The last image on the right also shows the presence of small angular particles (<5µm) very close to the highly irregular external borders of a large clast.

4.4.2 Morpho-textural characterization of volcanic ash

During fieldwork two stratigraphic sequences of fallout deposits were described and sampled.
Both the fallout sequences substantially consisted in the repeated alternation of fine and coarse ash layers with interbedded lapilli fragments (Fig. 4.2 and 4.3).
The componentry analysis provided for the ash grains revealed the dominant presence in the fallout deposits of four main categories of variably vesicular fragments (Fig. 4.23):
-*Fresh Vesicular* fragments (*Vesic,* in Fig.4.23a,b): characterized by vesicularity around 30% and by the presence of rounded bubbles with sharp inner borders, associated with poorly crystallized fresh glasses. Feldspars and Pyroxenes are found to represent the most abundant mineral classes. Vesicular clasts always display highly irregular morphologies.
-*Altered Vesicular* clasts (*V alter,* in Fig.4.23c,d): characterized by the presence of abundant microlites in the glass, mostly Feldspars and Pyroxenes, accompanied by a generally lower vesicularity than *Vesic* (around 20%) and by the presence of extensive, over-imposed growth of small Fe-Ti Oxides crystals. Small vesicles showing highly irregular perimeters also characterize this type of clasts. The overall shape of is weakly rounded even if occasional irregular shapes were also recognized.
-*Pumice fragments* (*P,* in Fig.4.23e,f): distinguished by the high vesicularity (higher than 45%) and by the very low microlite content in the glass associated to highly complex external perimeters.

-*Dense juvenile fragments* (*D,* in Fig.4.23g,h): characterized by the absence of vesicles and by a moderately crystallized groundmass. The shape of the clasts is typically sub-rounded to rounded.

Also, *Crystals* (CRY; Fig.4.23i) comprehensive of pyroxene, feldspars and Fe-Ti oxides and *Lithics* fragments (Fig. 4.23l)**,** including hydrothermally altered clasts with colors from grey to yellow and red, were found to represent minority percentages of the deposits.
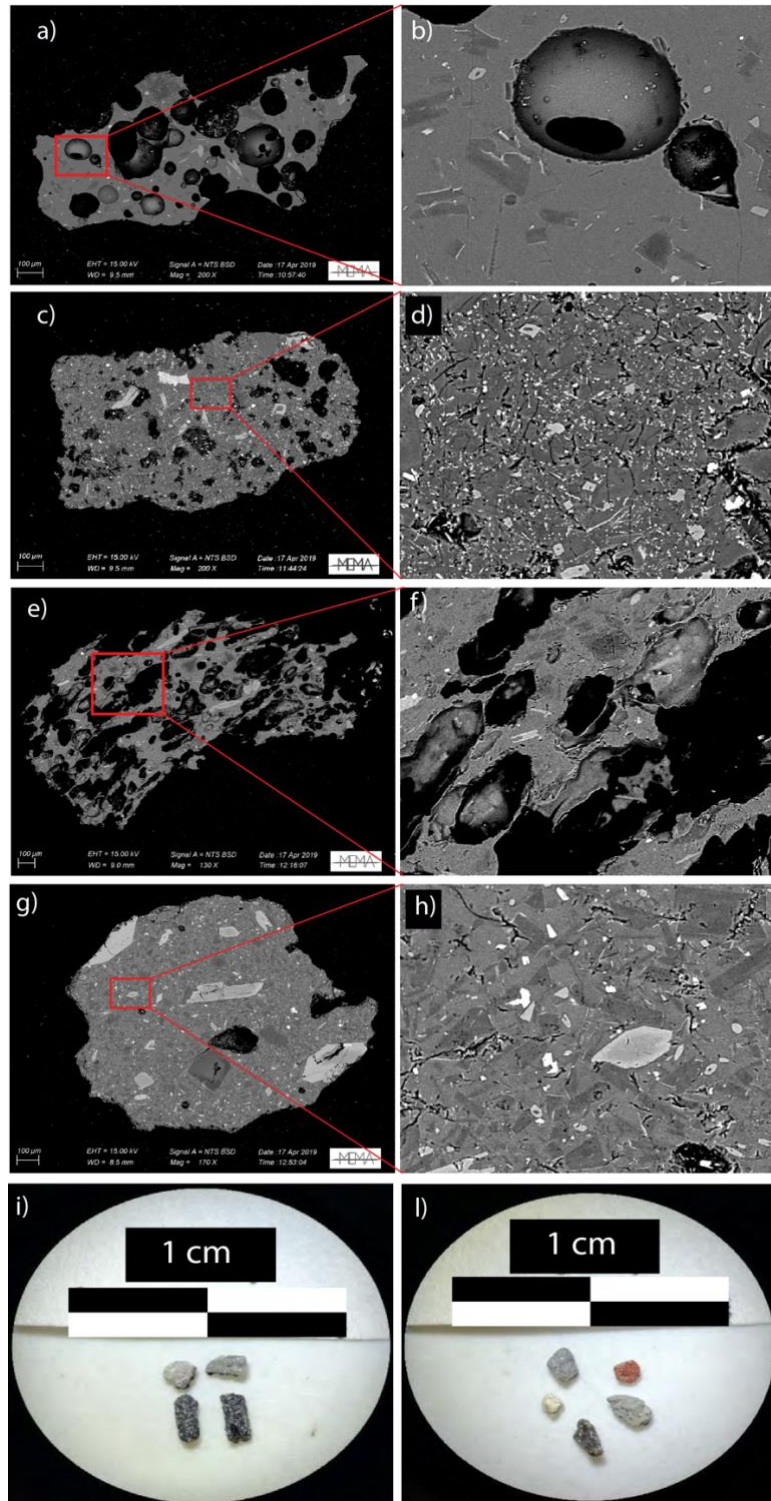
Fig. 4.23 BS-SEM images of components found to characterize fallout ash deposits. a-b) Fresh and altered Vesicular fragments; c,e) pumice fragments; d) dense clasts with evident pyroxene and feldspar micro-phenocrystals; f) altered lithic fragments with colors ranging from yellow to grey and red

4.4.2.1 GSD of the ash fallout deposits

The grain size distributions (GSD) of the fallout samples were measured and results relative to the first stratigraphic section of deposits are reported in Figure (4.24). The statistical descriptors of the GSDs relative to the proximal and the medio-proximal sequences of fallout deposits are reported in Table (4.3) together with information on deposit deconvolution provided only for the samples from the proximal section.

The shape and the general symmetry of the GSD curves is highly variable among the different samples. Ash samples range from unimodal and strongly peaked, nearly symmetric distributions (es. VUL-7), to bimodal, highly dispersed and asymmetric distributions (es. VUL-4). Also, the modal class of the different samples is distributed over a wide interval of class-sizes, ranging from 0 to 4 Phi, with the coarser deposits (mode comprised between 0-0.5 Phi; e.g. VUL-1-3-5-7) generally displaying better sorted GSDs (Tab. 4.3). The variations observed for the GSD shape are well accounted for by the variability of both the $Md(\phi)$ and the $\sigma(\phi)$ of deposits; the higher the $\sigma(\phi)$ of the curve, the higher (the finer-grained) the $Md(\phi)$ of the deposit (Tab. 4.3).

In general, all the GSDs are well described by the sum of two gaussian sub-populations: the coarse one (SP1) is typically set at around -0.3 - 1.5 Phi, close to the $Md(\phi)$ of the GSDs, and represents in most of the cases a large fraction of the sample (more than 60 % by weight). Conversely, the $Md(\phi)$ of the fine subpopulation (SP2) ranges from 3.8 and 5.1 Phi and generally represents less than 10 vol.% of the sample.

The two distinct SPs are particularly well visible in some samples (e.g. VUL-2, VUL-4, VUL-6, VUL-8, VUL-9; Fig. 4.24) in which SP2 always represents more than about 10 % of the total deposit volume (Tab. 4.3). In particular, VUL-2 clearly distinguishes from the others samples, being largely dominated by the finer fractions of the deposit with the SP2 ($Md(\phi) = 4.1$) representing more than 80 vol. % of the total sample. These samples are also characterized by highly dispersed, less sorted distributions ($\sigma(\phi)$ generally higher than 1.25).

On the other hand, VUL-1, VUL-3, VUL-5, VUL-7, VUL-10 samples (Fig. 4.24) are characterized by unimodal, strongly peaked, well sorted and poorly dispersed distributions ($\sigma(\phi)$ lower than 1.25), with most of the sample (> 93.4 vol.%) represented by the SP1, peaked around 0 Phi.

The systematic variation of the statistical descriptors (Tab. 4.3) of GSDs are reported in Fig. 4.25. in order to better highlight the marked fluctuations observed in the grain-size of the deposits throughout the eruptive sequences.

The base of the sequence is marked by a rapid increase in the values of $Md(\phi)$, culminating in sample VUL-9 with an $Md(\phi)$ value of 1.35. Then a slow and progressive decrease in the values of both $Md(\phi)$ and $\sigma(\phi)$ characterizes the ash deposits in the central part of the eruptive sequence toward the lowest $Md(\phi)$ values of -0.6 measured for the sample VUL-5. The top of the sequence is instead characterized by important fluctuations in the grain-size of the deposits, that are clearly evidenced by the oscillating values of both $Md(\phi)$ and $\sigma(\phi)$, with variations comprised respectively in the ranges of -0.1 - 3.6 Phi and 1.4 - 2.9 Phi.
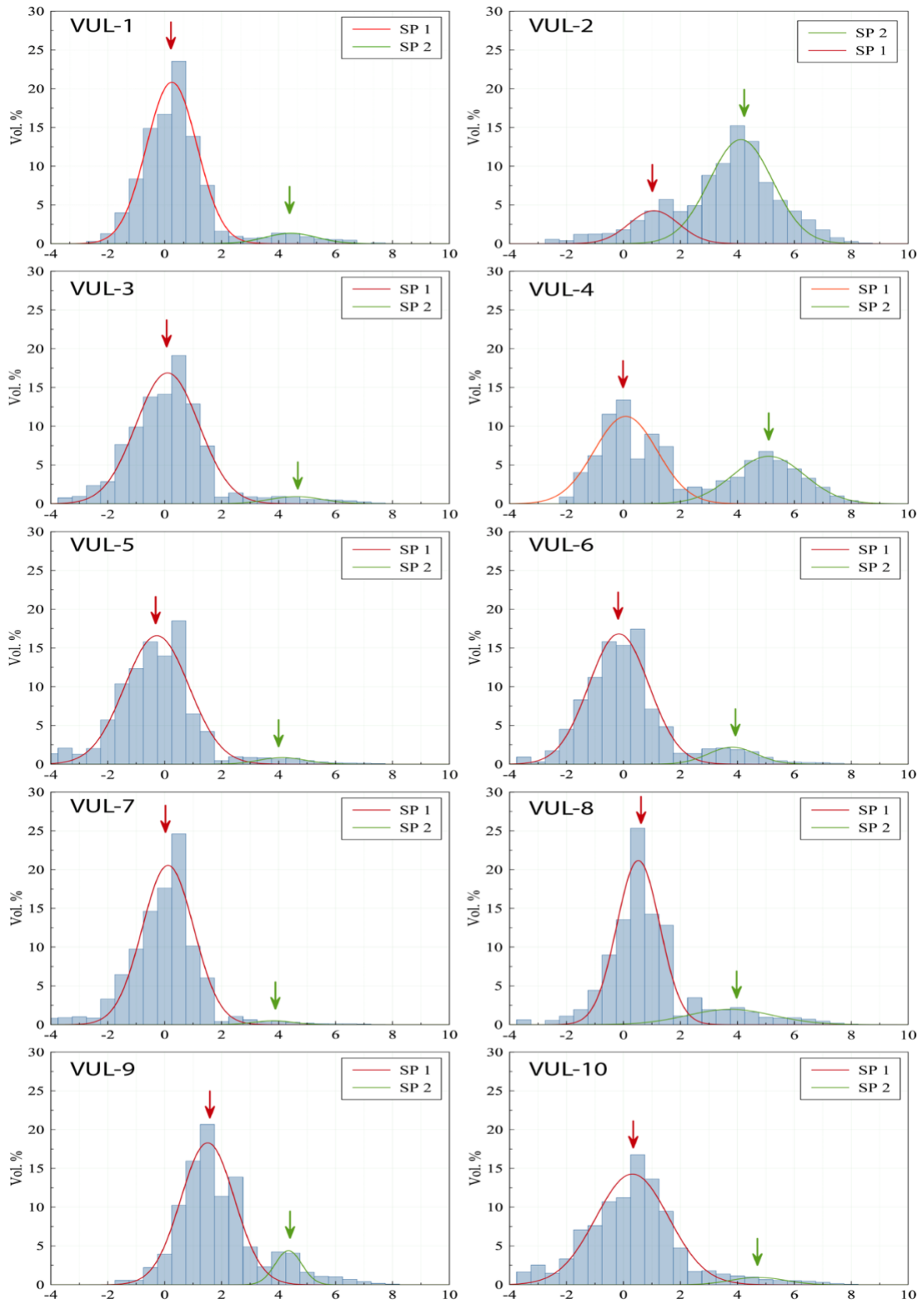
Fig. 4.24 GSDs of fallout samples collected in the proximal section with reported information on grain size deconvolution using gaussian curves (see Tab. 4.3). Red and green curves represent respectively the coarse (SP1) and the fine (SP2) sub-populations with the red and green arrows indicating the relative position of the $Md(\phi)$. The identifier code of the ash samples (specified in the upper left corner of the box), is also reported (as label) close to the stratigraphic section in Figure (4.25) in order to provide an exhaustive set of information ranging from granulometry to componentry of the analyzed ash deposits.

Proximal Section

Sample ID	Mode (Φ)	Md(Φ)	σ (Φ)	Sk	SP1 Vol.(%)	Md (Φ)	σ (Φ)	SP2 Vol.(%)	Md (Φ)	σ (Φ)
		GSDs			SP Deconvolution					
VUL-1	0.5	0.09	1.00	-0.03	93.8	0.3	0.89	6.2	4.4	0.91
VUL-2	4.0	3.57	1.90	-0.25	19.9	1.1	0.87	80.1	4.1	1.11
VUL-3	0.5	-0.08	1.21	-0.11	95.6	0.1	1.11	4.4	4.6	0.93
VUL-4	0.0	0.90	2.95	0.41	61.9	0.1	1.11	38.1	5.1	1.26
VUL-5	0.5	-0.60	1.18	-0.06	96.5	-0.3	1.13	3.5	4.1	0.81
VUL-6	0.5	-0.30	1.30	0.04	90.6	-0.2	1.06	9.4	3.8	0.84
VUL-7	0.5	-0.20	1.00	-0.2	98.2	0.1	0.91	1.8	3.8	0.68
VUL-8	0.5	0.30	1.10	0.14	84.4	0.5	0.76	15.6	3.8	1.50
VUL-9	1.5	1.35	1.25	0.24	89.4	1.5	0.94	10.6	4.3	0.47
VUL-10	0.5	0.10	1.45	-0.14	95.4	0.3	1.28	4.6	4.7	0.94

Medio-Proximal Section

Sample ID	Mode(Φ)	Md(Φ)	σ(Φ)	Sk
		GSDs		
VUL-12	0.5	0.05	1.25	0.16
VUL-13	1.5	2.55	1.78	0.15
VUL-14	0.5	-0.15	1.43	0.02
VUL-15	1.5	2.60	2.13	-0.04
VUL-16	0.5	0.10	1.78	0.13
VUL-17	1.5	2.90	2.08	-0.04
VUL-18	0.5	0.40	1.03	-0.07
VUL-19	2.5	1.95	1.33	-0.06

Tab. 4.3 Statistical descriptors calculated for the GSDs of ash samples collected at proximal (upper panel) and medio-proximal (lower panel) distances form the crater. In the upper panel are also reported the statistical information on the GSDs deconvolution for samples from the proximal section.

4.4.2.2 Componentry of the ash fallout deposits

Bar plots with the relative abundance measured for the different ash categories in the 0.5 Phi size fraction are also reported in Figure (4.25), together with the variation of the statistical descriptors. The *fresh Vesicular* and the *altered Vesicular* categories (respectively blue and red bars in Fig. 4.25) are dominant within the ash deposits with a cumulative relative abundancy generally higher than 50 %. The content of the juvenile *Dense* fragments (violet in Fig. 4.25) is stationary at around 15-20% throughout the sequence. On the contrary, the relative abundance of the *Pumice* category (Yellow bar in Fig. 4.25) shows the higher variability among the different deposits, with values ranging from 3 (VUL-5) up to 18% of VUL-6. Finally, the fraction of *Lithics* always represents about 15-20 % of the samples all along the sequence, with the only exception of VUL-10, at the beginning of the sequence, in which the amount of Lithics is higher (around 30%), and also correspond to markedly lower contents of vesiculated materials.

Straight correspondences were evidenced between the grain size and the componentry of the ash deposits (Fig. 4.25).
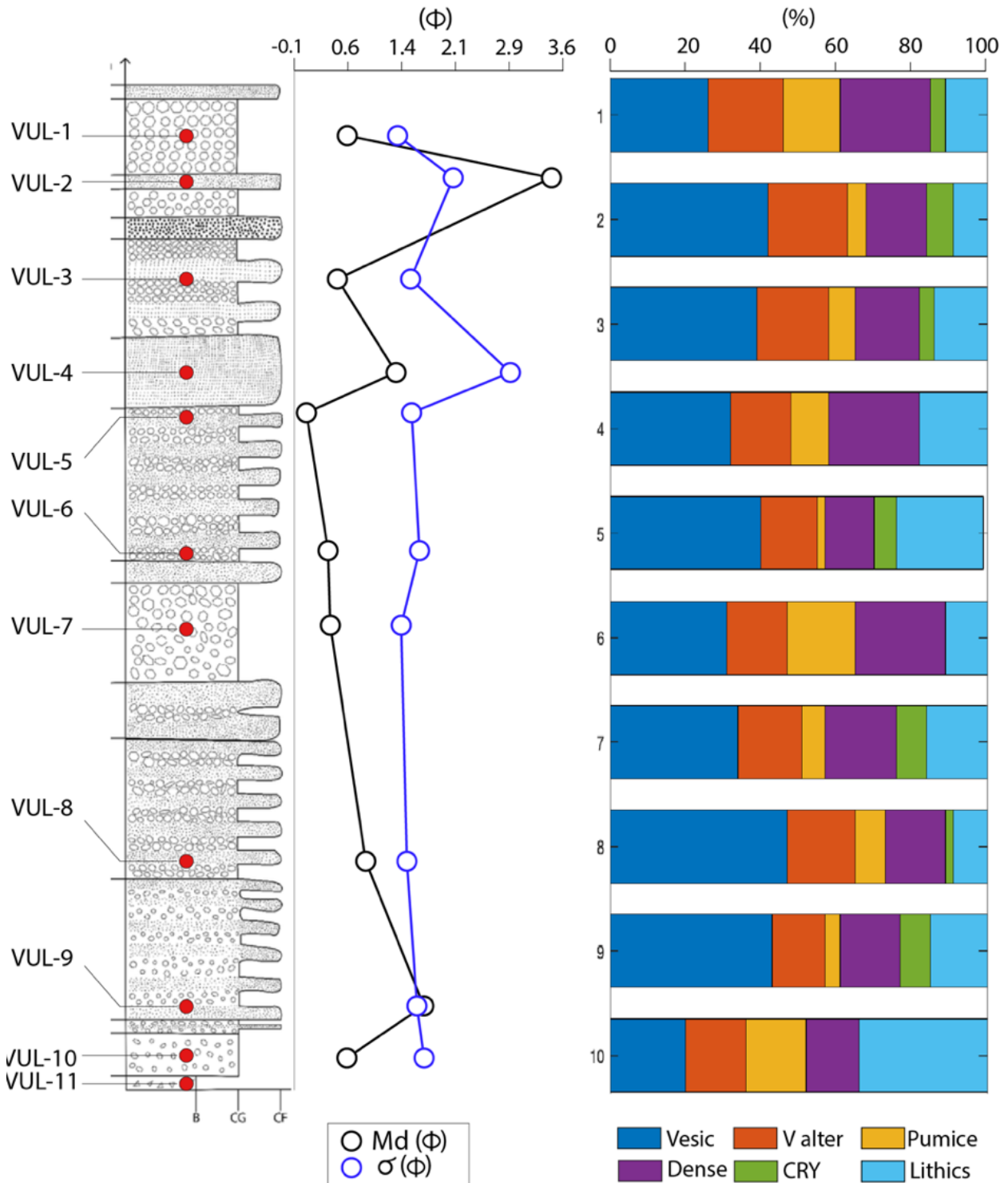
Fig. 4.25 Stratigraphical variation of grain-size and componentry of the paroxysmal ash fallout deposits. Progressive variation of the statistical descriptors associated to the ash deposits collected from the proximal stratigraphical section, are reported together with the corresponding variation in the relative componentry of ash.

The sample corresponding to the highest $Md(\phi)$ value (i.e. VUL-2) (Fig. 4.25), also presents the highest percentage of both *Fresh Vesicular* and *Pumice fragments*, that combined together represents more than

50% in volume of the deposits. Conversely, samples showing the lower values of both $Md(\phi)$ and $\sigma(\phi)$ (0.6 and 1.4 respectively) mainly present in the central region of the sequence, generally corresponds to lower amounts of fresh vesicular materials in the ash deposits.

As a result, the lower the $Md(\phi)$ and the $\sigma(\phi)$ values, the lower the total amount of vesiculated materials (i.e. Pumices plus fresh and altered Vesicular fragments) found to characterize the deposits.

4.4.2.3 Shape analysis of the ash fragments

Finally, results of the shape analysis of the ash grains are reported in Figure (4.26) for the VUL-4 sample, representative of an ash-dominated bed in the fallout sequence. The morphometry of the different size classes of the ash grains are presented to offer a direct comparison with the shape of the breccia-forming clasts.
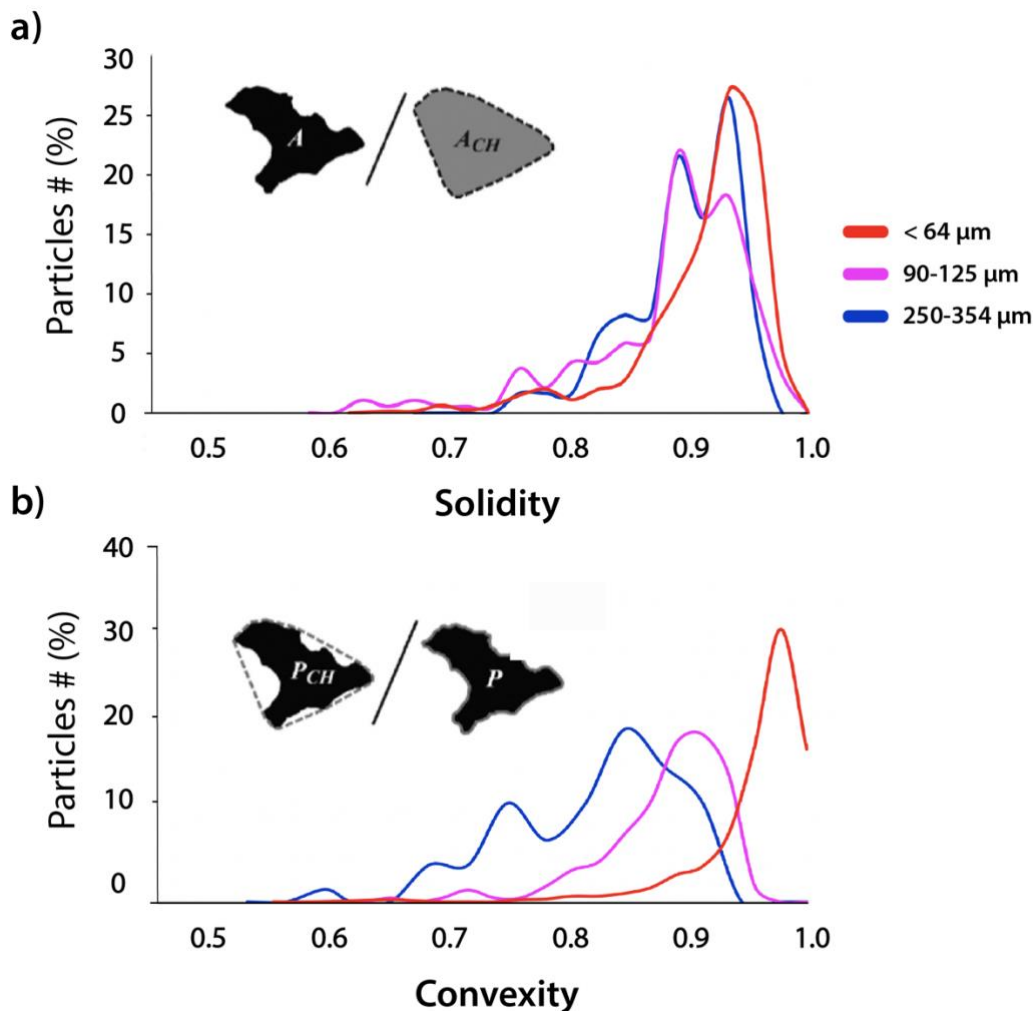
Fig. 4.26 Shape analysis of the VUL-4 ash fallout sample. Values of Solidity (a) and Convexity (b) were calculated for three intervals of particle size (see legend reported in plot (a)).

Generally, the morphology of the 2D outlines of the ash grains is quite regular, as indicated by the high Solidity values, mostly comprised between 0.85 and 1 (Fig. 4.26a). A weak decreasing trend in the

Solidity values, thus corresponding with an increasing irregularity of the overall particle morphology, is recorded for the coarser particles (Deq > 90µm), which display bimodal distributions with modes peaked around 0.89 and 0.93 (Fig. 4.26a).

On the other hand, a clear size-dependent variability in the irregularity of particles perimetral outlines was revealed based on the distribution of Convexity values (Fig. 4.26b). In particular, particles representing the finer fraction of the deposit (Deq<64 µm) are characterized by more regular perimetral outlines, as evidenced by the peaked distribution of Convexity across a narrow range of values (0-95-1). On the contrary, larger particles (90µm <Deq< 354µm) were generally associated to lower values of Convexity, mostly comprised between 0.7 and 0.9.

4.5   Discussion

Vulcanian eruptions are defined as short-lived, discrete explosions commonly associated to the production of characteristic bread-crusted bombs (e.g. Clarke et al., 2013; Clarke, 2015). However, several evidences resulting from the exhaustive field study carried out on the crater terrace of Vulcano for the deposits of the prototypal Vulcanian eruption of 1888-1890 clearly indicate that bread crust bombs of this benchmark Vulcanian activity only represent a minority (less than 10-15 %) respect to the total budget of the ballistic ejecta (Fig. 4.13). According to the interpretation provided by Wright et al., (2007) for similar products at Guagua Pichincha volcano, and considering the extremely high internal vesicularity shown by BcB samples at Vulcano, these bombs are possibly indicative of the involvement in the eruption dynamics of a deeper, more volatile rich magma still not completely degassed respect to the rest of the ejected coarse material. Moreover, according to data reporting the spatial distribution of these bombs (Fig. 4.14), BcBs are preferentially dispersed only in certain sectors of the crater rim, thus suggesting that their production has been exclusive of specific and discrete events during the eruption.

Conversely, results of the survey clearly show that the majority of the coarse ejecta (80-90 % of the total) is instead represented by dense, variably crystallized blocks (here identified as D blocks; Fig. 4.14). The lack of evident vesicularity gradients in the glass of these blocks, accompanied by a very low vesicularity and by a moderately high crystal contents, led us to interpret the D blocks as representing the upper portions of a highly degassed, extensively crystallized magma plug filling the upper portion of the conduit. Reported data from the relative abundance of bombs (Fig. 4.14) also indicated that significant amounts (around 20%) of the D blocks are characterized by the presence of extensive portions of clastic materials disposed within a complex network of internal fractures, or along portions of the external surface of the blocks (Fig. 4.10).

Interpretation of the genesis of this breccia material is not trivial. GSD analysis of the disaggregated clastic materials indicated the presence of significant amounts of fine ash within these breccia portions in the D-Br blocks (Fig. 4.15). Moreover, analyses provided on the breccia transects revealed a marked spatial and granulometric organization of the clastic materials across the breccia fractures (Fig. 4.16 - 4.17).

All the latter aspects posed important questions on the nature of these breccia portions, and on their importance in the context of non-explosive production of ash during Vulcanian eruptions. Only few studies in the volcanological literature account for the presence of similar volcanic breccia products present in lava domes (Cashman et al., 2008; Shukla et al., 2018, and references therein), although no one of these is directly focused on the specific characterization of breccia-bearing blocks associated to Vulcanian activity.

All the field evidences and textural analysis collected about the interior of breccia samples will be hereafter discussed in the light of the main available models accounting for the genesis of volcanic and tectonics-derived breccia, in order to address the principal processes involved in the formation of the D-Br blocks

4.5.1   Mechanisms of formation of the D-Br blocks

A variety of evidences deriving from the analysis of D-Br bombs can inform about the nature of the physical processes implicated in their formation. Importantly, all the data derived from the analysis of the transects across the clastic portions (Figs. 4.16 – 4.17 – 4.18) or from the thin sections of these samples (Fig. 4.12) testify for the substantial absence of highly vesicular clasts, also accompanied by a quite large textural heterogeneity of the constituent clasts (Fig. 4.11). Although the majority of the constituent clasts can be easily associated to the dense, moderately crystallized glass typical of the host rock, several types of allochthonous clasts, characterized by blocky dense to poorly vesicular textures, are also present among the components of the clastic portions (Fig. 4.15). On the other hand, this evident textrual variability is in a striking contrast respect to the large homogeneity of the dark glass that typically characterizes the internal portions of the dense blocks and the breccia wall rocks (4.11, 4.12). This aspect suggests that processes of material transport may have importantly affected the componentry and the internal architecture of the breccia samples, as a possible result of episodes of ash transport by fluidization that reasonably have characterized the circulation of pressurized volatiles inside the stiff magma column. This interpretation is also supported by the low structural compaction of the hand specimens (Fig. 4.11), as well as by the numerous voids that were recognized to frequently characterize the channels between the larger clasts in the most internal portions of the breccia samples (Fig. 4.11, 4.16). On the other hand, several other characteristics clearly suggest that most of the clastic material was possibly produced by the '*in situ*' processes of host rock shearing and comminution. For example, the SEM photomosaic of the cross-sectional breccia transect, displays a clear size grading of the clasts (Fig. 4.16a) and an important iso-orientation of the clasts along two preferential low-angle directions (~30°-40° & ~150°-160°) (Fig. 4.16b, Tab. 4.2) respect to the bounding fracture surfaces. This is the typical result of material comminution along zones of shear concentration (Sammis, et al., 1987), therefore suggesting the occurrence of organized processes of in-situ fragmentation of the granular material along a complex network of fault gouges. In the T1 transect, the latter aspects are also concurrent with a down-ward increase in the number of clasts per unit area (Fig. 4.17a), in the breccia porosity (Fig. 4.17b) and in the aspect ratio of clasts (Fig. 4.17c). Importantly, all these results consistently indicate an evident internal organization of the clastic materials that led us to exclude the

derivation of the breccia samples from a process of syn-eruptive infilling of pre-existent fractures with pre-fragmented materials within the crateric area. Conversely, all the structural and clast bedding evidences, coupled with the presence of kinematic indicators (i.e. slickenside structures and kinematic indicators revealed at the contact with brecciated surfaces) on the bounding planar surfaces of the hosting block, all concur in indicating a process of relative motion and variably intense shearing must have characterized the kinematics of the breccia wall rocks. For this reason, we suggest an active mechanical cata-clastic origin for the breccia samples.

This hypothesis of breccia formation appears also in agreement with the information on the shape of the breccia-forming clasts derived from the microscopic analysis of the transects (Fig. 4.18b) and from the shape analysis of disaggregated breccia samples (Fig. 4.21). In fact, although the generally high values of Solidity (0.75-0.95; Fig. 4.21a) indicate that a blocky and variably irregular morphology characterizes the overall shape of the breccia clasts, irrespective of the particle size, a marked size-dependent variability in the morphology of the external perimeters of the clasts is revealed by the Convexity values (Figs. 4.18 - 4.21b). Larger clasts show in fact a higher complexity and irregularity of their outlines respect to the smaller clasts (Figs. 4.18a-b, 4.21b). The reliability of the proposed interpretation is supported by the ubiquitous presence of a small-scale roughness that was shown to characterize the external outlines of the larger clasts (Fig. 4.22). All these evidences likely indicate a derivation of the smaller particle from progressive spalling and selective abrasion of the external surfaces of the coarse particles, which is possibly caused by the iterated collisions of these particles within an intermittent gas flows regime inside fractures. This aspect evidences the relevant influence that frictional mechanisms may have in the processes of breccia formation and ash production within a rigid, progressively stressed and fractured magma plug.

Essentially, two different genetic models can be invoked from the literature in order to explain the formation of similar breccia samples. The first model refers to the so-called *'tuffisitic breccia'* that are defined as veins of sintered, variably disorganized pyroclastic material resulting from the explosive fragmentation of pressurized magma intruding pre-fractured narrow conduits, or inside pre-fragmentated granular materials (Francis, 1989; Kendrick et al., 2016; Kaminski and Juapart., 1998). The second considered model is instead related to the formation of a breccia, namely a *'fault gouge'*, from the shear-induced mechanical fragmentation of competent rocks along surfaces subject to relative movement, to form bands of graded and variably compacted cata-clastic materials (e.g. Marone & Scholz, 1989; Sammis et al., 1991).

Considering that evidences of particle sintering has been only rarely observed in our breccia samples, and considering, on the other hand, the very low vesicularity of clastic material, the evident grain size grading and the iso-orientation of the clasts inside the transects, we interpret the analyzed breccia samples as more likely reflecting the process of shear-induced, mechanical fragmentation of a dense rigid material at relatively low-temperature conditions (below the temperature of glass transition), which are typical of the tectonic fault-gouges.
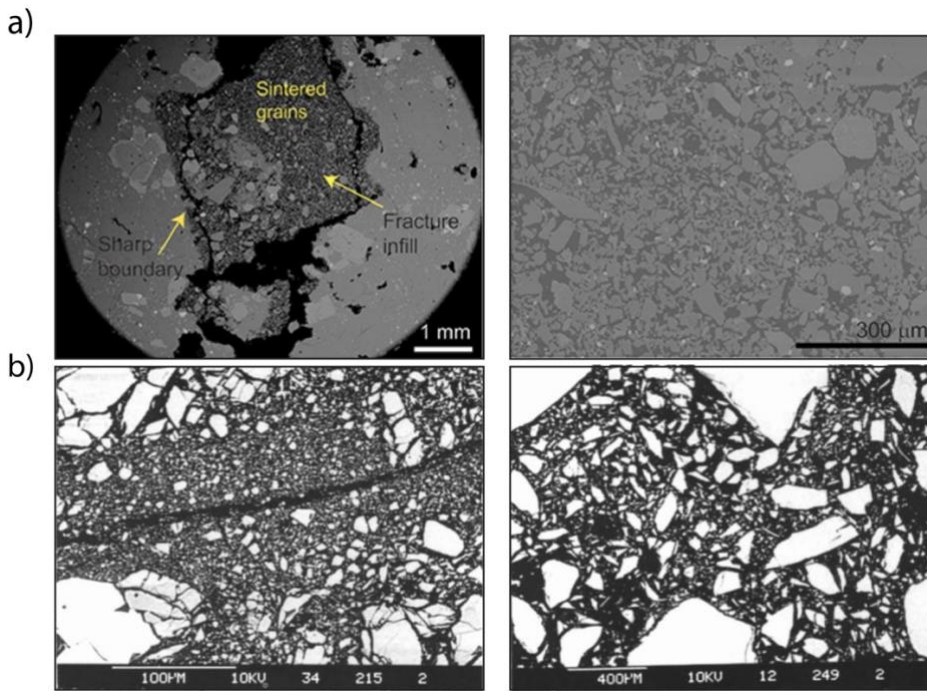
Fig. 4.27 (a) Tuffisite breccia from Colima volcano with diffused evidences of clast sintering (image modified from Kendrick et al., 2016). (b) Experimental fault-gouge breccia with evident shear bend and gradating GSDs (left), and with evident spalling of the external borders of the larger particles (right) (images modified from Marone & Scholz, 1989).

Several techniques have been proposed to describe the nature and to investigate the origin of the mechanically fragmented cataclastic breccias (Blenkinsop, 1991). One of these methods, useful to characterize their particle size distribution (PSD), considers the scale-invariant (i.e. fractal) relationship existing between the particle frequency and the size (Turcotte et al., 1986):

$$N(s) \approx S^{-D} \qquad \qquad \text{(Eq. 4.1)}$$

where $N(s)$ is the particle frequency expressed as the cumulative number of particles larger than a specific size (S), and D is the *fractal dimension* of the particle distribution.

Based on this relation, different mechanisms of rock fragmentation operating as scale-invariant processes are expected to result into different and characteristic D-values. It was theoretically demonstrated that PSDs of the cataclastic materials which produced by the pure mechanical cracking of a competent block closely follow a theoretical power-law distribution, and the corresponding slope on a log-log plot (namely, the D-value) is expected to assume values always lower than 2 (Turcotte, 1986). In particular, D-values ranging between 1 and 1.8 were measured for natural and experimental samples of cracked materials, depending on the intensity of the rock fracturing (e.g. Storti et al., 2003; Heilbronner et al., 2006). On the other hand, D-values higher than 2, and typically approaching the value of 2.58 (Sammis et al., 1987) or even higher (up to 3 or 4, Biegel et al., 1989; Marone et al., 1989), were measured for natural fault gauges characterized by a 'constrained comminution' of the larger particles. In these samples, the disproportion between the number of small and large particles was explained as the effect of not self-similar processes, like the selective frictional abrasion of the larger particles along shear bands (Sammis et al., 1987; Heilbronner et al., 2006).

Diagrams of log(grain-size) vs. log (Cumulative number of particles coarser than a given grain-size) for the studied breccia samples are easily fitted by two linear segments, thus suggesting that a combination of self-similar processes operating within different class-size intervals possibly characterized fragmentation of the breccia clasts (Fig. 4.19). A clear distinction corresponding to the break-in-slope of the log-log distributions was thus inferred for the finer and the coarser deposits fractions at around 125~300 μm. The distribution of the finer clasts (below 125-300 μm in size) was characterized by D-values equals to 1.7 and 1.9 (Fig. 4.19). These values are well in accord with a mature fractal nature of the clast distribution inside the breccia, and also stress the importance of the process of mechanical cracking in the formation of the breccia samples (Sammis et al., 1987; Heilbronner et al., 2006). On the other hand, higher D-values of 5.2 - 5.4 characterized the distribution of the coarser particles (Fig. 4.19), thus indicating a fully developed process of particle milling and constrained comminution typical of fault gouges, which is strongly in accord with the evidences of intense shearing presented by the breccia samples (i.e. kinematic indicators above planar contact surfaces, abrasion above the surface of larger particles, variably rounded constituents clasts).

Data collected along the two analyzed breccia transects show similar features of the PSD, always characterized by two linear segments and different D-values for coarse and fine-grained particles (Fig. 4.20). Importantly, these results clearly evidenced the occurrence of strong heterogeneities concerning the intensity and possibly also the nature of the clasts fragmentation processes all along the breccia transect. In fact, a progressive increase in the D values, suggesting thus a corresponding increase in the intensity of the coarser clasts comminution, was recorded across the breccia (Fig. 4.20). In particular, the recorded D-values, comprised in the range of 2-3.29, are well in accord with the value predicted by the 'constrained comminution model' of Sammis et al., (1987), and indicate a progressive increase in the fracturing of the coarser fragments toward the basal contact of the breccia. At the same time, very low D-values ranging between 0.83 and 1.45 (Fig. 4.20), always characterize the finer fraction of deposits, suggesting that a threshold in the degree of mechanical fragmentation was reached in this portion of the PSD. Considering the diffuse evidences of spalling revealed on the external rim of the larger particles, also supported by data on the shape of the larger clasts, we interpret the steeper log-log distributions for these clasts as indicating an important influence of the shear-induced frictional processes which resulted in the selective abrasion of the external rims of coarse particles to produce finer grains, particularly in the close proximity of the contact with the hosting block. The mechanism of increased fine particle production well correlates also with the GSD bimodality characterizing the loose breccia materials (Fig. 4.15).

While it is clear a derivation of the breccia material from a mechanical, shear-induced fragmentation of the dense, more rigid, fractured portions of the magma plug, several features possibly indicate the occurrence of transport processes in the fractures. Among these, we can recall the numerous void spaces in the breccia (Fig. 4.11), the common presence of fragments with textural features strikingly different from the host rock (Fig. 4.12), the generally open-framework structure (Fig. 4.16 b), the scarcity and often un-homogeneous spatial distribution of very fine-grained material (Fig. 4.16). The very low D-value of the fine-grained part of the breccia could be so related, at least partially, also to a process of

removal of the finer portion of this materials. We suggest that fine particles elutriation likely occurred during fluidization episodes associated to the accumulation and sudden release of pressurized volatiles within the three-dimensional network of breccia filled fractures that characterized the upper and degassed portions of the magma conduit of Vulcano, a typical process of Vulcanian activity. In this case, the nearly invariant size threshold (at about 100 µm) between the two linear segments describing the coarse and fine particles in the above discussed diagrams (Fig. 4.18) could represent the maximum size of the particles removed by elutriation. The fluidization process in monodisperse beds of granular materials is commonly described by the Ergun equation (Walters et al., 2006; Cocco et al., 2014) which allows to calculate a minimum fluidization velocity (U_{mf}), that is the velocity at which the beds start to get fluidized. However, fluidization of polydisperse beds of granular material is significantly different, since it can occur in a large range of upward gas velocities, comprised between U_{mf} of the finer particles and the terminal velocity (U_t) of the particles with the coarsest size (Teplinskii and Kovenskii, 2009). In this large velocity interval, conditions of partial fluidization characterized by the elutriation of part of the finer grained material, occur once the full fluidization velocity ($U_{ff;}$ Teplinskii and Kovenskii, 2009) is reached by the circulating fluids. Considering the size threshold of 100 µm inferred in our samples as the size of the coarsest particles elutriated by the circulating fluids, the velocity of full fluidization of the bed was calculated using the equation reported in Teplitskii & Kovenskii (2009) for spherical particles and polydisperse beds. The calculations assume particle density of 2500 kg$*$m^{-3}, kinematic gas viscosity of $1.5*10^{-5}$ Pa$*$s and gas density of 2 kg$*$m^{-3} (physical parameters for H_2O at 800°C and 1 Mpa). The obtained value for U_{ff} ($0.98*10^0$ m$*$s^{-1}) is in the same order of magnitude as the calculated terminal velocity for a spherical particle of 100 µm with a similar density ($0.57*10^0$ m$*$s^{-1}; calculated with the equation of Clift and Gauvin, 1971; Bagheri and Bonadonna, 2016). These considerations importantly support the possibility that fine material from the breccia-filled fracture network of the plug is efficiently elutriated by outflowing gas for particle size below 100 µm, and also give an estimation for the minimum gas velocity circulating inside the network of fractures.

As a matter of facts, the inferred model for the formation of breccia material holds important clues about the possibility of non-explosive production of fine material during pre or syn-eruptive stages of the Vulcanian activity. In the next section we will discuss the eruptive dynamics of the historical activity at the La Fossa cone of Vulcano, and we will critically discuss the role of mechanically fragmented magma inside fault-gouges in the light of the fragmentation mechanisms that were shown to control the ash-dominated activity.

4.5.2 Eruptive dynamics and mechanisms of magma fragmentation controlling the 1888-90 eruption

In the description of the 1888-90 eruption of Vulcano, Mercalli & Silvestri (1891) clearly identified two distinct eruptive periods, respectively from the 3rd to 5th of August 1888, and from the 18 of August 1888 to 22 of March 1890. The first period of activity represented the paroxysmal phase of the eruption, in which most of the fine tephra material was produced and dispersed. Conversely, the second, prolonged period was described as dominated by a pulsatory activity of variably intense, discrete

explosions, characterized by the dominant production of ballistic ejecta associated to release of variable amount of ash not able to form discrete ash beds at deposition.

The first period of activity is represented by the two succession of fallout deposits, and the collected evidences on the stratigraphy (Figs. 4.2- 4.3) and on the variability of the grain size (Fig. 4.24) inform about the occurrence of pulses of different intensity also in this first eruptive period. The different layers of the studied successions (Figs. 4.2 and 4.3) are characterized by the repeated alternation of fine and coarse ash deposits, and basically show two different groups of GSDs. The first group includes unimodal and strongly peaked GSDs, largely represented by the SP1 and described by a unique mode set at around 0.5 Phi, while the second group consists of poorly sorted GSDs with two distinct modes respectively comprised between 0-1 Phi and 3.5-5 Phi (Fig. 4.24, Tab. 4.3). In this second group the finer deposit population (SP2) represent more than 10 vol. % of the sample. The variability observed for the modal distribution of the particles, suggests a possible temporal overlap between different processes of magma fragmentation throughout the eruption, possibly related to internal gradients in the physical properties of the magma stored in the volcanic conduit.

Data from the shape analysis (Fig. 4.26a-b) reveal a high perimetral irregularity of the particles forming the ash deposits, consistent with the presence of the diffuse and moderately fine vesicularity which characterized all the different types of juvenile fragments (Fig. 4.23a, e). All these evidences are concordant in indicating an active role of volatiles exsolution in the process of magma fragmentation for the deposits of the studied stratigraphic sequence.

The variability observed in the deposits reflected in an oscillatory evolutive trends of the grain size parameters, that were mostly revealed for the final eruptive stages (Fig. 4.25). In particular, straightforward correspondences were inferred between the variability of the deposits grain size and the componentry of the ash grains, with the coarser deposits (higher $Md(\phi)$) being generally characterized by a higher amount of juvenile highly vesicular materials (Fig. 4.25).

According to the main textural characteristics for the different ash fragments, and based on the general large amounts of vesicular materials forming the tephra sequence, we suggest that a dominant process of decompression-driven fragmentation of variably vesicular magma possibly dominated the paroxysmal period of the Vulcanian activity (first period of the eruption).

The textural features of ash fragments also reflect a high variability in terms of the physical properties (i.e. vesicles and crystal contents) of fragmented magma, so informing about the pre-and syn-eruptive presence of important physical gradients in the conduit during the whole eruptive sequence. As a result, we interpret this early paroxysmal, ash-dominated phase of the 1888-90 Vulcanian activity as mostly controlled by the repeated decompression and fragmentation of a variably vesicular magma column, possibly fed by repeated arrivals of volatile-rich magma, resulting in the observed fluctuations in the intensity of the activity. The characteristic occurrence of large bombs and blocks mainly evident on the present surface of the crater terrace, without any important covering of lapilli or ash deposits, and the infrequent presence of very coarse material in the different beds of the observed stratigraphic sections strongly suggest that the second, prolonged phase of activity of the 1888-90 eruption was dominated by scattered deposition of mainly dense material. Given the large abundance (80-90%) of D blocks in the

coarse material, this likely indicates that the majority of the explosions of this second phase involved the upper, dense, completely degassed portion of a magma plug residing in the conduit. The relatively high frequency of the explosions, as clearly described by Mercalli (1891) implies however that each explosion possibly involved only a very minor part of this plug, without an important destruction of the plug itself, given the time needed to form this dense, crystal-rich magma portion. For all of these reasons, we suggest that the ash accompanying the impulsive activity of the second phase of the eruption was possibly generated following fragmentation mechanisms different from the first phase.

4.5.3 The role of mechanical, non-explosive magma fragmentation in the process of ash generation

Data on grain size and textural features of particles from the brecciated portions of the D-Br blocks clearly show a general difference with those described for the ash fallout deposits. First of all, breccias lack any evidence of vesicular fragments, which are instead dominating the ash fallouts. Furthermore, within breccia samples features like the similar lithology of most of the clasts respect to the host rock, the marked alignment of the larger grains (Figs. 4.6 and 4.16) and the evident grain size transversal grading (Figs. 4.6, 4.11 and 4.16) suggest an in-place origin for most the clast by mechanical fragmentation related to shearing. Conversely, the open-framework structure of the breccia, the spatially discontinuous presence of very fine material, and the textrual heterogeneity of the clasts (although all not vesicular) testify for the possibility of material transport in the breccia. This transport could have occurred through fluidization processes related to sudden high-pressure gas release episodes through in the complex, 3D network of breccia-bearing fractures. This mechanism of non-explosive fragmentation was possibly very efficient during the second phase of the eruption, when most of the coarse ballistic material visible on the crater terrace was ejected, mainly involving the denser, not-vesicular portion of the magma plug.

On the other hand, similarities emerged from the direct comparison between the characteristic shape and grain size of the breccia clasts with respect to ash sampled in the fallout sequence mainly recording the first, paroxysmal phase of the eruption. In fact, significant amounts of fine material (as small as 6-8 Phi) were produced in the complex fractures/faults network. In particular, the GSDs of the breccia samples (Fig. 4.15) showed high similarities with that of finer-grained fallout deposits (Fig. 4.24), both showing a variably pronounced bimodality of their size distributions. In particular, it is now clear that the finer grained sub-population (SP2) of the GSDs from ash fallouts (Tab. 4.3) and of the breccia samples (Tab. 4.1) practically span the same class-size intervals.

All the results from the shape analysis of the breccia clasts and ash grains (Figs. 4. 18 - 4.21 - 4.26) also confirm the similarities existing between the breccia-forming clasts and the ash from the vulcanian fallout. In fact, a high complexity in the external outlines of the clasts (Convexity mostly comprised between 0.7 and 0.9) mainly characterized the particles having Deq > 90~125µm both in the ash and in breccia deposits, and this size interval is also consistent with the D-slope break of the log-log distribution, as indicated by the fractal analysis. All these evidences, suggest that processes of

mechanical fragmentation of magma could have been active also during the first phase of the Vulcanian eruption, dominated by a classical process of decompression-drive magma fragmentation.

In the light of the latter considerations, we propose our results as indicative of the concurrency of both mechanical, shear-induced and classical decompression-driven mechanisms of magma fragmentation, during the higher intensity stages of the paroxysmal eruption occurred at the 1888-90 activity at La Fossa cone of Vulcano. Conversely, this process of mechanical fragmentation dominated during the lower intensity eruptive stages associated to the emission of ballistic products of the second period of the eruption.

4.6   Conclusions

A field survey was carried out across the crater rim of the La Fossa cone of Vulcano (Aeolian Island) in order to study the nature of ash and coarse ballistic products associated with the AD1888-1890 benchmark Vulcanian eruption, and to investigate the dominating processes that actively controlled its eruptive dynamics.

Results of the field work evidenced the presence of different types of ballistic products as mostly associated to the second period of the activity, in accord with the description of the eruption provided by Mercalli & Silvestri (1891). From the analysis of the ballistic spatial dispersion also emerged that bread-crusted bombs, generally considered a typical product of the Vulcanian activity, were shown to represent only a minor fraction with respect to whole bombs production. Conversely, it was shown that the ejection of bombs or blocks was generally largely dominated by dense, variably crystallized material. This dense material is largely interested by internal fracturing and by the presence of brecciated materials covering part of the external surfaces or of internal veins filled by finely comminuted materials. These breccia samples were shown to reflect the occurrence of non-explosive, shear-induced ash production operating inside a three-dimensional network of fractures with the formation of fault gouges. Evidence of material transport in these fault gouges informed about the circulation of fluids and about the selective elutriation of the finer materials from this fracture networks developed within the upper portions of the highly degassed magma conduit of Vulcano.

Mercalli & Silvestri, (1891) reported that the first eruptive stages of the Vulcanian eruption were characterized by an intense activity dominated by the important production of fine tephra material. Analysis performed on these ash samples revealed that a paroxysmal activity, mostly dominated by processes of decompression-driven fragmentation importantly characterized the early phases of the 1888-90 eruption. The fluctuations revealed in the eruptive dynamics were possibly interpreted to be controlled by the repeated involvement of high-vesicularity magma in the shallower system, thus reflecting in an important unsteadiness in the character of these early eruptive phases However, important similarities highlighted between the morpho-textural feature of the volcanic ash and the breccia-forming clasts led us to identify the possible evidence of the non-explosive production of ash inside fault gouges also during the first eruptive stage of the historical Vulcanian activity of Vulcano. Although the degassing related fragmentation proved to effectively controls the eruptive dynamic of

the paroxysmal Vulcanian activity, we interpret the ash-dominated stages of the activity as concurrently characterized by the presence of both explosive and mechanical mechanisms of magma fragmentation. We suggest here that mechanical, non-explosive fragmentation in fault gouges could represent a general mechanism of ash production during vulcanian activity characterized by low- to mid-intensity, frequent explosions not able to disrupt large portions of the plug and not involving the deeper, more volatile-rich portions of the magma conduit.

Appendix

Results of the field survey provided for the vulcanian bombs larger than 1m comprised in the North sector of the crateric area.

ID	L	I	S	Type	GPS position	
1	106	58	27	D-Br	497091 mE	4250909 mN
2	102	78	53	BCB – Tn Lv	497116 mE	4250899 mN
3	100	52	-	BCB – Tn Lv	497116 mE	4250899 mN
4	103	73	78	D	497119 mE	4250918 mN
5	121	58	39	D-Br	497133 mE	4250909 mN
6	150	150	66	D-Br	497103 mE	4250882 mN
7	111	111	-	D-Br	497091 mE	4250868 mN
8	200	100	120	D-Br	497090 mE	4250891 mN
9	120	88	67	D	497084 mE	4250892 mN
10	196	157	78	D-Br	497084 mE	4250868 mN
11	105	69	-	D-Br	497093 mE	4250890 mN
12	194	91	80	BCB - Tn Lv	497079 mE	4250877 mN
13	215	121	100	D	497061 mE	4250905 mN
14	101	67	52	D-Br	497064 mE	4250871 mN
15	116	86	68	D	497083 mE	4250861 mN
16	136	68	44	D	497060 mE	4250865 mN
17	103	78	23	D-Br	497066 mE	4250869 mN
18	150	100	65	D-Br	497064 mE	4250858 mN
19	106	73	33	D	497063 mE	4250861 mN
20	105	76	52	D-Br	497060 mE	4250851 mN
21	130	103	69	D-Br	497065 mE	4250857 mN
22	123	96	72	D	497057 mE	4250852 mN
23	138	67	59	D	497060 mE	4250858 mN
24	100	87	60	D-Br	497063 mE	4250869 mN
25	113	88	-	D	497033 mE	4250864 mN
26	121	76	-	D-Br	497033 mE	4250879 mN
27	105	80	68	D	497033 mE	4250879 mN
28	100	85	-	BCB - Tn Hv	497036 mE	4250887 mN
29	147	125	67	D con inclusi	497012 mE	4250878 mN
30	138	100	-	D-Br	497023 mE	4250886 mN
31	170	87	66	D-Br	497031 mE	4250889 mN
32	226	210	75	D	497028 mE	4250900 mN
33	152	90	-	D-Br	497027 mE	4250905 mN
34	190	130	56	D-Br	497029 mE	4250902 mN
35	113	82	57	D-Br	497031 mE	4250898 mN
36	161	143	-	D-Br	497017 mE	4250904 mN
37	185	130	119	BCB - Tn Lv	497029 mE	4250903 mN
38	147	84	76	BCB - Tn Lv	497022 mE	4250896 mN
39	116	109	-	D	497024 mE	4250894 mN
40	201	112	83	BCB - Tk	496999 mE	4250900 mN
41	190	74	-	D	497011 mE	4250919 mN
42	153	118	102	D-Br	497002 mE	4250905 mN
43	218	192	-	BCB - Tn Lv	497014 mE	4250927 mN
44	147	135	126	BCB - Tn	497068 mE	4250890 mN
45	227	112	-	D	497072 mE	4250880 mN
46	254	159	156	D	496898 mE	4250811 mN
47	133	68	-	D	496891 mE	4250807 mN
48	210	97	60	D	496892 mE	4250804 mN

	L	I	S	Type		
49	160	116	64	D-Br	496896 mE	4250796 mN
50	106	102	100	D-Br	496923 mE	4250835 mN
51	148	119	70	D-Br	4969902 mE	4250805 mN
52	253	163	114	D-Br	496899 mE	4250816 mN
53	152	95	72	D-Br	496896 mE	4250816 mN
54	114	113	79	D	496892 mE	4250807 mN
55	143	116	70	D-Br	496894 mE	4250812 mN
56	146	80	30	D	496900 mE	4250817 mN
57	147	116	80	BCB - Tk	496897 mE	4250818 mN
58	166	121	-	D	496898 mE	4250826 mN
59	300	152	150	D	496905 mE	4250833 mN
60	165	123	-	BCB - Tn Lv	496912 mE	4250825 mN
61	194	190	87	D-Br	496910 mE	4250830 mN
62	179	103	70	D	496909 mE	4250834 mN
63	152	73	70	BCB - Tn Lv	496904 mE	4250836 mN
64	203	100	48	D-Br	496907 mE	4250831 mN
65	173	75	59	D	496908 mE	4250829 mN
66	139	103	54	D-Br	496895 mE	4250832 mN
67	195	164	107	BCB - Tk	496893 mE	4250835 mN
68	106	92	43	D-Br	496894 mE	4250837 mN
69	160	60	57	D-Br	496887 mE	4250839 mN
70	136	46	36	D	496890 mE	4250839 mN
71	133	122	93	BCB - Tn	496889 mE	4250833 mN
72	117	96	-	BCB - Tn	496881 mE	4250843 mN
73	244	153	117	D	496895 mE	4250841 mN
74	183	102	-	D	496898 mE	4250852 mN
75	152	45	58	BCB - Tn Lv	496903 mE	4250859 mN
76	144	58	69	D	496904 mE	4250856 mN

Tab. A.1 Example of the field survey provided for vulcanian bombs. The three dimensions (**L** Largest, **I** Intermediate, **S** Shortest) of the bombs are reported together with their type and GPS position. Several bombs do not report the third measurement (S) since they were partially buried.

Chapter 5

Mechanisms of ash production and recycling during low-energy, mid-intensity eruptions: the March 2016 low-intensity activity of Copahue volcano (Argentina)

5.1 Introduction

Volcanic ash is the result of the extensive magma fragmentation and it depends on the combination of magma properties (rheology, vesicularity and permeability), modalities of volatiles degassing, gas overpressure and on the possible intervention of external fluids during magma ascent. Combination of monitoring geophysical data on the activity with the main features of the erupted ash can give important clues about the possible mechanisms of ash production and dispersal, as well as about the energy of the activity. As a general rule, the higher the overpressure in the magma, the higher should be the exit velocity of the ejected material and the acoustic pressure related to this process. This process is also responsible for the generation of infrasonic waves directly linked to the injection of the gas-particle mixture in the atmosphere. During violent eruptions, large quantities of volcanic ash are produced and injected in the atmosphere as a result of the high efficiency of the fragmentation process. Hereafter, results of the morpho-textural analysis of ash produced during the ash-dominated, low energy activity of Copahue volcano (Argentina) in 2016 are presented and discussed, also in the light of the interpreted signals from the infrasound-based monitoring of the activity conducted by the Laboratory of Experimental Geophysics (LGS) at the University of Florence.

5.2 The Copahue Volcano

Copahue volcano, one of the most active volcanoes in Argentina, is characterized by periods of constant emissions of gas and ash, which alternate to phreatic explosions with large release into the atmosphere of water vapor clouds (Caselli et al 2016a). This low- to mid-intensity eruptive activity (generally classified as VEI 2) poses serious risks to the health and daily life of local population for the large quantity of ash dispersed in the atmosphere (Caselli et al 2016b, Petrinovic et al 2014).

Nevertheless, the record of this volcanic activity is very poor in terms of geophysical data, as well as the knowledge of the explosive dynamics responsible for the large emission of ash. We present here an in-depth analysis of the ash products released during a week of activity in February 2016 coupled with the results of a large database of infrasound recordings collected between March and April 2016 and representative of a phase of intense ash-emission at Copahue volcano lasting at least from January 2016 (Tab. 5.1). This eruption was in fact recorded with an infrasonic array and compared with both visible camera and direct observations of the explosive activity, which allowed us to relate the infrasonic record to the eruptive style, the ash characteristics and the outflux.

The presented infrasonic data were recorded by the first permanent array installed in the southern Andes and elaborated by the LGS group, that is greatly acknowledged.

5.3   Geological setting and volcanological activity framework

The Copahue-Caviahue Volcano Complex (CCVC) is part of the Caviahue-Agrio caldera (Bonali et al., 2016). It is located in the Southern Andean Volcanic Zone (37°- 41,5°) and straddles the border between Argentina and Chile (Fig. 5.1), approximately 30 km east of the NS to NNE-trending volcanic arc (Melnick et al. 2006, Folguera et al. 2016).
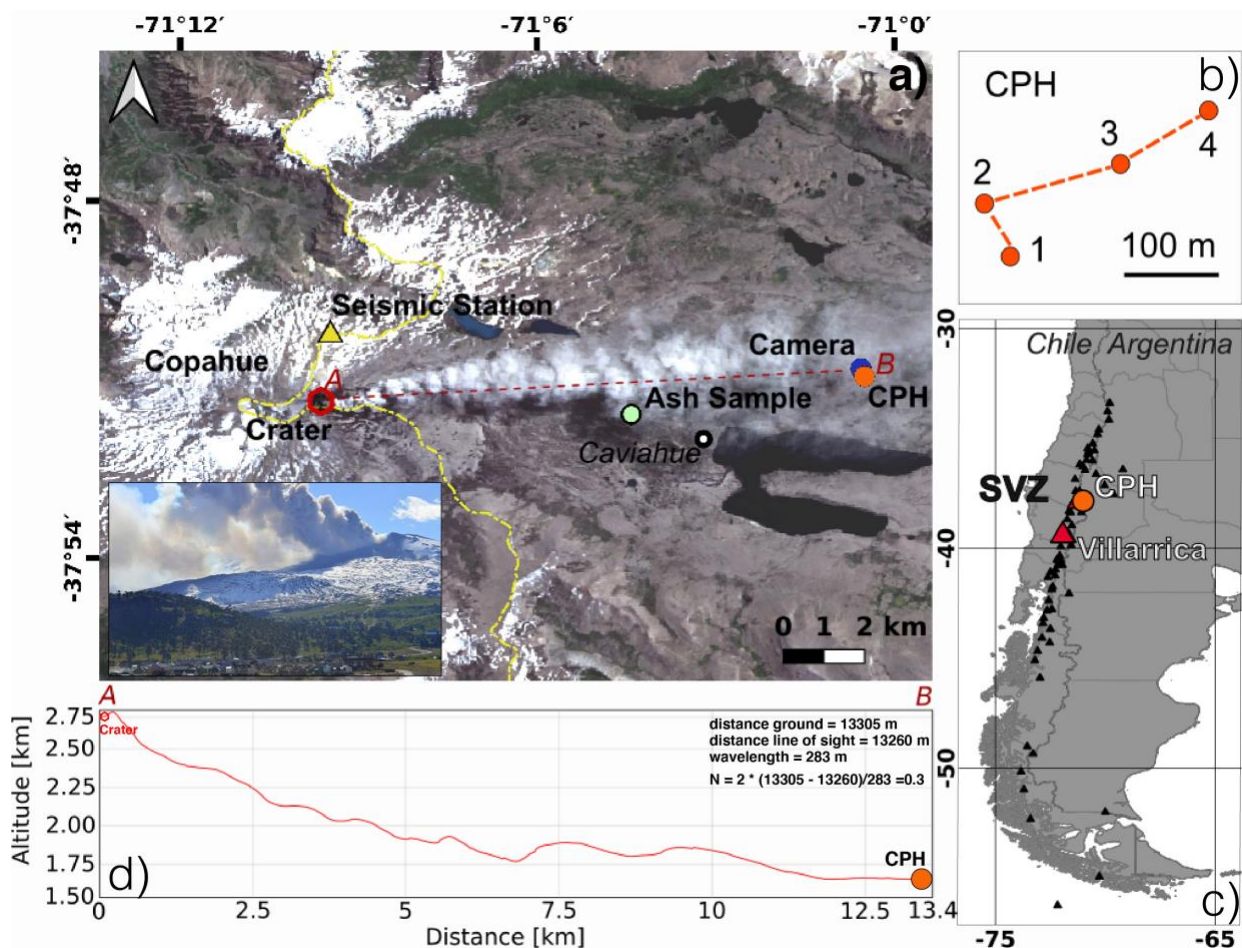
Fig. 5.1 Network of the monitoring sensors at Copahue volcano: a) Map with the positions of the infrasonic array (CPH, orange circle), video-camera (blue circle), ash sample (green circle) and seismic station (yellow triangle) relative to the Copahue volcano, where is evident the large ash-rich plume emitted during

the 2016 eruption is dispersed by the eastward winds During this type of activity, the ash plume is bent eastward by the wind immediately above the crater, revealing a weak gas thrust phase driven by a slow ascent rate (inset to the left) b) The geometry of CPH infrasonic array . c) Map of South America with the position of Copahue Volcano (orange circle) and Villarica Volcano (red triangle). d) Topographic section between the Copahue vent and CPH infrasonic array with the formula used to evaluate the Fresnel number N.

Copahue volcano is an active andesitic to basaltic-andesite stratovolcano, nested on the western rim of the caldera (Linares et al. 1999). It is elongated in the NE direction and has an elevation of 2997 m a.s.l. On its summit, nine craters are aligned in the N60°E direction (Naranjo and Polanco, 2004), whereof only the easternmost one is currently active. This active crater has a nearly circular shape of 300 m by 250 m large, a depth of 90 m and it contains a nearly permanent, hot hyper-acidic crater lake, active at least from 1937 (Caselli et al., 2016a; Agusto et al., 2017). At least 13 eruptions occurred during the last 260 years. Despite the scarce detailed historical information, reports and data available suggest low magnitude phreatic and phreato-magmatic eruptive styles over the last two centuries (Martini et al., 1997; Naranjo and Polanco, 2004). The recent eruptive events of 2000 and 2012 have a prevalent strombolian style, with a phreato-magmatic opening phase followed by the occurrence of repeated magmatic pulses (Caselli et al. 2016a). In July 2012, a new eruptive cycle began, with the occurrence of a phreato-magmatic eruption which ejected material from the volcanic conduit at the bottom of the crater lake, accompanied by juvenile material (Caselli et al. 2016a; Daga et al. 2017). In December 2012 the main phase of the phreatic/phreatomagmatic eruption culminated after a few hours in a magmatic phase. The crater lake drained during the eruption, and activity changed to small explosions and fumarolic emissions. Reactivation of the explosive activity in 2012 led to the formation of permanent fumaroles, the partial evaporation of water and the expulsion of water in the form of lahars (Caselli et al. 2016). A small crater lake formed and it was present until November 2015 (GVP, 2016; Agusto et al., 2017). Until early 2017, the volcano had a constant seismic activity associated with emission of gas and ash, with occasional explosions leading to visible nocturnal incandescence (Caselli et al 2017). This activity represents a serious risk to the population living around the volcano both in Argentina and in the Chile. In the 2012 eruption the volcanic plume drifted up to 350 km away from the source (Caselli et al., 2016b), demonstrating that even during these low intensity events the large amount of ash dispersed in the atmosphere can represent a major problem also for the civil aviation (Bonadonna et al., 2012) (Fig. 5.1).

5.3.1 The February-March 2016 Activity of Copahue

The vent area of Copahue was characterized from the end of November 2015 by the presence of a small, intra-crateric cone, and by a nearly emptied crater lake (GVP, 2016; Agusto et al., 2017). The cone was still present in the first weeks of February, together with a small lake inside the main crater. The period February – March 2016 was characterized by a continuous and quite constant level of activity (Tab. 5.1), which continued the trend of activity started since December 2015-January 2016 (Caselli et al 2017). Seismic tremor was higher than normal, reaching the highest amplitude since 2012 (Fig. 5.2) on March 3th, although maintaining at an intermediate level (reduced displacement RD

variable between 3-5 cm^2, Tab. 5.1). During the entire period a low-level ash plume (maximum height around 1000 m above the vent), generally traceable by satellite up to distances of 50-100 km in a SE-ESE direction, was continuously detected. The height of the plume was generally low and incandescence in the vent area was visible at night from a videocamera located at 13 km from the vent (Fig.5.1a). Minor peaks in the activity possibly occurred in concomitance with peaks in SO$_2$ flux (25 February, 23 March) and with the formation of slightly higher ash plumes, however always not higher than 1500 m. (Tab. 5.1).

Month:	JANUARY 2016		FEBRUARY 2016		MARCH 2016		APRIL 2016
Days	1-15	16-31	1-15	16-29	1-15	16-31	1-15
VT	68	28	15	9	7	12	33
LP/VLP	51	41	13	17	16	42	29
Tremor	Constant, intermediate level (RD < 1.8 cm^2)	Constant, intermediate level(RD < 4 cm^2)	Constant, intermediate level(RD < 4 cm^2)	Constant, intermediate level(RD < 5 cm^2)	Constant, intermediate level(RD < 5 cm^2)	Constant, intermediate level(RD < 3 cm^2)	Constant, intermediate level(RD < 3 cm^2)
Mean SO$_2$ (t/day)	691±184	724±91	753±199	1125±176	693±128	853±189	921±37
Max SO$_2$ (t/day)	2573 *January 12*	1380 *January 16*	2735 *February 13*	4264 *February 25*	2079 *March 8*	2830 *March 23*	2323 *April 4*
Activity	Continuous ash emission, grey plume, incandescence	Continuous ash emission, grey plume, incandescence	Continuous ash emission, grey plume, incandescence	Continuous ash emission, grey plume, incandescence	Continuous ash emission, grey plume, incandesce.	Continuous ash emission, grey plume, incandesc.	Continuous ash emission, grey plume, incandesc.
Max plume height *(above the vent)*	850 m *January 13*	-	-	1250 m	-	1500 m *March 22*	-

Tab. 5.1 Summary of the geophysical and observation data related to the January-April 2016 activity at Copahue volcano. Data from "Reporte de Actividad Volcánica (RAV), Regiòn del Biobío", OVDAS (http://sitiohistorico.sernageomin.cl/lista-region-8.php).

A more intense, explosive phase of the eruption began on March 21, 2016. During March up to the beginning of April, a videocamera showed a constant emission of ash and gases, as well as night incandescence occurring in the crater of Copahue volcano. This activity was directly related to a small increase of tremor recorded by the seismic stations (Fig. 5.2). From March 23 to 26 the plume reached a maximum height of about 1500 m above the vent (GVP, 2016, Tab. 5.1).
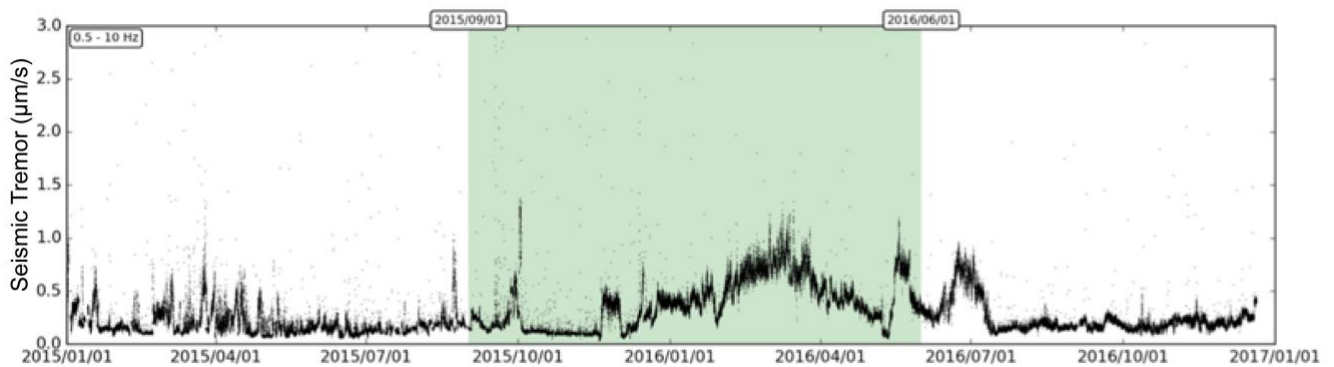
Fig. 5.2 Seismic tremor at Copahue volcano from Jan. 2015 to Jan. 2017. The seismic tremor was calculated in a station located at 2.1 km from the crater in the frequency band 0.5 – 10 Hz. Tremor amplitude shows a gradual but clear increase from the end of 2015 and reaches the maximum amplitude during March 2016

(green area). Courtesy of LGS, University of Florence.

Visual observations on March 25, 2016 reported the emission of ash and gases, intermittently with clouds of water vapor and the ejection of volcanic bombs coming from the cinder cone inside the crater. A small lake inside the crater and bombs ejected as far as 240 m from the vent were also observed. At the time, the intra-crateric cone was 150 m large at the base, 30 m high and the active crater was ~5 m wide (Caselli et al., 2017).

The activity of the entire period was interpreted by OVDAS as the result of an interaction of pockets of magma at shallow depth with the surface hydrothermal system.

5.4   Data from infrasound monitoring

On February 2014 the first permanent infrasound array in the South Andes for monitoring volcano activity was deployed near Copahue volcano by LGS personal (University of Florence).

Results obtained from the infrasound monitoring and main interpretation of geophysical data are reported here thanks to the collaborative work with M. Ripepe and the colleagues of LGS.

During the February – March 2016 period, infrasonic activity was generally low and in rare cases the array located coherent signal associated to explosive events and ash emission. On March 21 2016 at 6:09 UTC, array processing showed coherent small acoustic signals with amplitude between 0.05 and 0.18 Pa propagating with a back-azimuth of ~266°N, coinciding with the direction of the Copahue active crater (Fig. 5.3).
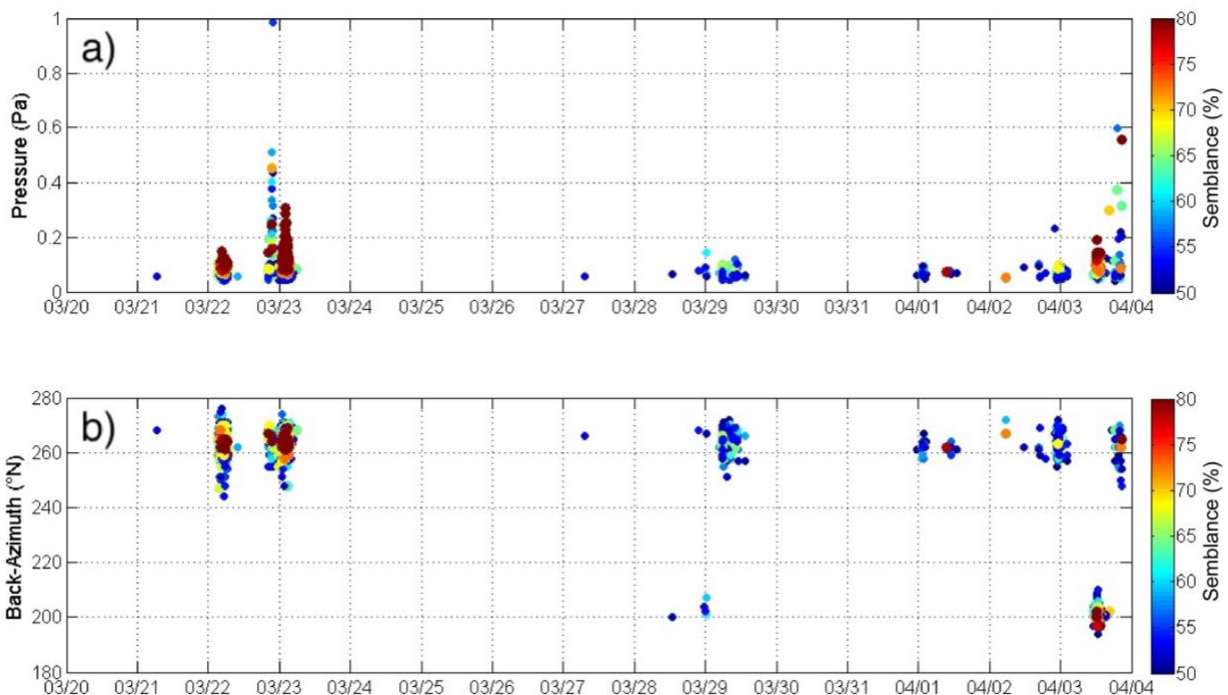
Fig. 5.3. Acoustic pressure and Back-Azimuth during 20 March - 4 April 2016 at Copahue volcano. a) Acoustic pressure; b) backazimuth detected by the array with semblance >50%. Explosive activity at Copahue volcano is identified by the signals coming from ~260°N with amplitude seldom above 0.3 Pa.

Detections with backazimuth around 200°N on March 29 and April 3, are instead relative to the explosive activity at Villarrica volcano (Chile). Courtesy of LGS, University of Florence.

These coherent acoustic signals were characterized by impulsive transients with a duration of a few seconds and a frequency of 1.12 Hz, typical of moderate explosive activity, or over-pressurized magma degassing. Infrasound detected by the array increased drastically both in amplitude and in the number of events (Fig. 5.3) at 03:13 UTC on March 22, 2016 and became almost continuous in the course of the day, reaching maximum amplitudes of ~1.0 Pa on March 23 (Fig. 5.3). This phase coincided with the maximum emission of ash, generating a plume that reached an elevation of 1500 m above the volcano (4350 m a.s.l.). The ash plume was visible on satellite imagery and at 12:10 UTC on 23 March 2016 it was traveling eastward at a distance of 37 km from the volcano (Fig. 5.1). This activity induced the Volcanic Ash Advisory Center (VAAC) of Buenos Aires to issue a notification of volcanic ash dispersion for Copahue volcano. The same VAAC reported ash drifting to a general distance of 150 km (GVP, 2016).

The eruption was also detected by the local video-camera, indicating that this moderate emission of ash continued also in the following days and it was associated to sporadic strong puffs of steam. Infrasonic activity with back-azimuth coherent with the direction of the active crater (~266°N) was also detected after March 23 but was characterized only by few events randomly distributed and with a very low pressure (rarely exceeding 0.12 Pa).

Infrasound during this phase is most probably associated to a weak strombolian phase evidenced by the incandescent volcanic bombs observed during the nights. Only after April 1, infrasonic activity increased again revealing a possible second large ash emission.

5.5 Infrasound measurements during ash eruption

The acoustic signals recorded during explosive activity at Copahue (characterized by a short impulse with mean duration of 1.5 s and a peak frequency of 1.12 Hz) are similar to explosive activity observed at other volcanoes (Johnson 2003; Johnson and Ripepe, 2011; Fee and Matoza, 2013; Ripepe and Marchetti, 2018). Recorded pressure amplitude (P) is generally around 0.2 Pa, which reduced at r_o=1 km from the source is equivalent to 2.6 Pa ($P_r = P\frac{r}{r_o}$), where r is the distance (13 km) between the array and the crater.

When compared to explosive activity at other volcanoes, infrasound at Copahue shows a comparable frequency range but smaller amplitudes (Johnson 2003, Johnson and Ripepe 2011, Fee and Matoza 2013, Ripepe and Marchetti, 2018). Strombolian activity at Stromboli volcano, for example, generates infrasonic transients with frequency content between 2-4 Hz and amplitudes (P) between 20-50 Pa at r_o~0.5 km from the source (e.g. Lacanna and Ripepe, 2013; Delle Donne et al 2016) which converts to a reduced pressure (P_r) of 10-25 Pa at 1 km. Interestingly, the low amplitude transient acoustic signals of the initial phase of the 2016 eruption at Copahue become more frequent and finally merge in a quasi-monochromatic continuous oscillation while approaching the more violent eruptive phase on March 22 (Fig. 5.4).
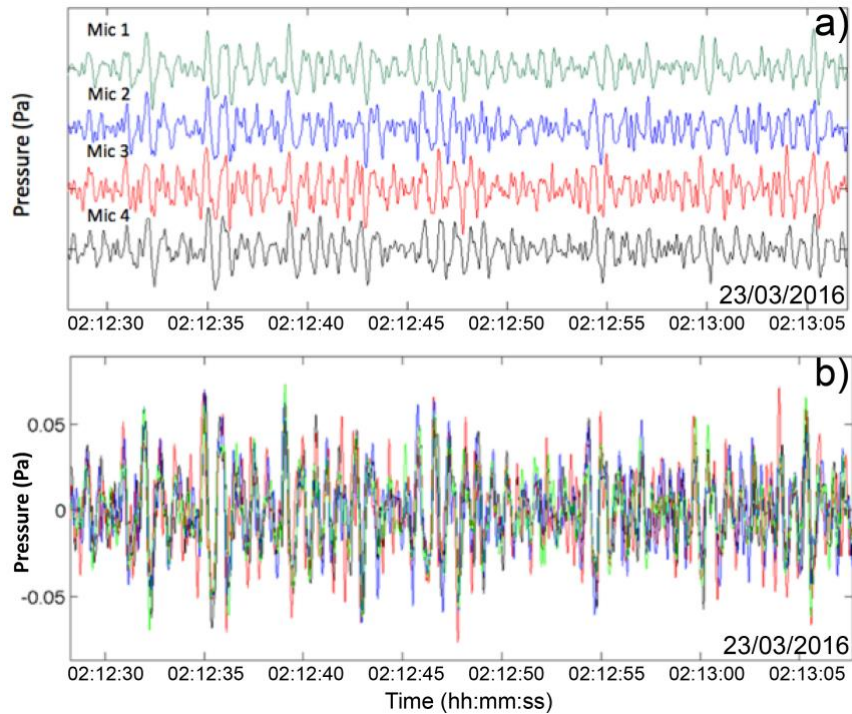
Fig. 5.4 a) Example of infrasonic signals recorded at 4 sensors of the array during the most intense ash eruption phase. b) Time shifted infrasound signals related to the Copahue activity shows a continuous quasi-monochromatic oscillation at 1.2 Hz coherent across the array. Courtesy of LGS, University of Florence.

Despite the different magma composition, similar however higher amplitude infrasonic behavior has been observed also during the more energetic lava fountain at Etna volcano (Italy). At Etna, explosive eruptions are in fact preceded by violent strombolian activity associated to a rapid sequence (every 2 seconds) of large infrasonic transients (P_r = 20-30 Pa at 1km) which merge to continuous acoustic pressure oscillation of 0.7 Hz during sustained eruptive column (Ulivieri et al., 2013).

5.6 Characteristics of the released ash fragments

In order to discuss the processes controlling ash production and emission during the constant activity of February – April 2016 at Copahue, ash was collected while falling (in dedicated plastic containers) during some days of this prolonged eruptive period of continuous ash emission. Details about ash samples collection are reported in Table 5.2. Unfortunately, we could not directly collect ash falling during the same days of the studied infrasound record. However, the analyzed samples are representative of a 5-days eruptive sequence, from February 19 to 23, 2016, during which activity was very similar to that observed in March and recorded by the infrasound array (GVP, 2016; Tab. 5.1).

Sample Id	Dist. from the vent	Type	Day	Time of collection (UTC -03.00)	Ash Plume observation	Sampling site (UTM)
CC2	~9 km	Total Fallout	Febr-19-2016	16:41-19:28	Low level ash plume	317584 m E 5807715 m S
CC2-3	~9 km	Total Fallout	Febr-20-2016	11:11-19:15	Low level ash plume	ibid
CC2-5	~9 km	Total Fallout	Febr-21-2016	10:03-19:00	Low level ash plume	ibid
CC2-7	~9 km	Total Fallout	Febr-22-2016	13:20-20:38	Low level ash plume	ibid
CC2-8	~9 km	Total Fallout	Febr-23-2016	20:40-19:56	Low level ash plume	ibid

Tab. 5.2 Information about the collection of ash samples and visual observations of the emitted ash plume. Site of ash collection is also reported in Figure 5.1a.

Ash samples were sieved and processed in order to derive the GSDs of the fallout deposits. Using the static particle analyzer (Morphologi G3s), a large number of particles ($1000 < \# < 9000$) belonging to the most representative dimensional classes (64-125 and 125-250 microns) were measured for each sample, and the morphometry of the external outline of each ash grain was characterized calculating three indicative shape parameters (Solidity, Convexity and Circularity). Then, the modal class of the grain size (125-250 μm) was selected for determining ash componentry of each ash sample. External and internal surfaces of a picked selection of ash grains, representative of the different classes, were analyzed with the SEM and the main textural features derived through image analysis (a more accurate description of the analytical procedures employed for the study of the ash is reported in Chapter 2.

Ash samples have a well sorted, nearly symmetric, leptokurtic grain size distribution with a mode between 2.5 and 3.5 phi and a very low content of fine ash (less than 10wt% > 4 phi; Fig. 5.5). Componentry of the ash (horizontal bar charts in Fig. 5.5) is constant throughout all the sampled activity, and distributed in similar proportions between 3 different components: vitric shards and micropumices (VS); black, dense to vesicular, glass-bearing clasts (BV); loose crystals (CRY). Also, sparse, hydrothermally altered lithic fragments (HYD in Fig. 5.5), from yellow to pinkish in color, are occasionally present, however with very low relative abundances (never exceeding 1%).
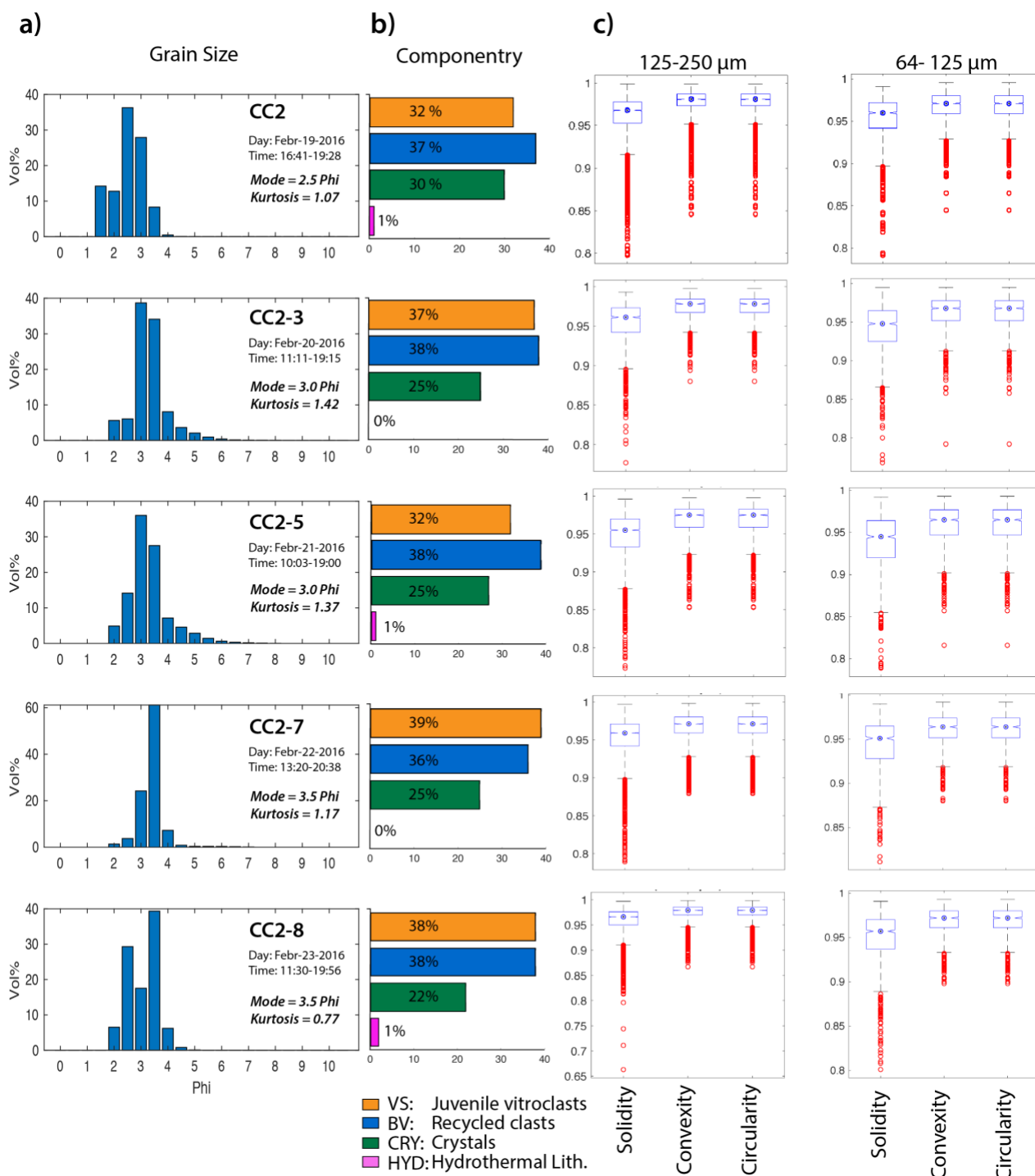
Fig. 5.5 Grain size, componentry (500-250 μm fraction) and shape parameters for the studied ash samples. (*Solidity* = Particle Area / Convex Hull Area; *Convexity* = Convex Hull Perimeter / Particle Perimeter; *Circularity* = 4π Particle Area / (Particle Perimeter)^2; further details on ash analysis, are given in Supplementary Materials). Red circles in the box plots represent data outliers that stands outside the 25th and 75th percentiles of the distribution.

VS are here considered as the dominant juvenile material; they are optically transparent and brownish in color (Fig. 5.6), and are characterized by fresh, nearly microlite-free glass. Vesicularity is intermediate (35-50 Vol%), with mainly isolated, unconnected, small (50 -200 microns in diameter) rounded vesicles. External surface of the particles is rugged due to the frequent intersection with vesicles, producing very sharp edges which characterize the external surface.

Clear intersections with larger vesicles are also visible as smooth concave external surfaces of the clasts (mean diameter around 400-500 microns) (Fig. 5.6). Fluidal surface textures, typical of the activity related to the initial, higher intensity phase of the 2012 eruption (Caselli et al., 2016a; Daga et al., 2017) have not been recognized in all the analyzed samples (Fig. 5.6).
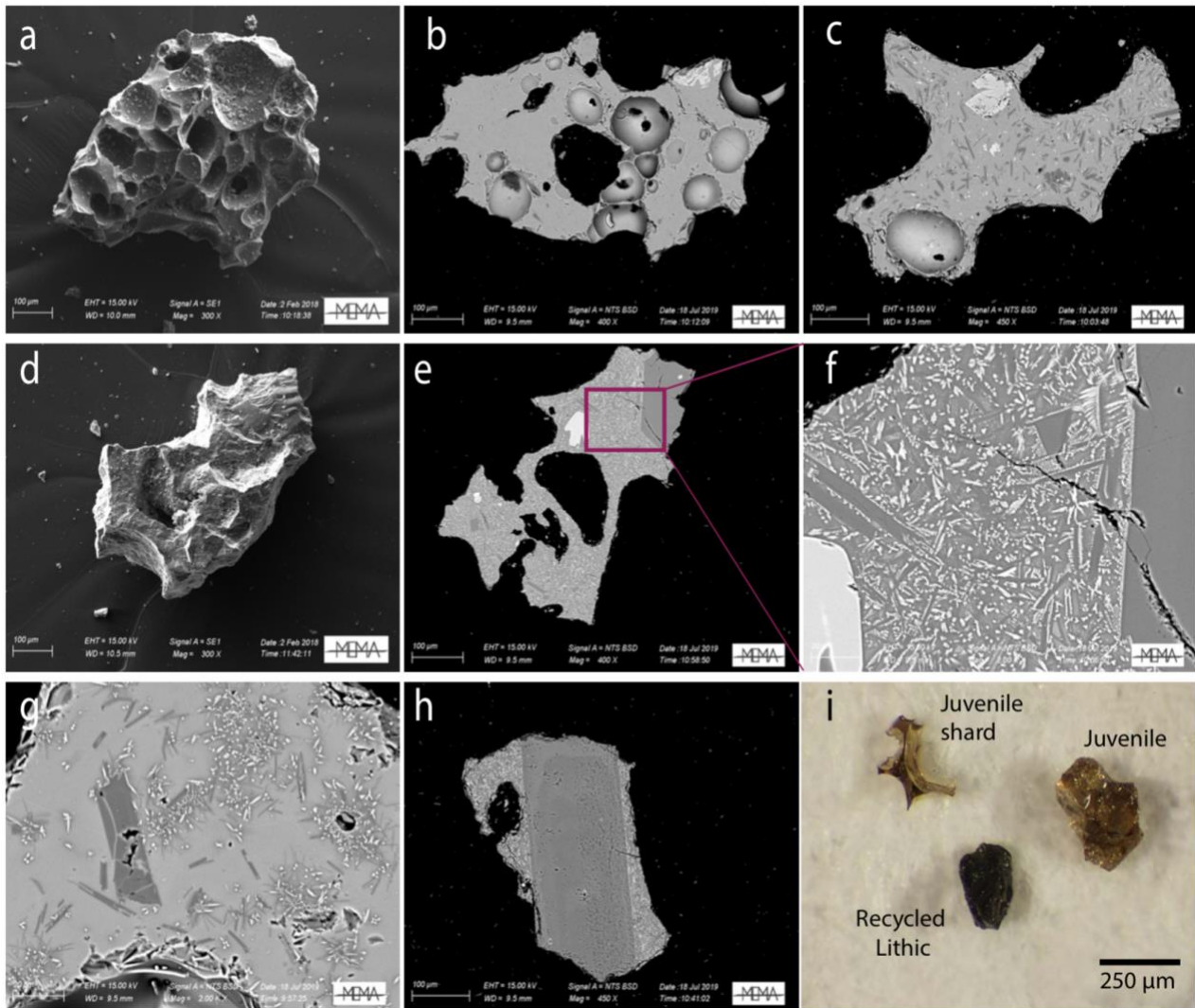
Fig. 5.6 Different types of ash fragments; a, b, c) secondary and back-scattered electrons images of juvenile ash, characterized by angular vesicular fragments with glass-rich groundmass; d, e, f, g) secondary and back-scattered electrons images of lithic fragments, characterized by an overall shape similar to the juvenile component, rough surface related to fine particle sintering and a variable growth of fine microlites typical of ash recycling in a hot environment; h) loose plagioclase crystal showing evidence of recycling on the adhering glass; i) optical microscope image of the different ash components.

BV involves black, variably vesicular, glass-bearing clasts that generally present more regular and blocky equant morphologies compared to VS. External surfaces are generally rough for the diffuse presence of tiny microlites in the glass. Bubble walls, as well, are often very irregular because of the strong crystallization of microlites from the surrounding glass. Accordingly, polished sections of these clasts typically reveal a highly crystallized groundmass (Fig. 5.6). Two distinct populations of microlites are recognized in terms of size. The first, is represented by sparse, euhedral and very

elongated microlites of plagioclase (20 μm), with typical skeletal textures and, for this reason, interpreted as possibly related to fast growth during degassing-induced crystallization of magma before fragmentation. The second population is formed by Fe-Ti oxides and plagioclase crystals typically smaller than 5 μm in size, that are characterized by a strong interface-controlled growth, and dendritic to plumose textures. They are mainly localized along the contact between groundmass glass and the micro-phenocrysts, or all along glass banding horizons, or else, as sparse spherulitic clusters in the glass. Vesicularity is generally lower (20-35 vol. %) with respect to the VS component. Bubbles present irregular and deformed shapes, as a possible result of partial collapse. All the textural and morphological features described above strongly correspond to what was observed in experiments of ash recycling simulating intra-crateric, high-temperature conditions (D'Oriano et al., 2012, 2014; Deardorff and Cashman, 2017). For this reason, this type of clast is here interpreted as recycled clasts (REC).

Another fundamental component of the analyzed ash fraction is represented by the CRY fraction: broken, typically euhedral, loose crystals. This fraction is dominated by transparent crystals of plagioclase (28 vol. %) and by only minor pyroxene and olivine (1-2 vol. %). Importantly, plagioclase crystals are commonly found to preserve contacts with a groundmass glass characterized by abundant μm-sized microlites arranged in a dendritic, sometimes plumose texture similar to that observed in the BV component (Fig. 5.6), suggesting also in this case an important secondary re-heating (and hence recycling) at least for a large part of the CRY component.

Clasts of different size were also characterized by their external shape using appropriate shape parameters (Solidity, Convexity and Circularity; see Chapter 2 of this thesis for definition). No significant variations in the average values of particles shape parameters are observed throughout all the samples (apart from minor variations in the interquartile spread of these values) not even considering different ash grain sizes. This confirms a generally constant mechanism of ash production and recycling during the entire period of ash collection, in agreement with the described activity (Tab. 5.1) and similar to the activity recorded by the infrasound array.

5.7 Discussion

5.7.1 The slow fluid flow explosive dynamics at Copahue

The high quantity of ash dispersed by the low-level eruptive plume (Fig. 5.1), together with the textural features of the ash produced during this phase (Fig. 5.6) suggest a good efficiency of the fragmentation process. In particular, the presence of highly vesicular juvenile fragments and vitric shards (Fig. 5.6 a,b,c) indicate the significant efficiency of magma fragmentation process mainly driven by volatile exsolution. These evidences, based on the analysis of the ash, are apparently in contrast with the low pressures recorded by the infrasound monitoring. In fact, infrasound and visual observations suggest that the explosive activity of Copahue volcano is characterized by a low velocity release of the ash-gas mixture from the vent, accompanied by a low general pressure associated to the pulsating release

of ash from the vent (Fig. 5.4).

The combination of information derived from the morpho-textural analysis of ash and infrasound data would suggest that ash-rich explosive activity at Copahue is related to efficient magma fragmentation/transport processes which is however operating at a low-energy regime. This apparent discrepancy poses important questions on the nature and dynamics of the fragmentation process.

5.7.2 Inferences on magma fragmentation processes

Ash morphology can give basic hints about the mechanism of magma fragmentation. The abundant presence of recycled material (Fig. 5.5), represented by the BV and at least part of the CRY components (reaching a maximum of 60-70% of the total), clearly demonstrates that a large portion of the erupted ash did not directly derive from syn-eruptive fragmentation, however representing a fundamental part of the erupting mixture dispersed in the atmosphere. Conversely, the textural and morphological features of the VS fraction (Fig. 5.6 a-c: sharp external edges; absence of fluidal shapes) suggest formation by rigid fragmentation of a mildly to low vesicular magma with a poorly developed permeability (absence of very large, deformed or coalescing vesicles) that rapidly ascends in the conduit in nearly closed degassing conditions (absence of groundmass microlites related to degassing-induced crystallization).

Explosive, rigid magma fragmentation can occur under different conditions, and it is generally associated to the release of an overpressure which mainly depends on magma vesicularity and permeability (Spieler et al., 2004; Kueppers et al., 2006; Cashman and Scheu, 2015). For intermediate values of vesicularity (40-50 vol.%; similar to those observed in the VS component) this overpressure is close to a minimum, however measured in the order of 2-4 MPa. As a general rule, the gas-ash mixture generated at fragmentation accelerates in the conduit, and its passage through an empty crater can result in the progressive decompression by expansion of the erupting mixture, finally increasing the velocity of the jet entering in the atmosphere (Woods and Bower, 1995). Conversely, in the observed activity at Copahue, the presence of a large amount of ash recycled under high-temperature (intra-crateric) conditions in the deposits suggests that, during the activity, the crater area was possibly filled up with a large amount of ash, and part of this ash was entrained and transported into the erupting mixture. The crater infilling was continuously fed by syn-eruptively produced ash, thanks to the pulsating character of the emission (Fig. 5.4). We suggest that incorporation of recycled ash, which could be described as an elutriation process following partial fluidization of the ash-dominated crater infill, contributed to strongly damp the already low overpressure of the erupting mixture, and hence to decrease its velocity, explaining the low amplitude of the infrasonic signal recorded at Copahue and the weak features of the ash plume. Assuming a thickness of 10 to 30 m for the ash-enriched zone at the crater base, a pressure drop on the order of 1 to 5 bars can be estimated through the application of the Ergun equation (Cocco et al., 2014), confirming an important damping effect upon the pressure of the ascending mixture.

The impulsive, high frequency nature of the activity, revealed by the infrasonic signal and by the billowing shape of the associated plumes (Fig. 5.1), suggest an unsteady character of the emission,

typical of these low intensity styles of activity.

While magma-water interaction has often been suggested as a main process of magma fragmentation at Copahue (Naranjo and Polanco, 2004; Petrinovic et al., 2014; Daga et al., 2017), based on ash characteristics (Figs. 5.5-5.6) and infrasound signals we discard here an important role for this process. Ash, in fact, does not present any textural or morphological feature recognized as typical of this fragmentation mechanism (absence of an important ash aggregation; no surface cracks or alteration of the ash fragments). Moreover, the very low amplitude of the pressure transients (Fig. 5.4) recorded in the infrasonic signal are not in agreement with an explosive activity driven by magma-water interaction, that should be accompanied by important pressure peaks for the impulsive, rapid vaporization and expansion of vapor created duirng the water-magma contact (Wohletz et al., 2013; Fee and Matoza, 2013). In addition, processes like a rapid dissipation of the overpressure related to the presence of an important surface water body (as for example observed at White Island volcano, New Zealand, when activity was characterized by near-continuous pulses of gas, ash emissions with exit velocities generally lower than 50 m/s and with generation of very weak plumes; Houghton and Nairn, 1991) cannot be invoked at Copahue, where the monitored activity was preceded by a large reduction (up to final disappearance) of the water volume of the crater lake.

5.8 Conclusions

The activity at Copahue is generally characterized by a large spectrum of explosive styles, which span from phreatic to magmatic accompanied by large quantity of erupted ash. The produced volcanic ash represents a serious risk to the health and daily life of population living in the volcano surroundings. Although dispersed at low elevation in the atmosphere, it can also represent a problem for the air traffic due to the presence of some small airports nearby the volcano. We know very little on how this activity changes at Copahue from one style to the other, which makes it difficult to understand how this activity will evolve in time. Integration of infrasound data with observations on the ash erupted during the same activity give however important hints to discuss the processes of magma fragmentation during this type of low-intensity, continuous ash emission.

In spite of the large ash plume dispersed at low level in the atmosphere, infrasound signals recorded during the explosive phases of March 2016 appear very weak, indicating a low overpressure involved in the eruptive process. Assuming a simplified linear theory of sound, we estimate that the gas-ash mixture was ejected with velocities around 10-20 m/s, also consistent with the immediate bending of the plume under the action of the wind observed during the explosive phases.

The study of the main features of the ash fragments helps discriminating the possible eruptive dynamics and fragmentation process associated with the periods of ash emission activity. The large amount of dispersed ash, together with morphological and textural evidences revealed in ash fragments (e.g. sharp edges, absence of fluidal morphologies, abundant rounded vesicles) are probably the result of the decompression-driven fragmentation of an ascending and degassing magma column at low overpressure under impulsive, high frequency explosive activity. Infrasound recordings evidence that

this process is driven at Copahue by a low decompression rate compared to the magmatic explosions typical of classic strombolian processes, here possibly related to the combination of low magma overpressure at fragmentation and the effect of the passage of the erupting mixture through an ash filled crater and by the incorporation of recycled ash into the mixture, as suggested by the large abundance of recycled ash recognized in the products. The recognition of the presence of a large amount of thermally-modified, recycled material in the erupted products have an important consequence in the interpretation of the general dynamics of the eruption. In fact, while in terms of fragmentation, and energy required for that process, BV fragments can be considered as lithic material, due to their high temperature at time of eruption they were clearly active in releasing heat to the plume, hence contributing to enhance its convective power and dispersal. We suggest that the recognition of such material, which could be common in low- to mid-intensity activity, is very important to understand the high, ash-related hazard potential of these eruptions.

Chapter 6

External features and internal structures of ash aggregates from Sakurajima volcano (Japan)

6.1 Introduction

During transport and dispersal of volcanic ash, fined-grained particles (generally <125µm) tend to adhere to each other as a result of different driving mechanisms (electrostatic attraction, moist adhesion due to hydrometeors or vapour condensation in the plume) to form ash aggregates (Sorem, 1982; Gilbert and Lane, 1994; James et al., 2002; Veitch and Woods, 2001; Textor et al., 2006; Durant et al., 2009). Aggregates are airborne clusters of ash particles typically displaying very different aerodynamical properties (i.e. settling velocity) with respect to their individual constituent particles (e.g. Sorem et al, 1982; Lane et al., 1993). In particular, they characterize for a different density and settling velocity respect to single ash grains, consequently resulting in different residence time into the atmosphere. The impact of aggregation processes on the atmospheric dispersal of volcanic ash is clearly demonstrated by several dedicated laboratory experiments (Gilbert & Lane, 1994; Schumacher and Schmincke, 1995; Kueppers et al., 2011) and by field studies focused on the distribution of the fallout deposits (e.g. Carey & Sirgudsson, 1982; Bonadonna & Phillips, 2003). The occurrence of secondary thickness in the distribution of fallout tephra associated to large explosive eruptions have been associated with the effect of ash aggregation and locally enhanced deposition (e.g. Brazier et al., 1983; Rose and Hoffman 1982, 1982; Sorem, 1982; Durant et al., 2009). The importance of ash aggregation so directly modifies the ash plume transport and sedimentation, largely affecting the hazards posed by atmospheric circulation of fine ash to public health, aviation, and agriculture (Guffanti et al., 2010; Bonadonna et al., 2012; Jenkins et al. 2015). For this reason, many efforts were recently spent by the scientific community in order to extend the knowledge about the mechanisms controlling the particle aggregation, as well as the modalities of tephra dispersal in the light of the different ash aggregation processes.

Several types of aggregates are proved to frequently populate the fallout material associated to explosive eruptions of variable scales and intensities (e.g. May 1980 Mt St Helens: Sorem, 1982; 1995-1999 Soufrière Hills Volcano, Montserrat; Bonadonna et al., 2002; March-June 2010 Eyjafjallajökull: Bonadonna et al., 2011, Taddeucci et al., 2011; ongoing activity at Sakurajima: Bagheri et al., 2016a, Miwa et al., 2020). However, as a consequence of their low preservation potential into the fallout

deposits, only a few direct (i.e. visual) descriptions exist about the internal structures associated to the different types of aggregates.

In the context of this thesis, a large set of completely preserved ash aggregates produced during different phases of Vulcanian activity at Sakurajima were collected and analyzed in order to provide a review of the main features associated to the different aggregate types with in-depth descriptions of their intimal structures. Aggregates were collected with preserved airborne structures and described using different procedures of "while-falling" sample collection and a state-of-the-art combination of analytical techniques involving both SEM and micro-CT X-ray analyses. This approach allowed us to provide original insights on the internal architecture of the different types of aggregates typically associated to the ash-dominated, Vulcanian activities.

6.2   Samples acquisition and processing

A total of three datasets comprehensive of different types of natural ash aggregates were collected on the field at Sakurajima volcano (Japan) during various phases of high-frequency, ash-dominated Vulcanian activity occurred at different times from July-August 2013 to November 2019. Datasets are thus referred to a wide temporal spectrum of Vulcanian activity, totally encompassing more than 6 years, and include aggregates derived from very different styles of eruptive activity, in turn associated also to highly variable meteorological conditions. The wide time window and eruptive conditions considered for sample acquisition, along with the similarity found between our samples with aggregates classification reported in literature (Brown et al., 2012), make the described samples a highly representative collection of the most common aggregates populating ash fallouts associated to mid-intensity, ash-dominated explosive activity at Sakurajima.

Different techniques were adopted for sample collection and for further data processing in order to extract as many information as possible about either the external and internal features characterizing the different aggregates. Hereafter, we present the different datasets of aggregates (following the chronological order of collection), together with information about the modalities of sample acquisition and processing.

A first dataset of aggregates was collected during the 2013 activity of Sakurajima, and it was used principally for investigating the aerodynamic properties of aggregates during the process of settling from the plume. The main results of this analysis will be presented and discussed in the next Chapter.

The second dataset is relative to ash aggregates collected during the period 22-25 October 2014 using dedicated adhesive carbon-coated tapes, which partially prevented the bouncing away of the settling aggregates as a consequence of the impact with the support. This technique was able to preserve several types of aggregates, and in particular at least the external, generally finer grained portion of the most fragile aggregates, often formed by an internal coarser core overgrown by an external shell of fine ash. Different types of aggregates from this dataset were identified and investigated using an SEM in order to collect a representative description and quantification of their internal constituents. The 2D projected

outlines of the individual constituent particles were manually segmented (using *Fiji* software) from the SEM images (Fig. 6.1), in order to estimate the particle dimension in terms of equivalent diameter, and convert it into volume frequency data.
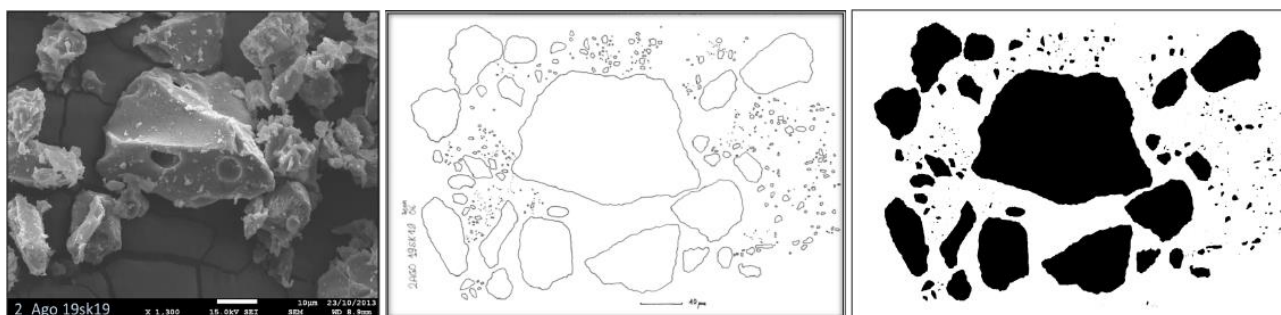
Fig. 6.1 Derivation of the size and shape of aggregate via image analysis. From left to right: SEM image of an aggregate (disrupted at impact) collected on adhesive papers; result of the manual contouring of particles from the SEM image; particle segmentation via image analysis to calculate the dimension of the fragments and derive the GSDs.

This information was used to present and discuss the GSDs associated to the different types of aggregates.

Furthermore, a large set of ash aggregates, entirely preserving their original structures, was collected from two different sequences of Vulcanian explosions occurred at Sakurajima during 16-17 May 2018, and 22-26 November 2019, respectively. Aggregates were collected using a dedicated thin glass support mounted with a thin layer of organic starch (tylose powder) in order to prevent disaggregation by impact of the fragile airborne structures at the moment of settling. A micro-CT was used to analyze the highly preserved original architecture of these aggregates, in order to obtain high-resolution 3D models of the aggregate interior (see Chapter 2 for the procedure of sample preparation and analysis). SEM analysis of sectioned samples was also used to analyze the internal structure of selected aggregates.
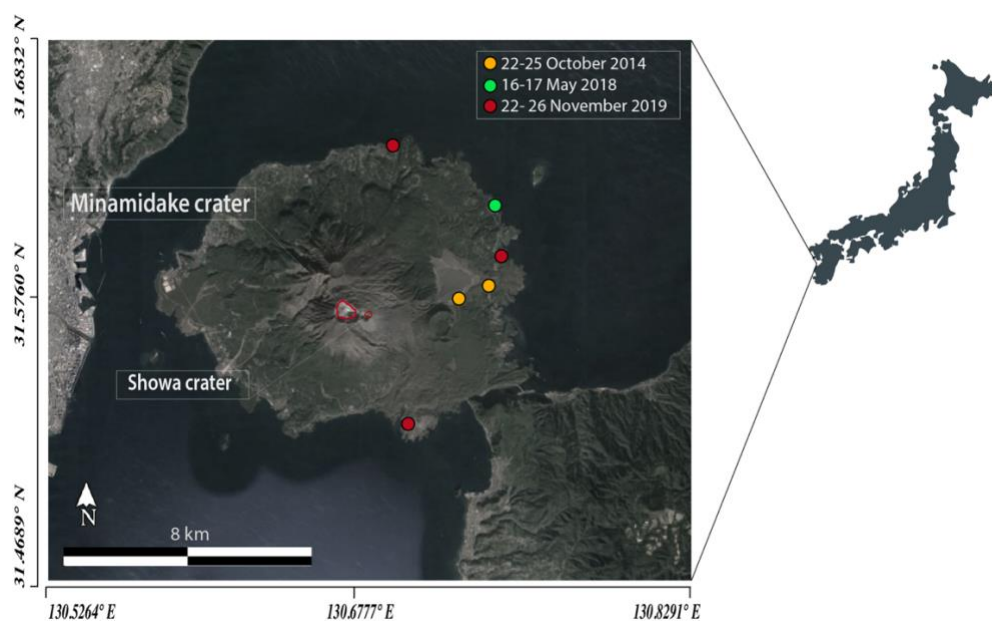
Fig. 6.2 Map of Sakurajima volcano with sites of aggregates collection during different periods.

Sample collection was performed at different locations approximatively set at a similar distance (around 4-6 km) from the active vents of Sakurajima. Sampling locations relative to all the acquired datasets are reported in Fig. 6.2 with different colors.

6.3   Description of the aggregates

Among all the investigated samples, different categories of ash aggregates were identified based on both external features and corresponding internal structures, unraveled by micro-CT analysis. The representative end-members of the different types are reported in Figure (6.3) together with the corresponding 3D model of their internal structure. Based on the nomenclature introduced by Brown et al. (2012), later integrated by Bagheri et al. (2016a) with the introduction of a new type of aggregate (namely, cored clusters (PC3)), analyzed aggregates were recognized and classified into four main categories: Ash Clusters (PC1) (Fig. 6.3a), Coated Particles (PC2) (Fig. 6.3b), Cored Clusters (PC3) (Fig. 6.3c), and spherical aggregates (Fig. 6.3d), representative of the Ash Pellets (AP) category described by Brown et. al. (2012).
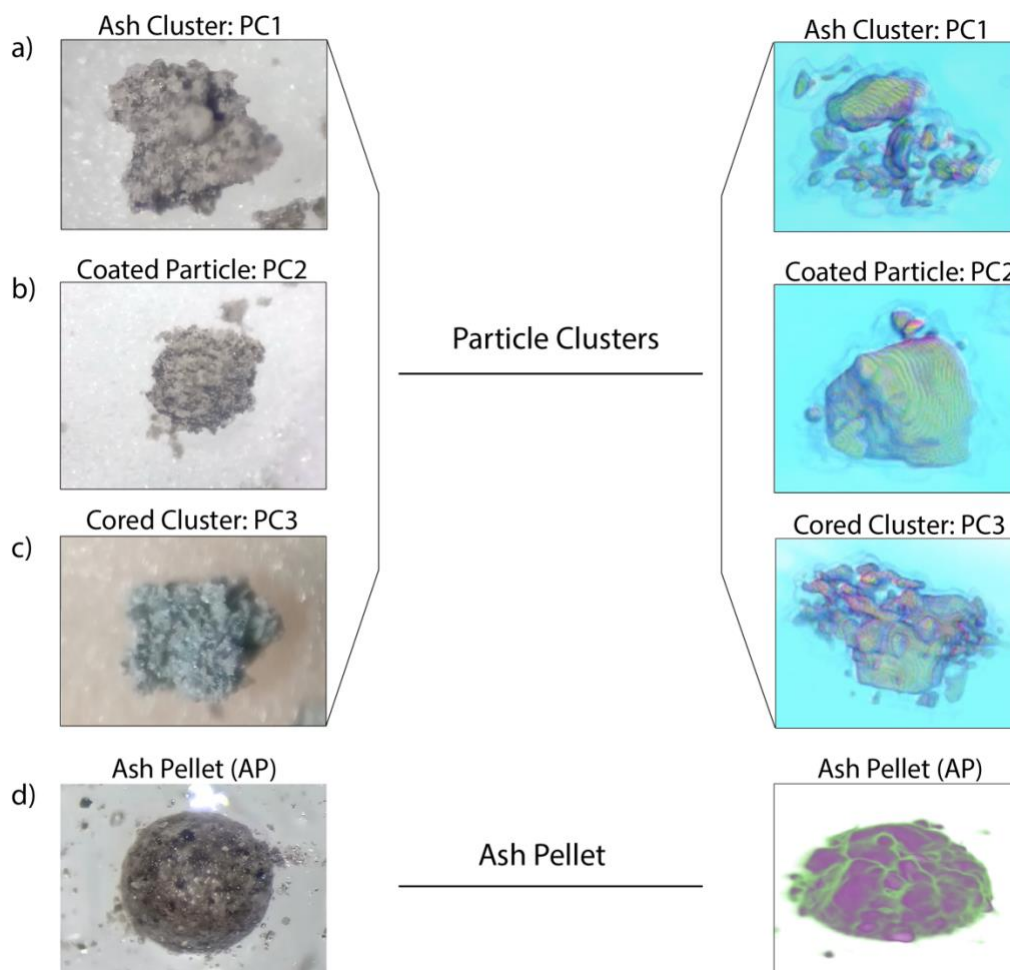
Fig. 6.3 Optical images of the different aggregates (left) with associated 3D models of their internal structure, presented here in a pseudo-color rendering in order to better display the internal distribution of grains (right). Optical mages were

obtained with a CCD camera coupled with a stereo microscope, while the 3D images correspond to the rendering of micro-CT images.

Hereafter, all the distinguished categories will be described based on their internal features, as revealed using both optical, scanning electron images and associated 3D rendering of the aggregating structures.

6.3.1 Ash Clusters (PC1):

PC1 aggregates (Fig. 6.4) are characterized by a very fragile structure (Fig. 6.4d) and sizes generally comprised in the range of 600 – 1000 μm. Considerably smaller clusters (Fig. 6.4e; in the range of 20-100 μm) were also found to occur particularly in deposits associated to low-intensity activity phases and high-concentration plumes. PC1 aggregates show a highly variable and irregular shape, which ranges from quite equant (Fig. 6.4a-b-c) to very elongated and chain-shaped morphologies (Fig. 6.4f).
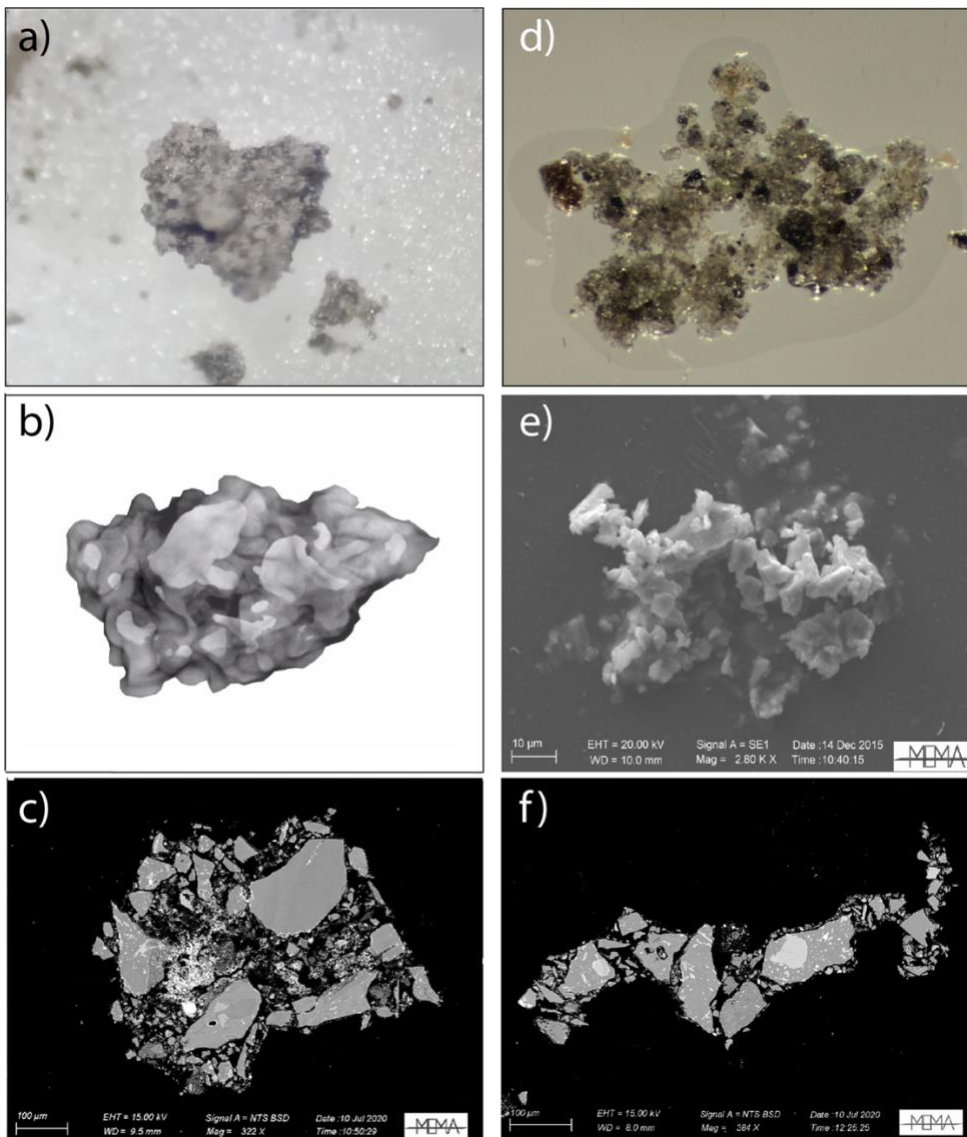
Fig. 6.4 Images of external and internal features of different types of Ash Clusters (PC1). (a) External aspect of an Ash Cluster (in optical image), associated to its internal structure unraveled through micro-CT 3D rendering (b), and a back-scattered SEM image of the median cross-sectional plane (c). Optical (d) and BS-SEM images of different types of Ash Clusters showing variable porosity and organization of the individual constituent particles.

Individual fragments forming PC1 aggregates show poorly sorted, platykurtic and moderately asymmetric grain size distributions (Fig. 6.5), with positive skewness and modes comprised in between 5.5 and 6.5 Phi. Internally, ash fragments do not show evident structural organization (Fig. 6.4b-c). These are often in contact with each other, forming a poorly organized 'open-framework' structure resulting in a high-porosity, low-density structure (Fig. 6.4c-f). Internal textures of the aggregating ash fragments are quite homogeneous, being generally characterized by low crystallinity, and in some cases also by aphyric textures associated to a massive aspect of the clasts. Highly vesicular particles have been never observed as included in PC1 aggregates. Morphometrical features of the different fragments are also very similar, with angular external perimeters with sharp edges which suggest a low mechanical abrasion of the surfaces.
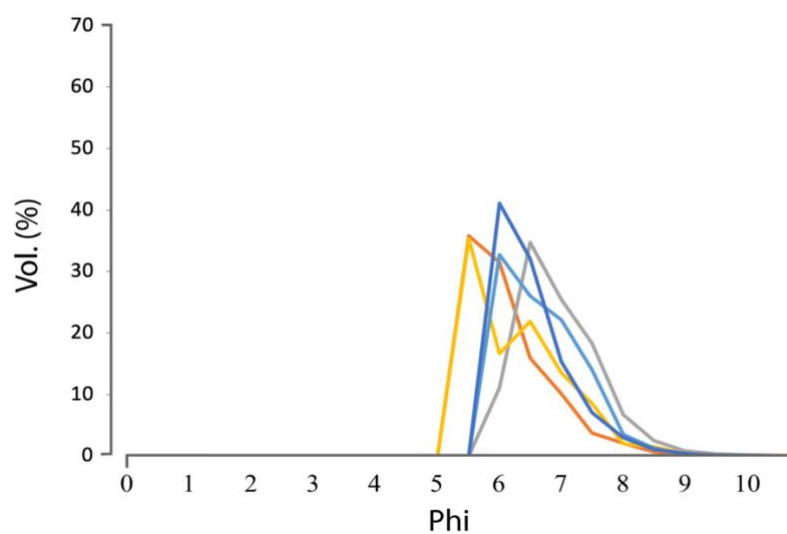
Fig. 6.5 GSD of PC1 aggregates. Different colored lines correspond to different aggregates.

6.3.2 Coated Particles (PC2)

Internal structure of PC2 aggregates (Fig. 6.6) is largely dominated by the presence of a coarse particle covered with a variable amount of finer material (<64 μm). Grain size of the coarse particle representing the nearly total mass of the aggregate is largely variable, from about 200 to 800 μm. The overall shape of PC2 particles is so strongly controlled by the shape of this internal particle (Fig. 6.6 d,e), being the external layer of aggregating ash often laterally discontinuous (Fig. 6.6 a,b). Observed PC2 aggregates showed a variable size (Fig. 6.6b) according to the available particle size distribution of the analyzed deposits, being therefore clearly related with the intensity of the activity. Sparse ash particles and crystals (on average <30 μm in size) are stacked around the central clast (Fig. 6.6f) to form a discontinuous mantling of aggregating particles or a thin shell. The thickness of this layer is in fact highly variable, from 0 up to 150 μm (Fig. 6.6b), and the porosity is apparently high, with numerous voids left between the aggregating particles. The ash forming the external cover showed a well sorted, leptokurtic GSDs with modes mostly set around 6.5-7 Phi (Fig. 6.7a).
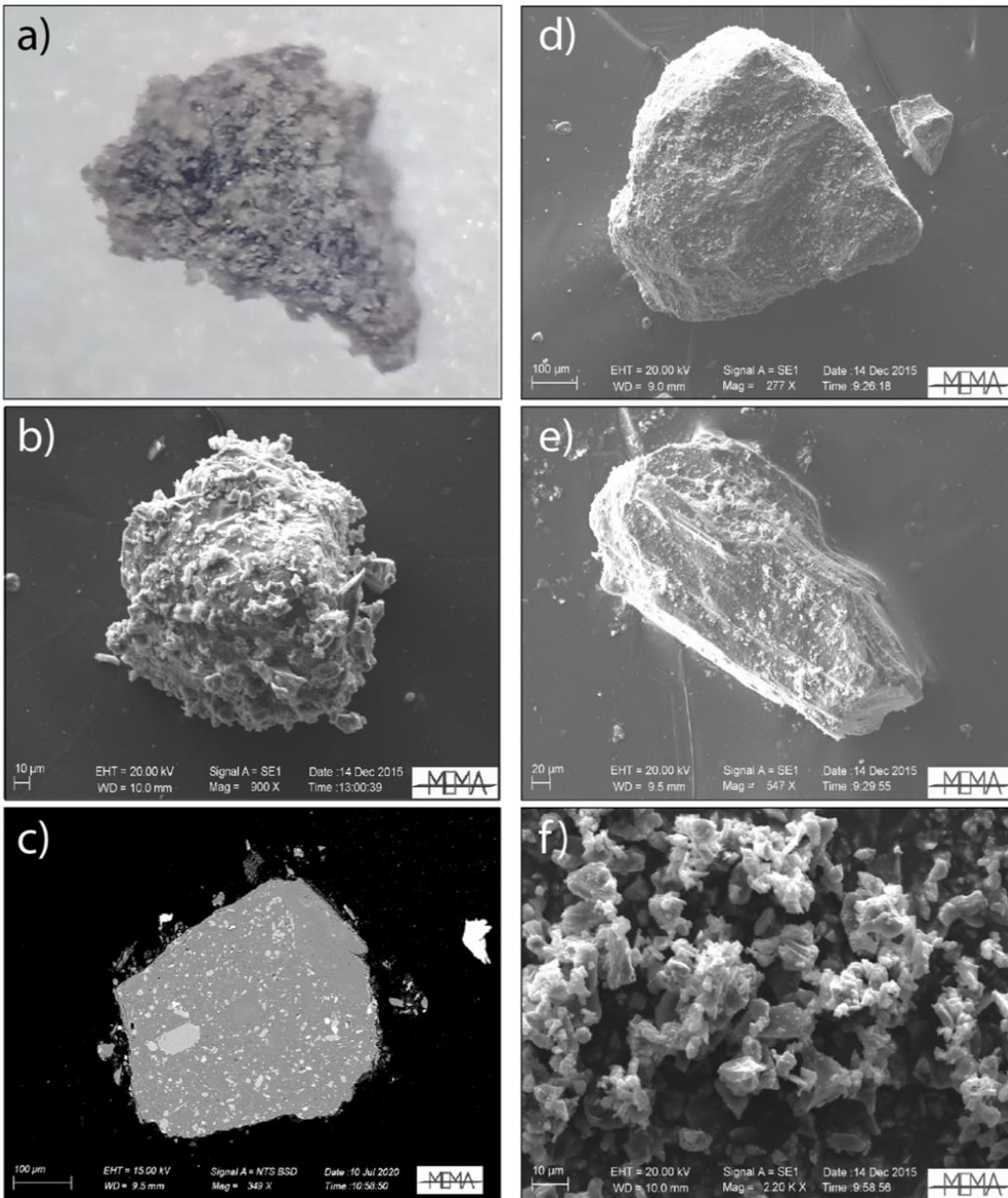
Fig. 6.6 Different types of PC2 (a, b, d, e) and particular of the external shell (f). A polished section of a PC2 aggregate is shown in c).

A direct comparison between the GSDs of the individual constituents forming PC1 aggregates and the GSDs of coated particles forming the layer of PC2 is presented in Figure (6.7b). Here, the cumulative curves calculated for the GSDs of several PC1 aggregates significantly differ from those measured for PC2 aggregates, indicating finer grain sizes for the PC1.
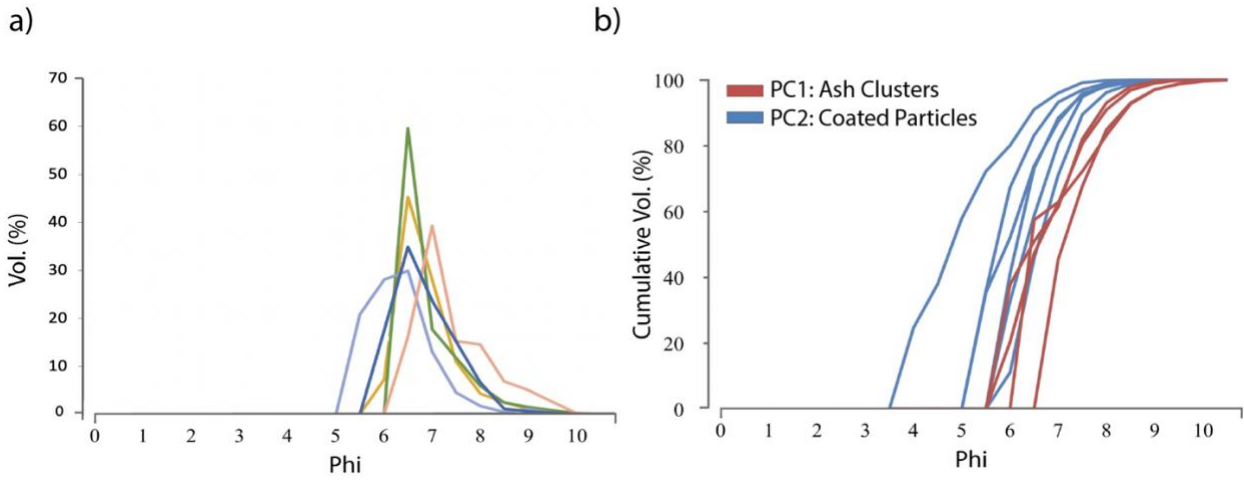
Fig. 6.7 a) GSDs of aggregating ash forming the external shell of PC2 and (b) cumulative GSDs of PC1 and PC2 aggregates.

6.3.3 Cored Clusters (PC3):

PC3 aggregates (Cored Clusters of Bagheri et al. (2016a)) show size mostly comprised in the range of 400-900 µm and are characterized by consistent amounts of aggregated ash coated around a central core to form a thick external shell (Fig. 6.8).
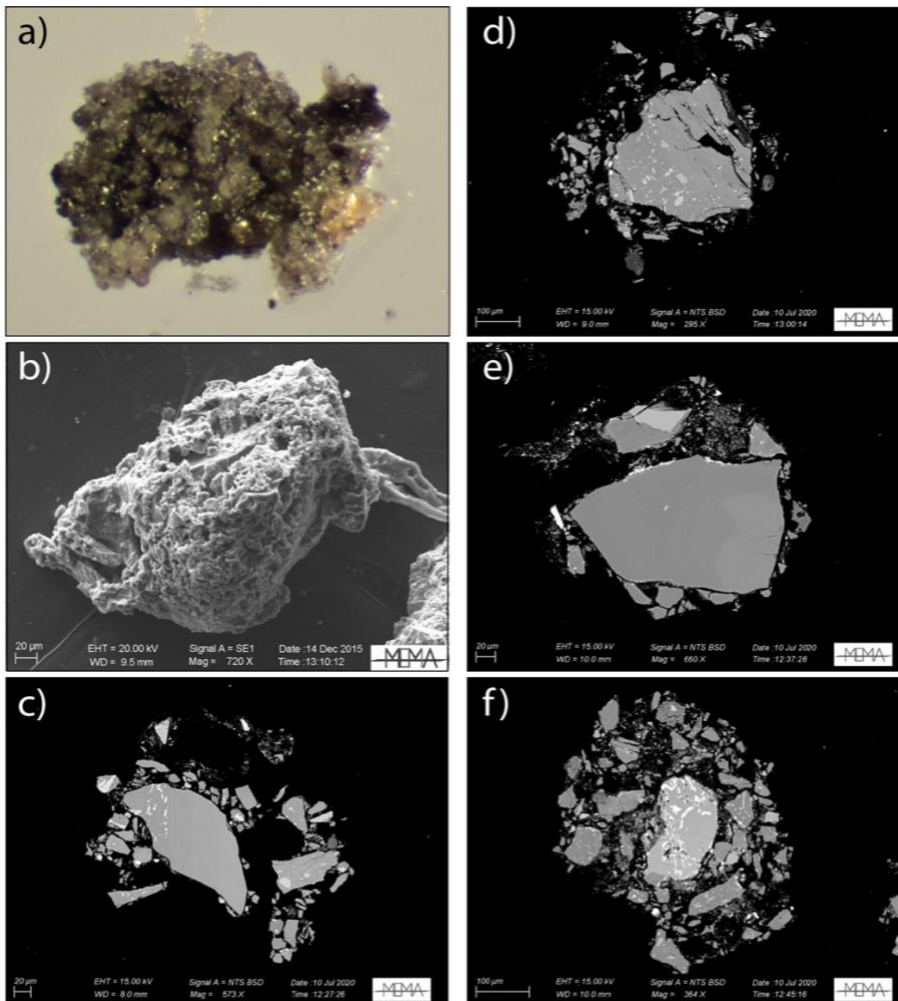
Fig. 6.8 Images of external and internal features of different Particle Clusters (PC3). Optical (a) and back-scattered SEM images (b-f) of the interior of Cored Clusters showing variable modalities of particle arrangement and internal structures.

Their structure appears very fragile, and their preservation potential to mechanical shocks is extremely low. The core of the PC3s is formed by a particle that is from 1 to 2 orders of magnitude larger than the coating ash, with a size generally comprised in the range of 300-700 μm (Fig. 6.8c).

The aggregate shell typically represents a significant volume fraction respect to the entire aggregate (Fig. 6.8c,d,f). Differently from PC2, aggregating ash in the shell forms a laterally continuous layer, which is characterized by a poor sorting of the ash, and by a variable thickness comprised between 200 and 20-30 μm. In fact, the GSD of the PC3 shells present highly asymmetrical and platykurtic distributions (Fig. 6.9) with main modes ranging in a wide spectrum of size classes, from 4 to 6.5 Phi. The GSD curves show a marked positive skewness, and are in many cases characterized by the presence of a secondary population of finer ash with modes set at around 5.5-7-5 Phi (Fig. 6.9).
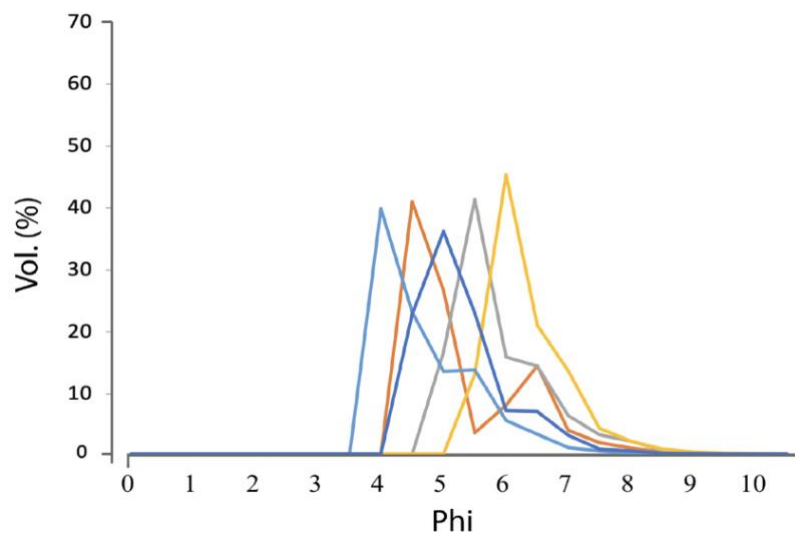
Fig. 6.9 GSDs of PC3 aggregates. Different colours correspond to different aggregates. The GSD do not include the core of the aggregates.

The external shape of PC3 is variable, from fairly irregular (Fig. 6.8c) to quite rounded (Fig. 6.8f) morphologies. The variability of the aggregate shape seems to be in accord with a different internal organization of the ash fragments. Aggregates showing higher irregularity in the external morphology (Fig. 6.8c) are typically associated to a poorly organized framework of the shell structure, with many individual constituents clearly in not direct contact. The interconnections left between larger particles are often relatively free from fine material (<10 μm) thus resulting in a generally 'Open-framework' architecture. On the other hand, a more organized internal structure of the ash grains (Fig. 6.8f), generally corresponds to a more regular external shape of the particle cluster, that shows also a lower porosity of the internal structure, with higher amounts of fine ash (<10μm) interspersed inside the interconnecting channels left by bigger particles. Figure (6.10) clearly shows the internal architecture of two PC3 aggregates dominated by the presence of a massive and irregular core at the centre of the particle cluster, totally incorporated in a thick, invariant coating of finer material. Importantly, the GSD

of the constituent ash grains seems to show a significant 3D spatial organization, with progressively decreasing sizes as approaching the external perimeter of the aggregate.
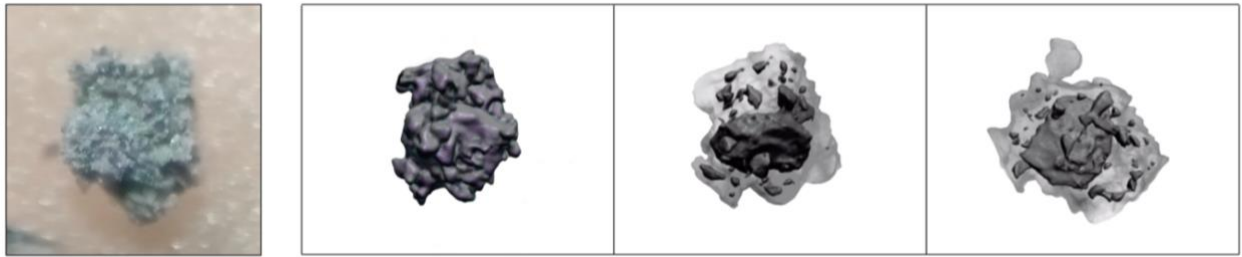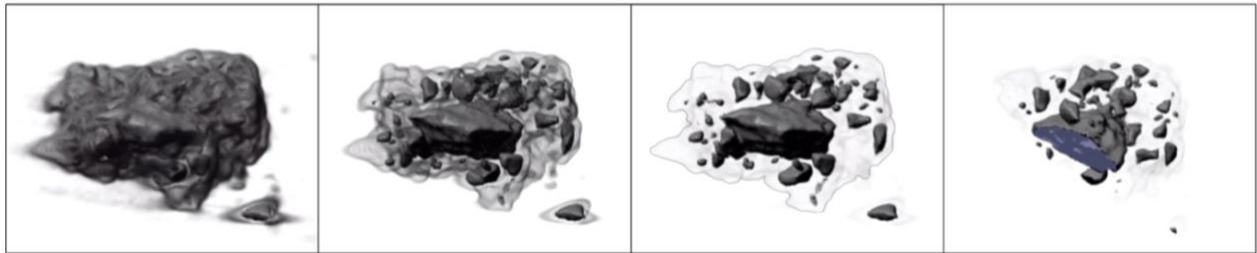
Fig. 6.10 3D, CT scan views of PC3 aggregates showing the spatial distribution of internal constituents. (a-b) Progressive unfolding of the internal architecture of a couple of PC3 aggregates. In aggregate (a), also the optical image is provided in order to better appreciate the internal arrangement of the coarser particles with respect to the external morphology.

6.3.4   Accretionary Pellets (AP1) and Liquid Pellets (AP3):

A heterogeneous population of poorly structured Accretionary Pellets (AP1: Fig. 6.11) and Liquid Pellets (AP3: Fig. 6.12) was found to characterize in particular the fallout deposits associated to humid and/or rainy meteorological conditions. Different types of spherical pellets were recognized based on different structural characteristics, however sharing a variably rounded general aspect (Fig. 6.11, 6.12). AP1 show size comprised between 500 µm and 1 mm, and roughly spherical shapes (6.11a,c). They are formed by moderately fine, poorly sorted GSD (Fig. 6.11b,e) of the internal ash constituents, that are mostly comprised in a range of size between 3.5 and 6 Phi. The GSD curve is highly asymmetric toward the finer size classes.

Their preservation potential appeared to be considerably higher than that of Particle Clusters described below, as a result of the weak cementation or low grade of compaction that characterize several AP1 analyzed. The individual fragments display poorly organized internal distribution of fragments, and include particles showing very different textures and compositions (Fig. 6.11 b). On the other hand, external surfaces appear densely coated by very fine and well sorted ash grains (Fig. 6.11c,d). The internal network of voids left by ash fragments is quite tight (Fig. 6.11b) and results in a lower internal porosity respect to the apparent porosity of Particle Clusters.
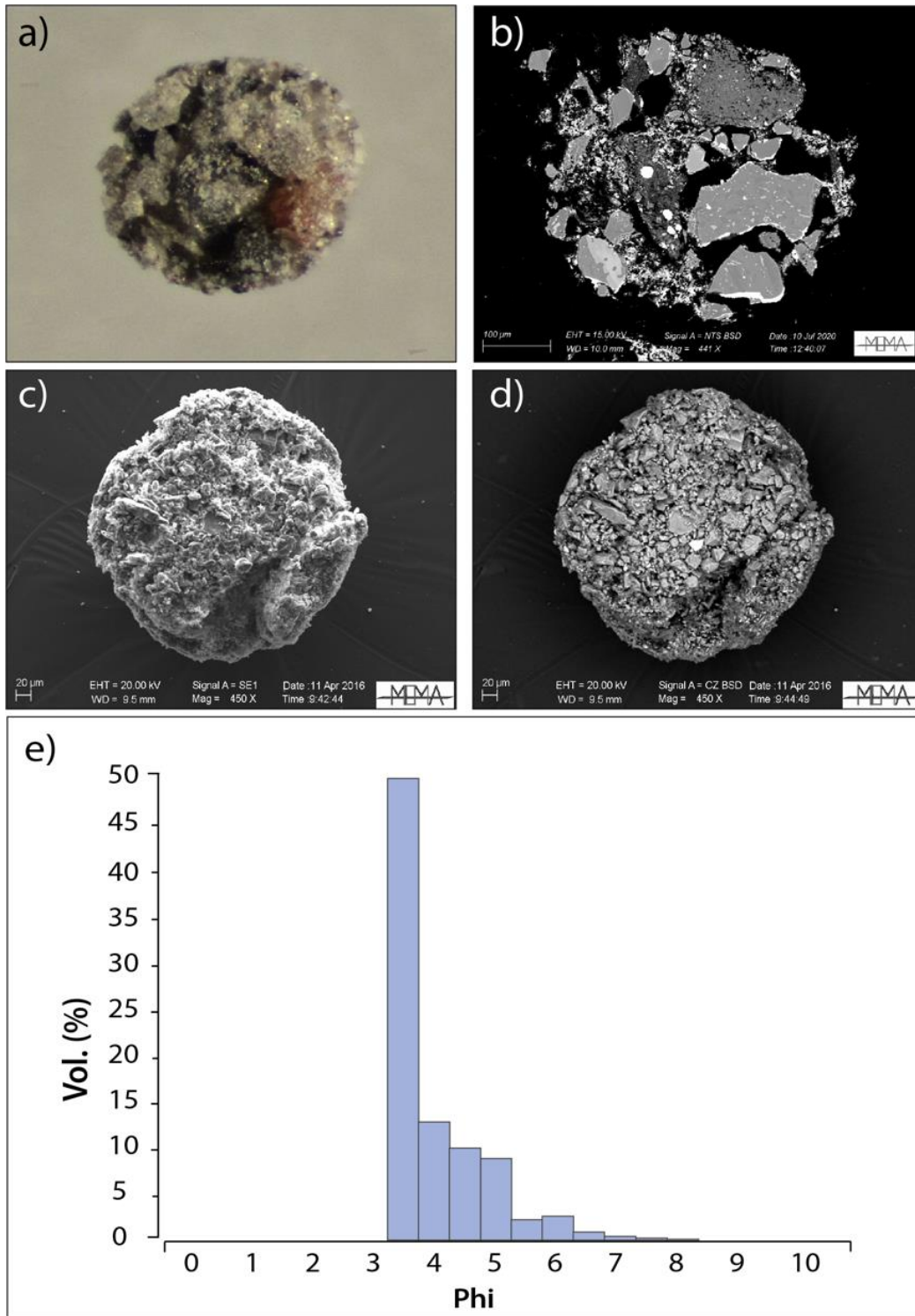
Fig. 6.11 Images and GSD of Accretionary Pellets (AP1). Optical image showing external morphologies of an AP1 aggregate (a) is compared with the SEM images of its median section plane, clearly evidencing features of the internal structures (b); (c,d) Comparison between secondary electron and back scattered electron images of an AP1 aggregate, showing fine ash coating the external surfaces. (e) GSD of the fine ash coating the external surfaces of an AP1 aggregate.

AP3 pellets (Fig. 6.12) distinguish from AP1s for the better sorted grain size distribution of finer ash constituents, that also display generally lower mean grain sizes (Fig. 6.12b, e). The sorting of individual constituents is still low and also the shape of the GSD curve is similar to that of AP1 aggregates, with an important asymmetry toward the finer grain sizes.
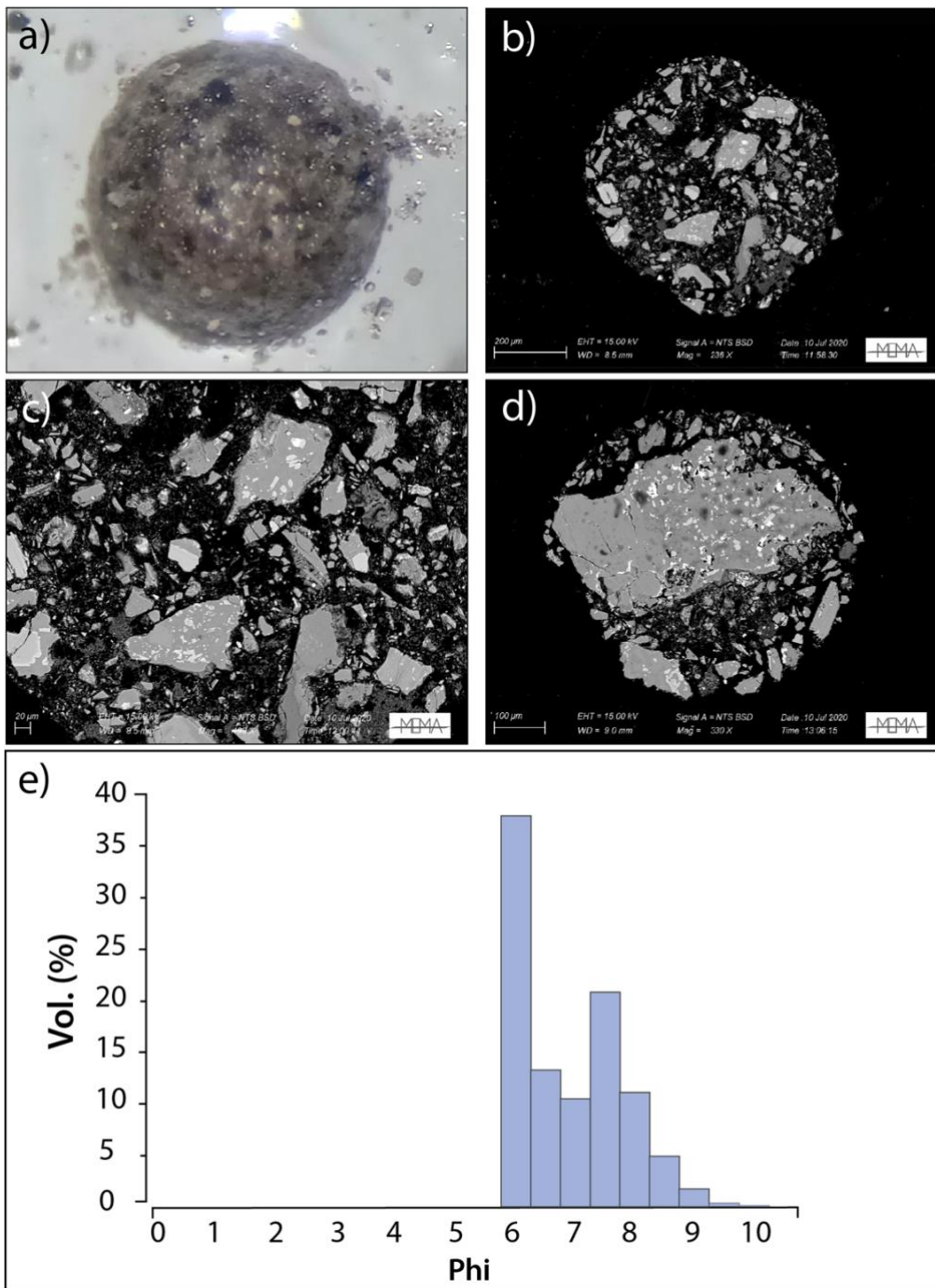
Fig. 6.12 Images of Liquid Pellets (AP3). Optical images showing external morphologies of an AP3 (a) are compared with SEM images of its median section (b) clearly evidencing features of the internal structures and the finer ash components (c). Internal structures of an AP3 with a massive particle included inside are also reported (d). e) GSD of ash particles from AP3 pellet.

However, in many cases the internal structure of AP3 is dominated by the presence of a large massive particle acting as a core (Fig. 6.12 c,d). This particle can be up to 2 or 3 orders of magnitude larger than other particles included in these types of aggregates. In particular, the spherical aspect of the external morphology of the aggregate is not influenced by the presence of these large and fairly irregularly shaped internal particles (Fig. 6.12c), being the latter fully and precisely inscribed within the aggregate

perimeter. Based on visual observations, during rainy conditions AP3 formation occurs with higher frequency respect to AP1. These aggregates show clearly deformed morphologies as a result of their water saturated state at the moment of impact with the dedicated support (evidence of the presence of water were found during sampling). This explains their extremely regular drop-like morphology, which appears evident in the 3D model reported in Figure 6.13. Here, several compositional heterogeneities in the aggregating ash are also highlighted, possibly resulting from the scavenging of crystals or high-density particles from the atmosphere.
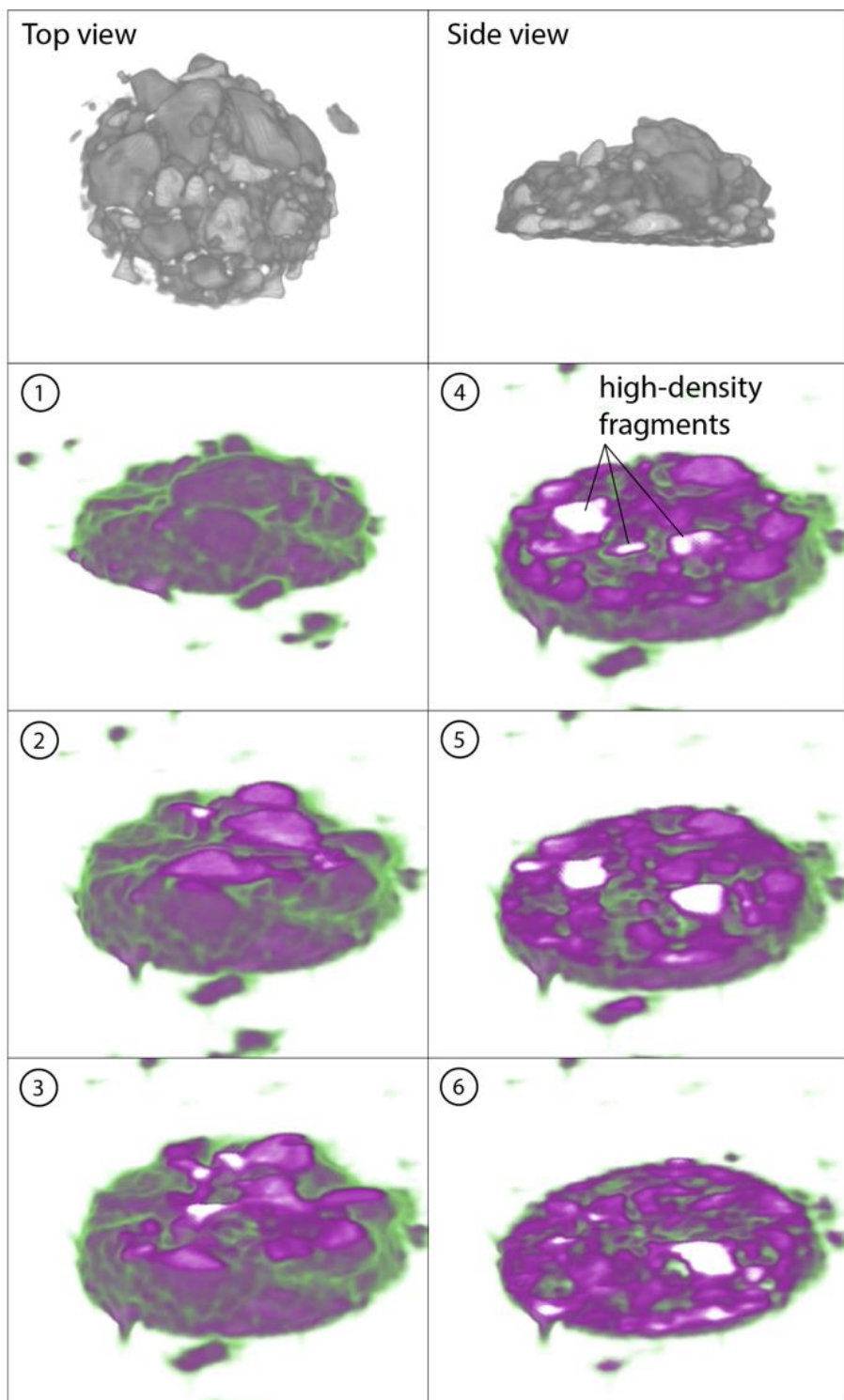
Fig. 6.13 3D CT-scan images of an AP3 aggregate. Top and side view of an AP3 aggregate rendered in a grey scale 3D model to highlight the external morphology. Images from 1 to 6: The progressive slicing of the aggregate volume evidences significant compositional heterogeneities in the individual constituent fragments (white particles).

6.4 Conclusion

Descriptive analyses on the internal characteristics of Particle Clusters and Ash Pellets were provided for a representative set of collected ash aggregates of different type. Four main categories of aggregates were recognized (according to Brown et al., (2012) and Bagheri et al., (2016a)) to populate the fallouts of the ash-dominated, Vulcanian eruptions at Sakurajima: Ash Clusters (PC1), Coated Particles (PC2), Cored Particles (PC3), and different types of Ash pellets (AP).

Detailed descriptions of the main morpho-textural and structural features of aggregates were provided using a combined approach involving both micro computed tomography (micro-CT) and SEM microscopy. Application of the micro-CT analysis to the study of natural, un-broken particle clusters has been never performed before in any other study due to the intrinsic difficulty to collect fully preserved aggregates, and these preliminary results represent thus a real novelty in the literature, confirming this as a highly innovative and powerful technique useful for a direct investigation of the internal structure of ash aggregates. Furthermore, the comparison between SEM images and micro-CT analyses represents a very promising approach valuable for the direct quantification of the internal porosity of different types of aggregates and for further investigations upon either the internal componentry of aggregates and the modalities of particle interlocking.

The analyzed datasets testify for the common occurrence of ash aggregates into the fallout deposits resulting from the recent Vulcanian activity at Sakurajima. In the next Chapter, we will focus on the aerodynamical properties of Particle Clusters, also investigating their influence in the process of ash dispersal at Sakurajima through the analysis of High-Speed, High resolution videos of falling aggregates directly collected during a stage of Vulcanian activity at Sakurajima in July-August 2013.

Chapter 7

Physical and aerodynamical parametrization of particle clusters at Sakurajima volcano (Japan)

Overview

In the previous Chapiter we presented a review of the different types of ash aggregates which are commonly associated to the ash-rich phases of cyclic Vulcanian activity. We also introduced the importance of ash aggregation process in the light of atmospheric dispersals of fine ash during ash-dominated activities, and its importance connected to the related hazards posed to human activities, particularly those connected with both land and aviation transports.

Several experiments have been carried out to investigate the physics of ash aggregation and dedicated numerical schemes have been developed to produce more accurate forecasting of ash dispersal and sedimentation. However, numerical description of particle aggregation is complicated by the lack of complete and realistic datasets on natural samples required for model validation and calibration.

In this chapter we intend to address this topic providing a systematic study on ash aggregates collected collected at Sakurjima volcano (Japan) during a sequence of Vulcanian explosions observed in July-August 2013. These measurements are intended for the calibration and validation of numerical schemes aimed at the description of the aggregation process connected with the modalities of aggregates formation and settling in the context of ash-dominated eruptions typical of the Vulcanian activity.

7.1   Introduction

In the last 30 years, several studies reported accurate descriptions of ash aggregates observed during fallout or in pyroclastic deposits of past eruptions (Brown et al., 2012 and references therein). The atmospheric dispersal and the settling dynamics of ash produced during explosive eruptions is significantly affected by the process of particle aggregation (e.g. Rose & Durant, 2009). As a result, many efforts have been made to improve the description of aggregates and our understanding of aggregation processes (e.g., Gilbert and Lane, 1994; James et al., 2002, 2003; Bonadonna et al., 2011;

Taddeucci et al., 2011; Brown et al., 2012; Bagheri et al., 2016a, Burns et al., 2017; Vogel et al., 2019; Van Eaton et al., 2012, 2013), as well as to provide increasingly accurate numerical descriptions for more effective hazard assessments (Cornell et al., 1983; Veitch and Woods 2001; Bonadonna et al., 2002b; Textor et al., 2006; Costa et al., 2010). Despite the importance of aggregation, due to the low preservation potential of particle clusters in tephra-fallout deposits, only a few examples exist that document the fundamental physical and aerodynamic parameters of ash aggregates, such as their bulk density, terminal velocity and size distribution of the constitutive particles (Bonadonna et al., 2002a, 2011; Taddeucci et al., 2011; Van Eaton et al., 2012; Bagheri et al., 2016a; Burns et al., 2017; Miwa et al., 2020). The lack of detailed and ground-based data for ash aggregates importantly affects the reliability of numerical model results (Brown et al., 2012).

7.1.1 High-Speed imaging of falling ash aggregates

Recently, the direct filming of aggregates during tephra fallout has emphasized the importance of a field-based approach to study particle clusters. For this reason, a large set of ash aggregates produced during a sequence of Vulcanian explosions at Sakurajima volcano (Japan) were filmed using a state-of-the-art technique involving a High-Speed, High-Resolution (HS-HR) camera coupled with ground observations, and ash aggregates collection on adhesive paper aimed at the detailed characterization of their internal structure (Bagheri et al., 2016a). The combination of the HS-HR videos of falling particles (i.e., single particles and particle clusters) with their analysis provided through the Scanning Electron Microscope (SEM) has the main advantage to provide an unbiased description of aggregates and their constituents before and after their impact on the adhesive paper. The analysis of HR-HS video of falling aggregates prior to their sedimentation is important to derive their aerodynamical behaviour. In fact, such a strategy allowed for physical and aerodynamic parameters of particle clusters to be derived before their disruption at the moment of impact with the ground (Taddeucci et al., 2011; Bagheri et al., 2016a; Miwa et al., 2020).

On the other hand, the analysis of aggregates collected on SEM tapes and the grain size distribution of bulk ash deposits allowed to investigate the links connecting internal structure of aggregates (i.e. grain size distribution of aggregating ash) with their aerodynamics, and with the characteristics of the analysed tephra samples. In fact, the analysis of collected particle clusters with the SEM allowed to estimate the grain size distribution (GSD) of either the complete aggregate or only of the external layer of coated ash particles. As a matter of fact, while most of the shell is preserved on the adhesive paper, one or more (up to 4) large particles generally bounce away upon impact. Their main properties can only be derived from the analysis of the HS-HR camera footages.

7.2 Sakurajima volcano

Sakurajima Volcano (Japan) is one of the most active volcanoes of the world, with a persistent activity that started in 1955 and is continuing to present days. Conduit dynamics responsible for the typical

eruptive patterns of Sakurajima during this recent period were already introduced and exhaustively investigated in the Chapter 3 of this thesis, using morphological and textural information from the analyses of ash.

The highly populated urban area of Kagoshima city lies ~10 km from the volcano, which represents a primary source of hazard for both the local population and civil aviation due to its continuous emission of large amounts of ash. On the other hand, for the high frequency of the activity characterised by the nearly daily injection in the atmosphere of a large amount of ash, Sakurajima represents a unique, natural laboratory for the investigation of volcanic ash dispersal, aggregation and fallout and for the study of the implications on life and safety in highly urbanized contexts.

7.3   Samples collection

Different types of samples were collected at Sakurajima volcano during several Vulcanian explosions occurred between the 28 July and the 3 of August 2013. In detail, the examined dataset consists of: i) HS-HR footage of falling ash aggregates; ii) aggregates collected on adhesive papers; iii) tephra samples accumulated in dedicated trays.

All the sampling sites are located downwind of the active vent (i.e. Showa crater), approximately along the dispersal axis at a distance of about 5 km from the crater (Fig. 7.1; Tab. A1 in the Appendices, section 7.8 of this Chapter). Timing of most videos (53 out of 62) is synchronous with tephra sampling (Tab. A2 of the Appendices).
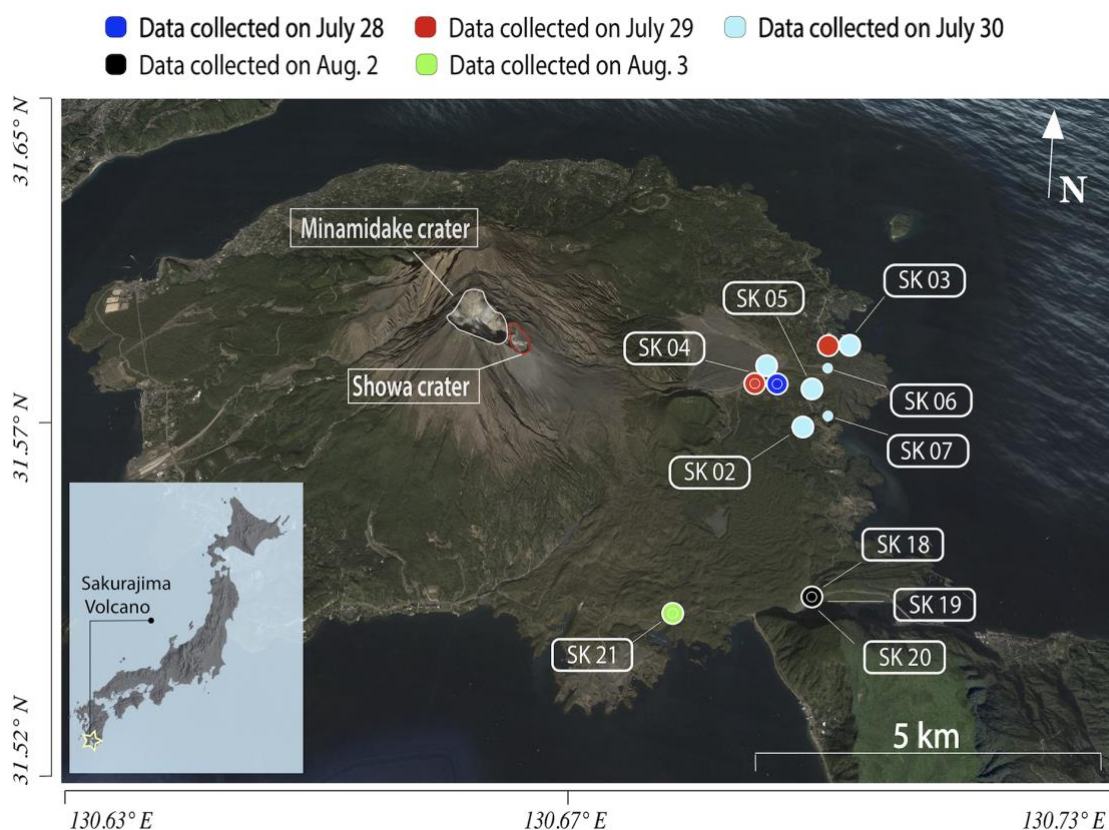
Fig. 7.1 The map shows the location of the tephra-fallout samples (large circles) and the

As reported by the Japan Meteorological Agency (JMA), the activity of Sakurajima in that period was defined as *'high level'*, with around 10 major explosions recorded per week from the Showa crater. During the five-day-long sampling period, the height of the eruption plumes ranged between 1.5–3 km above sea level. The observed activity was a series of Vulcanian explosions, associated with low-to-moderate ash emissions and ash venting (Yamanoi et al., 2008; Miwa et al., 2009). The wind direction and intensity at different heights above sea level (University of Wyoming Soundings, 2013) is presented in Figure 7.2, together with indication of meteorological conditions during the same period. Wind conditions (Fig. 7.2a) remained almost constant both in direction (eastward) and intensity throughout the entire study period, while atmospheric parameters (Fig. 7.2b) showed significant daily variations. Despite this, the collection of aggregates and of HS-HR videos was carried out under very similar meteorological conditions (Fig. 7.2b).
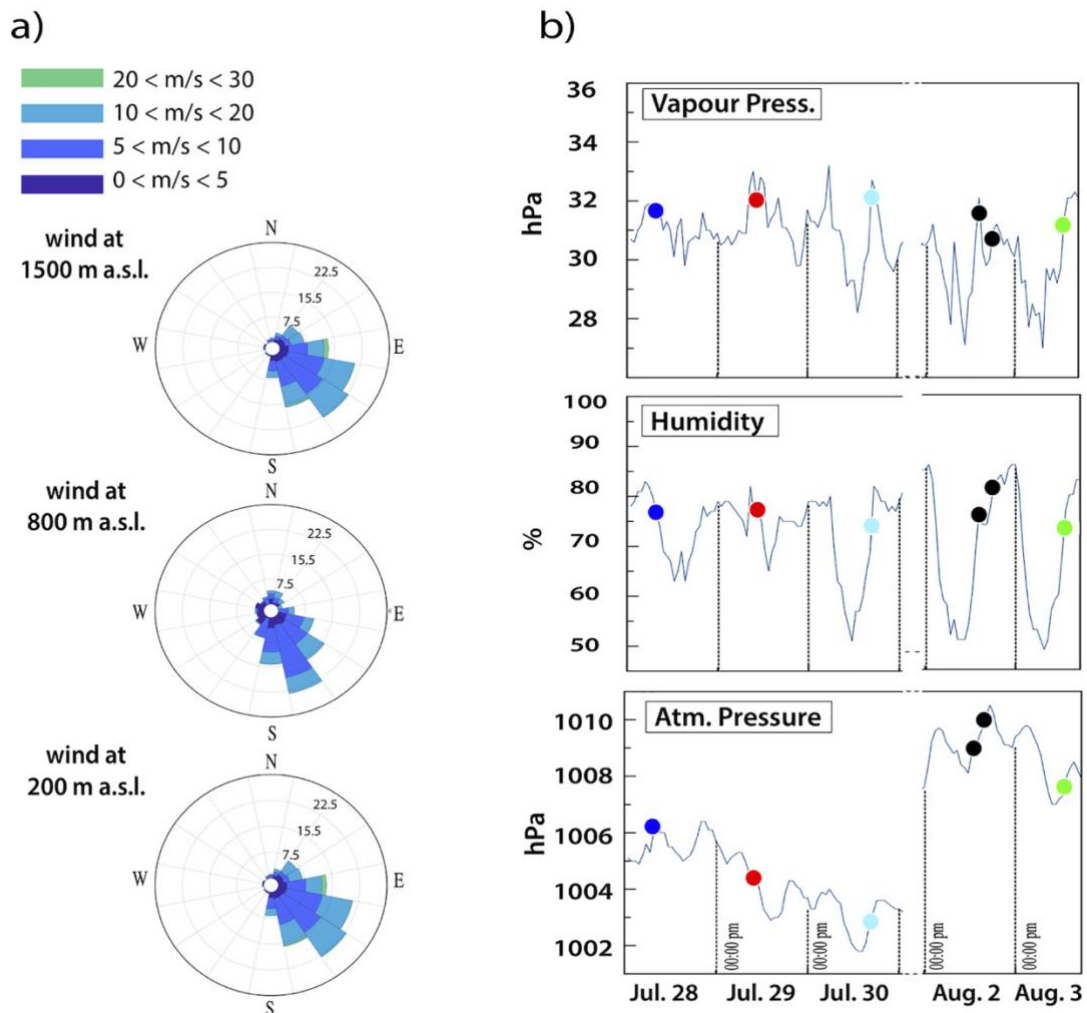
Fig. 7.2 Meteorological conditions measured at Sakurajima during the period of sample collection (July 28 - August 3). (a) Cumulative rose diagrams of the wind direction measured at different height above sea level during the full period of data collection; (b) time variation of the most relevant meteorological parameters (vapor pressure, humidity and atmospheric pressure). Coloured circles indicate the meteorological conditions at the exact time of the aggregate collection with HS-HR video and SEM tapes (same colour as in Fig. 7.1 representing different days of collection).

7.4   Methods

7.4.1   Field setup and rationale of the experiment

The aggregates were filmed while falling using a Phantom Pro High-Speed-Camera equipped with a Nikon 60 mm f/2.8 D AF Micro Nikkor lens. These were sampled on a 2 x 2.5 cm sheet of adhesive paper placed within the camera field of view. A detailed description of the field setup can be found in figure (3) of Bagheri et al. (2016a). A total of 62 HS-HR videos were selected and analysed with Fiji software. Aggregate size, terminal velocity and density were estimated following different methodological approaches (Tab. 7.1). Associated errors and uncertainties to the derived quantities are addressed in the Appendices (section A2).

DATA	Origin of the data	Size	Shape	Density	Term. Velocity
Aggregates observed with HS-HR setup	Image analysis on the HS-HR video	Measured as the diameter of the equivalent circle from HS-HR videos (averaging the area along all the frames)	L, I, S measured directly from HS-HR video	Derived from the formal equation of Vt	Measured comparing the changing position of particles along Y axis in different frames of HS-HR video
Internal Cores of aggregates	Image analysis on the post-rebound frames in the video + manual collection	Measured from post-rebound frames in the video with ImageJ as the diameter of the equivalent circle	L, I and S measured from post-rebound frames in the video with ImageJ	Directly measured with a water pycnometer	Calculated using the formal equation of Vt
Fine Ash Coating (external shell)	SEM investigation of the adhesive paper located in front of the HS-HR setup	Size represents the mean mode of the GSD derived from Image analysis of SEM images	Considered as spherical (L=I=S=0)	Assumed equal to the density of the cores (i.e. measured with water pycnometer) and corrected for difference in size	same as above
Tephra sample in trays: Coarse mode	CILAS analysis + deconvolution of the obtained GSDs as a sum of gaussian subpopulations (SP)	Size represents the mean value of the coarse mode characterizing the deposit	Considered as spherical (L=I=S=0)	same as above	same as above
Tephra sample in trays:	CILAS analysis + deconvolution of the GSD using MagicPlot	Size represents the mean value of the fine mode characterizing the deposit	Considered as spherical (L=I=S=0)	same as above	same as above

Tab. 7.1 Overview of the different measurements (first column from the left) together with the related methodology used for the sample acquisition and for the derivation of related quantities.

7.4.2   Primary quantities extracted from HR-HS video analysis using Fiji

The collection setup (HR-HS video associated with direct collection of filmed aggregates on adhesive paper) allowed us to constrain the dynamical properties of each falling object (velocity, size) as well as to associate the aerodynamic behaviour of an aggregate with the corresponding structure and grain size distribution of constituting particles through the analysis of the same aggregate collected on the adhesive paper. For post-processing, videos were selected according to their quality, discarding those affected by bad light conditions or showing particles out of focus. In particular, only videos with the ash aggregate in focus for a minimum number of five consecutive frames were considered as acceptable in the analysis. This enhanced the accuracy of the measured quantities, i.e. the terminal velocity and size of the aggregate, but reduced the number of available aggregates.

Each video collected with HR-HS camera was analysed using the freeware software Fiji (Schindelin et al., 2012) in order to extract a set of primary information relative to the morphometry and the cartesian position of the falling aggregates. In particular, the area in pixel of the falling object (A), the Cartesian coordinates of the centroid (X-Y), the external perimeter of the object (P), the minimum and maximum Feret determined by means of the analysis of images, are all reported in Table 7.2:

PARAMETERS	*Definition*
Area	Dark pixel, defining the projection of the object in each single frame
X	Horizontal coordinate of the centroid
Y	Vertical coordinate of the centroid
P	Length of particle's perimeter
Feret Min	Minimum caliper distance
Feret Max	Maximum caliper distance
dt	Interval time between each frame within the video

Tab. 7.2 Definition of the geometrical parameters extracted during the HS-HR video analysis using the software ImageJ. The frame rate of the camera is also reported as a crucial information useful for extracting further information from video footage.

7.4.3   Measure of particle Terminal Velocity

The terminal velocity relative to the observed falling aggregates was measured based on the HS-HR video analysis considering the ratio between the position of the centroid relative to the particle in each frame and the sampling rate of the camera. Both vertical, v_{ty}, and horizontal, v_h, components of the velocity were measured. Initially, terminal velocity was measured using the "step-by-step" technique, in which the velocity is obtained for couples of consecutive frames. These values were then compared to the mean velocity (along the full particles' path in the video), estimated using the first and the last

frames, and with a value of velocity obtained considering incremental steps of frames. For a motion where no acceleration occurs, the three techniques provide the same value of the velocity. This multi-technique approach helps to discriminate and discard objects that are not falling at their terminal velocity. All the reported terminal velocities use values deriving from the "step-by-step" technique. Values of horizontal velocities, v_h, have been used to discriminate and discard those data accidentally affected by lateral wind at the time of recording.

7.4.4 Size and shape of aggregates and cores

Size and shape of aggregates were characterised based on HS-HR videos by considering only the best-focused frames. Since the aggregates observed in the video were not exactly spherical, we adopted the method proposed by Bagheri et al. (2016b) for the estimation of aggregate dimension (D). Equation (1) was used considering three shape parameters (L, I and S):

$$d_{eq} = 0.928 * (L * I * S)^{1/3} \qquad \text{(Eq. 1)}$$

The three dimensionless parameters (L, I and S) were chosen to account for the complex morphology of the aggregates (Bagheri et al., 2016b); if adequately combined they define the Flatness and Elongation of the particle (Flatness: S/I; Elongation: I/L). L, I and S enter in the definition of the drag coefficient (Cd) which was calculated according to equation (34) of Bagheri et al. (2016b). They were defined considering only the aggregate projections with maximum and minimum areas, according to new the approach introduced by Bagheri et al. (2016b). In particular, L and I are defined respectively as the maximum and minimum Feret diameters (callipers) measured on the maximum-area projection, while S corresponds to the minimum Feret diameter measured on the minimum-projection area. Since aggregates were typically observed while rotating, and thus offering different face-projections to the camera, the parameters were calculated considering the different aggregates projections inferred from videos during the settling. Aggregate dimension was also estimated by assuming the shape as spherical: the equivalent diameter was calculated by averaging the area in pixel of the different aggregate projections revealed within the frames of the videos. For spherical aggregates either one of the calculated diameters can be used without differences, but for natural (i.e. irregular) aggregates using the diameter estimated with the spherical assumption can lead to considerable errors in the determination of aggregate density.

As already reported by Bagheri et al. (2016a), a large number of aggregates were observed to disaggregate after colliding with the adhesive paper. In most of the cases, the observed aggregates show the presence of coarse cores that usually bounce away after the impact, leaving the particles forming the external shell attached to the adhesive paper. In 15 cases out of the 62 analysed videos, we were able to measure both the grain size of the shell of the aggregate left on the adhesive paper and the size and shape of the rebounding core. The difference between the diameter of the aggregate (inferred prior

the landing on the adhesive paper) and that of the associated cores (inferred from post-rebound frames of the videos) was calculated to derive the average thickness and the volume fraction of the shell.

7.4.5   Estimate of aggregate and core density

The measure of the terminal velocity and size of a given object allows the bulk density of the aggregate to be constrained from:

$$\rho_p = \frac{3}{4} \frac{C_d \cdot \rho_a \cdot V_t^{\,2}}{g \cdot d_{eq}} + \rho_a \tag{Eq. 2}$$

where d_{eq} is the particle equivalent diameter, ρ_p is the density of the falling particles, ρ_a is the surrounding fluid density, V_t is the particle terminal velocity, and C_d is the drag coefficient (Bagheri et al. 2016b), defined considering the three shape parameters L, I, S. The air density is taken constant and equal to $\rho_a = 1.177 \, \text{kg/m}^3$; the kinematic viscosity of the air is $v_a = 1.568 \cdot 10^{-5} \, \text{m}^2/\text{s}$ (http://weather.uwyo.edu/upperair/sounding.html).

Since aggregate density is a derived quantity having a non-linear relation with the measured terminal velocity, shape, size, and air density, we used a Monte Carlo simulation in order to provide a better estimation of the density, also considering the uncertainties related to the different variables entering in Eq. (2) (see section A2 of the Appendices).

Density of the core was calculated using the size-vs-density trend reported in figure (4) of Bagheri et al. (2016b).

7.4.6   Grain size analysis of aggregates collected on adhesive paper

A subset of the aggregates filmed and collected on adhesive paper was analysed with the SEM, extracting information on the aggregate type, the GSD of the shell and, where still preserved, the dimension of the core that was measured through video analysis. The GSD of the shell, combined with the information about the size of the inner core, where present, provides a reliable picture of the total GSD of each aggregate prior to the impact. The technique used for calculating the GSD of the aggregates shell consisted of: (1) manual contouring of the ash particles from SEM images using Fiji; (2) estimation of the area of each particle and derivation of the related equivalent circle diameter; (3) conversion of diameters number frequency for classes of size, into volume frequency data (view Figure (6.1) in Chapter 6 of this thesis). The volume-based GSD of each aggregate shell was then described as a sum of two independent Gaussian subpopulations: a coarse-grained subpopulation (SP1) and a fine grained one (SP2). The fitting operations are obtained by means of a residual minimization algorithm using the MagicPlot software (https://magicplot.com). The modal value, the graphical skewness and the ratio between the fraction of the coarse (SP2) and the fine (SP1) subpopulations (defined as *SP-ratio)*, were used to characterise the GSD of each aggregate shell.

7.4.7 Grain size analysis of tephra samples

A set of tephra samples was collected in the days between 28 July and 3 of August 2013 placing 40 x 28 cm plastic trays at various locations (Fig. 7.1 and Tab. A1). The tephra samples analysed for GSD were collected, at the same time and location of the samples collected on adhesive paper, successively analysed with SEM, and videos acquired with HS-HR camera (Fig. 7.1).

Multiple tephra samples were collected on July 30 during the same event at different locations (SK02-03-04-05; cyan empty circles in Fig. 7.1) with respect to the synchronous HS-HR videos (SK 06-07) (cyan filled dots in Fig. 7.1). The closest collection point of tephra samples is located in this case about 200 m from the HS-HR camera setup. The GSD of the different samples was calculated following methodological approach already described in section 2.1 (Methods Chapter) of this thesis. As in the case of the aggregate shells, the GSDs of tephra samples were all deconvoluted into the sum of two Gaussian subpopulations SP1 and SP2, always getting $R^2 > 0.94$ (Tab. 7.3). Each subpopulation was then described in terms of mean (μ), standard deviation (σ) and volume fraction (in percent with respect to the total sample).

7.5 Results

7.5.1 Grain size distribution of tephra samples

The adopted sampling strategy resulted in a close spatial and temporal correspondence between the information derived from tephra samples collected in trays (Fig. 7.3, Tab. 7.3), the information derived from SEM analyses on aggregates collected on adhesive tapes (Fig. 7.4, Table 7.4) and the information of the falling aggregates extracted from the analysis of the HS-HR videos (Fig. 7.5, Tab. A2).
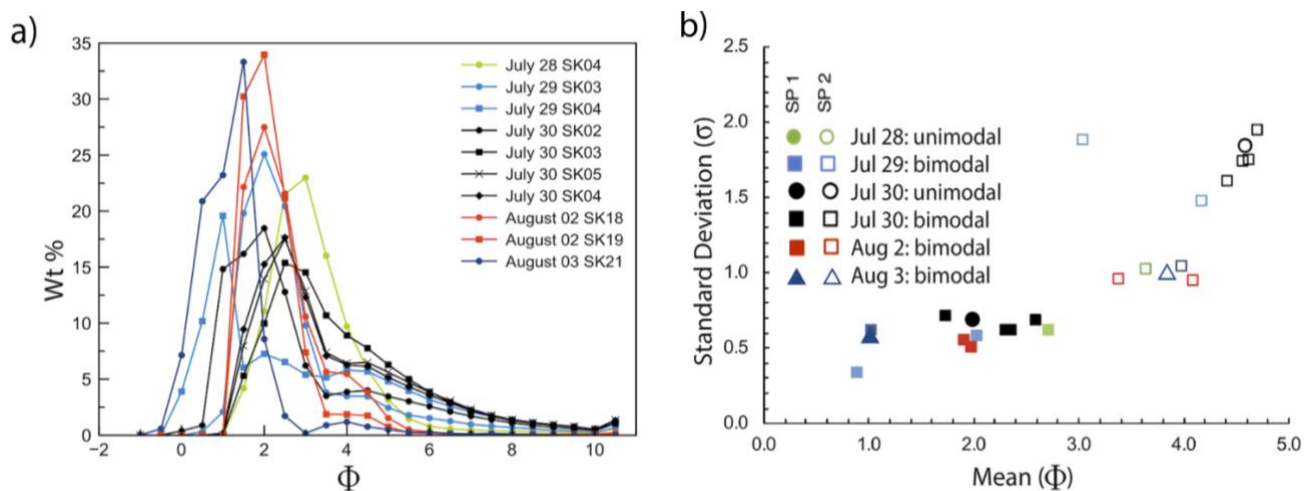
Fig. 7.3 Grain-size of the tephra-fallout samples collected simultaneously with HS-HR videos. (a) Grain-size distributions associated to the different days of video collection (colours); (b) standard deviation (s) and mean (μ) of the two gaussian sub-populations (SP1 and SP2) derived from deconvolution of the grain-size distributions (see Section 2.3 for further information). In particular, circles refer to unimodal GSDs while squares and triangles to bimodal GSDs. Filled and open symbols indicate sub-populations 1 and 2, respectively, and colours refers to the day of collection.

In Figure 7.3, Most of the analysed tephra samples show similar, clearly bimodal GSD with a main mode peaked around 1-2.5 ϕ, and a secondary mode ranging between 4 and 4.5 ϕ (Fig. 7.3a). Only two samples (July 28 SK04 and July 30 SK03) show a unimodal, positively skewed distribution with the mode peaked at about 2.5 and 3 ϕ, respectively. In addition, the sample SK04 of July 29 is characterised by three modes: a primary mode at 1 ϕ, and two poorly prominent secondary modes at 2 and 4.5 ϕ, respectively. Regardless of the GSD type (i.e. unimodal or polymodal), all the distributions were deconvoluted, with low residuals (Tab. 7.3), into a coarse (SP1) and a fine (SP2) subpopulation, described in terms of mean, standard deviation and weight fraction (Fig. 7.3b, Tab. 7.3). It is interesting to note that the relative weight of each SP, for samples collected during the same event, is dependent on sampling position with respect to the dispersal axis (Tab. 7.3): the relative amount of the finer-grained SP2 shows a sharp cross-wind increase (e.g. tephra samples collected at SK02 and SK03 on July 30, or at SK03 and SK04 on July 29; Tab. 7.3). Moreover, the relative weight of each SP depends also on the day of collection, and hence probably on the eruptive conditions (e.g. wt% of SP1 of the August 3 tephra sample is significantly larger with respect to all the others; Tab. 7.3).

Day of collection	Erupt time (JST)	Collect. time (JST)	Distance from the dispersal axis (km)	Sample location	GSD Mode (Phi)	Mean (SP1) (Phi)	Fraction (SP1) (wt%)	Mean (SP2) (Phi)	Fraction (SP2) (wt%)	R^2
Day 28 July	Nd	11.50-12.04	~0.3	SK04	3.0	2.7	58	3.6	42	0.978
Day 29 July	11.10	11.19-11.31	~0.2	SK03	2.0	2	75	4.2	25	0.979
		11.19-11.31	~0.9	SK04	1.0	1.1	25	4	75	0.988
Day 30 July	17.03	14.43-19.24	~1.4	SK03	2.5	2.6	42	4.4	58	0.982
	17.03	15.30-19.03	~0.3	SK02	2.0	1.7	62	4.4	38	0.95
	17.03	16.25-19.19	~0.6	SK05	2.5	2.4	47	4.6	53	0.979
	17.03	16.30-19.06	~0.5	SK04	2.5	2.3	50	4.6	50	0.976
Day 02 August	Nd	13.07-14.03	~0.3	SK18	2.0	2	69	3.4	31	0.97
	Nd	14.15-15.25	~0.3	SK19	2.0	1.9	78	2.7	22	0.966
Day 03 August	17.47	18.00-18.12	~0.8	SK21	1.5	1.0	94	4.1	6	0.94

Tab. 7.3 Information relative to tephra samples collected in dedicated trays. Eruption times (according to communications from the Sakurajima Volcano Observatory: SVO) are reported together with the time of collection and the map location

codes (see map in Fig. 1). Eruption times not reported on SVO archives are indicated as 'Nd' and refer probably to low intensity events. SP1 and SP2 represent the coarse and fine subpopulations (see the text for more details). The Determination coefficient R^2 indicates the goodness of fit associated with the deconvolution of the grainsize in two Gaussian subpopulations (i.e. SP1 and SP2).

7.5.2 Types of aggregates from visual observations

Three different types of aggregates were identified during the period of data collection. Visual observations were accomplished thanks to the analysis of the HS-HR camera videos coupled with the investigation, using stereo microscope and SEM analysis, of the collected adhesive papers. The occurrence of the identified aggregates types was also confirmed by the critical interpretation of aerodynamics data, obtained from the analysis of the HS-HR videos (Fig. 7.5, Table A2):

- PC1 (Ash Clusters of Brown et al. (2012)): ash aggregates of irregular shape and variable size (from around 400 µm up to 1200 µm), formed by fine ash. This type of aggregates represents 10-15% of aggregates analysed through videos (Fig. 7.5); unfortunately, the presence and abundance of PC1 aggregates was inferred only from HS-HR video since no PC1 was directly collected on adhesive paper.

- PC2 (Coated Particles of Brown et al. (2012)): large particles (>200 µm) partially covered by fine ash (on average <20 µm) forming a thin shell coating the external surface. Aerodynamical behaviour of discontinuously covered single particles can be considered an end-member of this category (about 25-30% of all aggregates observed in videos, Fig. 7.5).

- PC3 (Cored Clusters of Bagheri et al. (2016a)): aggregates (>200 µm) characterised by a significant amount of aggregated ash around a central core formed by one or more particles (up to 4) with size 1 to 2 orders of magnitude larger than coating ash. PC3 is the most frequently observed particle cluster category (55-65% of all aggregates observed in videos; Fig. 7.5).

7.5.3 Grain size distribution of the aggregate shells

The GSD of the aggregate shells (Fig. 7.4) was determined, through SEM analysis, for 10 out of the 62 aggregates captured by HS-HR video footages (Tab. A2); these aggregates were collected during two days of activity (August 2 and 3). For all the aggregates, the main measured (or calculated) physical parameters and the statistical parameters describing the GSDs are reported in Table (7.4). Also, in this case, GSDs were deconvoluted into two main Gaussian subpopulations (SPs), with the ratio between the relative weight of the two SPs ('*SP-ratio*' in Tab. 7.4) being one of the distinctive features between the different types of GSD.

Aggr ID	Collection Time(JST)	Available Data	Aggregate Size (µm)	Aggregate Terminal Velocity (m/s)	Aggregate Density (kg/m³)	Core Size (µm)	Core Density(kg/m³)	Aggregate shell GSD type	Aggregate shell SP-ratio	Aggregate shell Median (Phi)	Aggregate shell Skew.
16SK19	Aug. 2 14:54:30	Video/GSD/Core	362±35	0.89±0.08	561[475, 751]	202	2648	Type 1	1.55	4.6 (41µm)	0.32
17SK19	Aug. 2 14:56:15	Video/Core	441±31	1.52±0.05	854 [761, 1000]	288	2618	-	-	-	-
18SK19	Aug. 2 15:04:54	Video/Core	268±20	1.56±0.07	1783 [1574, 2094]	260	2606	-	-	-	-
19SK19	Aug. 2 15:08:15	Video/GSD/Core	290±30	1.14±0.1	1121 [964, 1576]	205	2647	Type 2	0.30	4.8 (33µm)	0.62
20SK20	Aug. 2 16:47:00	Video/GSD/Core	559±38	2.14±0.01	804 [739, 911]	474	2551	Type 2	0.37	5.9 (17µm)	0.53
21SK20	Aug. 2 16:49:23	Video/GSD/Core	237±18	1.38±0.01	1778 [1590, 2066]	232	2628	Type 1	1.92	6.3 (13µm)	0.30
22SK20	Aug. 2 16:53:55	Video/GSD/Core	495±39	2.7±0.05	1432 [1303, 1704]	487	2510	Type 2	0.26	5.9 (17µm)	0.76
23SK20	Aug. 2 17:02:41	Video/GSD/Core	269±25	1.52±0.08	1951 [1697, 2546]	262	2621	-	-	-	-
1SK21	Aug.3 18:04:06	Video/Core	787±54	2.92±0.01	831 [766, 943]	755	2451	-	-	-	-
2SK21	Aug. 3 18:04:07	Video/GSD/Core	757±55	2.83±0.01	848 [779, 974]	677	2479	Type 1	0.66	3.8 (72µm)	0.80
4SK21	Aug. 3 18:04:09	Core	775±54	2.71±0.03	739 [674, 838]	584	2512	-	-	-	-
7SK21	Aug. 3 18:04:10	Core	830±61	2.8±0.09	722 [663, 848]	581	2513	-	-	-	-
10SK21	Aug. 3 18:04:12	GSD	-	-	-	-	-	Type 2	0.58	7.5 (6µm)	0.03
15SK21	Aug. 3 18:08:47	GSD	-	-	-	-	-	Type 2	0.35	5.4 (24µm)	0.65
16SK21	Aug. 3 18:08:48	Video/Core	621±47	1.87±0.06	617 [560, 736]	427	2568	-	-	-	-
19SK21	Aug. 3 18:08:51	Video/GSD/Core	504±36	1.61±0.02	677 [615, 779]	413	2573	Type 1	0.76	5.1 (29µm)	0.09
21SK21	Aug. 3 18:08:52	Video/GSD/Core	613±42	1.38±0.01	382 [349, 434]	388	2582	Type 1	0.76	5.2 (27µm)	0.49
27SK21	Aug. 3 18:08:55	Video/Core	675±50	1.29±0.01	307 [281, 356]	373	2587	-	-	-	-
28SK21	Aug. 3 18:08:56	Core	-	-	-	260	2628	-	-	-	-

Tab. 7.4 Synoptic table reporting data of the aggregates collected during 2 and 3 August. The third column clarifies the source and type of available information (Video: high-speed video; GSD: grainsize of associated deposit collected in tray; Core: information on aggregates core). Statistic of the grainsize distribution of the aggregate shells (when available) are reported (SP-ratio, Median, Skewness) together with physical and aerodynamical parameters measured thanks to the analysis of the high-speed, high resolution videos (size and density of both aggregate and core and velocity of aggregate). Among the aerodynamical parameters, the values of density for each aggregate are also reported (first value outside brackets), calculated as the mode of the generated distribution for density using the Monte Carlo simulations. Density values are listed together with their associated uncertainties, equal to the 68% confidence interval of the generated distribution and displayed as the value corresponding to the 16th and 84th percentile $[\rho_i^{pc16}; \rho_i^{pc84}]$ of the distribution. Aerodynamical parameters relative to samples 4 SK 21 and 21 SK 21 are taken from Bagheri et al. (2016b). SP-ratio is the ratio between the two subpopulations (see main text for details).

Two main types of GSDs are distinguished for the aggregate shells (Fig. 7.4), mostly based on the mode, the values of graphical skewness (Folk, 1968), and the proportion between the internal subpopulations (i.e. SP-ratio = relative weight of SP2 / relative weight of SP1):

- Type 1: bimodal GSDs with the main mode comprised between 4 and 6 ϕ, and a secondary mode (where present) peaked at around 7 ϕ (Fig. 7.4 a-b). This GSD type is characterised by nearly symmetrical to positively skewed distributions (Folk, 1968) and a value of skewness mostly comprised between 0.09 and 0.49, with a single value up to 0.80 (Tab. 7.4). Both the SP1 and the SP2 display similar volume fractions, with an SP-ratio ranging from 0.66 to 1.92 (Tab. 7.4).

- Type 2: bimodal GSDs with a more pronounced main mode peaking mostly around 4.5-5 ϕ; a secondary mode peaked around 7-8 ϕ is also present in two samples (Fig. 7.4 c-d). This GSD type is strongly positively skewed, with skewness values ranging from 0.53-0.75; only one sample shows a

lower value at 0.02 (Tab. 7.4). The coarser SP represents a large volume fraction of the whole GSD (SP-ratio between 0.30 and 0.57; Tab. 7.4).

The two types of GSDs can be roughly related to the aggregate characteristics derived by both the HS-HR videos and the analysis of adhesive paper (Tab. 7.4):

- Shells with Type 1 GSD are mainly associated with aggregates with a thick, fine-ash rind completely enveloping a core formed by one or more larger clasts (classified as PC3) (e.g., samples 16sk19, 21sk21; Fig. 7.4 a-b).

- Shells with Type 2 GSD are mostly related to aggregates with very thin coatings that do not form a discrete and thick rind (classified as PC2) (e.g. samples 20SK20 or 10SK21; Fig. 7.4 c-d).

The dimension of the cores increases with the aggregate size (Fig. 7.4e), although no clear relation appears between the aggregate size and the GSD of the shell (Tab. 7.4). In addition, the diameter of the core in PC2 and PC3 aggregates ranges between 0.5 and 2.5 ϕ (between 180 and 710 µm) resulting in several (up to 2) orders of magnitude larger than the particles forming the shell (Fig. 7.4f). It is also interesting to note that the GSD of the tephra samples corresponding to the aggregates collected on August 2 and 3 are bimodal (orange and dark blue lines in Figure 7.3). Importantly, the average GSD of the shell of all the aggregates (green curve in Figure 7.4f) and the size of aggregate cores (red circles in Figure 7.4f) well correlate with the subpopulations SP2 and SP1 (Tab. 7.3) of the of tephra samples, respectively (blue curve in Figure 7.4f). Since the shell of PC3 is thicker than the shell of PC2 aggregates, we suggest that SP2 of tephra sample GSD mostly contribute to the formation of the external shell of PC3 aggregates.
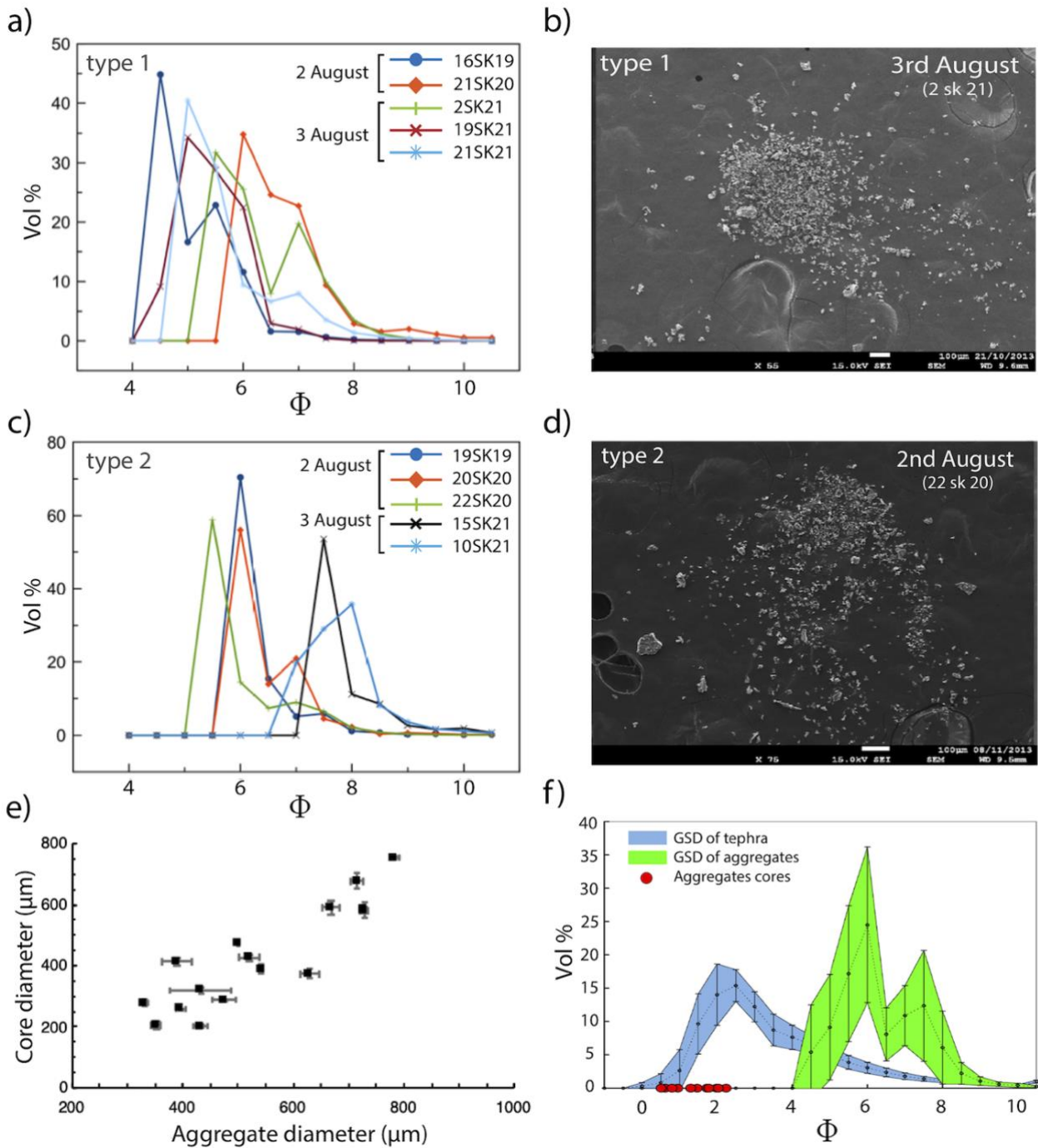
Fig. 7.4 Grain-size distributions of aggregates collected on 2-3 August are reported in different panels according to the type of distribution, together with representative SEM image of the associated coatings. (a-b) Type 1: GSD with high SP-ratio and low skewness; (c-d) GSD with low SP-ratio and high skewness; (e) aggregate size compared with size of the associated cores. (f) Comparison between the average GSD of tephra-fallout samples (blue area), and the average GSD of aggregates (green area). The size of the measured aggregate cores is also reported (red dots).

7.5.4 Aerodynamics of aggregates from HS-HR videos

Obtained dataset on particle settling dynamics and textural features resulted in a larger database compared with previous studies (e.g., Taddeucci et al., 2011, Bagheri et al., 2016a, Miwa et al., 2020). Results of HS-HR video analysis (in terms of the aggregate terminal velocity, density and size) are shown in Figure 7.5 (and summarized in Tab. A2 of the Appendices).
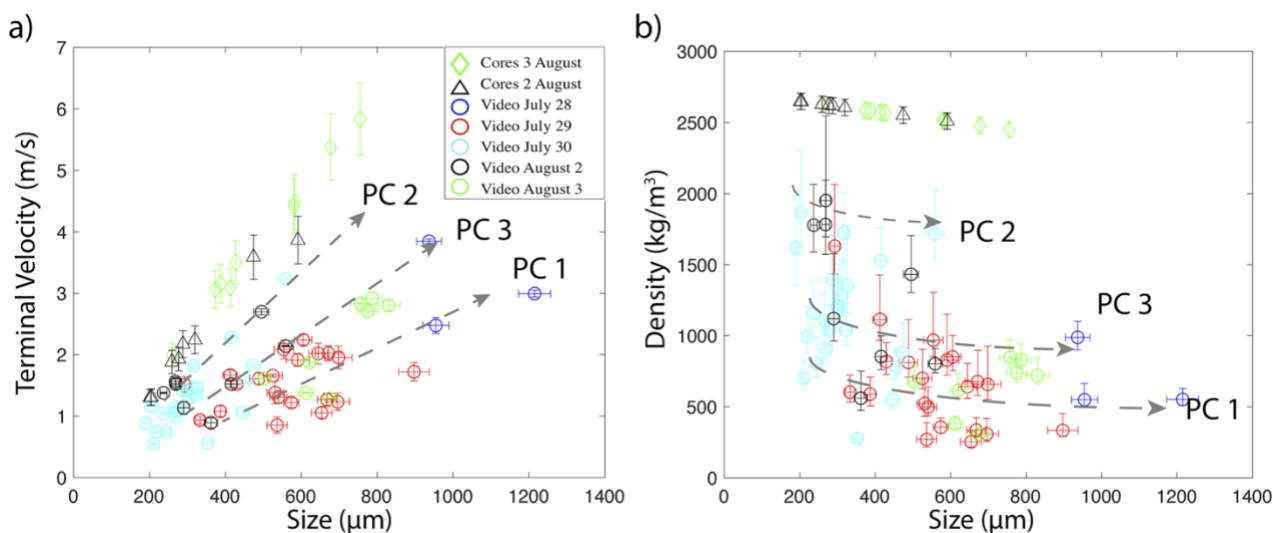
Fig. 7.5 Aerodynamic properties of aggregates (circles) and aggregate cores (triangles and diamonds) analysed with HS-HR camera (colours refer to the day of collection). Terminal velocity of aggregates is measured directly from videos; terminal velocity of cores is calculated with Eq. (2) based on the density derived from the density-size trend obtained by Bagheri et al., (2016a). a) Terminal velocity against size, and (b) aggregate density against size. Dotted arrows define different aggregate types in the space velocity-density-size determined based on visual observations (see main text for more details).

A clustering of the aggregate aerodynamics with the day of collection (different colours in Figure 7.5) is observed. In addition, indicative trends relating the physical properties of the three different types of aggregates that were observed (i.e. PC1, PC2 and PC3) can be tentatively traced based on visual identification (grey dashed lines; Fig. 7.5). In particular, PC1, PC2 and PC3 were distinguished based on a qualitative assessment of the amount of material left on the adhesive paper at the moment of impact. Measured aggregate sizes range between 200 and 1200 μm (Tab. A2). Corresponding terminal velocity varies between 0.5 and 4 m/s, with a large variability (up to 100%) observed for aggregates of similar size. The derived density values range between 250 and 2000 kg/m³. In many cases, PC3 were clearly recognised at impact on the adhesive paper, where the external shell disaggregated and deposited while coarse-grained particles forming the core bounced away. Size of measured cores varies between 200 and 750 μm. Furthermore, in few cases large particles having diameters comprised in the range of 90-250 μm were observed to bounce away together with cores at impact with the adhesive papers. Terminal velocity of the aggregate cores (diamonds and triangles in Figure 7.5 a-b) was calculated using Eq. (2), with volume estimates based on the three measured diameters from videos (Feret diameters: L, I, S) and the density of the cores estimated according to the density-size trend found by Bagheri et al. (2016a). Density values, ranging between 2450-2700 kg/m³, are in agreement with the typical density of Sakurajima magmas (Miwa et al., 2009; Hickley et al., 2016), and with values derived for similar

particles by Bagheri et al. (2016a). Terminal velocity, for these particles, ranges between 1 and 6 m/s and is strongly controlled by size. We assume that the trends defined by the cores (diamond and triangle markers in Figure 7.5a-b), of velocity and density versus size, can be considered as representative of the aerodynamic behaviour of individually falling particles (i.e. not aggregated particles). Consequently, these trends were taken as a reference to better interpret the aerodynamic behaviour of the measured aggregates. Aggregates observed in the analysed HS-HR footages (Fig. 7.5a) generally show a slower increase of terminal velocity with size compared to those calculated for cores, although with a larger scatter.

Iso-velocity sections in the space Density – Aggregate diameter – Terminal velocity clearly show how a given range of terminal velocity can be associated with aggregates of very different size and bulk density (Fig. 7.6). The type of the aggregates collected on 2 and 3 August, visually determined during the video analysis, is specified with labels in the diagram, in order to ease the interpretation of the presented aerodynamics data.
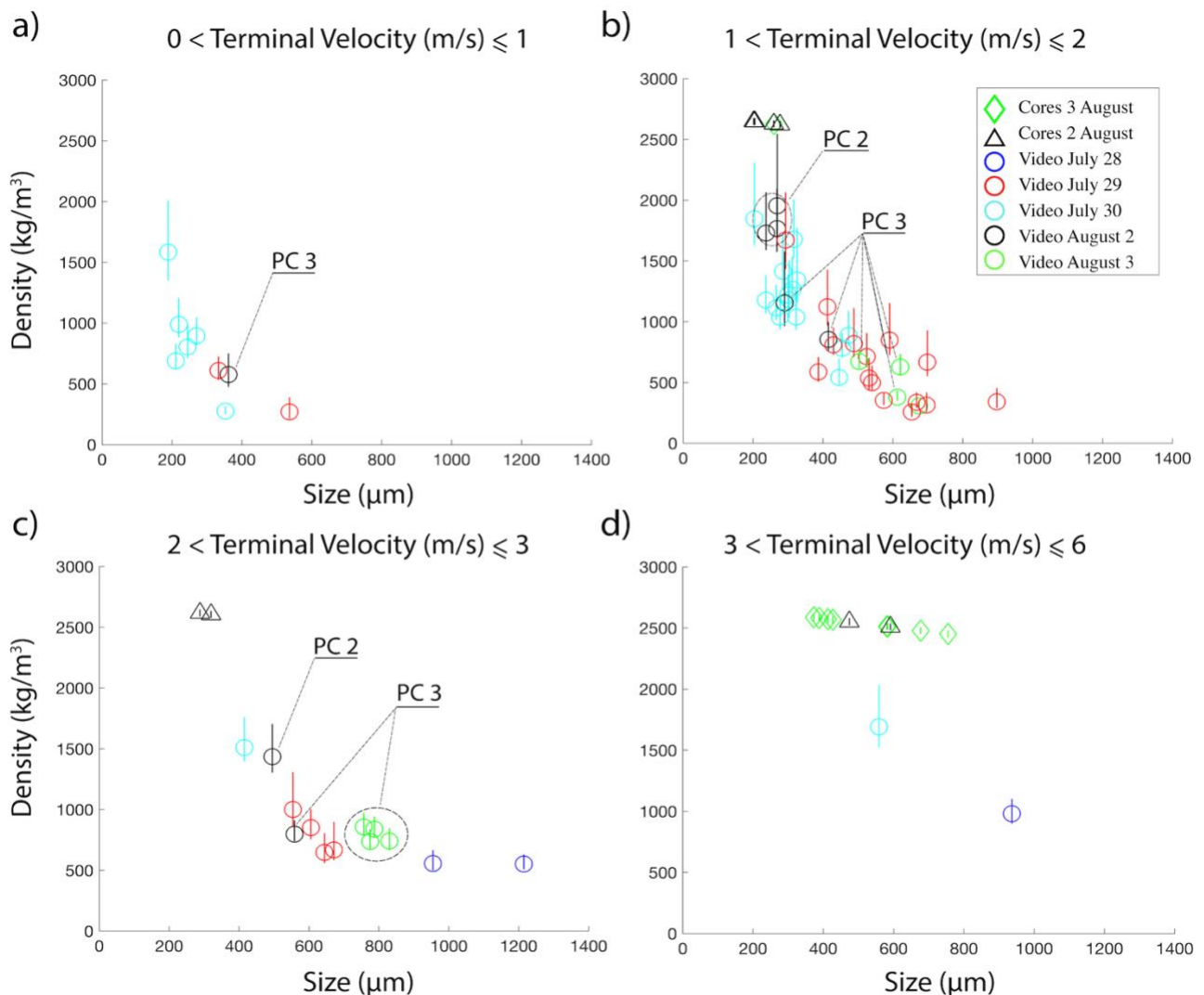
Fig. 7.6 Iso-velocity sections in the space Density – Terminal Velocity – Size for the studied aggregates. (a) Aggregates falling with velocity lower than 1 m/s, (b) between 1 and 2 m/s, (c) between 3 and 4 m/s, and (d) aggregates falling with velocity higher than 3 m/s up to a maximum of 6 m/s. Types of aggregates collected on 2 and 3 August was determined based on video analysis and is specified with labels.

The smallest aggregates (<400 μm) are associated with the lowest terminal velocity (< 2 m/s), the highest density values and the largest density range (mostly 1000-2000 kg/m^3; Fig. 7.6a-b). Three PC2 and one PC3 with low density (around 500 kg/m^3) fall in this space (Fig. 7.6b). On the other hand, large aggregates (>400 μm) generally correspond to lower density values (<800 kg/m^3) and have terminal velocities between 1 and 3 m/s (Fig. 7.6b-c-d). The majority of the identified aggregates from 2 and 3 August falling in this space are PC3. In general, less than 15% of aggregates fall with velocity lower than 1 m/s, and 60% fall with velocity in between 1 and 2 m/s. Velocities higher than 2 m/s are quite uncommon and are generally associated with the cores (diamonds and triangles in Figure 7.6d). Information relative to the internal structure of selected aggregates collected on 2 and 3 August are presented in Figure (7.7).
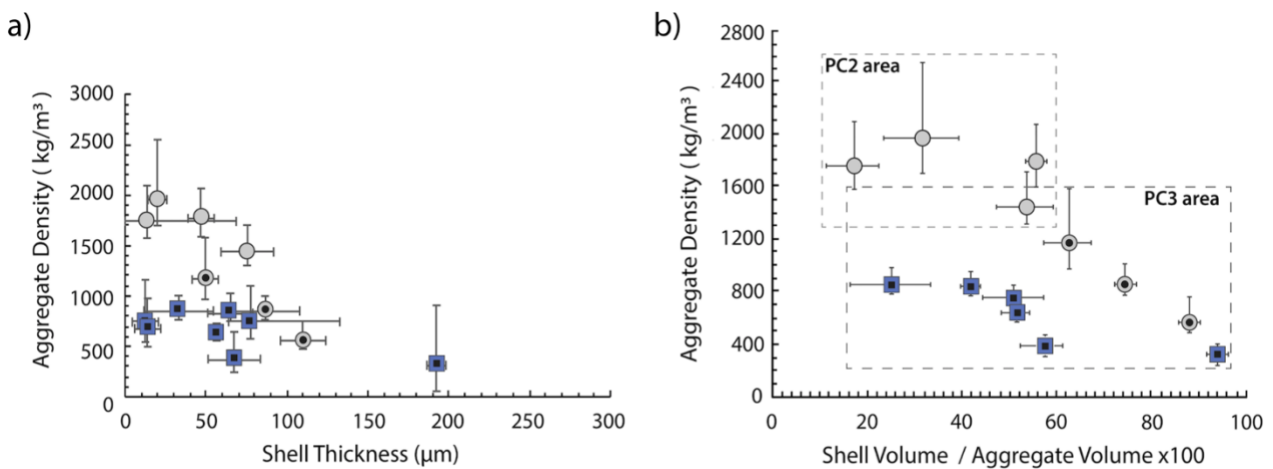
Fig. 7.7 Comparison between the derived aggregate density and quantities related to the aggregate structure (i.e. shell volume and thickness, aggregate volume): grey circles and blue squares refer to aggregates collected on August, 2 and 3, respectively; empty symbols indicate PC2 aggregates and symbols with black internal markers indicate PC3 aggregates. In a) the thickness of the shell (i.e. fine ash layer coating the core) is compared with the aggregate density, while in b) the relative volume of the shell is compared with the aggregate density. The two dashed rectangles represent the fields of existence of the measured PC2 and PC3 aggregates in terms of density and relative volume of shell.

Here, the thickness and the relative volume fraction of the shell with respect to the whole aggregate are compared with the derived density of 11 PC3 and 4 PC2 that were visually identified from HS-HR videos. Based on the evidences reported in Figures 7.5 and 7.6, generally, PC2 aggregates are characterised by a higher density and a lower volume fraction of the shell with respect to PC3 aggregates, while the thickness of the shell is largely variable in both aggregate types. In particular, the measured PC2 aggregates are characterised by density values variable in the range of 1500 and 2000 kg/m^3, and a thickness of the shell between 10 and 80 μm (Fig. 7.7a). On the other hand, the PC3 reported here have density values in the range 400 - 1200 kg/m^3 and a shell thickness between 35 and 200 μm (Fig. 7.7a). A preliminary distinction of the variability of the typical structural characteristics of PC2 and PC3 aggregates was tempted in Figure 7.7b. In particular, these data indicate a volume fraction of the shell mostly comprised > 40% for the PC3 aggregates, associated with an aggregate density generally lower than 1200 kg/m^3. On the other hand, PC2 aggregates are characterised by density values higher than 1200 kg/m^3, and a relative volume fraction of the shell typically < 60%. A sort of

overlap area, in which aggregates can have intermediate shell-volume fraction between that typical of PC2 and PC3, was revealed for volume fractions of the shell in the range 40-60%.

7.6   Discussion

7.6.1   GSD of tephra samples and of aggregating particles

The GSDs of tephra samples are mostly bimodal and can be described as the result of the superposition of two Gaussian subpopulations (SP1 and SP2) (Fig. 7.3, Tab. 7.3). The internal structure of aggregates, characterised by the presence of a core and a shell of fine aggregating ash, well correlates with the bimodal GSD of tephra samples. In particular, the average GSD of the aggregate shells corresponds to the fine subpopulation (SP2) of the tephra GSDs, while the mode of their coarse subpopulation (SP1) corresponds to the size of the internal cores of aggregates (Fig. 7.4f, Tab. 7.4). Furthermore, direct observations indicate that ash aggregation was always active during sedimentation. The variable presence of SP2 in all the ash deposits can be thus considered a direct result of ash aggregation efficiency during the different eruptions. The increasing amount of SP2 generally observed in samples at increasing cross-wind distance (Tab. 7.3) could be also related to an increasing off-axis occurrence of low-density aggregates, generally characterised by a thicker, poorly compacted, low-density external shell formed by fine-grained particles. The relative amount of SP2 in the bulk samples is always lower than SP1, since the fine ash forming the shell of the aggregates only represents, on a weight basis, a low proportion (from few percent to a maximum of around 50 wt.%) of the total GSD of the most common aggregates (PC2 and PC3, dominated by the core particle). The GSD of aggregate shells compares well with those reported in Bonadonna et al. (2011), who estimated an Mdϕ of 5.4 for the aggregates of the 2010 Eyjafjallajökull eruption, and in Bagheri et al. (2016a), who measured Mdϕ between 4.5 and 5.5 ϕ for other PC3 Sakurajima aggregates. These observations confirm that the process of aggregation is highly efficient for ash finer than around 4-5 ϕ (i.e. around 45 μm) (Fig. 7.4f, Tab. 7.4).

The analysis of the video footages also reveals that aggregates are rarely larger than 800-900 μm (Tab. A2), and cores found in the aggregates rarely exceed 500 μm, confirming thus the results reported in Bagheri et al. (2016a) that found a core size comprised between 200 and 600 μm. We suggest that the cores of PC3 as well as the poorly covered particles of PC2 contributed to form SP1, while the SP2 present in each sample is mostly associated with the shell of the PC3 aggregates and, albeit in minor proportion, also with particles forming the shell of PC1 (Figs. 7.4f, 7.7). As the ash particles forming the shell of the aggregates represent a largely variable proportion of each aggregate in terms of volume (Fig. 7.7b), we conclude that GSD of tephra samples is the complex result of the accumulation of different types of aggregated particles, each contributing in different proportions to SP1 and to the early fallout of the finer-grained fraction (SP2). On the other hand, the variability observed in the GSDs of aggregating ash (Fig. 7.4, Tab. 7.4) is in accord with the difference revealed in internal structures of the identified aggregates (Figs. 7.6, 7.7). The GSD of aggregating ash is generally bimodal and shows

a positively skewed distribution (Fig. 7.4 a-c). In particular, PC3 aggregates, showing a distinct external shell formed by fine ash, are indeed characterised by a bimodal, dispersed GSD (aggregates of Figure 7.4 a-b), very different from that shown by the ash adhering to coated particles PC2, which is generally strongly peaked and fine to very fine-grained (aggregates of Fig. 7.4 c-d). This results in a general higher density of PC2 with respect to PC3 aggregates, since they are characterised by lower relative volume fractions of the shell respect to the aggregate (Fig. 7.7).

In the context of the same eruption, these two types of aggregates possibly indicate either variable conditions of ash aggregation under different eruptive and environmental conditions (in terms, for example, of ash concentration), or different time steps of the same aggregation process around a core. Unfortunately, PC1 aggregates were only observed in videos (Fig. 7.5) but were not collected in adhesive paper and, therefore, the associated structure and GSD could not be analysed and compared with the characteristic of PC2 and PC3 types.

7.6.2   The dynamics of aggregates deposition

The analysis of the HS-HR footages allowed us to characterise the aerodynamic behaviour of falling aggregates and to describe their internal structure before impact and disruption on the adhesive paper. The analysis of the filmed aggregates revealed a wide range in both terminal velocity and density (Fig. 7.5). Measured terminal velocities are between 0.5 and 4 m/s, with most values between 1 and 2 m/s (Fig. 7.6). Density and size vary in a wide range (250 - 2000 kg/m^3 and 200 - 1200 µm, respectively). In particular, Figure 7.6 shows a large variation either in the values of density and terminal velocity for aggregates having a size in the range of 200 – 650 µm. This aspect suggests that, given an average density of single particles (non-aggregated) in the range of 2400-2700 kg/m^3, the small aggregates (200-300 µm) associated with the highest density (>1000 kg/m^3) and velocity in the range of 1 and 2 m/s, are possibly formed by large particles covered by a very thin and discontinuous shell of ash (PC2). If this is the case, the thickness of the shell has a minor effect on the aerodynamics of the whole aggregate, whose behaviour is similar to non-aggregated particles. Conversely, large aggregates (>350 µm) falling with velocities between 1 and 3 m/s, are always associated with a density lower than 1000 kg/m^3, suggesting the presence of a thick ash shell, which represents a large fraction of the total volume of the aggregate (PC3). This strongly affects the aerodynamics of these aggregates, making them clearly distinct from single particles.

All these values are in good agreement with the results of Bagheri et al. (2016a) and Miwa et al. (2020) for similar eruptions of Sakurajima volcano, even though Miwa et al. (2020) also report some higher values of terminal velocity (i.e. 6.5 m/s), corresponding however to unlikely density for volcanic particles (i.e. 4400 kg/m^3).

The very similar meteorological conditions during sample collection in the eruptions of August 2 and 3 (Fig. 7.2) suggest a stronger dependence of the aggregation modalities on eruptive conditions and aggregation dynamics rather than on atmospheric parameters. In particular, the few aggregates measured on July 28 show size greater than 900 µm and density lower than 1000 kg/m^3, while aggregates collected on July 30 are all below 500 µm in size and have a largely variable density, between 500 and 2000

kg/m³ (Fig. 7.5). Aggregates from July 29 and August 3 have instead a large size (between 400 and 800 μm) associated with density values lower than 1000 kg/m³. Moreover, the relation between the relative volume of the shell with the density of the aggregates collected on August 2 and 3 confirmed an important difference between physical and structural characteristics of PC2 and PC3 aggregates (Fig. 7.7). The same data also indicate that aggregates collected on August 2 slightly differ from those collected on August 3 since the PC3 aggregates collected during this latter eruption are less dense and characterised by a lower relative volume of the shell (Fig. 7.7b). These high-detail data provided for selected aggregates are well in accord with the trends shown by the general dataset (Fig. 7.5) where, again, there is a clear relationship between the aerodynamics of aggregates (and hence structure) and day of collection. Finally, the link between the internal structure, and hence the type of aggregates, and their aerodynamic behaviour is unravelled in Figure 7.6, where the type of selected aggregates collected on August 2 and 3 is indicated. These aggregates, together with their cores (i.e. single particles), represent a reference useful to interpret the nature of all the other aggregates measured in the context of this study, and justify the trends traced in Figure 7.5. The critical analysis of all the presented data, combined with direct observations of the video footages, can inform about the nature of the different falling aggregates allowing the quantitative characterisation of three different aggregate categories, reported below in decreasing order of abundance:

1) *PC3:* aggregates with diameters comprised between 400 and 900 μm, velocity in the range 0.5-3.5 m/s and density between 500-1500 kg/m³. They represent the majority of the aggregates falling during the entire period of observation (with around 40 aggregates detected) and are characterised by an internal core and an external shell which is largely variable in thickness. The relative volume of the shell with respect to the aggregate is typically higher than 55%. The thickness of the shell controls the density, with the lowest calculated values (around 500 kg/m³) corresponding to aggregates having a shell thick around 200 μm that represents the 90% of the volume of the whole aggregate (Fig. 7.7a). The structural framework of these aggregates shows also a good relation with the day of collection, being particles collected on August 2 generally characterised by a higher volume fraction of the external shell (Fig. 7.7b). This group of aggregates corresponds to the cored clusters observed by Bagheri et al. (2016a) and, possibly, by Miwa et al. (2020).

2) *PC2*: some aggregates from July 30 and August 2, plotting close to the core trend-line and showing high velocities compared with the diameters (up to 3 m/s and 200-550 μm, respectively; Fig. 7.5a), possibly represent the PC2 of Brown et al. (2012), with an associated density of 1500-2000 kg/m³ (Fig. 7.5b). The aerodynamic properties of these aggregates, similar to those of single particles, can be explained as related to the presence of a very thin, discontinuous layer of coating ash on a coarse particle, which only weakly influenced its fallout behaviour. Normally, the relative volume of the shell is below 30%.

3) *PC1:* few aggregates (less than 10) showing large diameters and very low density (350 to 1200 μm and <500 kg/m³, respectively; Fig. 7.5b), together with a terminal velocity generally below 2 m/s (except for two of the coarser aggregates, larger than 900 μm; Fig. 7.5b). If present, the volume of the central particle is negligible with respect to the shell (Fig. 7.7a-b). These aggregates, not always

clearly distinguishable on samples collected on adhesive papers, can be associated to PC1 of Brown et al. (2012). The low density is similar to that estimated for electrostatically aggregated ash by James et al. (2003).

Particle clusters similar to those analyzed and described here are frequently observed during fallout from ash-dominated eruptions worldwide. As a consequence, the presented dataset of measurements is of primary importance particularly for the in-depth characterization of natural ash aggregates. In particular, data collected on the numerous PC3 aggregates observed here represent a novel, very important step forward in the recognition of the effects of aggregation on ash sedimentation and formation of tephra deposits. Even though these aggregates are typically not preserved in the deposits, they have been shown to control the main features of the resulting ash deposit due to their abundance. In fact, their bimodal GSD related to a thick, fine-grained external shell mantling few (although mass-dominant) coarser particles, well correlates with the GSD bimodality of the associated ash deposits.

7.7 Conclusion

The presented results form a wide and reliable dataset of particle clusters including important physical and aerodynamic parameters (i.e. terminal velocity, density and size), which are extremely valuable for the physical characterisation of aggregates and aggregating ash, and for the validation of volcanic ash transport and dispersal models in the context of explosive Vulcanian activity. Three main types of aggregates (Cored Clusters (PC3), Coated Particles (PC2), and Ash Clusters (PC1)) were identified and characterised based on direct measurements of size and terminal velocity, on the derived estimates of their density and on their internal characteristics: size of the core, GSD of the external shell, and relative volume fraction of the aggregating shell. The discovery of highly variable limits for density and terminal velocity of aggregates collected at the same time and location, along with the accurate quantification of the average grain size and the relative volume fraction of the aggregating ash internal to PC2 and PC3 aggregates and the typical size of the inner cores, shed new light on the characterisation volcanic ash aggregates. Our detailed investigations show how:

- PC3-type is the most abundant group representing more than 60% of the observed aggregates; they show important variations in size (200-800 μm) and in density (500-1500 kg/m^3). PC3 size is positively correlated with the size of the internal core, while aggregate density shows a negative relation with the thickness of the shell, with the thickest shells (90% in volume respect to the aggregate) being associated with an overall low density of the aggregate (down to around 500 kg/m^3) (Fig. 7.7).

- The relative volume fraction of the external shell of PC3 with respect to the whole aggregate is mostly > 40%. The GSDs of the ash enclosed in the shell of these aggregates display a positively skewed and bimodal GSD, with around 50% of the associated tephra-fallout sample represented by SP2 and the modes peaked around 5-6 ϕ (Fig. 7.4). Considering that PC3 are abundant during all the investigated period, and the shell of PC3 can represent a significant volume fraction of the whole aggregate volume (> 40 % vol.), we suggest this category as the one that mostly controlled the

dynamics of the fine ash dispersal during the analysed eruptions at Sakurajima. PC2 aggregates have the highest density, in the range of 1500-2000 kg/m^3, and are characterised by terminal velocities similar to those calculated for single particles, since they have a very thin external shell.

- The relative volume of the shell with respect to PC2 aggregate is between 10 and 60 % vol. (Fig. 7.7). The shell GSD is highly sorted and peaked around 6-8 ϕ, with low deposit fractions (around 25 %) represented by the SP2 (Fig. 7.4). We suggest that this median size is mainly related to the availability of fine ash within the eruptive plume.

- Aggregate shells consist of ash particles < 45 µm for both PC2 and PC3 (Fig. 7.4). Moreover, the GSD of tephra samples is strongly influenced by the type and the availability of aggregates in the deposits, being the cores and the shells of particle clusters similar in size to the coarser and finer subpopulation of tephra samples, respectively (Fig. 7.4). Despite the identification of a semi-quantitative limit to distinguish between PC2 and PC3 based on the aggregate density (approx. 1200 kg/m^3) and the relative volume of the shell (approx. 40-60 % vol.), we suggest that a progressive transition should exist between the structural features of these two categories of aggregates. The few detected PC1, showing large diameters (400-1000 µm) and very low density (200-500kg/m^3), are the result of fine ash aggregation in the absence of an aggregating core. Due to their low abundances, no PC1 aggregate was directly collected with adhesive tapes, and consequently no GSD was provided for this type of aggregates.

- The physical parameters (i.e. size, density and terminal velocity) of aggregates show a very wide variation amongst the different eruptive events, with the largest and least dense aggregates being associated with the activity of 28 July, and the smallest and highest density aggregates associated with the activity of July 30 (eruption registered at 17.03 JST) (Figs. 7.5, 7.6). A strong relation was found between the aggregate aerodynamics and structure (and hence type), with the day of activity. In particular, we note that size and density of aggregates analysed during August 2 and 3 are variable, with the largest and least dense PC3 aggregates being associated with the activity of August 3. According to the stable atmospheric conditions at the time of aggregate formation and collection, differences in the internal structure observed between the aggregates of the different days of activity could be mostly related to primary differences in eruptive conditions (e.g., ash concentration and grain size of the eruptive mixture in the plume).

- The combination of kinetic data, measured from HS-HR imaging, with information extracted from tephra samples and aggregates collected on adhesive papers, confirmed to be a state-of-the-art technique necessary to provide important insights into the understanding of aggregation processes, and the associated impact on fallout dynamics. The statistical treatment of aerodynamic and physical data, and the large number of investigated aggregates make the presented results a benchmark reference for the validation and calibration of numerical schemes for particle aggregation. Such a wide dataset derived from our multidisciplinary strategy is particularly important for the characterisation of particle clusters, which have recently been shown to be amongst the most common aggregate types during ash-rich fallout but are not preserved in tephra deposits. In particular, the abundancy of PC3 aggregates reconciles the presence of a large amount of fine ash (aggregate shell)

with coarse ash (aggregate core) and better explains GSD bimodality of deposits and high aggregate settling velocities.

7.8 Appendices

A1 GPS coordinates of the field sampling positions

During the field sampling, HS-HR videos and tephra samples were collected in a set of locations labelled with 'SK' codes. The GPS coordinates corresponding to all the sampling locations is reported in Table (A1):

Sample Location	Latitude°	Longitude°
SK 2	31.577324	130.706517
SK 3	31.592497	130.708307
SK 4	31.587353	130.701114
SK 5	31.587337	130.706022
SK 6	31.58977	130.709186
SK 7	31.579322	130.704066
SK 18	31.557901	130.704302
SK 19	ibid.	ibid.
SK 20	ibid.	ibid.
SK 21	31.553007	130.688873

Tab. A1 The 'SK' codes used for displaying the sampling locations in Fig. 7.1, together with the corresponding GPS coordinates (Decimal format).

A2 Uncertainties on measured and derived quantities

A2.1 Uncertainties on measured and derived quantities from video analysis:

Terminal velocity, aggregates dimension and shape are the primary quantities directly extracted from the HS-HR video analysis; these parameters are then used to derive equivalent diameters and densities of the aggregates.

The measurement procedure generally consists of a frame-by-frame analysis of each video. However, several aspects contribute to the uncertainty. The falling objects are assumed to move vertically at their terminal velocity V_t. This assumption has been verified measuring the maximum variability of the vertical component of the velocity vector along the trajectory, i.e. $\Delta V_t = \frac{V_t^{max} - V_t^{min}}{2}$, where V_t^{min} and V_t^{max} represent the minimum and maximum velocities recorded for each single aggregate in the video frames. The average value of the variability ΔV_t measured over all the population of aggregates is about 4% respect to the values of the terminal velocities (i.e. $\langle \frac{\Delta V_t}{V_t} \; x \; 100 \rangle \approx 4\%$). The uncertainty δV_t associated with the terminal velocity is assumed to be equal to the standard deviation of the velocity measurements of each object (uncertainty of type A, i.e. the statistical component of the error), with the assumption

that the uncertainty related to other components (uncertainty of type B), such as the error associated with the internal clock of the camera and the pixel size, is negligible. The terminal velocities measured for all the samples are characterized by a minimum relative error of 0.02% and a maximum relative error of 9%.

Aggregate sizes and shape are derived from the measurement of the long (L), intermediate (I) and short (S) axes as defined in Bagheri et al. (2015). From a practical point of view, Fiji allows measuring the three axes as follows: L is taken as the maximum Feret diameter of the frame where the aggregate shows the largest projected area in pixels; I is the minimum Feret of the same frame; S is the minimum Feret of the image where the aggregate has the minimum area. The equivalent diameter of the falling object is finally calculated using Eq. A1 (Bagheri et al., 2015).

The uncertainty δL has been evaluated as the standard deviation of all the maximum Feret diameters of the particle as measured on different frame; δS as standard deviation of all the minimum Feret diameters along the trajectory; finally, we attributed the maximum between $\delta L/L$ and $\delta S/S$ to the relative of each δL. This means assuming that the relative error on the parameter L is of the same order of magnitude of the largest relative error on the other two parameters.

The uncertainty over the equivalent diameter, δd_{eq}, is calculated using the linearized propagation of errors for mutually independent variables applied to Eq. (1), where $\alpha = L \cdot I \cdot S$:

$$\delta d_{eq} = \frac{0.928}{3} \cdot \alpha^{-2/3} \cdot \sqrt{(IS)^2 \cdot \delta L^2 + (LS)^2 \cdot \delta I^2 + (LI)^2 \cdot \delta S^2}$$

Eq. (A1)

The equivalent diameters calculated for all the samples are characterized by a minimum relative error of 16% and a maximum relative error of 19%.

Additionally, the size of either the cores and the aggregates collected during 2-3 August was also evaluated separately. Each video has been investigated in order to select the two frames where particles were best resolved. Their size was then measured as the diameter of the equivalent circle, and the related error estimated as the maximal associated uncertainty:

$\Delta d_{eq} = abs|\frac{deq^{f1} - deq^{f2}}{2}|$, where deq^{f1} and deq^{f2} represent the particles diameters in the two frames. These data were then used to make a morphometrical comparison between the different constituents forming aggregates.

As reported in Eq. (1) the density of aggregates is a derived parameter and has a non-linear relationship with many variables (i.e. the measured terminal velocity, shape, diameter, and fluid density). It is worth noticing that in Eq. (2) the terminal velocity enters both explicitly and implicitly in the drag coefficient C_d. In this case, the procedure followed for the estimation of the uncertainty consists in a Monte Carlo approach to the resolution of the problem. In detail, the Monte Carlo simulation allows computing the Probability Density Function (PDF) associated with the parameter *density* for a generic object i, starting from the initial PDF of its terminal velocity and size. Both these PDFs are assumed to be Gaussian with mean equal to V_t^i and d_{eq}^i, and standard deviation δV_t^i and δd_{eq}^i respectively. The i-th density PDF is the result of 10^6 randomly sampled combinations of terminal velocity and diameter; air density is assumed

to be known with a negligible error. Once that the density of the i-th object is described in terms of its PDF, the *mode $\tilde{\rho}_i$* of the distribution has been used as final indicator for the i-th aggregate density. The uncertainty interval associated to each density has been taken equal to $[\rho_i^{pc16}; \rho_i^{pc84}]$, where ρ_i^{pc16} and ρ_i^{pc84} indicate the 16th and 84th percentile of the distribution respectively. This interval corresponds to a 68% confidence interval and it is the one represented in Figs. 7.4b-7.5-7.6a and the values reported in Table (A2).

A2.2 Uncertainties in the estimation of GSDs of aggregating particles:

The GSD of the coating ash (stacked on adhesive tapes) is derived by image analysis through the particle-by-particle manual contouring of the collected SEM images. Two possible sources of uncertainty are introduced by this method: 1) the statistical representativeness of the number of measured particles; 2) the precision with which the value of the particle area is derived trough the manual contouring. The first uncertainty was approached checking the stability of the grain size distribution by increasing the number of considered particles until no significant changes in the distribution has occurred. Typically, the distributions tend to become statistically representative when the numbers of considered particles exceeds 1000-1500. In Fig. A1 a and b, is reported, as an example, the comparison between particles counted within a manually defined area (i.e. red box) during the contouring operations in tracking the shell exactly above the real contour line. Considering an SEM image relative to a single cluster of fine ash collected on adhesive tape, all the particles forming the aggregate coating have been contoured two times applying different strategies. Results were then compared in order to show the highest uncertainty associated to the operation of manual contouring. The selected SEM image was contoured a first time selecting the internal shell of each particles. Then, a second contouring was done focusing the tracing of the contour of the particle along the external side. Values obtained from both the contouring approaches were compared considering the equivalent area of segmented particles, in order to derive the largest relative uncertainty due to operator-dependent errors. As it clearly appears from Fig. A1 c, the maximum uncertainty is associated to the very fine fraction of contoured particles (<2 μm in size) which always represent a negligible fraction of the coating particles, since both the manual error and the thickness of the pen-line (which is constant despite the variation of the particles size) are more important. The optical resolution of acquired SEM images is constant, thus a constant dependency of uncertainty with size is expected for all the images.
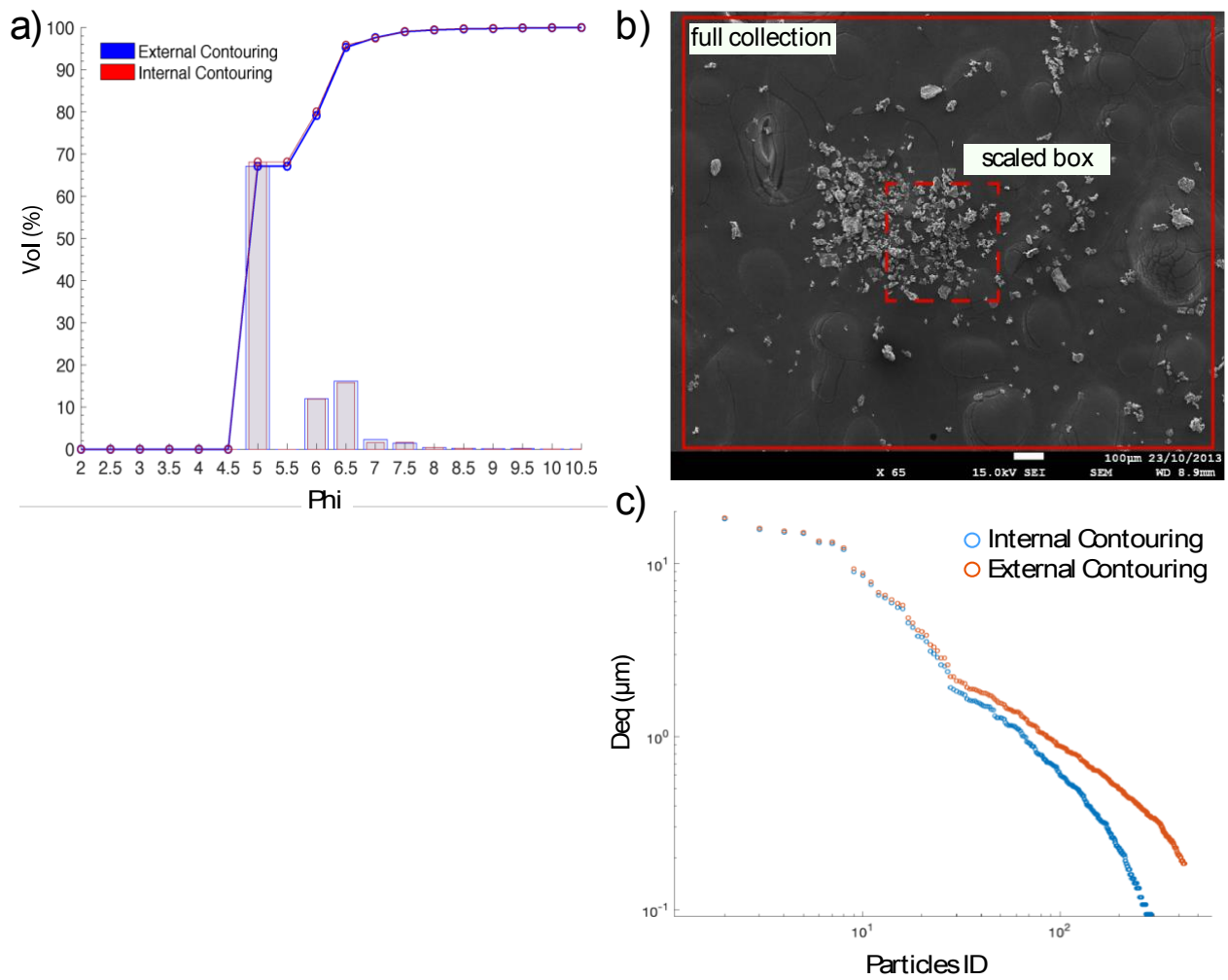
Fig. A1. Treatment of uncertainties relative to the methods employed for particles selection and contouring during image analysis. a-c) GSD and size frequency of particles derived from a full image collection (full scale box) are compared with data from collection over a reduced area (scaled dotted box). d) Size variation between particles contoured along the internal (Blue dots) and external (Red dots) shell.

A3 Aerodynamics parameters of aggregates

The aerodynamics parameters extracted from the HR-HS video analysis for the 62 aggregates collected are listed in the Table (A2) together with information relative on the eruptive time and the timing of video and aggregates collection.

Video ID	Timing of Eruption	Timing of video collection	Timing of aggregate collection	Particle ID	Site	Aerodynamics parameters		
						Size	Terminal Velocity	Density
	(JST)	(JST)	(JST)			(µm)	(m/s)	(kg/m3)
July 28 SK04	Nd	11.31-11.49	11:49:03	2	SK 04	1215 ± 84	2.99 ± 0.06	552 [508, 629]
			11:49:05	3	SK 04	937 ± 65	3.85 ± 0.04	989 [899, 1102]
			11:31:54	4	SK 04	955 ± 69	2.48 ± 0.13	550 [498, 665]
July 29 SK04	11:10	11.20-11.27	11:27:16	2	SK 04	525 ± 50	1.66 ± 0.03	700 [627, 906]
			11:27:17	5	SK 04	605 ± 45	2.24 ± 0.09	851 [756, 1001]
			11:27:19	6	SK 04	668 ± 50	1.27 ± 0.11	337 [290, 422]
			11:20:54	7	SK 04	333 ± 24	0.94 ± 0.07	604 [533, 724]
			11:20:55	8	SK 04	644 ± 50	2.02 ± 0.17	642 [559, 806]
			11:20:55	9	SK 04	654 ± 55	1.06 ± 0.09	254 [219, 326]
			11:20:55	10	SK 04	591 ± 61	1.91 ± 0.11	830 [724, 1153]
			11:20:55	11	SK 04	897 ± 81	1.72 ± 0.15	334 [290, 455]
			11:20:55	12	SK 04	540 ± 45	1.31 ± 0.1	499 [438, 638]
			11:20:55	13	SK 04	430 ± 32	1.52 ± 0.06	819 [727, 952]
			11:20:56	14	SK 04	531 ± 42	1.38 ± 0.18	524 [434, 702]
			11:20:56	15	SK 04	696 ± 61	1.23 ± 0.14	309 [257, 418]
			11:20:56	17	SK 04	554 ± 51	2.09 ± 0.15	969 [853, 1306]
			11:20:56	18	SK 04	671 ± 68	2.02 ± 0.12	677 [581, 897]
			11:20:57	21	SK 04	293 ± 24	1.52 ± 0.13	1630 [1434, 2066]
			11:20:57	22	SK 04	488 ± 49	1.61 ± 0.1	812 [709, 1114]
			11:20:57	23	SK 04	536 ± 52	0.85 ± 0.13	271 [217, 389]
			11:20:58	25	SK 04	698 ± 71	1.96 ± 0.18	658 [553, 928]
			11:20:59	26	SK 04	413 ± 37	1.67 ± 0.08	1115 [968, 1428]
			11:20:59	27	SK 04	386 ± 29	1.08 ± 0.09	590 [507, 709]
			11:20:59	28	SK 04	574 ± 40	1.22 ± 0.08	357 [315, 420]
July 30 SK06	Nd	11.38	11:38:40	9	SK 06	270 ± 20	0.98 ± 0.01	907 [250, 316]
July 30 SK06	Nd	14.37	14:37:41	3	SK 06	353 ± 24	0.56 ± 0.01	276 [1014, 1304]
July 30 SK05	Nd	16:16-16:24	16:16:10	4	SK 05	266 ± 20	1.14 ± 0.01	1104 [1069, 1381]
			16:17:45	5	SK 05	236 ± 17	1.04 ± 0.02	1161 [1094, 1390]
			16:19:45	6	SK 05	300 ± 22	1.42 ± 0.01	1201 [1138, 1537]

Date/Location	Eruption time	Time range	Exact time	#	SK code			Density $[\rho_i^{pc16}; \rho_i^{pc84}]$
			16:21:41	7	SK 05	312 ± 26	1.46 ± 0.04	1288 [936, 1216]
			16:24:04	8	SK 05	277 ± 20	1.11 ± 0.03	1044 [817, 1049]
July 30 SK07	17.03	17:17- 18:30	17:17:52	13	SK 07	245 ± 21	0.74 ± 0.04	806 [711, 991]
			17:17:52	17	SK 07	204 ± 17	1.16 ± 0.08	1867 [1626, 2308]
			17:17:56	18	SK 07	446 ± 38	1.06 ± 0.05	552 [482, 695]
			17:27:47	19	SK 07	326 ± 33	1.46 ± 0.07	1354 [1161, 1775]
			17:27:47	21	SK 07	285 ± 24	1.42 ± 0.05	1397 [1259, 1710]
			17:27:47	22	SK 07	473 ± 41	1.82 ± 0.04	884 [799, 1089]
			17:27:48	23	SK 07	558 ± 49	3.23 ± 0.05	1717 [1525, 2034]
			17:27:48	24	SK 07	323 ± 24	1.34 ± 0.05	1039 [931, 1231]
			17:27:50	26	SK 07	455 ± 33	1.59 ± 0.04	778 [705, 908]
			17:48:05	31	SK 07	316 ± 25	1.81 ± 0.04	1722 [1522, 2005]
			17:48:05	32	SK 07	415 ± 29	2.28 ± 0.03	1525 [1396, 1760]
			17:48:05	33	SK 07	220 ± 18	0.74 ± 0.02	994 [882, 1207]
			17:48:07	34	SK 07	303 ± 27	1.28 ± 0.06	1180 [1034, 1506]
			18:30:19	37	SK 07	189 ± 15	0.88 ± 0.09	1619 [1351, 2010]
			18:30:27	39	SK 07	211 ± 17	0.55 ± 0.01	701 [617, 830]
August 2 SK19	Nd	14:54- 15:08	14:54:30	16	SK 19	362 ± 35	0.89 ± 0.08	561 [475, 751]
			14:56:15	17	SK 19	416 ± 31	1.52 ± 0.05	854 [761, 1000]
			15:04:54	18	SK 19	268 ± 20	1.56 ± 0.07	1783 [1574, 2094]
			15:08:15	19	SK 19	290 ± 30	1.14 ± 0.10	1121 [964, 1576]
August 2 SK20	Nd	16:47- 17:02	16:47:00	20	SK 20	559 ± 38	2.14 ± 0.01	804 [739, 911]
			16:49:23	21	SK 20	237 ± 18	1.38 ± 0.01	1778 [1590, 2066]
			16:53:55	22	SK 20	495 ± 39	2.7 ± 0.05	1432 [1303, 1704]
			17:02:41	23	SK 20	269 ± 25	1.52 ± 0.08	1951 [1697, 2546]
August 3 SK21	17:46	18:04- 18:09	18:04:06	1	SK 21	787 ± 54	2.92 ± 0.01	831 [766, 943]
			18:04:07	2	SK 21	757 ± 55	2.83 ± 0.01	848 [779, 974]
			18:04:09	4	SK 21	775 ± 54	2.71 ± 0.03	739 [674, 838]
			18:04:10	7	SK 21	830 ± 61	2.8 ± 0.09	722 [663, 848]
			18:08:48	16	SK 21	621 ± 47	1.87 ± 0.06	617 [560, 736]
			18:08:51	19	SK 21	504 ± 36	1.61 ± 0.02	677 [615, 779]
			18:08:52	21	SK 21	613 ± 42	1.38 ± 0.01	382 [349, 434]
			18:08:55	27	SK 21	675 ± 50	1.29 ± 0.01	307 [281, 356]

Tab. A2 Information relative to the HR-HS videos dataset. The sampling location (SK codes) and the exact time of collection of the 62 observed aggregates is reported, together with physical and aerodynamics parameters. The timing of the eruptions is reported according to communications with SVO (Sakurajima Volcano Observatory); eruption timings that were not available in SVO archives are reported here as 'Nd'. In the last column, are reported the values of density (first value outside parenthesis) calculated for each aggregate using the Monte Carlo simulation together with the associated uncertainty (equal to the 68% confidence interval of the generated distribution) displayed as the value corresponding to the 16th and 84th percentile of the distribution $[\rho_i^{pc16}; \rho_i^{pc84}]$.

A4 Selected HS-HR camera videos of falling aggregates

Selection of HS-HR videos used in this study to derive the aerodynamics and physical parameters of aggregates and the associated cores.
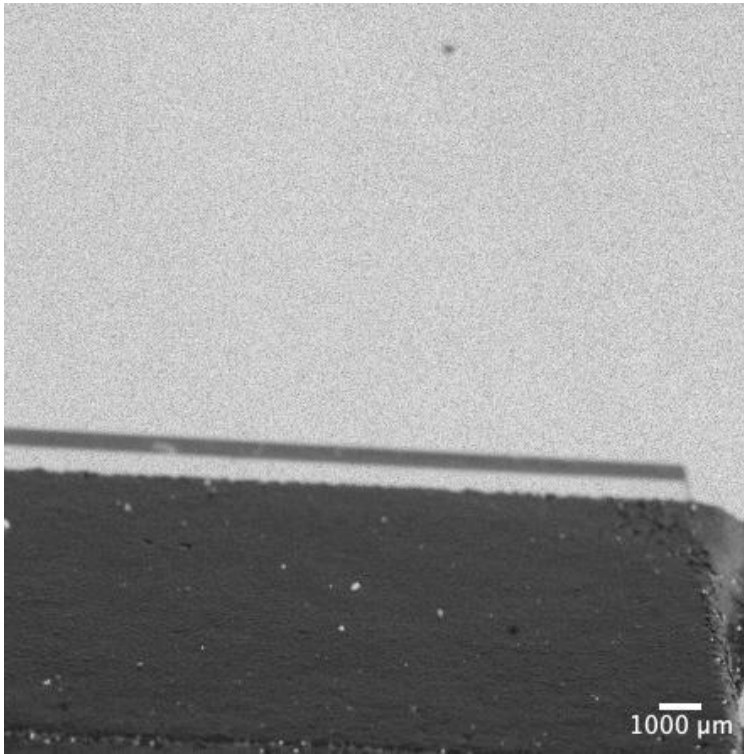
Movie 1. *HS-HR* video of the aggregate 21SK20 collected on 2 August and filmed at impact with the adhesive paper. This aggregate is a PC2, and has a diameter of 237±18 µm, a terminal velocity of 1.38±0.01 m/s, and a density of 1778[1590, 2066] kg/m³. The internal core has a diameter of 232 µm.
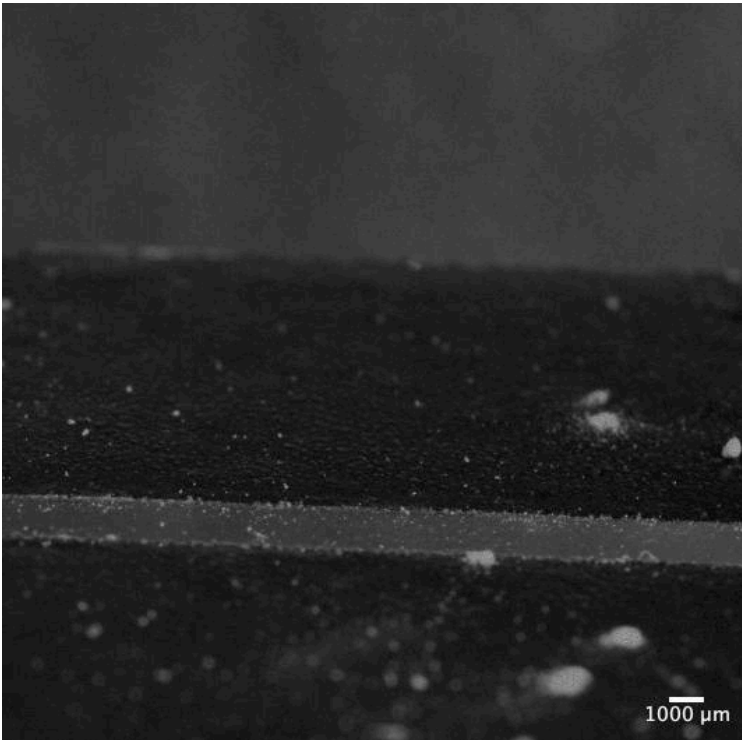
Movie 2. HS-HR video of the aggregate 1SK21 collected on 3 August and filmed at impact with the adhesive paper. This aggregate is a PC3, and has a diameter of 787±54, a terminal velocity of 2.92±0.01 and a density of 831 [766, 943]. The internal core has a diameter of 755 µm.

Chapter 8
Conclusive remarks

8.1   A general outlook on the ash life-cycle in the context of Vulcanian activity

Several aspects of the unsteady, mid-intensity Vulcanian activity are addressed in the dedicated literature, including seismological and acoustic observation of magma migration inside the conduit (e.g. Cannata et al., 2009; Johnson et al., 2011; Valade et al., 2016), numerical modeling and simulations of the explosive processes (e.g. Melnik & Sparks, 1999; Clarke et al., 2002), and also petrological study that fairly clarify what are the relations existing between the deeper magma reservoirs and the shallower feeding dyke/s (Clocchiatti et al., 1994; Couch et al, 2003; Clarke et al., 2007; Palano et al., 2017). However, the accurate observation of the different types of juvenile and lithic material ejected during this activity still represents a unique, powerful tool to gain direct insights on the variety of processes and the complex dynamics of this highly transient eruptive activity. Consequently, numerous outstanding issues about the complex interplay between conduit mechanisms affecting magma during its ascent along the conduit, and their relationships with the resulting eruptive dynamics, are to date still unsolved topics. This thesis explores some of the most important aspects involved in the natural life-cycle of volcanic ash produced in the context of the mid-intensity, unsteady and cyclic Vulcanian activity, trying to answer to fundamental and long-standing questions like:

- Why do sudden transitions in the eruptive style occur during cyclic Vulcanian activity, and what are the corresponding dynamics and conduit processes that drive these abrupt shifts in the style and intensity of eruptions?
- During the different phases of a vulcanian cycle, characterized by largely different eruption energies, is magma fragmentation the result of multiple processes?
- Which are the main modalities of ash aggregation during transport in the atmosphere, and what are the main physical parameters controlling the deposition of ash aggregates?

This chapter is intended to summarize all the most relevant findings of this work, based on the conclusive remarks provided in most of the previous chapters and finally highlighting the general validity for some of the obtained results.

During this project, several case-studies were considered for sample collection and for providing field experiments aimed at the characterization of the eruptive dynamics. We acquired a very wide data-base of observations upon samples of moderate-to-high magma compositions including volcanic ash, ballistic products and ash aggregates associated with disparate eruptive processes related to Vulcanian-type eruptions like:

- ash and unbroken ash aggregates from different periods of the recent activity of Sakurajima volcano (Japan))
- ash from the ash-dominated low-energy eruptive activity at Copahue volcano (Argentina-Chile);
- ash and ballistic products (different types of bombs and blocks) from the historical activity of Vulcano (Italy), representative of a prototypal Vulcanian activity.

Analysis carried out on these products allowed us to highlight the general validity of some of the obtained results, linking together all the gained information to tie up a general view upon the processes that mostly control the moderate-scale, unsteady and cyclic Vulcanian activity.

8.2 New insights on conduit mechanisms controlling the eruptive pattern of unsteady moderate-scale Vulcanian activity

A variety of evidences emerged from the study of ash about the interplay between the physical processes affecting magma during its ascent, and the resulting eruptive dynamics and modality of ash emission. They included alternative and poorly documented mechanisms of magma fragmentation and ash production, evidences of gas and ash circulating pathways inside vertically variable degassing magma conduits, and indications about the importance of the intra-crateric residence of pre-fragmentated vent-hosted materials.

Our first result consisted in proving the primary importance of the progressive degassing from a vertically layered and quasi-static magma column in controlling the unsteadiness that characterized the observed cyclic activity at Sakurajima volcano. Differently from previous works, we distinguished two general patterns of eruptive activity, dominated respectively by high and low-frequency of explosions. In this work we focused on a period characterized by a low frequency activity, and we showed that the sudden transients observed in the intensity of the ash emission were mostly driven by a slow magma dynamics, that promoted the establishing of a vertical physical and rheological gradient along the conduit and the formation of a viscous plug at the top of the magma column. We showed that prominent and energetic Vulcanian explosion were essentially triggered by cyclic episodes of over-pressurization of the upper system possibly due to gas accumulation at the base of the poorly permeable plug without the direct involvement of volatile-rich magma addition to the system. According with the time-scales estimated for plug regeneration (15-30 days) and the frequency of the Vulcanian explosions (1 every 3-4 days) we suggested that the plug removal had always to be only partial and likely due to small gas pockets that locally fragmented only the upper portions of the rigid plug. In other words, we proposed

an alternative view to interpret such kind of activity, showing that cycles of unsteady Vulcanian explosivity at Sakurajima are not only related to a classical process of cyclic fresh magma feeding from a deeper reservoir, but can also occur following a repeated processes of pressure accumulation and discharge supported by a sustained magma degassing and the progressive formation of a sealing plug at top of the conduit.

8.3 The role of recycled material in the unsteady dynamics of mid-intensity eruptions

The studied examples (Sakurajima, Copahue) demonstrate that considerable amounts of fragments with textural features suggestive of ash recycling in a hot, fluid-rich, intra-crateric environment are often observed in the material deposited during unsteady and low energy eruptive activity. Due to their not fresh appearance these particles, characterized by highly re-crystallized groundmass textures and rounded, surface-pitted external surfaces, have been commonly interpreted as lithic materials and therefore poorly considered in the interpretation of the dynamics of the associated eruptions. However, we have shown how, in the context of the sequential activity at Sakurajima volcano or during the ash emission activity of Copahue volcano, the presence in the ash deposits of these recycled particles can be highly informative about the mechanisms of particle entrapment and forced convection of the erupting gas-particle mixture. Similarly, these mechanisms can also explain some important features of the geophysical signals recorded during sluggish, ash-dominated eruptive activity. At Sakurajima, we demonstrated that the process of ash recycling was mostly active during the long-lasting periods of low explosivity preceding an explosion, characterized by a very weak ash plume and by the absence of important pulses of activity. The continuative intra-crateric accumulation of recycled materials was typical of these periods of activity, during which the low overpressure driving the degassing was mainly dissipated in the process of fluidization of the loose ash intra-crater infilling. This fact was very clear in the analysis of the 2016 Copahue volcano activity, for which it was possible to couple ash analysis with data derived from the geophysical monitoring of the activity. During this activity, the vigorous and continuous emission of an ash-rich plume, and the evidences of gas-driven magmatic fragmentation obtained from the textures of fresh juvenile materials, were associated with unusually low pressure recorded by the infrasound monitoring. This apparent disagreement was solved by interpreting the activity as possibly related to the passage of the erupting mixture through crater in which ash and other previously ejected material are continuously recycled, so operating an important buffering on the magmatic over-pressure of the ascending mixture. As suggested by the large abundance of recycled ash recognized in the products, we believe that even in this eruptive context an important part of the initial overpressure, partially consumed in the process of magma fragmentation, was possibly dissipated for the fluidization of the hot vent-hosted mixture of pre-fragmentated materials, that were largely incorporated in the ash plume.

Elutriation of recycled fine ash during this process revealed also important for the convective stability of the weak buoyant plume, since this still hot, vent-hosted material can release important quantities of

thermal energy, with only minor energy consumption for the fragmentation of magma. In fact, while this recycled material cannot be considered as juvenile (in terms of the magma really propelling the eruption), it does not play the classical role of lithic material, as its important thermal energy cargo can be of primary importance in the development of the eruptive plumes related to these weak phases of the eruption. Actually, this aspect is not considered or only poorly accounted by the numerical schemes aimed at representing the dispersal of thermal convective plumes typical of Vulcanian activity. This is therefore of primary interest, also for hazard assessment studies related with fine ash dispersal.

8.4 Explosive vs. non-explosive fragmentation: the role of ash production by shear in fault gouges

The abundant presence of dense ash fragments in the tephra products of Vulcanian eruptions opens important questions about the possible origin of this material. Recent evidences reported in the literature (Cashman et al., 2008; Kennedy et al., 2009) highlight the potential for a mechanical production of volcanic ash inside fault gouges associated to the extrusion and emplacement of viscous domes or plugs. Innovative insights about the occurrence of similar processes of mechanical ash production derived from the analysis of the dense, breccia-bearing ballistic products associated with the AD 1888-90 Vulcanian eruption of the La Fossa cone at Vulcano (Eolian Islands, Italy). Although this eruption represents the classical Vulcanian activity and it was not associated to the extrusion of a viscous lava dome, we first described the common occurrence of important amounts of finely brecciated materials (comparable in size with fine ash < 4Phi) within a pervasive three-dimensional network of connected fractures which characterized the syn-eruptive magma plug. Furthermore, the evidence of internal ash transport revealed by the dimensional, textural and compositional features of the breccia material suggest the occurrence of cyclic episodes of fluidization. These possibly promoted the selective elutriation of the finer materials (clasts finer than around 100-125µm) from the porous system, enhancing thus the emission and dispersion of mechanically produced volcanic ash. This latter interpretation is also strongly supported by several similarities concerning the size distribution and the external shape of the ash grains from the fallout sequences with those from the clasts produced within fault gouges.

As a result, these evidences enlarge the spectrum of fragmentation processes that are currently accounted for the production of ash in mid-intensity explosive activity, also opening alternative scenarios about the role of mechanical production of ash during the long-lasting stages of low-intensity Vulcanian activity.

8.5 The structure and aerodynamical behavior of ash aggregates

In the previous sections we provided an overview upon the most relevant findings about alternative mechanisms of ash formation and magma conduit dynamics associated to different contexts of Vulcanian activity. All these speculations highlighted that large quantities of volcanic ash are produced

during this cyclic, ash-dominated activity, like in the case studied at Sakurajima. In spite of a large importance attributed to particles clusters for what concerns the modifying effect on the ash transport and dispersal, the direct description and field observation of these aggregates are still very few in the literature (Bonadonna et al., 2011; Taddeucci et al., 2011; Bagheri et al., 2016a; Miwa et al., 2020), likely due the very low preservation potential of ash aggregates at deposition. Therefore, part of this thesis has been also focused on to the study of the volcanic ash aggregation process, since it was widely proven that it represents one of the most impacting and modifying processes for the atmospheric dispersal and ground sedimentation of volcanic ash. Several original insights were provided on the internal structure of different types of aggregates, and on their aerodynamic behavior.

In particular, dedicated techniques were pointed out in order to allow the collection of several types of unbroken ash aggregates resulting from different periods of the ongoing Vulcanian activity of Sakurajima and associated to the variable meteorological conditions. As a result, it was provided a wide descriptive systematics for ash aggregates and particles clusters of different nature. Original, unprecedented data on the air-borne features (internal and external structure, GSD of the constituent particles) of the different types of aggregates have been so exhaustively collected. The internal structure of some of the most interesting aggregates was also resolved using a state-of-the-art Micro-CT based analysis. Although the information resulting from this kind of analyses are, at least for the moment, still qualitative, they allowed to characterize the internal architecture of cored (PC3) aggregates as well as of other, more common types of aggregates (AP, PC1, PC2), up to now never resolved with such a detail. A large number of particle clusters (including PC1, PC2, PC3) were also investigated using a High-Speed, High-Resolution camera in order to characterize their aerodynamical behavior and to evaluate the potential impact of ash aggregates on the ash dispersal at Sakurajima.

The result of this study is the production of a large database of some of the most important physical features of particle clusters. Size, shape, GSD of constituent ash and aerodynamical parameters of the different types of falling aggregates like terminal velocity and density were so directly measured or derived. Importantly, the typical fields of existence in the space size-velocity-density were provided for the different types of aggregates. It was shown that aerodynamical properties of particle clusters is mostly controlled by their internal structure, and in particular by the ratio between the core size and the thickness of the aggregating ash shell (when present). The relative volume fraction of the shell with respect to the internal core was also pointed out for the different observed particle clusters, in order to provide preliminary quantitative limits for distinguishing between the various types observed. The obtained dataset of measurements are of primary interest for the validation and calibration of those numerical models which include the process of ash aggregation, for providing forecasts of atmospheric ash dispersal. These data also helped in quantifying the variable influence that the different types of ash aggregates can have on the ground tephra dispersal at Sakurajima and possibly elsewhere. In fact, a strong relation was inferred between size and relative abundancy of the individual constituents of the aggregates, with features of the deposits GSDs, thus proving the high efficiency particularly for PC3 ash aggregates in modifying the ground dispersal of the finer tephra ($<45\mu m$).

8.6 Future perspectives

As a result of the work performed, new constraints were provided for a large variety of process, including novel insights on alternative mechanisms of magma fragmentation, processes affecting ash transport and circulation within the conduit, and finally information about the structure and the influence of ash aggregates in the process of dispersal.

The wide framework of field-based observations deriving from the different case-studies considered in this study allowed us to tie up a comprehensive overview about some important aspects and processes that are involved into the life-cycle of volcanic ash. The joint application of volcanological field studies, new practices of sample collection and direct data recording and applications of novel and classical laboratory studies still plays a primary role in catching and describing the main processes driving Vulcanian activity that, when coupled with physical modelling of these eruptions, can really promote a fundamental step forward in the understanding of this very frequent explosive activity. Based on the discussed results, we can so conclude that all the processes summarized in the present chapter possibly represent cardinal issues deserving of further focusing and study in order to reach an enlarged understanding upon the eruptive dynamics and ash production processes related to moderate-scale, unsteady and cyclic Vulcanian activity.

Chapter 9

References

Agusto, M. R., Caselli, A., Daga, R., Varekamp, J., Trinelli, A., Afonso, M. D. S., Veez, M. L., Euillades, P., Guevara, S. R. (2017). The crater lake of Copahue volcano (Argentina): geochemical and thermal changes between 1995 and 2015. Geological Society, London, Special Publications, 437(1), 107-130.

Alfano, F., Bonadonna, C., Delmelle, P., and Costantini, L. (2011). Insights on tephra settling velocity from morphological observations. Journal of Volcanology and Geothermal Research, 208(3-4), 86-98.

Alidibirov, M., and Dingwell, D. B. (2000). Three fragmentation mechanisms for highly viscous magma under rapid decompression. Journal of Volcanology and Geothermal Research, 100(1-4), 413-421.

Anderson, J. F., Johnson, J. B., Steele, A. L., Ruiz, M. C., and Brand, B. D. (2018). Diverse eruptive activity revealed by acoustic and electromagnetic observations of the 14 July 2013 intense vulcanian eruption of Tungurahua Volcano, Ecuador. Geophysical Research Letters, 45(7), 2976-2985.

Andronico, D., Cristaldi, A., Del Carlo, P., and Taddeucci, J. (2009). Shifting styles of basaltic explosive activity during the 2002–03 eruption of Mt. Etna, Italy. Journal of Volcanology and Geothermal Research, 180(2-4), 110-122.

Asahina, D., and Taylor, M. A. (2011). Geometry of irregular particles: Direct surface measurements by 3-D laser scanner. Powder technology, 213(1-3), 70-78.

Bagheri, G. H., Bonadonna, C., Manzella, I., and Vonlanthen, P. (2015). On the Characterization of Size and Shape of Irregular Particles. Powder Technology 270 (Part A): 141–53. https://doi.org/10.1016/j.powtec.2014.10.015.

Bagheri, G. H., Rossi, E., Biass, S., and Bonadonna, C. (2016a). Timing and Nature of Volcanic Particle Clusters Based on Field and Numerical Investigations. Journal of Volcanology and Geothermal Research 327: 520–30. https://doi.org/10.1016/j.jvolgeores.2016.09.009.

Bagheri, G., & Bonadonna, C. (2016). Aerodynamics of volcanic particles: characterization of size, shape, and settling velocity. In *Volcanic ash* (pp. 39-52). Elsevier.

Bagheri, G. H., and Bonadonna, C. (2016b). On the Drag of Freely Falling Non-Spherical Particles. Powder Technology 301 (November): 526–44. https://doi.org/10.1016/j.powtec.2016.06.015.

Battaglia, J., Hidalgo, S., Bernard, B., Steele, A., Arellano, S., & Acuña, K. (2019). Autopsy of an eruptive phase of Tungurahua volcano (Ecuador) through coupling of seismo-acoustic and SO2 recordings with ash characteristics. *Earth and Planetary Science Letters*, *511*, 223-232.

Baxter, P. J., and Horwell, C. J. (2015). Impacts of eruptions on human health. In The Encyclopedia of Volcanoes (pp. 1035-1047). Academic Press.

Befus, K. S., Manga, M., Gardner, J. E., and Williams, M. (2015). Ascent and emplacement dynamics of obsidian lavas inferred from microlite textures. Bulletin of Volcanology, 77(10), 88.

\

Belousov, A., Voight, B., Belousova, M., and Petukhin, A. (2002). Pyroclastic surges and flows from the 8–10 May 1997 explosive eruption of Bezymianny volcano, Kamchatka, Russia. Bulletin of Volcanology, 64(7), 455-471.

Benage, M. C., Dufek, J., Degruyter, W., Geist, D., Harpp, K., and Rader, E. (2014). Tying textures of breadcrust bombs to their transport regime and cooling history. Journal of volcanology and geothermal research, 274, 92-107.

Bernard, B., Battaglia, J., Proaño, A., Hidalgo, S., Vásconez, F., Hernandez, S., & Ruiz, M. (2016). Relationship between volcanic ash fallouts and seismic tremor: quantitative assessment of the 2015 eruptive period at Cotopaxi volcano, Ecuador. *Bulletin of Volcanology*, *78*(11), 1-11.

Biass, S., Falcone, J. L., Bonadonna, C., Di Traglia, F., Pistolesi, M., Rosi, M., and Lestuzzi, P. (2016). Great Balls of Fire: A probabilistic approach to quantify the hazard related to ballistics—A case study at La Fossa volcano, Vulcano Island, Italy. Journal of Volcanology and Geothermal Research, 325, 1-14.

Biass, S., Falcone, J. L., Bonadonna, C., Di Traglia, F., Pistolesi, M., Rosi, M., and Lestuzzi, P. (2016). Great Balls of Fire: A probabilistic approach to quantify the hazard related to ballistics—A case study at La Fossa volcano, Vulcano Island, Italy. *Journal of Volcanology and Geothermal Research*, *325*, 1-14.

Biegel, R. L., Sammis, C. G., and Dieterich, J. H. (1989). The frictional properties of a simulated gouge having a fractal particle distribution. Journal of Structural Geology, 11(7), 827-846.

Blenkinsop, T. G. (1991). Cataclasis and processes of particle size reduction. Pure and Applied Geophysics, 136(1), 59-86.

Blong, R. J. (1984). Volcanic Hazards, 424 pp.

Bonadonna, C., Ernst, G. G. J., and Sparks, R. S. J. (1998). Thickness variations and volume estimates of tephra fall deposits: the importance of particle Reynolds number. Journal of Volcanology and Geothermal Research, 81(3-4), 173-18.

Bonadonna, C, G C Mayberry, E S Calder, R S J Sparks, C Choux, P Jackson, A M Lejeune, et al. (2002a). Tephra Fallout in the Eruption of Soufrière Hills Volcano, Montserrat. Geological Society, London, Memoirs 21 (1): 483 LP – 516. https://doi.org/10.1144/GSL.MEM.2002.021.01.22.

Bonadonna, C, Macedonio, G., and Sparks, R. S. J. (2002b). Numerical Modelling of Tephra Fallout Associated with Dome Collapses and Vulcanian Explosions: Application to Hazard Assessment on Montserrat. Geological Society, London, Memoirs 21 (1): 517 LP – 537. https://doi.org/10.1144/GSL.MEM.2002.021.01.23.

Bonadonna, C., and Phillips, J. C. (2003). Sedimentation from strong volcanic plumes. Journal of Geophysical Research: Solid Earth, 108(B7).

Bonadonna, C., Genco, R., Gouhier, M., Pistolesi, M., Cioni, R., Alfano, F., Hoskuldsson, A., and Ripepe, M. (2011). Tephra Sedimentation during the 2010 Eyjafjallajkull Eruption (Iceland) from Deposit, Radar, and Satellite Observations. Journal of Geophysical Research: Solid Earth 116 (12). https://doi.org/10.1029/2011JB008462.

Bonadonna, C., Folch, A., Loughlin, S., and Puempel. H. (2012). Future Developments in Modelling and Monitoring of Volcanic Ash Clouds: Outcomes from the First IAVCEI-WMO Workshop on Ash Dispersal Forecast and Civil Aviation. Bulletin of Volcanology 74 (1): 1–10. https://doi.org/10.1007/s00445-011-0508-6.

Bonadonna, C., Costa, A., Folch, A., and Koyaguchi, T. (2015). Tephra dispersal and sedimentation. In The Encyclopedia of Volcanoes (pp. 587-597). Academic Press.

Bonali, F. L., Corazzato, C., Bellotti, F., and Groppelli, G. (2016). Active tectonics and its interactions with Copahue volcano. In Copahue Volcano (pp. 23-45). Springer, Berlin, Heidelberg.Caselli, A. T., Sommer, C., Daga,

R., Baez, A., Albite, J., Barion, G. (2017). Caracterización de las fases eruptivas del volcán Copahue durante el ciclo 2012-2017 (Andes argentino-chileno). Actas del XX Congreso Geológico Argentino, San Miguel de Tucmuna, Tucuman, Argentina. 27-29.

Brazier, S., Sparks, R. S. J., Carey, S. N., Sigurdsson, H., and Westgate, J. A. (1983). Bimodal grain size distribution and secondary thickening in air-fall ash layers. Nature, 301(5896), 115-119.

Brown, R. J., Bonadonna, C., and Durant A. J. (2012). A Review of Volcanic Ash Aggregation. Physics and Chemistry of the Earth 45–46: 65–78. https://doi.org/10.1016/j.pce.2011.11.001.

Brugger, C. R., and Hammer, J. E. (2010a). Crystal size distribution analysis of plagioclase in experimentally decompressed hydrous rhyodacite magma. Earth and Planetary Science Letters, 300(3-4), 246-254.

Brugger, C. R., and Hammer, J. E. (2010b). Crystallization kinetics in continuous decompression experiments: implications for interpreting natural magma ascent processes. Journal of Petrology, 51(9), 1941-1965.

Burgisser, A., and Gardner, J. E. (2004). Experimental constraints on degassing and permeability in volcanic conduit flow. Bulletin of volcanology, 67(1), 42-56.

Burns, F A, Bonadonna, C., Pioli, L., Cole, P. D., and Stinton, A. (2017). Ash Aggregation during the 11 February 2010 Partial Dome Collapse of the Soufrière Hills Volcano, Montserrat." Journal of Volcanology and Geothermal Research 335: 92–112. https://doi.org/https://doi.org/10.1016/j.jvolgeores.2017.01.024.

Büttner, R., Dellino, P., and Zimanowski, B. (1999). Identifying magma–water interaction from the surface features of ash particles. Nature, 401(6754), 688-690.

Cannata, A., Montalto, P., Privitera, E., and Russo, G. (2009). Characterization and location of infrasonic sources in active volcanoes: Mount Etna, September–November 2007. Journal of Geophysical Research: Solid Earth, 114(B8).

Cas, R., and Wright, J. (2012). Volcanic successions modern and ancient: A geological approach to processes, products and successions. Springer Science & Business Media.

Casadevall, T. J., and Krohn, M. D. (1995). Effects of the 1992 Crater Peak eruptions on airports and aviation operations in the United States and Canada. US Geological Survey Bulletin, 2139, 205-220.

Caselli, A.T., Agusto, M., Velez, M.L., Forte, P., Bengoa, C., Daga, R., Albite, J.M. y Capaccioni, B. (2016a). The 2012 eruption. En: Tassi, F., Vaselli, O. y Caselli, A.T. (eds) Copahue Volcano. Active volcanoes of the world. Book Series. Springer-Verlag: 61-77. Heidelberg.

Caselli, A. T., Liccioli, C., and Tassi, F. (2016b). Risk assessment and mitigation at Copahue volcano. In Copahue Volcano (pp. 239-254). Springer, Berlin, Heidelberg.

Caselli, A.T., Sommer, C., Barion, G. (2017). Conos piroclásticos anidados en el crater del volcán Copahue, Argentina. Actas del XX Congreso Geológico Argentino, San Miguel de Tucmuna, Agentina. 27-29. 24-26.

Carey, S. N., and Sigurdsson, H. (1982). Influence of particle aggregation on deposition of distal tephra from the May 18, 1980, eruption of Mount St. Helens volcano. Journal of Geophysical Research: Solid Earth, 87(B8), 7061-7072.

Cashman, K. V., and Marsh, B. D. (1988). Crystal size distribution (CSD) in rocks and the kinetics and dynamics of crystallization II: Makaopuhi lava lake. Contributions to Mineralogy and Petrology, 99(3), 292-305.

Cashman, K. V. (1992). Groundmass crystallization of Mount St. Helens dacite, 1980–1986: a tool for interpreting shallow magmatic processes. Contributions to Mineralogy and Petrology, 109(4), 431-449.

Cashman, K., and Blundy, J. (2000). Degassing and crystallization of ascending andesite and dacite. Philosophical Transactions of the Royal Society of London. Series A: Mathematical, Physical and Engineering Sciences, 358(1770), 1487-1513.

Cashman, K. V., and Hoblitt, R. P. (2004). Magmatic precursors to the 18 May 1980 eruption of Mount St. Helens, USA. Geology, 32(2), 141-144.

Cashman, K. V., Thornber, C. R., and Pallister, J. S. (2008). From dome to dust: Shallow crystallization and fragmentation of conduit magma during the 2004-2006 dome extrusion of Mount St. Helens, Washington (No. 1750-19, pp. 387-413). US Geological Survey.

Cashman, K. V., and Scheu, B. (2015). Magmatic fragmentation. In The Encyclopedia of Volcanoes (pp. 459-471). Academic Press.

Cashman, K. V. (2020). Crystal size distribution (CSD) analysis of volcanic samples: advances and challenges. Front. Earth Sci., 8, 291.

Cassidy, M., Cole, P. D., Hicks, K. E., Varley, N. R., Peters, N., and Lerner, A. H. (2015). Rapid and slow: Varying magma ascent rates as a mechanism for Vulcanian explosions. *Earth and Planetary Science Letters*, *420*, 73-84.

Cassidy, M., Manga, M., Cashman, K., and Bachmann, O. (2018). Controls on explosive-effusive volcanic eruption styles. Nature Communications, 9(1), 1-16.

Castro, J. M., and Dingwell, D. B. (2009). Rapid ascent of rhyolitic magma at Chaitén volcano, Chile. *Nature*, *461*(7265), 780-783.

Cioni, R., D'Oriano, C. and Bertagnini, A. (2008). Fingerprinting ash deposits of small-scale eruptions by their physical and textural features. Journal of Volcanology and Geothermal Research, 177(1), 277-287.

Cioni, R., Pistolesi, M., Bertagnini, A., Bonadonna, C., Hoskuldsson, A., and Scateni, B. (2014). Insights into the dynamics and evolution of the 2010 Eyjafjallajökull summit eruption (Iceland) provided by volcanic ash textures. Earth and Planetary Science Letters, 394, 111-123.

Clarke, A. B., Voight, B., Neri, A., and Macedonio, G. (2002a). Transient dynamics of vulcanian explosions and column collapse. Nature, 415(6874), 897-901.

Clarke, A. B., Neri, A., Voight, B., Macedonio, G., and Druitt, T. H. (2002b). Computational modelling of the transient dynamics of the August 1997 Vulcanian explosions at Soufriere Hills Volcano, Montserrat: influence of initial conduit conditions on near-vent pyroclastic dispersal. MEMOIRS-GEOLOGICAL SOCIETY OF LONDON, 21, 319-348.

Clarke, A. B., Stephens, S., Teasdale, R., Sparks, R. S. J., and Diller, K. (2007). Petrologic constraints on the decompression history of magma prior to Vulcanian explosions at the Soufrière Hills volcano, Montserrat. *Journal of Volcanology and Geothermal Research*, *161*(4), 261-274.

Clarke, A. B. (2013). Unsteady explosive activity: Vulcanian eruptions. Fagents SA, Tracy KP G, Rosaly MC L (eds) Modeling Volcanic Processes: The Physics and Mathematics of Volcanism. Cambridge University Press, England, 129-152.

Clarke, A. B., Ongaro, T. E., and Belousov, A. (2015). Vulcanian eruptions. In The Encyclopedia of Volcanoes (pp. 505-518). Academic Press.

Clocchiatti, R., Del Moro, A., Gioncada, A. N. N. A., Joron, J. L., Mosbah, M., Pinarelli, L., and Sbrana, A. (1994). Assessment of a shallow magmatic system: the 1888–90 eruption, Vulcano Island, Italy. Bulletin of Volcanology, 56(6-7), 466-486.

Cocco, R., Karri, S. R., & Knowlton, T. (2014). Introduction to fluidization. *Chem. Eng. Prog*, *110*(11), 21-29.

Coltelli, M., Miraglia, L., and Scollo, S. (2008). Characterization of shape and terminal velocity of tephra particles erupted during the 2002 eruption of Etna volcano, Italy. Bulletin of volcanology, 70(9), 1103-1112.

Cornell, W., Carey, S., and Sigurdsson, H. (1983). Computer simulation of transport and deposition of the Campanian Y-5 ash. Journal of Volcanology and Geothermal Research, 17(1-4), 89-109.

Corsaro, R. A., Miraglia, L., and Pompilio, M. (2007). Petrologic evidence of a complex plumbing system feeding the July–August 2001 eruption of Mt. Etna, Sicily, Italy. Bulletin of Volcanology, 69(4), 401.

Costa, A., Folch, A., and Macedonio, G., (2010). A model for wet aggregation of ash particles in volcanic plumes and clouds: 1. Theoretical formulation. J. Geophys. Res. Solid Earth 115.

Couch, S., Sparks, R. S. J., and Carroll, M. R. (2003). The kinetics of degassing-induced crystallization at Soufriere Hills Volcano, Montserrat. *Journal of Petrology*, *44*(8), 1477-1502.

D'Oriano, C., Cioni, R., Bertagnini, A., Andronico, D., Cole, P.D., (2011). Dynamics of ash-dominated eruptions at Vesuvius: the post-512 AD AS1a event. Bull Volcanol 73, 699–715. doi:10.1007/s00445-010-0432-1.

D'Oriano, C., Pompilio, M., Bertagnini, A., Cioni, R., and Pichavant, M. (2013). Effects of experimental reheating of natural basaltic ash at different temperatures and redox conditions. Contributions to Mineralogy and Petrology, 165(5), 863-883.

D'Oriano, C., Bertagnini, A., Cioni, R., Pompilio, M., (2014). Identifying recycled ash in basaltic eruptions. Sci. Rep. 4. doi:10.1038/srep05851

Daga, R., Caselli, A., Ribeiro guevara, S., Agusto, M..(2016) Tefras emitidas durante la fase inicial hidromagmática (julio de 2012) del ciclo eruptivo 2012-actual (2016) del volcán Copahue (Andes del Sur). Revista de la Asociación Geológica Argentina, Argentina, 74.

Daga, R., Caselli, A., Ribeiro Guevara, S., Agusto, M., (2017). Tefras emitidas durante la fase inicial hidromagmática (Julio de 2012) del ciclo eruptivo 2012 – actual (2016) del Volcán Copahue (ander del Sur). Revista de la Asociación Geológica Argentina 74, 191–206.

De Angelis, S., Lamb, O.D., Lamur, A., Hornby, A.J., von Aulock, F.W., Chigna, G., Lavallée, Y.,Rietbrock, A., (2016). Characterization of moderate ash-and-gas explosions at Santiaguito volcano, Guatemala, from infrasound waveform inversion and thermal infrared measurements. Geophysical Research Letters 43, 6220–6227. https://doi.org/10.1002/2016GL069098.

De Astis, G., La Volpe, L., Peccerillo, A., and Civetta, L. (1997). Volcanological and petrological evolution of Vulcano island (Aeolian Arc, southern Tyrrhenian Sea). Journal of Geophysical Research: Solid Earth, 102(B4), 8021-8050.

de' Michieli Vitturi, M., Neri, A., Esposti Ongaro, T., Lo Savio, S., and Boschi, E. (2010). Lagrangian modeling of large volcanic particles: Application to Vulcanian explosions. Journal of Geophysical Research: Solid Earth, 115(B8).

De Groot-Hedlin, C., M. A. H. Hedlin, K. T. Walker, D. Drop, and M. Zumberge (2008). Evaluation of infrasound signals from the shuttle Atlantis using a large seismic network, J. Acoust. Soc. Am., 124, 1442 - 1452.

Deardorff, N., and Cashman, K. (2017). Rapid crystallization during recycling of basaltic andesite tephra: timescales determined by reheating experiments. Scientific reports, 7, 46364.

Degruyter, W., Bachmann, O., Burgisser, A., and Manga, M. (2012). The effects of outgassing on the transition between effusive and explosive silicic eruptions. Earth and Planetary Science Letters, 349, 161-170.

Delle Donne D., M. Ripepe, G. Lacanna, G. Tamburello, M. Bitetto and A. Aiuppa. (2016). Gas mass derived by infrasound and UV cameras: Implications for mass flow rate. Journal of Volcanology and Geothermal Reserach. 325, 169-178.

Dellino, P., and La Volpe, L. (1996). Image processing analysis in reconstructing fragmentation and transportation mechanisms of pyroclastic deposits. The case of Monte Pilato-Rocche Rosse eruptions, Lipari (Aeolian islands, Italy). Journal of Volcanology and Geothermal Research, 71(1), 13-29.

Dellino, P., and Liotino, G. (2002). The fractal and multifractal dimension of volcanic ash particles contour: a test study on the utility and volcanological relevance. Journal of Volcanology and Geothermal Research, 113(1-2), 1-18.

Dellino, P., Mele, D., Bonasia, R., Braia, G., La Volpe, L., and Sulpizio, R. (2005). The analysis of the influence of pumice shape on its terminal velocity. Geophysical Research Letters, 32(21).

Dellino, P., Gudmundsson, M. T., Larsen, G., Mele, D., Stevenson, J. A., Thordarson, T., and Zimanowski, B. (2012). Ash from the Eyjafjallajökull eruption (Iceland): Fragmentation processes and aerodynamic behavior. Journal of Geophysical Research: Solid Earth, 117(B9).

Diller, K., Clarke, A. B., Voight, B., and Neri, A. (2006). Mechanisms of conduit plug formation: Implications for vulcanian explosions. Geophysical Research Letters, 33(20).

Dingwell, D. B., Lavallée, Y., and Kueppers, U. (2012). Volcanic ash: A primary agent in the Earth system. Physics and Chemistry of the Earth, Parts A/B/C, 45, 2-4.

Druitt, T. H., Young, S. R., Baptie, B., Bonadonna, C., Calder, E. S., Clarke, A. B., ... and Ryan, G. (2002). Episodes of cyclic Vulcanian explosive activity with fountain collapse at Soufrière Hills Volcano, Montserrat. Memoirs-Geological Society of London, 21, 281-306.

Dufek, J., Manga, M., & Patel, A. (2012). Granular disruption during explosive volcanic eruptions. *Nature Geoscience*, *5*(8), 561-564.

Durant, A.J., Rose, W.I., Sarna-Wojcicki, A.M., Carey, S., and Volentik, A.C.M., (2009). Hydrometeor-enhanced tephra sedimentation: Constraints from the 18 May 1980 eruption of Mount St. Helens. J. Geophys. Res. Solid Earth 114.

Durant, A.J. (2015). RESEARCH FOCUS: Toward a realistic formulation of fine-ash lifetime in volcanic clouds. Geology 43, 271–272. https://doi.org/10.1130/focus032015.1.

Ersoy, O., Aydar, E., Gourgaud, A., Artuner, H., and Bayhan, H. (2007). Clustering of volcanic ash arising from different fragmentation mechanisms using Kohonen self-organizing maps. Computers & geosciences, 33(6), 821-828.

Ersoy, O., Şen, E., Aydar, E., Tatar, İ., and Çelik, H. H. (2010). Surface area and volume measurements of volcanic ash particles using micro-computed tomography (micro-CT): A comparison with scanning electron microscope (SEM) stereoscopic imaging and geometric considerations. Journal of Volcanology and Geothermal Research, 196(3-4), 281-286.

Eychenne, J., Le Pennec, J. L., Ramon, P., and Yepes, H. (2013). Dynamics of explosive paroxysms at open-vent andesitic systems: high-resolution mass distribution analyses of the 2006 Tungurahua fall deposit (Ecuador). Earth and Planetary Science Letters, 361, 343-355.

Eychenne, J., Houghton, B. F., Swanson, D. A., Carey, R. J., and Swavely, L. (2015). Dynamics of an open basaltic magma system: the 2008 activity of the Halema 'uma 'u Overlook vent, Kīlauea Caldera. Earth and Planetary Science Letters, 409, 49-60.

Fee D., Izbekov P., Kim K., Yokoo A., Lopez T., Prata F., Kazahaya R., Nakamichi H. and Iguchi M. (2017). Eruption mass estimation using infrasound waveform inversion and ash and gas measurements: Evaluation at Sakurajima Volcano, Japan. Earth and Planetary Science Letters. 480, 42-52. Folguera, A., Vera, E. R., Vélez, L., Tobal, J., Orts, D., Agusto, M., et al. (2016). "A review of the geology, structural controls, and tectonic setting of Copahue volcano, Southern Volcanic Zone, Andes, Argentina", in Copahue Volcano, ed. Tassi, F., Vaselli, O. y Caselli, A, (Springer, Berlin, Heidelberg), 3-22.

Fee, D. and Matoza, R.S. (2013). An overview of volcano infrasound: From hawaiian to plinian, local to global. Journal of Volcanology and Geothermal Research 249, 123–139. doi:10.1016/j.jvolgeores.2012.09.002.

Folch, A., Costa, A., Durant, A., and Macedonio, G. (2010). A model for wet aggregation of ash particles in volcanic plumes and clouds: 2. Model application. Journal of Geophysical Research: Solid Earth, 115(B9).

Folguera, A., Vera, E. R., Vélez, L., Tobal, J., Orts, D., Agusto, M., ... and Ramos, V. A. (2016). A review of the geology, structural controls, and tectonic setting of Copahue volcano, Southern Volcanic Zone, Andes, Argentina. In Copahue Volcano (pp. 3-22). Springer, Berlin, Heidelberg.

Folk, R. L. (1968). Petrology of sedimentary rocks: Hemphill's. *Austin, Texas*, *170*, 85.

Francis E.H. (1989) Tuffisite. In: Petrology. Encyclopedia of Earth Science. Springer, Boston, MA. https://doi.org/10.1007/0-387-30845-8_246

Fukuyama, H. (1981). Geological map of Sakurajima volcano 1: 25,000. Geol. Map Volcanoes, Geol. Surv. Japan, 1, 1-8.

Garboczi, E. J., Liu, X., and Taylor, M. A. (2012). The 3-D shape of blasted and crushed rocks: From 20 μm to 38 mm. Powder technology, 229, 84-89.

Garcés, M. A., Hansen R. A., Lindquist K. G. (1998). Traveltimes for infrasonic waves propagating in a stratified atmosphere. Geophysical Journal International, 135, 255-263.

Garcés, M. A., Willis M., Hetzer C., Pichon A. L., Drob D. (1998). Traveltimes for infrasonic waves propagating in a stratified atmosphere. Geophys. Res. Lett., 31, L19304, doi:10.1029/2004GL020696.

Gaunt, H. E., Bernard, B., Hidalgo, S., Proaño, A., Wright, H., Mothes, P., ... and Kueppers, U. (2016). Juvenile magma recognition and eruptive dynamics inferred from the analysis of ash time series: The 2015 reawakening of Cotopaxi volcano. Journal of Volcanology and Geothermal Research, 328, 134-146.

Gaunt, H. E., Burgisser, A., Mothes, P. A., Browning, J., Meredith, P. G., Criollo, E., & Bernard, B. (2020). Triggering of the powerful 14 July 2013 Vulcanian explosion at Tungurahua Volcano, Ecuador. *Journal of Volcanology and Geothermal Research*, *392*, 106762.

Giachetti, T., Druitt, T. H., Burgisser, A., Arbaret, L., & Galven, C. (2010). Bubble nucleation, growth and coalescence during the 1997 Vulcanian explosions of Soufrière Hills Volcano, Montserrat. *Journal of Volcanology and Geothermal Research*, *193*(3-4), 215-231.

Gilbert, J.S., Lane, S.J., 1994. The origin of accretionary lapilli. Bull Volcanol 56, 398–411.

Gioncada A., Mazzuoli R., Bisson M., Pareschi M. T., (2003). Petrology of volcanic products younger than 42 Ka on the Lipari – Vulcano complex (Aeolian Island; Italy): an example of volcanism controlled by tectonics. Journal of Volcanology and Geothermal research, 122, 191 – 220.

Glaze, L. S., Francis, P. W., Self, S., and Rothery, D. A. (1989). The 16 September 1986 eruption of Lascar volcano, north Chile: satellite investigations. Bulletin of Volcanology, 51(3), 149-160.

Gonnermann, H. M., and Houghton, B. F. (2012). Magma degassing during the Plinian eruption of Novarupta, Alaska, 1912. Geochemistry, Geophysics, Geosystems, 13(10).

Goto, A., and Johnson, J. B. (2011) Monotonic infrasound and Helmholtz resonance at volcano Villarrica (Chile). Geophysical Research Letter, 38, L06301, doi:10.1029/2011GL046858

Guffanti, M., Casadevall, T. J., and Budding K. (2010). Encounters of Aircraft with Volcanic Ash Clouds; A Compilation of Known Incidents, 1953-2009. Data Series. https://doi.org/10.3133/ds545.

GVP (2016) https://volcano.si.edu/volcano.cfm?vn=357090#February2016.

Hammer, J. E., Cashman, K. V., Hoblitt, R. P., and Newman, S. (1999). Degassing and microlite crystallization during pre-climactic events of the 1991 eruption of Mt. Pinatubo, Philippines. Bulletin of Volcanology, 60(5), 355-380.

Hall, M. L., Steele, A. L., Bernard, B., Mothes, P. A., Vallejo, S. X., Douillet, G. A., ... & Ruiz, M. C. (2015). Sequential plug formation, disintegration by Vulcanian explosions, and the generation of granular Pyroclastic Density Currents at Tungurahua volcano (2013–2014), Ecuador. *Journal of Volcanology and Geothermal Research*, *306*, 90-103.

Heilbronner, R., and Keulen, N. (2006). Grain size and grain shape analysis of fault rocks. Tectonophysics, 427(1-4), 199-216.

Heiken, G., and Wohletz, K. (1985). Volcanic ash. University Presses of California, Chicago, Harvard and MIT.

Hickey, J., Gottsmann J., Nakamichi H., and Iguchi M. (2016). Thermomechanical Controls on Magma Supply and Volcanic Deformation: Application to Aira Caldera, Japan. Scientific Reports 6 (September): 1–10. https://doi.org/10.1038/srep32691.

Higgins, M. D. (1996). Magma dynamics beneath Kameni volcano, Thera, Greece, as revealed by crystal size and shape measurements. Journal of Volcanology and Geothermal Research, 70(1-2), 37-48.

Higgins, M. D. (2000). Measurement of crystal size distributions. American Mineralogist, 85(9), 1105-1116.

Higgins, M. D., and Roberge, J. (2006). Three Magmatic Components in the 1973 Eruption of Eldfell Volcano, Iceland: Evidence From Plagioclase Crystal Size Distribution (CSD) and Geochemistry. AGUFM, 2006, V23C-0640.

Hoblitt, R. P. (1986). Observations of the eruptions of July 22 and August 7, 1980, at Mount St. Helens, Washington (Vol. 1335). US Government Printing Office.

Horwell, C. J., Sparks, R. S. J., Brewer, T. S., Llewellin, E. W., and Williamson, B. J. (2003). Characterization of respirable volcanic ash from the Soufrière Hills volcano, Montserrat, with implications for human health hazards. Bulletin of Volcanology, 65(5), 346-362.

Horwell, C. J., and Baxter, P. J. (2006). The respiratory health hazards of volcanic ash: a review for volcanic risk mitigation. Bulletin of volcanology, 69(1), 1-24.

Houghton, B. F., and Nairn, I. A. (1991). The 1976–1982 Strombolian and phreatomagmatic eruptions of White Island, New Zealand: eruptive and depositional mechanisms at a 'wet' volcano. Bulletin of volcanology, 54, 1, 25-49.

Houghton, B. F., and Wilson, C. J. N. (1989). A vesicularity index for pyroclastic deposits. Bulletin of volcanology, 51(6), 451-462.

Iguchi M., Yakiwara, H., Tameguri, T., Hendrasto, M., and Hirabayashi, J. I. (2008). Mechanism of Explosive Eruption Revealed by Geophysical Observations at the Sakurajima, Suwanosejima and Semeru Volcanoes. Journal of Volcanology and Geothermal Research 178 (1): 1–9. https://doi.org/10.1016/j.jvolgeores.2007.10.010.

Iguchi, M., Yokoo, A., and Tameguri, T. (2010). Intensity of volcanic explosions at Showa crater of Sakurajima volcano. Annuals of Disaster Prevention Research Institute of Kyoto University, 53, 233-240.

Iguchi, M., Tameguri, T., Ohta, Y., Ueki, S., and Nakao, S. (2013a). Characteristics of Volcanic Activity at Sakurajima Volcano's Showa Crater During the Period 2006 to 2011 (< Special Section> Sakurajima Special Issue). Bulletin of the Volcanological Society of Japan, 58(1), 115-135.

Iguchi, M. (2013b). Magma Movement from the Deep to Shallow Sakurajima Volcano as Revealed by Geophysical Observations (< Special Section> Sakurajima Special Issue). Bulletin of the Volcanological Society of Japan, 58(1), 1-18.

Inman, D. L. (1952). Measures for describing the size distribution of sediments. Journal of Sedimentary Research, 22(3), 125-145.

Ishihara, K., (1985). Dynamical Analysis of Volcanic Explosion. Journal of Geodynamics 3 (3): 327–49. https://doi.org/https://doi.org/10.1016/0264-3707(85)90041-9.

Ishihara, K. (1990). Pressure sources and induced ground deformation associated with explosive eruptions at an andesitic volcano: Sakurajima volcano, Japan. Magma transport and storage.

Ishihara K., (2000) Characteristics and the occurring field of vulcanian eruption. Chikyu Monthly 22:308–314

James, M R, Gilbert, J. S., and Lane, S. J. (2002). Experimental Investigation of Volcanic Particle Aggregation in the Absence of a Liquid Phase. Journal of Geophysical Research: Solid Earth 107 (B9): ECV 4-1-ECV 4-13. https://doi.org/10.1029/2001JB000950.

James, M. R., Lane J. S., and Gilbert J. S. (2003). Density, Construction, and Drag Coefficient of Electrostatic Volcanic Ash Aggregates. Journal of Geophysical Research: Solid Earth 108 (B9): 1–12. https://doi.org/10.1029/2002jb002011.

Jenkins, S., Komorowski, J. C., Baxter, P. J., Spence, R., Picquout, A., and Lavigne, F. (2013). The Merapi 2010 eruption: an interdisciplinary impact assessment methodology for studying pyroclastic density current dynamics. Journal of Volcanology and Geothermal Research, 261, 316-329.

Jenkins, S F, T M Wilson, C Magill, V Miller, C Stewart, R Blong, W Marzocchi, M Boulton, Costanza Bonadonna, and A Costa. (2015). Volcanic Ash Fall Hazard and Risk. Global Volcanic Hazards and Risk, 173–222.

Johnson J.B. (2003). Generation and propagation of infrasonic airwaves from volcanic explosions. J. Volcanol. Geotherm. Res., 121, 1-14, doi:10.1016/S0377-0273(02)00408-0.

Johnson, J. B., and M. Ripepe (2011). Volcano infrasound: A review, J. Volcanol. Geoth. Res., 206, 61–69, doi:10.1016/j.jvolgeores.2011.06.006.

Jordan, S. C., Dürig, T., Cas, R. A. F., and Zimanowski, B. (2014). Processes controlling the shape of ash particles: results of statistical IPA. Journal of volcanology and geothermal research, 288, 19-27.

Kamo, K., (1978). Some phenomena before the summit eruptions at Sakura-zima volcano. Bull. Volcanol. Soc. Jpn. 23, 53–64 (in Japanese with English abstract).

Kamo, K., and Ishihara, K. (1989). A preliminary experiment on automated judgement of the stages of eruptive activity using tiltmeter records at Sakurajima, Japan. In Volcanic Hazards (pp. 585-598). Springer Berlin Heidelberg.

Kaminski, E., & Jaupart, C. (1998). The size distribution of pyroclasts and the fragmentation sequence in explosive volcanic eruptions. *Journal of Geophysical Research: Solid Earth*, *103*(B12), 29759-29779.

Kendrick, J. E., Lavallée, Y., Varley, N. R., Wadsworth, F. B., Lamb, O. D., and Vasseur, J. (2016). Blowing off steam: tuffisite formation as a regulator for lava dome eruptions. Frontiers in Earth Science, 4, 41.

Kennedy, L.A., Russell, J.K., Nelles, E., (2009). Origins of Mount St. Helens cataclasites: Experimental insights. American Mineralogist 94, 995–1004. doi:10.2138/am.2009.3129.

Kienle, J., and Shaw, G. E. (1979). Plume dynamics, thermal energy and long-distance transport of vulcanian eruption clouds from Augustine volcano, Alaska. Journal of Volcanology and Geothermal Research, 6(1-2), 139-164.

Kim K., Fee D., Yokoo A., and Lees J.M. 2015. Acoustic source inversion to estimate volume flux from volcanic explosions, Geophys. Res. Lett., 42, 5243-5249, doi:10.1002/2015GL064466.

Kueppers, U., Scheu, B., Spieler, O., and Dingwell, D. B. (2006). Fragmentation efficiency of explosive volcanic eruptions: A study of experimentally generated pyroclasts. Journal of Volcanology and Geothermal Research, 153(1-2), 125-135.

Kueppers, U., Auer, B., Cimarelli, C., Scolamacchia, T., Guenthel, M., and Dingwell, D. B. (2011). Experimentally constraining the boundary conditions for volcanic ash aggregation. AGUFM, 2011, V51F-2576.

Kurniawan, I. A., Sakakibara, M., and Suparka, E. (2016). Petrological Monitoring of the AD 2011–2012 Volcanic Ash from Sakurajima Volcano, Southern Kyushu, Japan. Geosciences, 6(1), 12.

Lacanna, G., Ichihara, M., Iwakuni, M., Takeo, M., Iguchi, M., Ripepe, M. (2014). Influence of atmospheric structure and topography on infrasonic wave propagation. Journal of Geophisical research: Solid Earth, 119 (4), pp. 2988-3005 DOI: 10.1002/2013JB010827.

Lacanna, G., Ripepe, M. (2013). Influence of near-source volcano topography on the acoustic wavefield and implication for source modeling. Journal of Volcanology and Geothermal Research, 250, pp. 9-18 DOI: 10.1016/j.jvolgeores.2012.10.005.

Lacanna, G., Ripepe, M. (2020). Modelling the acoustic flux inside the magmatic conduit by 3D-FDTD simulation.. Journal of Geophysical research: Solid Earth.

Lane, S. J., Gilbert, J. S., and Hilton, M. (1993). The aerodynamic behaviour of volcanic aggregates. Bulletin of Volcanology, 55(7), 481-488.

Leibrandt, S., and Le Pennec, J. L., (2015). Towards fast and routine analyses of volcanic ash morphometry for eruption surveillance applications. Journal of Volcanology and Geothermal Research 297, 11–27. doi:10.1016/j.jvolgeores.2015.03.014.

Lighthill, M.J. (1979). Waves in fluids, Cambridge Univ. Press, New York (504 pages, Reissue).

Lin, C. L., and Miller, J. D. (2005). 3D characterization and analysis of particle shape using X-ray microtomography (XMT). Powder Technology, 154(1), 61-69.

Linares, E., Ostera, H.A. y Mas, L. (1999). Cronología Potasio-Argón del complejo efusivo Copahue–Caviahue, Provincia de Neuquén. Revista de la Asociación Geológica Argentina, 54 (3): 240–247.

Liu, E.J., Cashman, K.V., Rust, A.C. (2015). Optimising shape analysis to quantify volcanic ash morphology. GeoResJ 8, 14–30. doi:10.1016/j.grj.2015.09.001.

Liu, E.J., Cashman, K.V., Rust, A.C., Höskuldsson, Á. (2017). Contrasting mechanisms of magma fragmentation during coeval magmatic and hydromagmatic activity: the Hverfjall Fires fissure eruption, Iceland 1–26. doi:10.1007/s00445-017-1150-8.

Magee, C., Stevenson, C. T., Ebmeier, S. K., Keir, D., Hammond, J. O., Gottsmann, J. H., ... and O'Driscoll, B. (2018). Magma plumbing systems: a geophysical perspective. Journal of Petrology, 59(6), 1217-1251.

Maekawa, Z. (1968). Noise reduction by Screens, Appl. Acoust., 1, 157 – 173.

Mackie, S., Cashman, K., Ricketts, H., Rust, A., and Watson, M. (Eds.). (2016). Volcanic ash: hazard observation. Elsevier.

Mangan, M. T. (1990). Crystal size distribution systematics and the determination of magma storage times: the 1959 eruption of Kilauea volcano, Hawaii. Journal of Volcanology and geothermal Research, 44(3-4), 295-302.

Marone, C., and Scholz, C. H. (1989). Particle-size distribution and microstructures within simulated fault gouge. Journal of Structural Geology, 11(7), 799-814.

Marsh, B. D. (1988). Crystal size distribution (CSD) in rocks and the kinetics and dynamics of crystallization. Contributions to Mineralogy and Petrology, 99(3), 277-291.

Marsh BD (1998) On the interpretation of crystal size distributions in magmatic systems. J Petrol 39:553–599

Martini, M., Bermúdez, A. Delfino, D. and Giannini, L., (1997). The thermal manifestations of Copahue Volcano area. Neuquén. Argentina. VIII Congreso Geológico Chileno, Antofagasta. 4: 352-356.

Mastin, L. G., Van Eaton, A. R., and Durant, A. J. (2016). Adjusting particle-size distributions to account for aggregation in tephra-deposit model forecasts. Atmospheric Chemistry and Physics, 16(14), 9399.

Matoza, R.S., Le Pichon, A., Vergos, J., Herry, P, Lalande,J.M., Lee H., Che Il-Young, Rybin, A. Infrasonic observations of the June 2009 Sarychev Peak eruption, Kuril Islands: Implications for infrasonic monitoring of remote explosive volcanism. Journal of Volcanology and Geothermal Research, 200, (2011), 35-38.

Mele, D., Dellino, P., Sulpizio, R., and Braia, G. (2011). A systematic investigation on the aerodynamics of ash particles. Journal of Volcanology and Geothermal Research, 203(1-2), 1-11.

Melnick, D., Folguera, A. y Ramos, V.A. (2006). Structural control on arc volcanism: the Copahue- Agrio complex, South-Central Andes (37°50′S). Journal of South American Earth Sciences, 22: 66–88.

Melnik, O., and Sparks, R. S. J. (1999). Nonlinear dynamics of lava dome extrusion. Nature, 402(6757), 37-41.

Melnik, O., and Sparks, R. S. J. (2002). Dynamics of magma ascent and lava extrusion at Soufrière Hills Volcano, Montserrat. Geological Society, London, Memoirs, 21(1), 153-171.

Melnik, O., and Sparks, R. S. J. (2005). Controls on conduit magma flow dynamics during lava dome building eruptions. Journal of Geophysical Research: Solid Earth, 110(B2).

Mercalli, G., and Silvestri, O., (1891). Le eruzioni dell'isola di Vulcano, incominciate il 3 Augusto 1888 e terminate il 22 Marzo 1890, Ann. Uffic. Cent. Meteorol. Geodin., 10(4), 213 pp.

Mills, O. P., and Rose, W. I. (2010). Shape and surface area measurements using scanning electron microscope stereo-pair images of volcanic ash particles. Geosphere, 6(6), 805-811.

Miwa, T., Toramaru, A., and Iguchi, M. (2009). Correlations of volcanic ash texture with explosion earthquakes from vulcanian eruptions at Sakurajima volcano, Japan. Journal of Volcanology and Geothermal Research, 184(3-4), 473-486.

Miwa, T., and Geshi, N. (2012). Decompression rate of magma at fragmentation: Inference from broken crystals in pumice of vulcanian eruption. Journal of Volcanology and Geothermal Research, 227, 76-84.

Miwa, T., and Toramaru, A. (2013a). Conduit process in vulcanian eruptions at Sakurajima volcano, Japan: Inference from comparison of volcanic ash with pressure wave and seismic data. Bulletin of Volcanology, 75(1), 685.

Miwa, T., Geshi, N., and Shinohara, H. (2013b). Temporal Variation in Volcanic Ash Texture during a Vulcanian Eruption at the Sakurajima Volcano, Japan. Journal of Volcanology and Geothermal Research 260: 80–89. https://doi.org/10.1016/j.jvolgeores.2013.05.010.

Miwa, T., Shimano, T., and Nishimura, T. (2015). Characterization of the luminance and shape of ash particles at Sakurajima volcano, Japan, using CCD camera images. Bulletin of Volcanology, 77(1), 5.

Miwa, T., Iriyama, Y., Nagai, M., and Nanayama, F. (2020). Sedimentation Process of Ashfall during a Vulcanian Eruption as Revealed by High-Temporal-Resolution Grain Size Analysis and High-Speed Camera Imaging. Progress in Earth and Planetary Science 7 (1). https://doi.org/10.1186/s40645-019-0316-8.

Miyagi, I., Ito, J., and Shinohara, H. (2010). Re-activation process of Showa volcanic vent at Sakura jima Volcano in 2008: evidence from volcanic ash. Bulletin of Volcanological Society of Japan, 55, 21-39.

Moore, J.G., Peck, D.L., 1962. Accretionary lapilli in volcanic rocks of the western continental United States. J GEOL 182–193.

Morgan, D. J., and Jerram, D. A. (2006). On estimating crystal shape for crystal size distribution analysis. Journal of Volcanology and Geothermal Research, 154(1-2), 1-7.

Morrisey, M., and Mastin, L. (2000). Vulcanian eruptions in Encyclopedia of Volcanoes, H. Sigurrsson.

Naranjo, J.A. and Polanco, E. (2004). The 2000 AD eruption of Copahue Volcano, Southern Andes. Revista Geológica de Chile, 31 (2): 279–292.

Newman, S., and Lowenstern, J. B. (2002). VolatileCalc: a silicate melt–H_2O–CO_2 solution model written in Visual Basic for excel. Computers and Geosciences, 28(5), 597-604.

Nguyen, C. T., Gonnermann, H. M., Chen, Y., Huber, C., Maiorano, A. A., Gouldstone, A., and Dufek, J. (2013). Film drainage and the lifetime of bubbles. Geochemistry, Geophysics, Geosystems, 14(9), 3616-3631.

Nogami, K., Iguchi, M., Ishihara, K., Hirabayashi, J. I., and Miki, D. (2006). Behavior of fluorine and chlorine in volcanic ash of Sakurajima volcano, Japan in the sequence of its eruptive activity. Earth, planets and space, 58(5), 595-600.

Noguchi, S., Toramaru, A., and Shimano, T. (2006). Crystallization of microlites and degassing during magma ascent: constraints on the fluid mechanical behavior of magma during the Tenjo Eruption on Kozu Island, Japan. Bulletin of Volcanology, 68(5), 432-449.

Noguchi, S., Toramaru, A., and Nakada, S. (2008). Relation between microlite textures and discharge rate during the 1991–1995 eruptions at Unzen, Japan. Journal of Volcanology and Geothermal Research, 175(1-2), 141-155.

Oba, N., Tomita, K., Yamamoto, M., Ohsako, N., and Inoue, K. (1980). Mineral and chemical composition, and mechanism of formation of volcanic ashes from Sakurajima volcano, Kyushu, Japan. The Journal of the Japanese Association of Mineralogists, Petrologists and Economic Geologists 75 (10): 329–36. https://doi.org/10.2465/ganko1941.75.329.

Oishi, M., Nishiki, K., Geshi, N., Furukawa, R., Ishizuka, Y., Oikawa, T., ... and Miwa, T. (2018). Distribution and mass of tephra-fall deposits from volcanic eruptions of Sakurajima Volcano based on posteruption surveys. Bulletin of Volcanology, 80(4), 42.

Oláh, L., Tanaka, H. K., Ohminato, T., Hamar, G., and Varga, D. (2019). Plug formation imaged beneath the active craters of Sakurajima volcano with muography. Geophysical Research Letters, 46(17-18), 10417-10424.

OVDAS-SERNAGEOMIN (2016). Reporte de Actividad Volcanica (RAV), Region del Biobío, marzo – Volumen 06.

OVDAS-SERNAGEOMIN (2016). Reporte de Actividad Volcanica (RAV), Region de la Araucanía, abril – Volumen 04.

Palano, M., Viccaro, M., Zuccarello, F., and Gresta, S. (2017). Magma transport and storage at Mt. Etna (Italy): A review of geodetic and petrological data for the 2002–03, 2004 and 2006 eruptions. Journal of Volcanology and Geothermal Research, 347, 149-164.

Palladino, D. M., and Taddeucci, J. (1998). The basal ash deposit of the Sovana Eruption (Vulsini Volcanoes, central Italy): the product of a dilute pyroclastic density current. Journal of Volcanology and Geothermal Research, 87(1-4), 233-254.

Papale, P. (1999). Strain-induced magma fragmentation in explosive eruptions. Nature, 397(6718), 425-428.

Peccerillo, A., Frezzotti, M. L., De Astis, G., and Ventura, G. (2006). Modeling the magma plumbing system of Vulcano (Aeolian Islands, Italy) by integrated fluid-inclusion geobarometry, petrology, and geophysics. Geology, 34(1), 17-20.

Petrinovic, I. A., Villarosa, G., D´Elia, L., Guzmán, S. P., Páez, G. N., Outes, V., Manzoni, C., Delménico, A., Balbis, C., Carniel, R., Hernando, I. R. (2014). La erupción del 22 de diciembre de 2012 del volcán Copahue, Neuquén, Argentina: caracterización del ciclo eruptivo y sus productos. Revista de la Asociación Geológica Argentina, 71(2), 161-173.

Riley, C. M., Rose, W. I., and Bluth, G. J. (2003). Quantitative shape measurements of distal volcanic ash. Journal of Geophysical Research: Solid Earth, 108(B10).

Ripepe, M., and Marchetti, E. (2002) Array tracking of infrasonic sources at Stromboli volcano, Geophys. Res. Lett., 29(22), 2076, doi:10.1029/2002GL015452.

Ripepe, M., E. Marchetti, and G. Ulivieri (2007), Infrasonic monitoring at Stromboli volcano during the 2003 effusive eruption: Insights on the explosive and degassing process of an open conduit system, J. Geophys. Res. , 112 , B09207, doi:10.1029/2006JB004613.

Ripepe, M., E. Marchetti, C. Bonadonna, A. J. L. Harris, L. Pioli, and G. Ulivieri (2010), Monochromatic infrasonic tremor driven by persistent degassing and convection at Villarrica Volcano, Chile, Geophys. Res. Lett.,37, L15303, doi:10.1029/2010GL043516.

Ripepe, M., Bonadonna, C., Folch, A., Delle Donne, D., Lacanna G., Marchetti, E., Höskuldsson A. (2013). Ash-plume dynamics and eruption source parameters by infrasound and thermal imagery: The 2010 Eyjafjallajökull eruption. Earth and Planetary Science Letters 366, 112–121, http://dx.doi.org/10.1016/j.epsl.2013.02.005

Ripepe, M., Marchetti, E., Delle Donne, D., Genco, R., Innocenti, L., Lacanna G., Valade, S. (2018). Infrasonic early-warning for explosive eruption. Journal of Geophysical Research, Volume 123, doi:10.1029/2018JB015561.

Ripepe, M. and Marchetti, E., (2018) Infrasound Monitoring of volcanic-related hazard for civil protection, in Infrasound Monitoring for Atmospheric Studies: Challenge in Middle-atmosphere Dynamics and Societal benefits, 2nd edition, edited by Le Pichon A., Blanc, E., Hauchecome A., pp , Springer, doi 10.1007/978-3-319-75140-5.

Rose Jr, W. I., and Hoffman, M. F. (1982). THE MAY 18, 1980, ERUPTION OF MOUNT ST. HELENS. In Atmospheric Effects and Potential Climatic Impact of the 1980 Eruptions of Mount St. Helens: Proceedings of a Symposium (Vol. 2240, p. 1). National Aeronautics and Space Administration, Scientific and Technical Information Branch.

Rose Jr, W. I., Anderson Jr, A. T., Woodruff, L. G., and Bonis, S. B. (1978). The October 1974 basaltic tephra from Fuego volcano: description and history of the magma body. Journal of Volcanology and Geothermal Research, 4(1-2), 3-53.

Rose, W. I., and Durant, A. J. (2009). Fine ash content of explosive eruptions. Journal of Volcanology and Geothermal Research, 186(1-2), 32-39.

Rose, W. I., and Durant, A. J. (2011). Fate of Volcanic Ash: Aggregation and Fallout. Geology 39 (9): 895–96. https://doi.org/10.1130/focus092011.1.

Rust, A. C., and Cashman, K. V. (2011). Permeability controls on expansion and size distributions of pyroclasts. Journal of Geophysical Research: Solid Earth, 116(B11).

Sammis, C., King, G., and Biegel, R. (1987). The kinematics of gouge deformation. Pure and Applied Geophysics, 125(5), 777-812.

Savov, I. P., Luhr, J. F., and Navarro-Ochoa, C. (2008). Petrology and geochemistry of lava and ash erupted from Volcán Colima, Mexico, during 1998–2005. Journal of Volcanology and Geothermal Research, 174(4), 241-256.

Scasso, R. A., and Carey, S. (2005). Morphology and formation of glassy volcanic ash from the August 12-15, 1991 eruption of Hudson Volcano, Chile.

Schiavi, F., Kobayashi, K., Moriguti, T., Nakamura, E., Pompilio, M., Tiepolo, M., and Vannucci, R. (2010). Degassing, crystallization and eruption dynamics at Stromboli: trace element and lithium isotopic evidence from 2003 ashes. Contributions to Mineralogy and Petrology, 159(4), 541-561.

Schindelin, J., Arganda-Carreras, I., Frise, E., Kaynig, V., Longair, M., Pietzsch, T., ... and Tinevez, J. Y. (2012). Fiji: an open-source platform for biological-image analysis. Nature methods, 9(7), 676-682.

Schmincke, H. U. (2012). *Volcanism*. Springer Science and Business Media.

Schmith, J., Höskuldsson, Á., and Holm, P. M. (2017). Grain shape of basaltic ash populations: implications for fragmentation. Bulletin of Volcanology, 79(2), 14.

Schumacher, R., and Schmincke, H. U. (1995). Models for the origin of accretionary lapilli. Bulletin of Volcanology, 56(8), 626-639.

Scollo, S., Coltelli, M., Prodi, F., Folegani, M., and Natali, S. (2005). Terminal settling velocity measurements of volcanic ash during the 2002–2003 Etna eruption by an X-band microwave rain gauge disdrometer. Geophysical Research Letters, 32(10).

Self, S., Wilson, L., and Nairn, I. A. (1978). Vulcanian eruption mechanisms.

Shea, T., Houghton, B. F., Gurioli, L., Cashman, K. V., Hammer, J. E., and Hobden, B. J. (2010). Textural studies of vesicles in volcanic rocks: an integrated methodology. Journal of Volcanology and Geothermal Research, 190(3-4), 271-289.

Shea, T. (2017). Bubble nucleation in magmas: a dominantly heterogeneous process?. *Journal of Volcanology and Geothermal Research*, *343*, 155-170.

Sheridan, M. F., and Marshall, J. R. (1987). Comparative charts for quantitative analysis of grain-textural elements on pyroclasts. In Clastic particles. Scanning electron microscopy and shape analysis of sedimentary and volcanic clasts (pp. 98-121).

Sheridan, M. F., and Wohletz, K. H. (1983). Hydrovolcanism: basic considerations and review. *Journal of Volcanology and Geothermal Research*, *17*(1-4), 1-29.

Shukla, M. K., and Sharma, A. (2018). A brief review on breccia: it's contrasting origin and diagnostic signatures. Solid Earth Sciences, 3(2), 50-59.

Smith, C. M., Van Eaton, A. R., Charbonnier, S., McNutt, S. R., Behnke, S. A., Thomas, R. J., ... and Thompson, G. (2018). Correlating the electrification of volcanic plumes with ashfall textures at Sakurajima Volcano, Japan. Earth and Planetary Science Letters, 492, 47-58.

Sorem, R K. (1982). Volcanic Ash Clusters: Tephra Rafts and Scavengers. Journal of Volcanology and Geothermal Research 13 (1): 63–71. https://doi.org/https://doi.org/10.1016/0377-0273(82)90019-1.

Sparks, R. S. J., Bursik, M. I., Carey, S. N., Gilbert, J., Glaze, L. S., Sigurdsson, H., and Woods, A. W. (1997). Volcanic plumes. Wiley.

Sparks, R. S. J., and Brazier, S. (1982). New evidence for degassing processes during explosive eruptions. Nature, 295(5846), 218-220.

Sparks, R., (2003). Causes and consequences of pressurisation in lava dome eruptions. Earth and Planetary Science Letters 150, 177–189.

Spieler, O., Dingwell, D. B., and Alidibirov, M. (2004). Magma fragmentation speed: an experimental determination. Journal of Volcanology and Geothermal Research, 129(1-3), 109-123.

Stix, J., Torres, R. C., Narváez, L., Raigosa, J. A., Gómez, D., and Castonguay, R. (1997). A model of vulcanian eruptions at Galeras volcano, Colombia. Journal of Volcanology and Geothermal Research, 77(1-4), 285-303.

Storti, F., and Balsamo, F. (2010). Particle size distributions by laser diffraction: sensitivity of granular matter strength to analytical operating procedures. *Solid Earth*, *1*(1), 25.

Suzuki, Y., Nagai, M., Maeno, F., Yasuda, A., Hokanishi, N., Shimano, T., ... and Nakada, S. (2013). Precursory activity and evolution of the 2011 eruption of Shinmoe-dake in Kirishima volcano—insights from ash samples. Earth, planets and space, 65(6), 11.

Storti, F., Billi, A., and Salvini, F. (2003). Particle size distributions in natural carbonate fault rocks: insights for non-self-similar cataclasis. Earth and Planetary Science Letters, 206(1-2), 173-186.

Taddeucci, J., Pompilio, M., and Scarlato, P. (2002). Monitoring the explosive activity of the July–August 2001 eruption of Mt. Etna (Italy) by ash characterization. Geophysical Research Letters, 29(8), 71-1.

Taddeucci, J., Pompilio, M., and Scarlato, P. (2004). Conduit processes during the July–August 2001 explosive activity of Mt. Etna (Italy): inferences from glass chemistry and crystal size distribution of ash particles. Journal of Volcanology and Geothermal Research, 137(1-3), 33-54.

Taddeucci, J., Scarlato, P., Montanaro, C., Cimarelli, C., Del Bello, E., Freda, C., Andronico, D., Gudmundsson, M. T., and Dingwell, D. B. (2011). Aggregation-Dominated Ash Settling from the Eyjafjallajokull Volcanic Cloud Illuminated by Field and Laboratory High-Speed Imaging. Geology. https://doi.org/10.1130/G32016.1.

Tait, S., and Jaupart, C. (1989). Compositional convection in viscous melts. Nature, 338(6216), 571-574.

Tameguri, T., Iguchi, M., and Ishihara, K. (2002). Mechanism of explosive eruptions from moment tensor analyses of explosion earthquakes at Sakurajima volcano, Japan. Bulletin of the Volcanological Society of Japan, 47(4), 197-215.

Tasirin, S. M., and Geldart, D. (1999). The elutriation of fine and cohesive particles from gas fluidized beds. Chemical Engineering Communications, 173(1), 175-195.

Teplitskii, Y., & Kovenskii, V. (2009). Velocity of full fluidization of a bed of polydisperse granular materials. *Journal of Engineering Physics & Thermophysics*, *82*(2).

Textor, C., Graf, H. F., Herzog, M., Oberhuber, J. M., Rose, W. I., and Ernst, G. G. (2006). Volcanic particle aggregation in explosive eruption columns. Part I: Parameterization of the microphysics of hydrometeors and ash. Journal of Volcanology and Geothermal Research, 150(4), 359-377.

Toramaru, A. (1989). Vesiculation process and bubble size distributions in ascending magmas with constant velocities. Journal of Geophysical Research: Solid Earth, 94(B12), 17523-17542.

Toramaru, A. (1990). Measurement of bubble size distributions in vesiculated rocks with implications for quantitative estimation of eruption processes. Journal of Volcanology and Geothermal Research, 43(1-4), 71-90.

Toramaru, A., Noguchi, S., Oyoshihara, S., and Tsune, A. (2008). MND (microlite number density) water exsolution rate meter. Journal of Volcanology and Geothermal Research, 175(1-2), 156-167.

Tuffen, H., and Dingwell, D. (2005). Fault textures in volcanic conduits: evidence for seismic trigger mechanisms during silicic eruptions. *Bulletin of Volcanology*, *67*(4), 370-387.

Tuffen, H., Smith, R., and Sammonds, P. R. (2008). Evidence for seismogenic fracture of silicic magma. *Nature*, *453*(7194), 511-514.

Turcotte, D. L. (1986). Fractals and fragmentation. Journal of Geophysical Research: Solid Earth, 91(B2), 1921-1926.

Turcotte, D. L., Ockendon, H., Ockendon, J. R., and Cowley, S. J. (1990). A mathematical model of vulcanian eruptions. Geophysical Journal International, 103(1), 211-217.

Turcotte, D. L. (1997). Fractals and chaos in geology and geophysics. Cambridge university press.

Ulivieri, G., Ripepe, M., Marchetti, E. (2013). Infrasound reveals transition to oscillatory discharge regime during lava fountaining: Implication for early warning. Geophysical Research Letters, Volume 40, Issue 12, pages 3008-3013.

Valade, S., Lacanna, G., Coppola, D., Laiolo, M., Pistolesi, M., Delle Donne, D., ... and Cigolini, C. (2016). Tracking dynamics of magma migration in open-conduit systems. Bulletin of Volcanology, 78(11), 78.

Van Eaton, A.R., Muirhead, J.D., Wilson, C.J.N., and Cimarelli, C., (2012). Growth of volcanic ash aggregates in the presence of liquid water and ice: an experimental approach. Bull. Volcanol. 74, 1963–1984.

Van Eaton, A.R., and Wilson, C.J.N. (2013). The Nature, Origins and Distribution of Ash Aggregates in a Large-Scale Wet Eruption Deposit: Oruanui, New Zealand. Journal of Volcanology and Geothermal Research 250: 129–54. https://doi.org/https://doi.org/10.1016/j.jvolgeores.2012.10.016

Veitch, G., and Woods, A. W. (2001). Particle Aggregation in Volcanic Eruption Columns. Journal of Geophysical Research: Solid Earth 106 (B11): 26425–41.

Vetere, F., Petrelli, M., Morgavi, D., and Perugini, D. (2015). Dynamics and time evolution of a shallow plumbing system: the 1739 and 1888–90 eruptions, Vulcano Island, Italy. Journal of Volcanology and Geothermal Research, 306, 74-82.

Vogel, A., Durant, A.J., Cassiani, M., Clarkson, R.J, Slaby, M., Diplas, S., Krüger, K., and Stohl. A. (2019). Simulation of Volcanic Ash Ingestion Into a Large Aero Engine: Particle–Fan Interactions. Journal of Turbomachinery 141 (1). https://doi.org/10.1115/1.4041464.

Waitt, R. B., Mastin, L. G., and Miller, T. P. (1995). Ballistic showers during crater peak eruptions of Mount Spurr volcano, summer 1992. USGS Bull, 2139, 89-106.

Walters, A. L., Phillips, J. C., Brown, R. J., Field, M., Gernon, T., Stripp, G., & Sparks, R. S. J. (2006). The role of fluidisation in the formation of volcaniclastic kimberlite: grain size observations and experimental investigation. Journal of volcanology and geothermal research, 155(1-2), 119-137.

Watanabe, K., Danhara, T., Watanabe, K., Terai, K., and Yamashita, T. (1999). Juvenile volcanic glass erupted before the appearance of the 1991 lava dome, Unzen volcano, Kyushu, Japan. Journal of volcanology and geothermal research, 89(1-4), 113-121.

Weather, W. (2015). University of Wyoming, College of Engineering, Department of Atmospheric Science. Worldwide Radiosonde Soundings of the Atmosphere.

Wilson, L., and Huang, T. C. (1979). The influence of shape on the atmospheric settling velocity of volcanic ash particles. Earth and Planetary Science Letters, 44(2), 311-324.

Wohletz, K. H. (1983). Mechanisms of hydrothermal pyroclast formation: grain-size, scanning electron microscopy and experimental studies. Journal of Volcanology and Geothermal Research, 17, 31-63.

Wohletz, K. H. (1986). Explosive magma-water interactions: Thermodynamics, explosion mechanisms, and field studies. Bulletin of Volcanology, 48(5), 245-264.

Wohletz, K., Zimanowski, B., and Büttner, R. (2013). Magma-water interactions. Modeling volcanic processes. Cambridge University Press, New York, 230-257.

Woods, A. W. (1995). A model of vulcanian explosions. Nuclear Engineering and Design, 155(1-2), 345-357.

Woods, A. W., and Bower, S. M. (1995). The decompression of volcanic jets in a crater during explosive volcanic eruptions. Earth and Planetary Science Letters, 131(3-4), 189-205.

Wright, H. M., Cashman, K., Rosi, M., and Cioni, R. (2003). Physical parameters of vulcanian eruptions at Pichincha Volcano, Ecuador: bomb morphologies and textures. AGUFM, 2003, V12A-0566.

Wright, H. M., Cashman, K. V., Rosi, M., and Cioni, R. (2007). Breadcrust bombs as indicators of Vulcanian eruption dynamics at Guagua Pichincha volcano, Ecuador. Bulletin of Volcanology, 69(3), 281-300.

Wright, H. M., Cashman, K. V., Mothes, P. A., Hall, M. L., Ruiz, A. G., and Le Pennec, J. L. (2012). Estimating rates of decompression from textures of erupted ash particles produced by 1999–2006 eruptions of Tungurahua volcano, Ecuador. Geology, 40(7), 619-622.

Yamamoto, H., Watson, I. M., Phillips, J. C., and Bluth, G. J. (2008). Rise dynamics and relative ash distribution in vulcanian eruption plumes at Santiaguito Volcano, Guatemala, revealed using an ultraviolet imaging camera. Geophysical research letters, 35(8).

Yamanoi, Y., Takeuchi, S., Okumura, S., Nakashima, S., and Yokoyama, T. (2008). Color Measurements of Volcanic Ash Deposits from Three Different Styles of Summit Activity at Sakurajima Volcano, Japan: Conduit Processes Recorded in Color of Volcanic Ash. Journal of Volcanology and Geothermal Research 178 (1): 81–93. https://doi.org/10.1016/j.jvolgeores.2007.11.013.

Yokoo, A., Iguchi, M., Tamerugi, T., and Yamamoto, K. (2013). Processes Prior to Outbursts of Vulcanian Eruption at Showa Crater of Sakurajima Volcano (<Special Section> Sakurajima Special Issue). Bulletin of the Volcanological Society of Japan, 58(1), 163-181.

Zimanowski, B., Büttner, R., Dellino, P., White, J. D., and Wohletz, K. H. (2015). Magma–water interaction and phreatomagmatic fragmentation. In The encyclopedia of volcanoes (pp. 473-484). Academic Press.